May 2, 1989

TO: Distribution

FROM: Jeanne Collins, x4-4438

Attached is a new cover for Galileo Project Document 1625-210. This document was erroneously issued as 625-210. Please replace the cover on your copy of the document.

Sorry for any inconvenience.

1625-210

Galileo

Solid-State Imaging Subsystem Calibration Report: Part 1

H. Breneman
K. Klaasen

November 1, 1988

Jet Propulsion Laboratory
California Institute of Technology

JPL D-5880

Distribution

Galileo Imaging Science Team
SSI Associated IDSs
Imaging Science Group

D. Alexander	168-514
R. Carlson	183-301
M. Clary	168-222
A. Collins	179-206
J. Collins	111-130
E. Danielson	Caltech
R. Davis	264-211
J. Dunne	264-122
G. Ervin	183-133
W. Fawcett	264-419
M. Hine (5)	264-419
T. Johnson	183-501
K. Jones	168-514
C. Kahn	168-222
S. Lavoie	168-514
R. Locke	168-222
W. O'Neil	264-419
S.T. Smith	179-225
C. Stevens	168-227
L .Wynn	168-514
G. Yagi	168-427
C. Yeates	264-419
Vellum (2)	111-B25

ACKNOWLEDGMENTS

Calibration of the Galileo Solid State Imaging (SSI) Subsystem camera was the result of well-organized teamwork. Many individuals participated in these activities and their dedicated efforts contributed significantly to the success of the calibration program. Their help and contributions are greatly appreciated by all concerned.

Special thanks are due to C. Kahn for her untiring support in this whole effort and to L. Douglass and D. Thiessen for their coordination of all hardware over the two-year effort. They are also due thanks as members of the Calibration Team in obtaining data, sometimes under difficult and demanding conditions. The authors wish to express their special appreciation to M. Benesh, P. Jepsen and A. Collins for their continued organizational and moral support.

Particular acknowledgments are expressed to the Engineering Team under the coordination of M. Clary for their unfailing technical assistance: R. Locke, J. Tomey, J. Johnston, S. Seng, D. Speer, J. Kangas, D. Dunn, D. Winther, J. Janesick, W. Hornaday, T. Bursch, S. Geller, J. Stellman, D. Hagar, D. Perrenoud, D. Thiessen, K. Meredith and P. Kobzeff.

Last, but not least, the authors are indebted to the Multimission Image Processing Laboratory (MIPL) personnel for their support in data processing and analysis: E. Korsmo, D. Alexander, L. Wainio, S. LaVoie, G. Garneau, G. Yagi, M. Morrill and A. Ocampo.

DEFINITION OF ABBREVIATIONS

ADC	Analog-to-Digital Converter
CCD	Charge Coupled Device
CIE	Commission Internationale de l'Eclairage (International Commission on Illumination)
D/C	Dark Current
ftL	foot-Lamberts
GLL	Galileo
IFU	Interface Unit of the SSI SE
IPL	Image Processing Laboratory (at JPL)
MIPL	Multimission Image Processing Laboratory
MTF	Modulation Transfer Function
SAF	Spacecraft Assembly Facility
SE	Support Equipment
S/N	Serial Number
SSI	Solid State Imaging

CONTENTS

SECTION 1

INTRODUCTION

This calibration report compiles the results of laboratory calibrations and tests performed prior to 1986 on the Solid-State Imager (SSI) camera, which was designed and built for the Galileo mission to Jupiter. A comprehensive analysis of the data obtained and a detailed discussion of their accuracy are also included. Brief descriptions of the methods, techniques and equipment are provided so that the report can also be used as a convenient calibration manual for future space-flight projects.

The ultimate goal of this report is to provide information and data that will satisfy the basic purpose of the Galileo imaging experiment, which is to perform an exploratory orbital mission of Jupiter and its satellites. The objective of SSI calibrations, then, was to define the characteristics of the instrument so that data obtained by it can be reliably interpreted without limitations because of uncertainties about instrumental performance.

The calibration program can be divided into four parts:

(a) Component calibrations.

(b) Pre-1986 subsystem calibrations (bench and thermal vacuum chamber). The flight SSI was calibrated in the thermal vacuum chamber three times: June, 1983; April, 1984; and May, 1985.

(c) Post-1986 laboratory subsystem calibrations.

(d) In-flight calibrations.

Parts (a) and (b) are fully documented in this report. Results from parts (c) and (d) will be discussed in separate reports. The in-flight calibrations are very important because they will verify and update the data contained in this document and will enable the Multimission Image Processing Laboratory (MIPL) to finalize the SSI calibration program.

Every effort has been made to include all substantial and important calibration results, but a great deal of supplementary data has been omitted to reduce this document to a size technically and economically feasible for publication. These data have been filed at JPL and can be made available to all users upon request to the authors.

A number of abbreviations are used throughout this report. Most of them are widely known or self-explanatory, but it may be beneficial for

the user to become familiar with them before attempting to read the report (see "Definition of Abbreviations" on page vii).

SECTION II

CALIBRATION EQUIPMENT

Successful implementation of all Galileo (GLL) SSI tests and calibrations required by References 2-1 and 2-2 necessitated utilization of a complex set of calibration equipment including a Texas Instruments (TI) 990/12 computer with peripherals (referred to as Support Equipment), two JPL light cannons, two collimators, and a set of specially designed targets. Their purpose and technical mode of application are described in this section. Also described are the optical bench and the thermal vacuum chamber used in performing the various calibrations. Because of the need to cool the SSI detector to -110° C, all subsystem-level calibrations had to be carried out in the thermal vacuum chamber.

A. SSI SUPPORT EQUIPMENT (SE)

The SSI Support Equipment (SE) provides a means of functional testing and calibration of the Galileo SSI camera. It consists of six basic units: the central processor, two disk drives, the DeAnza display unit, two tape recorders, two printers, and two monitors (see schematic, Figure 2-1). In addition to these, there is an A-Trace, Zeta Plotter, Unifax, and Time Code Generator which can be utilized. To connect the support equipment to the camera, an Interface Unit (IFU) is used along with a set of power supplies and various diagnostic aids. (For a detailed description of the SE, see Reference 2-3.)

The SE was used for sending commands (such as shutter speed, filter wheel position, camera mode, frame rate, gain state, light flood on/off, etc.), for monitoring the camera condition, and for recording engineering and pixel data. Engineering data were recorded on floppy disks, which were constantly monitored for full capacity. Pixel data were recorded in sets of up to 80 frames on each mountable hard disk. All computer test sequences were written to comply with this maximum data-disk capacity. Data could be acquired either by pre-programmed sequences or by individually commanded frames. Recorded frames are labeled, and real-time and non-real-time displays are available for monitoring data quality.

B. LIGHT CANNONS

Two different JPL light cannons were used as light sources for SSI calibrations:

(1) The tungsten light cannon (Figure 2-2) for most subsystem-level radiometric calibrations.

(2) The xenon light cannon (Figure 2-3) for illumination of targets

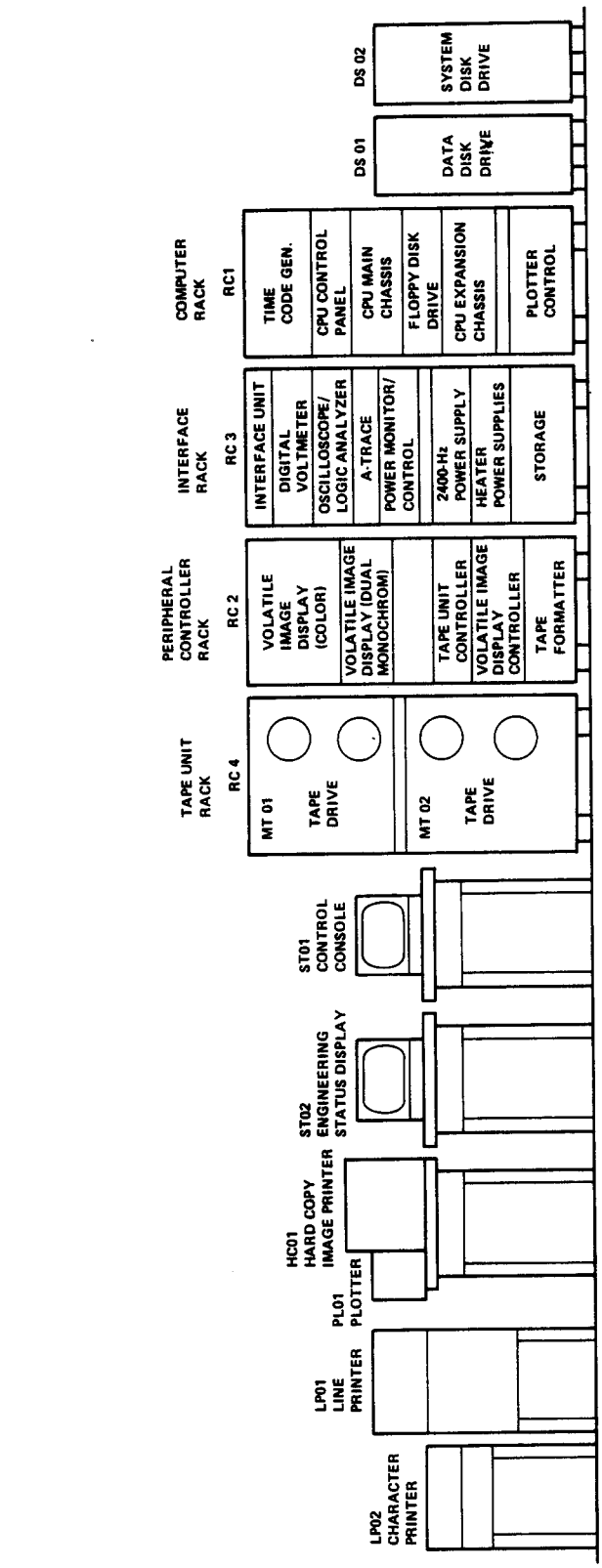

Figure 2-1. Schematic diagram of Support Equipment (SE) for the Galileo SSI calibration.

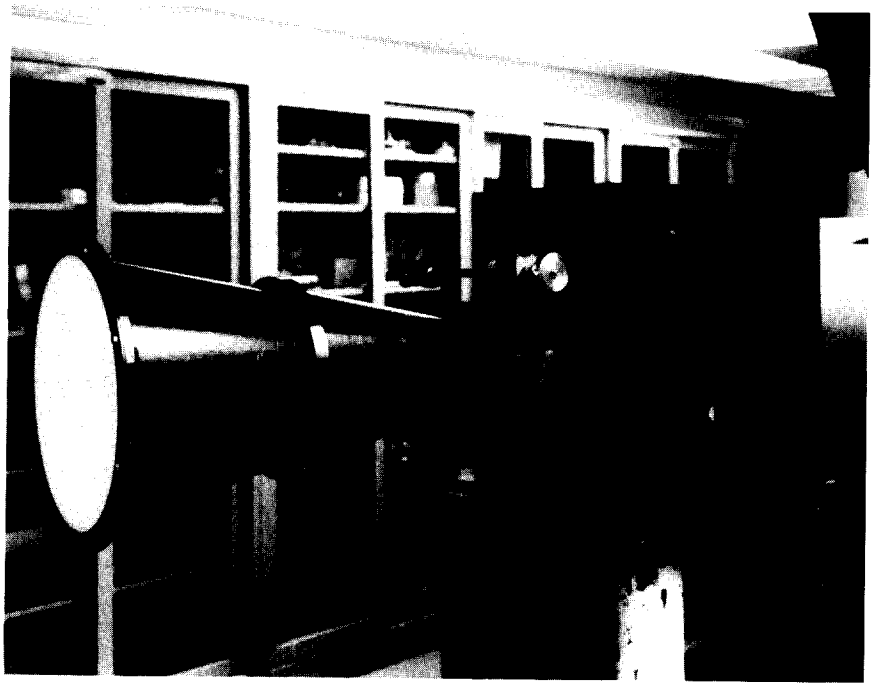

Figure 2-2. Tungsten light cannon.

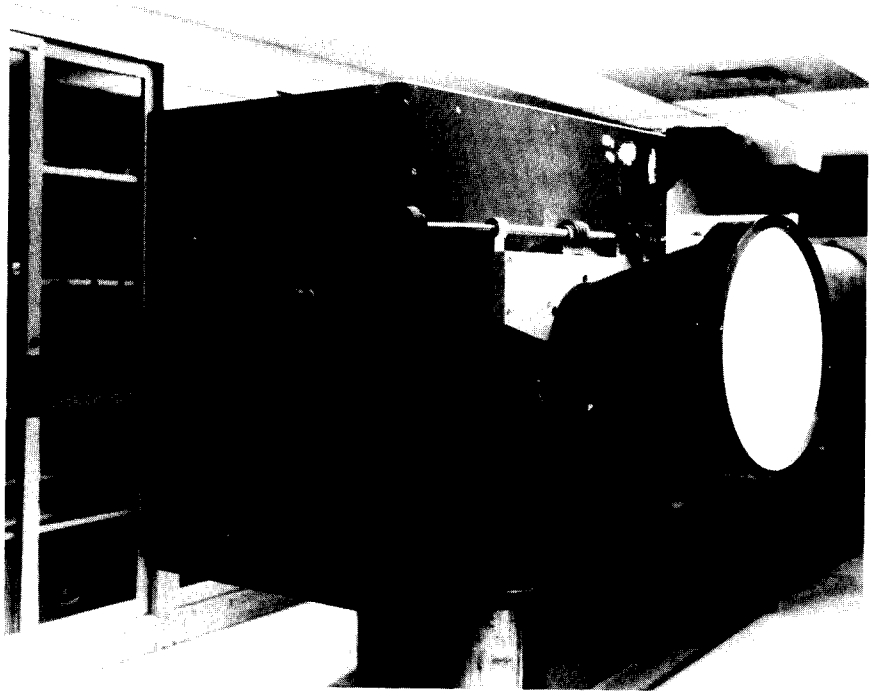

Figure 2-3. Xenon light cannon.

in the Fairchild collimator and for other calibrations in which a high-intensity source was required.

The tungsten cannon is equipped with one 100-W tungsten-halogen bulb in an integrating cavity. A power supply, current-regulated for stability and mounted inside the cannon box, is required for operation of the bulb. The xenon cannon is equipped with two 1600-W high-pressure xenon arc discharge lamps in an integrating cavity. Two 2000-W power supplies, also current-regulated for stability, are required for operation of this light cannon. Both cannons have a variable iris diaphragm for brightness regulation, a second conical integrating cavity, and a 30-cm diameter neutral Plexiglas diffuser.

1. Spectral Curves

The spectral radiance of the tungsten light cannon was measured for use in reduction of the calibration data, particularly the light transfer curves. The light cannon radiance was measured using a Gamma Scientific C-3 Spectro-radiometer[1] by comparing its brightness to that of a calibrated spectral radiance standard[2]. The approximate color temperature of the spectral irradiance standard was 2850 K. The calibration accuracy of the reference standard was ± 2.5% with respect to National Bureau of Standards radiance standards. The tungsten cannon spectral curve, obtained in April, 1985, at a brightness of about 40 foot-Lamberts (ftL) at the center of the diffuser, is shown in Figure 2-4.

The spectral output of the tungsten cannon has changed gradually with time. Its output in the green and red progressively increased over a period of three years relative to its output in the violet and the near IR. The relative output at 650 nm was about 20% higher in April, 1985, than in July, 1982, while that at 400 nm and 1000 nm was about 20% lower. The approximate color temperature of the tungsten cannon with its diffuser has gone from about 2640 K in May, 1983 to about 2560 K in April, 1985. No variations in the tungsten light cannon spectrum have been measured for different locations on the face of the diffuser to within the achievable measurement accuracy (< 1% above 500 nm, ±4% at 450 nm, ±13% at 400 nm, and ±50% below 370 nm).

---

1 For information on the Gamma Scientific Radiometer refer to Reference 2-4.

2. The radiance standard, RS-10A, was purchased from and calibrated by Gamma Scientific. See above for reference.

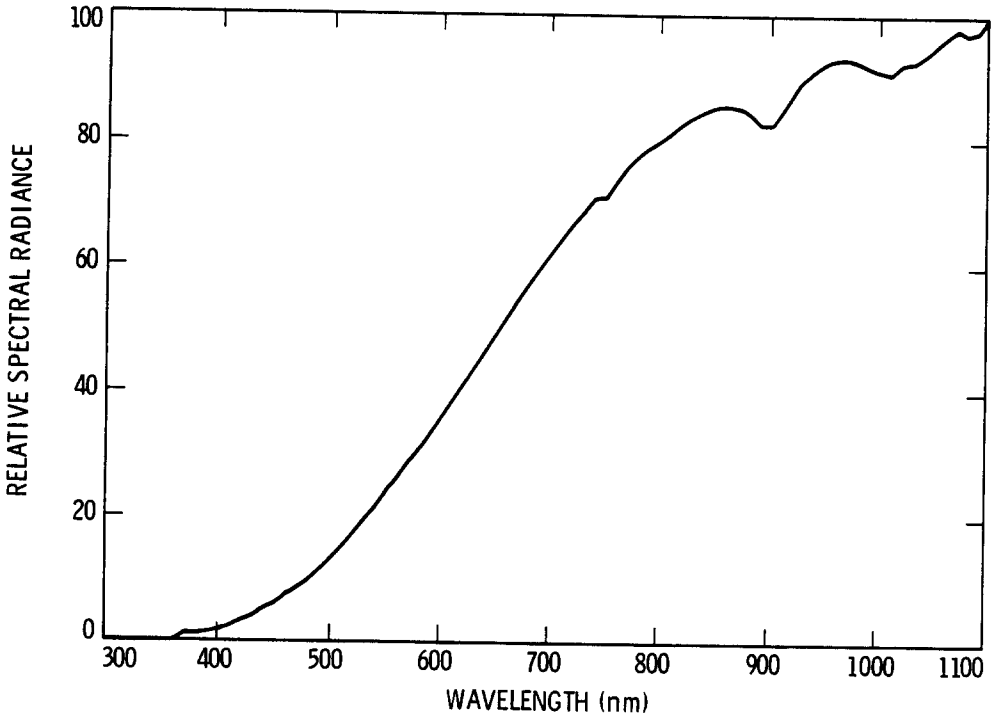

Figure 2-4. Spectral radiance of the tungsten light cannon at 40 ftL brightness.

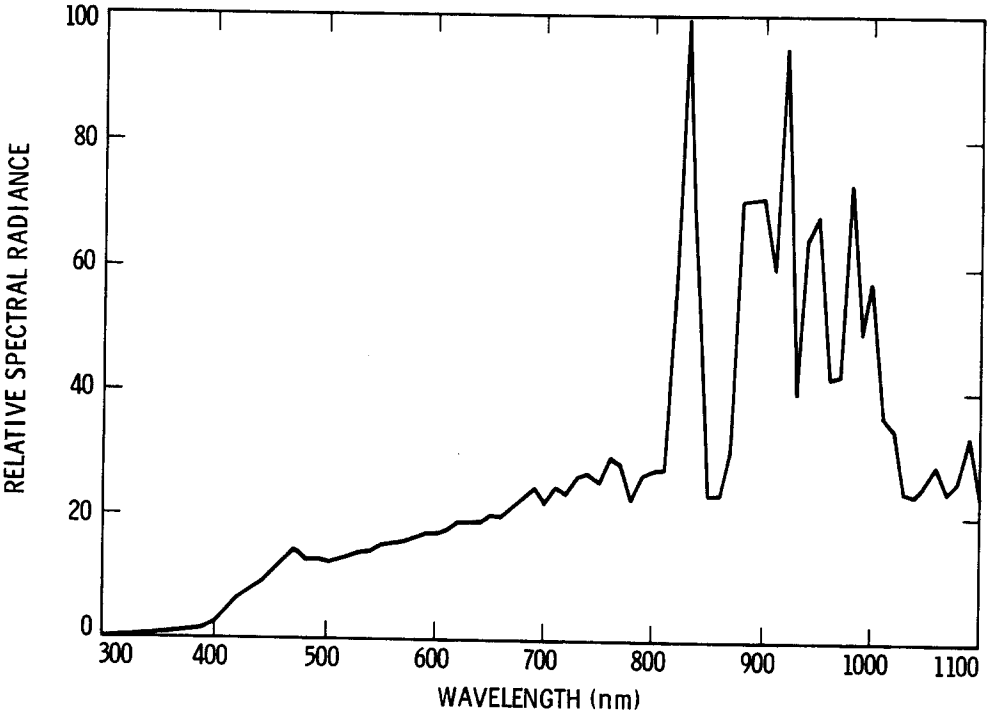

Figure 2-5. Spectral radiance of the xenon light cannon at 100 ftL brightness.

The xenon cannon spectral radiance was measured in a similar way. These results are documented in Figure 2-5 for a brightness level of 100 ftL.

For those who require numerical data for computer applications, the spectral data are summarized in Tables 2-1 and 2-2.

2. Field Flatness

The field flatness (brightness distribution) across the Plexiglas diffuser of the tungsten light cannon was measured perpendicular to the diffuser using the Gamma model 700 photometer at 0.5-inch intervals in a cross pattern, in both the horizontal and the vertical directions. The average of the four measurements at each radial distance from the center of the diffuser are shown in Figure 2-6 for a brightness level of about 40 ftL at the center of the diffuser. The average relative brightness at any radial distance from the center changes by <1.0% over the entire range of absolute brightness levels of the light cannon.

The flatness may seem to be rather poor, but its effect upon radiometric calibrations, especially as it pertains to shading, is insignificant since the diffuser was always out of focus to the camera during radiometric calibration, which meant that each light-source point was blurred across a large part of the CCD. (The closest focal point of the camera is approximately 18 km.) The net result, then, was an extremely flat-field illumination in the image plane. Because of the secondary-mirror center-obscuration of the telescope, the SSI detector only sees an annulus of diameter between 89 and 181 mm of the diffuser during radiometric calibrations.

The brightness falloff is only approximately radially symmetric, with the relative brightness varying by as much as ±3% over the four points at a given radial distance. However, because each CCD pixel is affected by the average light level over the annulus described above shifted off center only by the actual lateral distance of the pixel from the CCD center (8.62 mm maximum), the shading introduced by any radial asymmetry in brightness falloff will be insignificant compared to that due to the brightness falloff itself, which is < 0.1% to begin with. Thus, any radial asymmetries in the brightness falloff can be ignored. The brightness falloff has varied by < 2% at a given radial distance over a period of more than 3 years. Measurements of the brightness of any point on the diffuser relative to that at the center are repeatable to better than 1% on a given day.

The field flatness of the tungsten light cannon was also measured using the Gamma 2000 telephotometer viewing the diffuser from a point 46

Table 2-1. Tungsten Light Cannon Relative Spectral Radiance

λ (nm)	value	λ (nm)	value	λ (nm)	value	λ (nm)	value
350	0.00	540	21.40	730	68.27	920	87.92
360	0.00	550	24.42	740	71.00	930	90.17
370	1.04	560	26.13	750	71.08	940	91.53
380	0.88	570	28.73	760	73.50	950	92.92
390	1.41	580	30.63	770	76.12	960	93.28
400	1.72	590	33.50	780	77.97	970	93.42
410	2.35	600	36.00	790	79.18	980	92.65
420	3.18	610	38.52	800	80.35	990	91.82
430	3.96	620	41.06	810	81.76	1000	91.30
440	5.17	630	43.79	820	83.03	1010	91.01
450	6.07	640	46.28	830	84.13	1020	92.63
460	7.61	650	49.20	840	85.09	1030	92.75
470	8.70	660	51.86	850	85.76	1040	93.77
480	9.95	670	54.32	860	85.65	1050	95.11
490	11.47	680	56.92	870	85.45	1060	96.81
500	13.34	690	59.40	880	84.72	1070	98.11
510	15.32	700	61.82	890	82.78	1080	97.25
520	17.37	710	64.38	900	82.64	1090	97.75
530	19.48	720	66.58	910	84.95	1100	100.00

Table 2-2. Xenon Light Cannon Relative Spectral Radiance

λ (nm)	value	λ (nm)	value	λ (nm)	value	λ (nm)	value
300	0.13	510	12.87	710	24.81	910	59.76
310	0.19	520	13.44	720	23.69	920	94.83
320	0.28	540	13.95	730	26.35	930	39.62
330	0.40	550	14.28	740	26.99	940	64.43
340	0.53	560	15.23	750	25.50	950	68.49
350	0.70	570	15.48	760	29.68	960	42.22
360	0.87	590	15.81	770	28.43	970	42.71
370	1.09	600	16.37	780	22.80	980	73.41
380	1.35	610	17.06	790	26.57	990	49.81
390	1.75	620	17.04	800	27.34	1000	57.45
400	2.66	630	17.75	810	27.60	1010	36.09
410	4.54	640	18.94	820	55.11	1020	34.08
420	6.52	650	19.09	830	100.00	1030	23.99
430	7.74	660	19.01	840	52.56	1040	23.48
440	8.96	670	20.22	850	23.51	1050	25.44
450	10.82	680	20.12	860	23.65	1060	28.20
460	12.58	690	21.43	870	30.78	1070	23.93
470	14.48	700	23.01	880	70.49	1080	25.81
480	12.68	710	24.79	890	70.69	1090	33.02
490	12.83	720	22.13	900	70.89	1100	24.67
500	12.42						

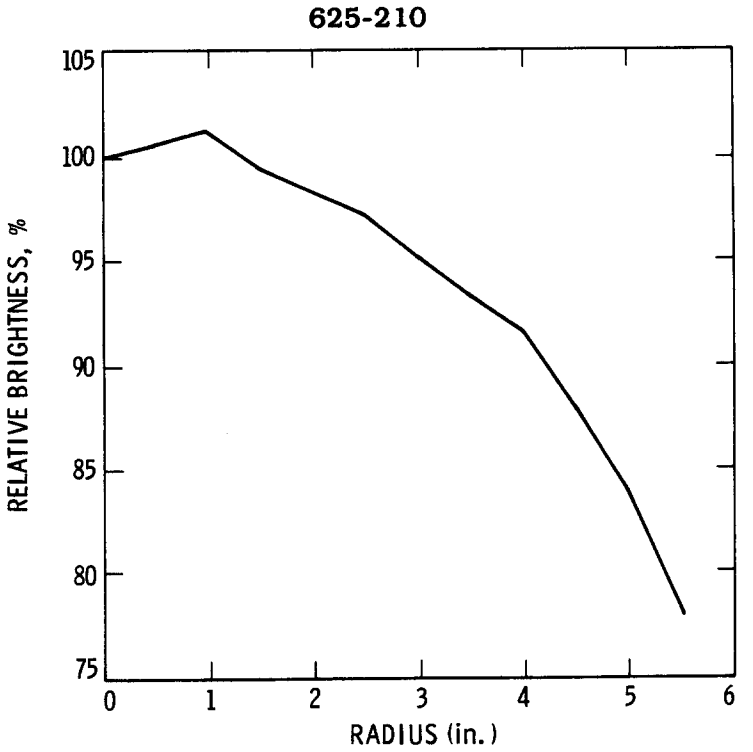

Figure 2-6. Field flatness (brightness distribution) vs. radius for the tungsten light cannon at 40 ftL luminance, measured perpendicular to the diffuser.

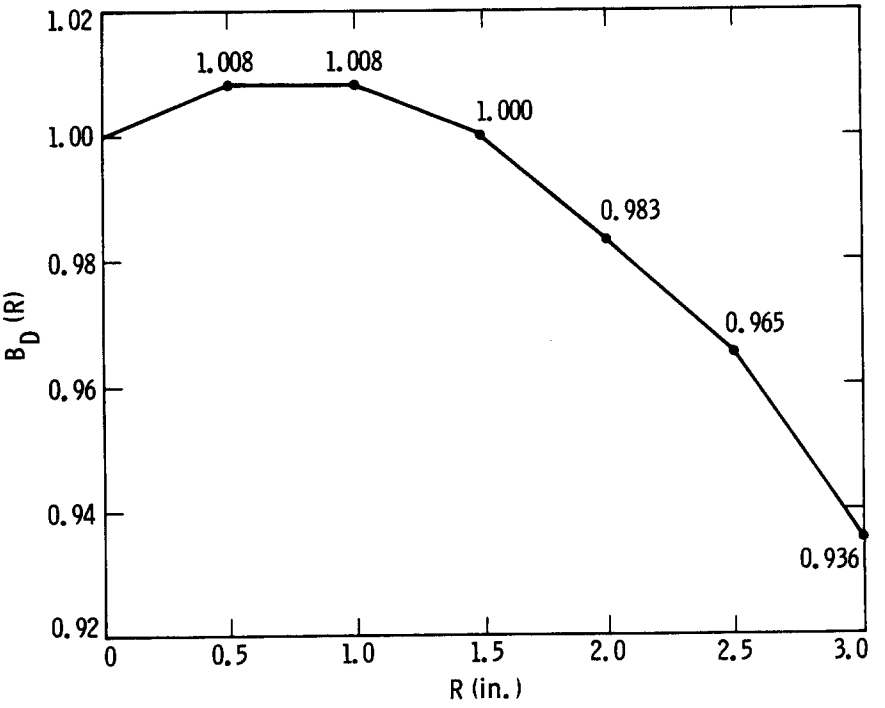

Figure 2-7. Field flatness (brightness distribution) vs. radius for the tungsten light cannon measured from fixed point 46 in. from diffuser.

inches away from and perpendicular to the diffuser. This measurement, therefore, included any effects of a slightly non-perpendicular viewing direction. These data were required for the T/# calibration described in Section III-A-2. The results are plotted in Figure 2-7 out to 3 inches from the center. The differences from the perpendicular measurement are slight, as expected for such small angles.

The field flatness of the xenon cannon measured perpendicular to the diffuser is shown in Figure 2-8. It is slightly less flat than the tungsten cannon, but again any shading effects during radiometric calibrations of the SSI are negligible.

3. Brightness Calibration

The success of radiometric calibrations is dependent, to a large degree, upon the reliability of the light cannons to produce consistent illumination levels over an extended period of time. Therefore, the light cannons were equipped with a variable iris mechanism and a Veeder root counter which allows regulation of the iris diameter. To determine the Veeder-root/brightness relationship, a calibrated variable-transmission standard of the crossed-polarizer type was used in combination with the Gamma 700 photometer, as shown schematically in Figure 2-9. Based on the method of constant output, the resulting Veeder-root count versus inverse-filter transmission curve was plotted on log-log paper, forming the light cannon relative brightness curve.

The Veeder root counts are supposed to be linearly proportional to the iris diameter and hence to the square root of the radiance generated in the second conical integrating cavity. However, the zero point on the dial usually does not correspond to a fully closed iris. The absolute scaling of the relative brightness curve had to be determined by comparing the light cannon output with a known light standard source. The Gamma scientific telephotometer, model 2000, was used for this purpose. A typical light-cannon calibration curve, showing both the relative and absolute scales, is presented in Figure 2-10 for the tungsten cannon. Figure 2-11 shows a comparable curve for the xenon cannon.

Although the relative brightness curves remained fairly constant throughout the SSI calibrations, they were remeasured periodically. The absolute brightness scales were established and rechecked by using the telephotometer in connection with a calibrated luminance standard at the beginning and end of each calibration. Calibration of the tungsten cannon required a reference light standard source which had a low-level output (~35 ftL). This goal was achieved in two ways. Prior to 1984, a calibrated

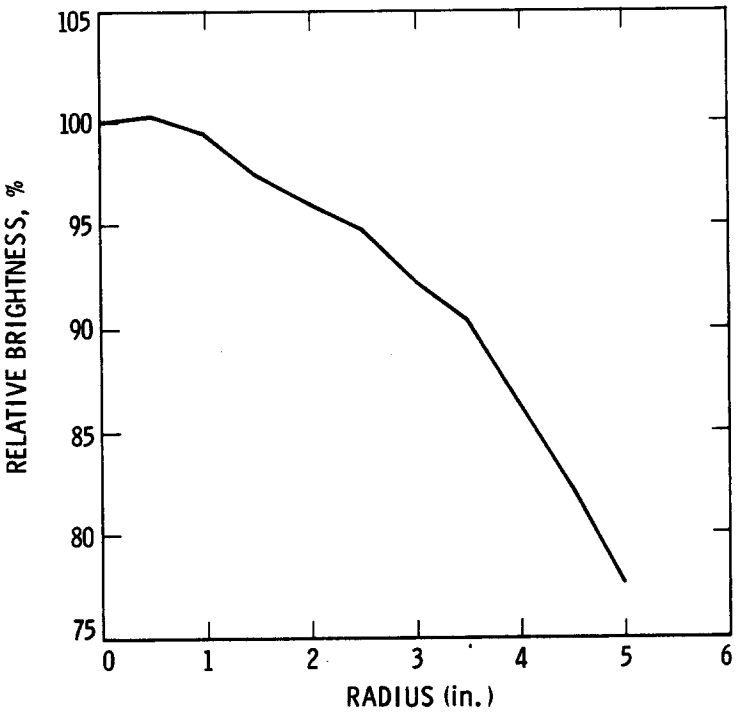

Figure 2-8. Field flatness (brightness distribution) vs. radius for the xenon light cannon at 100 ftL luminance, measured perpendicular to the diffuser.

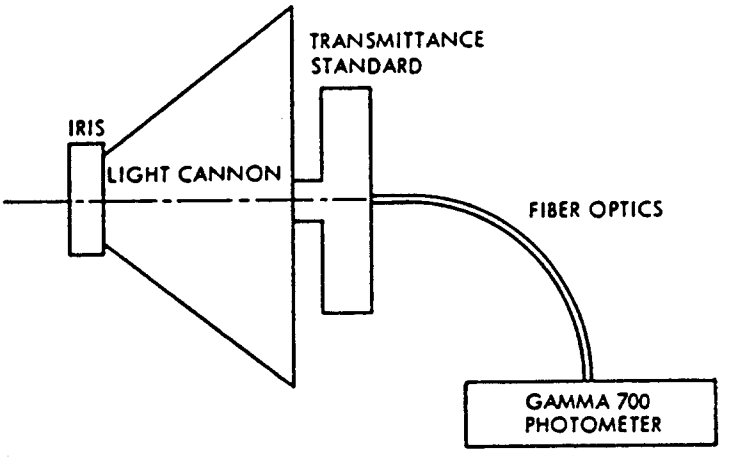

Figure 2-9. Schematic diagram of equipment setup for the light cannon relative brightness calibration.

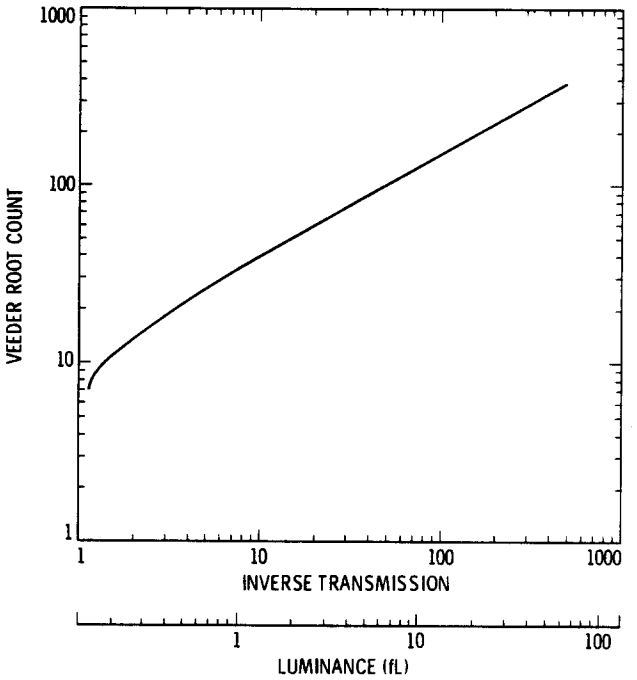

Figure 2-10. Brightness calibration curve for the tungsten light cannon.

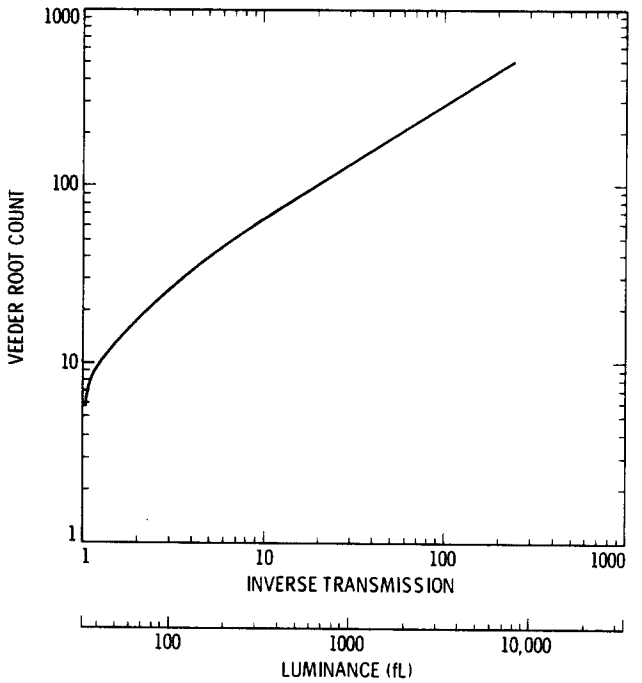

Figure 2-11. Brightness calibration curve for the xenon light cannon.

100-ftL standard source was fitted with a calibrated neutral density screen. This arrangement provided a standard light source which emitted 36.9 ftL. For 1984 and beyond, a Photo Research LS-65 self-checking variable-setting luminance standard was used with a standard setting of 37.5 ftL. For the xenon cannon, the 100-ftL standard without the screen was used prior to 1984, and the Photo Research variable standard set to 100 ftL was used after that. The projected field of view of the telephotometer on the diffuser was between 7 and 11 mm in diameter, depending upon its distance from the light cannon.

The precautions and techniques described above have allowed a consistent series of radiometric measurements over the entire SSI calibration phase. The limiting accuracy of the light cannon output was a function of random variations of the light standards (up to ±2%) and also by the backlash of the variable iris mechanism, which results in an approximate ±0.5 Veeder root count accuracy, or in terms of brightness, 0.9% at 500 ftL (xenon cannon), 0.3% at 40 ftL and 2.4% at 1 ftL. Long-term drifts of ±10% in tungsten light cannon output for a given iris setting have been observed over the two-year calibration period. However, changes over a period of 1 to 2 weeks, as required to conduct a thermal vacuum calibration, were typically only about ±1% (including both light cannon and reference standard variations).

C. COLLIMATORS

Two different types of collimators were used for SSI imaging calibrations, such as focal length, modulation transfer function (MTF), point-response function and color reconstruction. They were the Fairchild collimator and the GLL 1:1 collimator.

The focal length calibration (as well as focusing the SSI itself) utilized the Fairchild collimator (Figure 2-12), which is located in the JPL optical tunnel. Its axis is aligned with the axis of the Askania optical bench (see Section II-E), and its focal length is 4040.05 ± 0.98 mm.

The Fairchild collimator consists of four basic elements, mounted in a fiberglass tube with black velvet lining.

(1) Ross triplet lens corrector.

(2) Beam splitter.

(3) Primary mirror with a 10.668-m spherical radius of curvature.

(4) Front field-corrector plate.

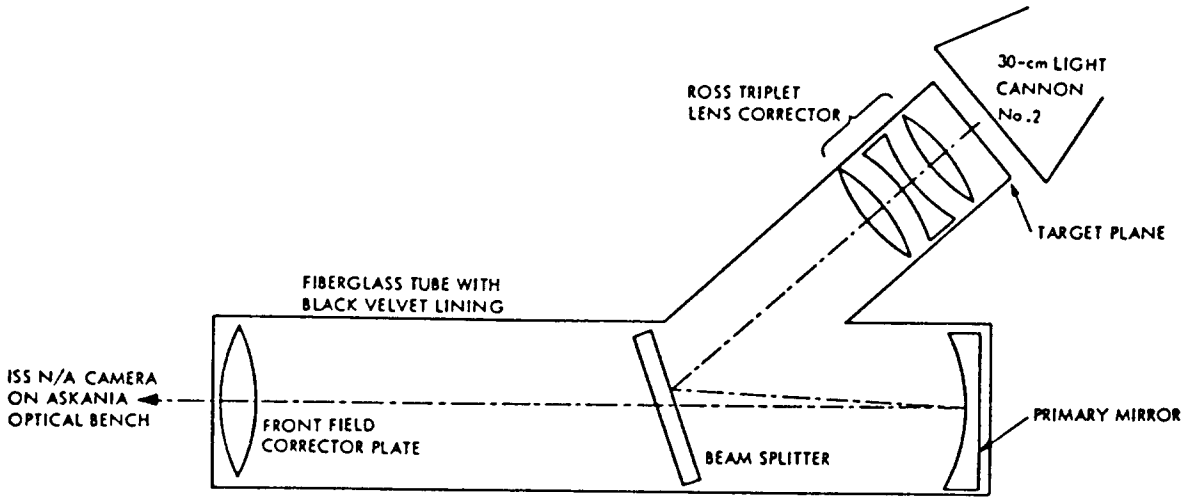

Figure 2-12. Schematic diagram of the Fairchild collimator.

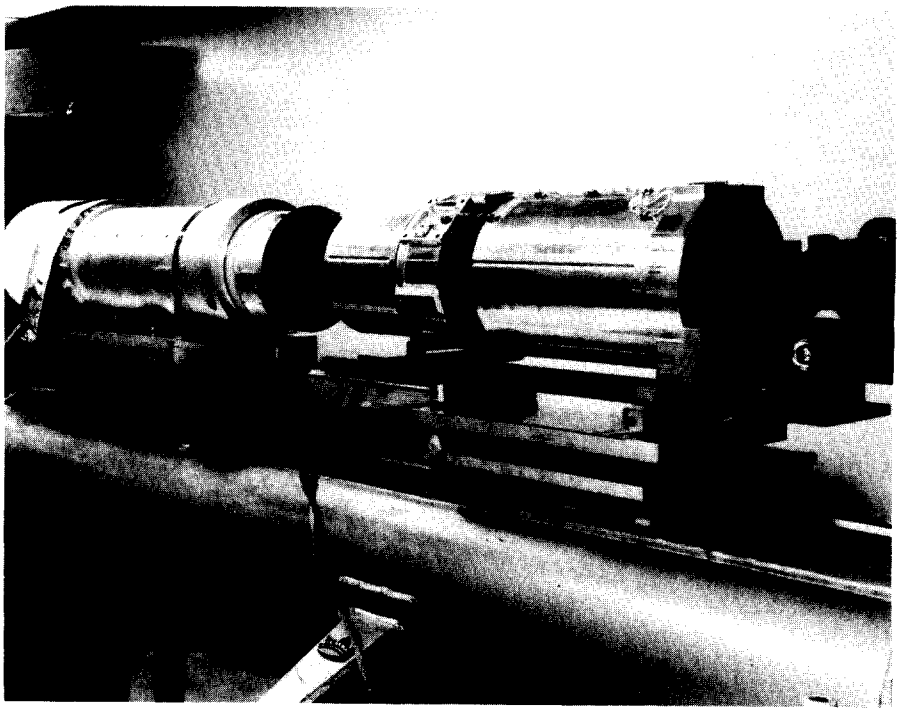

Figure 2-13. GLL 1:1 collimator (right) with SSI.

A special holder was constructed to hold the targets in the focal plane of the collimator to prevent focusing inaccuracies. The targets were illuminated with the xenon light cannon (see Section II-B).

All of the image calibration tests at the subsystem level were performed with the GLL 1:1 collimator. This collimator consists of a modified spare MVM 1973 imaging telescope with a custom target holder in the focal plane and a light source (Figure 2-13). The relative spectral transmission of the MVM telescope used is shown in Figure 2-14 and listed in Table 2-3. The refractive elements in this telescope are uncoated, which provides the broad spectral transmission range but does not attempt to minimize scattered light within the telescope. Such scattered light may result in an apparent reduction in the measured MTF and point-response function of the SSI subsystem. The collimator light source is a quartz-iodide 5-cm lamp in an enclosure with a variable iris mechanism and a diffuser. The relative spectral radiance of this light source is shown in Figure 2-15 and listed in Table 2-4. Only one target at a time can be inserted in the target holder between the lamp and the optics. With this arrangement, practically identical opto-mechanical conditions were established between the collimator and the tested camera, thereby resulting in the 1:1 scale factor.

The focus position of the Fairchild collimator was established by autocollimation. The GLL 1:1 collimator was focused against the Fairchild collimator. The MVM telescope was placed on the Askania optical bench (see Section II-E) facing the Fairchild collimator, which had a grid target (see Section II-D) illuminated in its target holder. A traveling microscope was positioned behind the MVM telescope and was focused on the image of the grid target in the MVM telescope focal plane. The target holder for the GLL 1:1 collimator was then attached to the MVM telescope such that a second grid target in its target holder was also in focus to the traveling microscope along with the image of the Fairchild grid target. This method ensured that the GLL collimator was within 0.0005 inches of focus.

The SSI itself was also focused against the Fairchild collimator. This was accomplished by placing the SSI on the Askania bench, facing the Fairchild with a slant-bar target in its focal plane. Images of the slant-bar target were acquired through each SSI filter with the CCD detector assembly shimmed to different locations along the optical axis relative to the SSI telescope. The shim value that resulted in the highest contrast levels in areas of the target having spatial frequencies of 0.6 and 0.8 of the Nyquist frequency averaged over all filter positions was selected to obtain the best focus for the SSI camera.

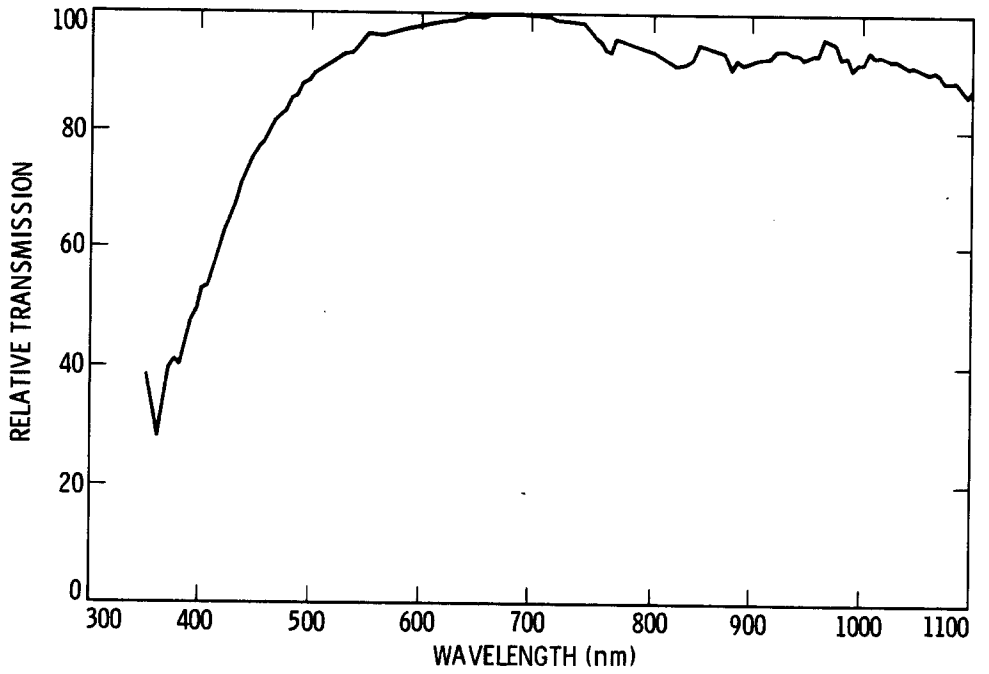

Figure 2-14. Relative spectral transmission of the MVM 1973 imaging telescope used for the GLL 1:1 collimator.

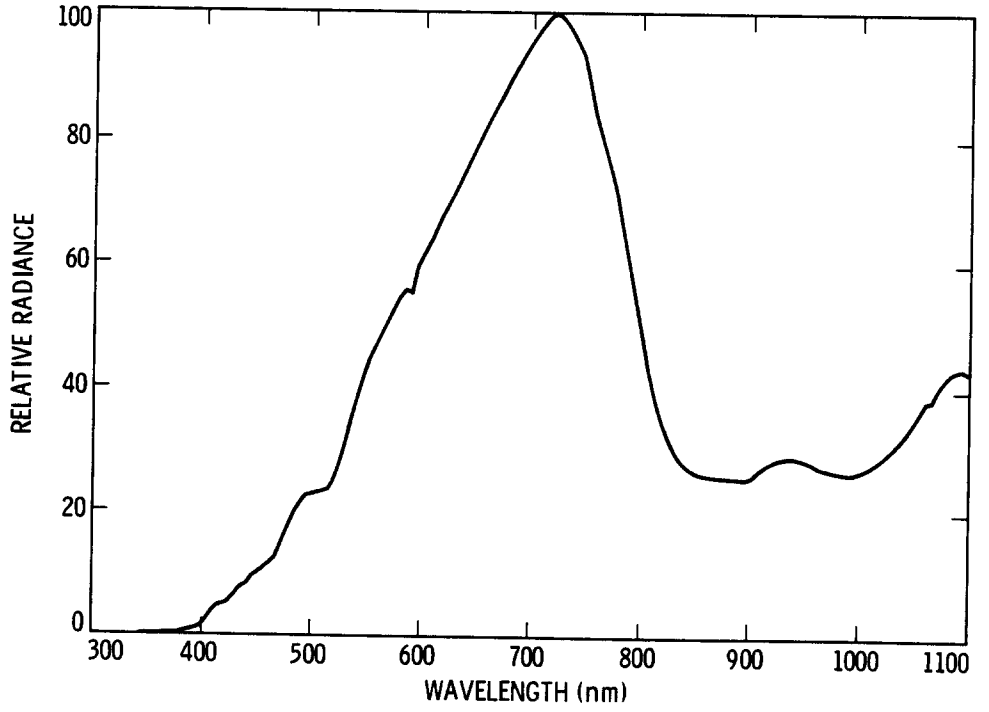

Figure 2-15. Relative spectral radiance of the quartz-iodide 5-cm lamp (GLL 1:1 collimator light source).

Table 2-3. MVM Collimator Relative Spectral Transmission

λ(nm)	value	λ(nm)	value	λ(nm)	value	λ(nm)	value
350	38.6	540	94.1	730	99.0	920	93.8
355	33.1	545	95.6	735	98.8	925	93.8
360	27.8	550	96.5	740	98.6	930	93.9
365	34.7	555	96.4	745	98.4	935	93.3
370	39.7	560	96.2	750	97.3	940	93.3
375	41.3	565	96.5	755	96.1	945	92.6
380	40.1	570	96.6	760	95.4	950	92.8
385	43.4	575	96.9	765	94.0	955	93.3
390	47.8	580	97.1	770	93.4	960	93.2
395	49.6	585	97.4	775	95.8	965	96.0
400	53.2	590	97.4	780	95.6	970	95.5
405	53.7	595	97.6	785	95.0	975	95.0
410	56.3	600	97.7	790	94.7	980	92.6
415	59.8	605	98.0	795	94.3	985	92.9
420	63.1	610	98.2	800	94.1	990	90.6
425	65.3	615	98.6	805	93.7	995	91.8
430	67.8	620	98.7	810	93.5	1000	91.8
435	71.1	625	98.8	815	92.8	1005	94.0
440	73.1	630	98.9	820	92.3	1010	92.8
445	75.5	635	99.2	825	91.8	1015	92.9
450	77.0	640	99.4	830	91.2	1020	92.8
455	78.0	645	99.5	835	91.5	1025	92.2
460	79.9	650	99.5	840	91.6	1030	92.2
465	81.7	655	99.4	845	92.3	1035	91.6
470	82.5	660	99.7	850	94.8	1040	91.2
475	83.5	665	99.9	855	94.5	1045	91.4
480	85.4	670	100.0	860	94.4	1050	90.9
485	86.1	675	99.8	865	94.0	1055	90.4
490	87.8	680	100.0	870	93.7	1060	90.1
495	88.3	685	100.0	875	93.5	1065	90.5
500	89.4	690	100.0	880	90.7	1070	89.9
505	90.1	695	99.8	885	92.3	1075	88.7
510	90.9	700	99.7	890	91.5	1080	88.8
515	91.5	705	99.6	895	91.7	1085	88.7
520	92.0	710	99.7	900	92.1	1090	87.3
525	92.6	715	99.5	905	92.5	1095	86.2
530	93.1	720	99.0	910	92.5	1100	87.7
535	93.3	725	98.9	915	92.8		

Table 2-4. Quartz-Iodide 5-cm Lamp (MVM Collimator Light Source) Relative Spectral Transmission

λ(nm)	value	λ(nm)	value	λ(nm)	value	λ(nm)	value
350	0.1	540	36.8	730	98.1	920	28.3
355	0.2	545	40.4	735	96.6	925	28.7
360	0.2	550	43.6	740	94.8	930	28.9
365	0.2	555	45.3	745	93.0	935	28.9
370	0.2	560	47.2	750	88.8	940	28.9
375	0.3	565	49.0	755	84.1	945	28.7
380	0.4	570	50.7	760	80.9	950	28.5
385	0.7	575	52.8	765	77.6	955	28.0
390	1.0	580	54.4	770	74.0	960	27.5
395	1.0	585	55.5	775	71.2	965	27.2
400	1.5	590	55.0	780	67.1	970	27.0
405	2.9	595	59.2	785	62.4	975	26.8
410	4.0	600	60.7	790	57.3	980	26.6
415	4.7	605	62.5	795	52.5	985	26.5
420	5.0	610	64.4	800	47.7	990	26.3
425	5.7	615	66.5	805	43.4	995	26.6
430	6.7	620	68.1	810	39.8	1000	26.8
435	7.8	625	69.7	815	36.4	1005	27.1
440	8.2	630	71.5	820	37.7	1010	27.7
445	9.5	635	73.5	825	31.5	1015	28.3
450	10.1	640	75.5	830	29.7	1020	29.1
455	10.7	645	77.6	835	28.4	1025	29.8
460	11.4	650	79.5	840	27.5	1030	30.6
465	12.1	655	81.3	845	26.8	1035	31.5
470	13.9	660	83.1	850	26.4	1040	32.5
475	16.2	665	84.9	855	26.1	1045	33.8
480	18.1	670	86.3	860	25.9	1050	35.2
485	20.2	675	88.2	865	25.8	1055	36.7
490	21.5	680	90.1	870	25.7	1060	38.1
495	22.6	685	91.5	875	25.7	1065	38.2
500	22.8	690	93.1	880	25.6	1070	39.8
505	23.1	695	94.7	885	25.5	1075	41.3
510	23.4	700	96.0	890	25.4	1080	42.3
515	23.5	705	97.4	895	25.4	1085	43.1
520	25.0	710	98.5	900	25.7	1090	43.4
525	27.8	715	99.8	905	26.3	1095	43.0
530	30.9	720	100.0	910	27.1	1100	42.9
535	34.2	725	99.4	915	27.8		

D. TARGETS

The following targets were used for various Galileo SSI photoscience tests and calibrations in connection with the applicable collimators, which were described in Section II-C:

(1) CCD blooming target (Figure 2-16) -- saturated detector response (virtual-phase CCD test set).

(2) Residual image target (Figure 2-17) -- detector charge retention (virtual-phase CCD test set).

(3) Geometric grid target (Figure 2-18) -- focal length calibration (Fairchild collimator) and geometric distortion measurement (GLL 1:1 collimator).

(4) MTF target (Figure 2-19) -- modulation transfer function calibration (GLL 1:1 collimator).

(5) Point response function target (Figure 2-20) -- point response function calibration for star simulation (GLL 1:1 collimator).

(6) Color reconstruction target (Figure 2-21) -- color reconstruction calibration (GLL 1:1 collimator).

(7) Navigation target (Figure 2-22) -- navigation calibration test for planet limb simulation (GLL 1:1 collimator and virtual-phase CCD test set).

The CCD blooming and residual-image targets were manufactured at JPL for CCD component-level testing. The geometric grid target was manufactured according to JPL specifications. Coordinates of all grid intersections were measured by the manufacturer[1] and then verified at JPL on a Moore measuring machine. The resulting positional accuracy is claimed to be approximately ±1 μm according to the manufacturer. JPL measurements indicate departures from perfect regularity of 1.6 μm r.m.s.

The modulation transfer function (MTF) target is composed of equal-width opaque and clear bars spread across the entire camera field of view. The edges of the bars are straight and sharp to within ±1 μm to guarantee reliable results. During SSI calibrations, the MTF target was used in both its horizontal and vertical positions.

---

1 Electromask Co., Woodland Hills, California.

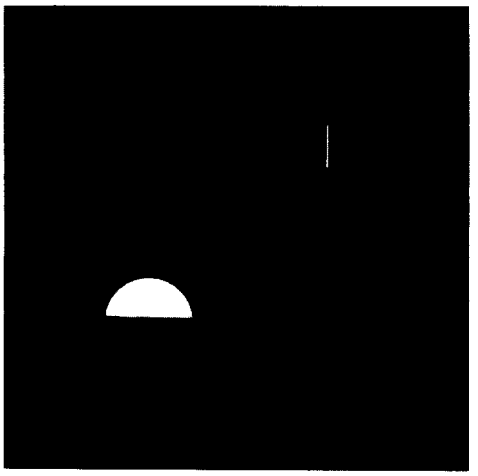

Figure 2-16.
CCD blooming target.

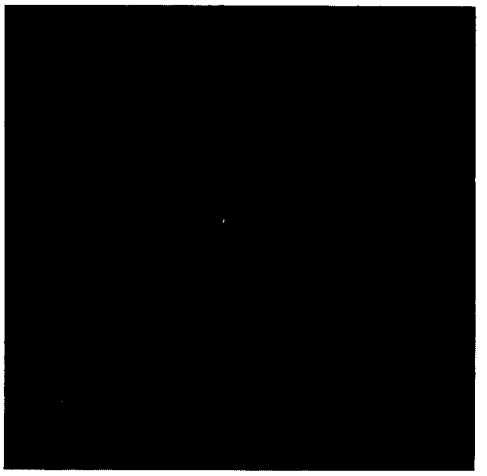

Figure 2-17.
Residual image target.

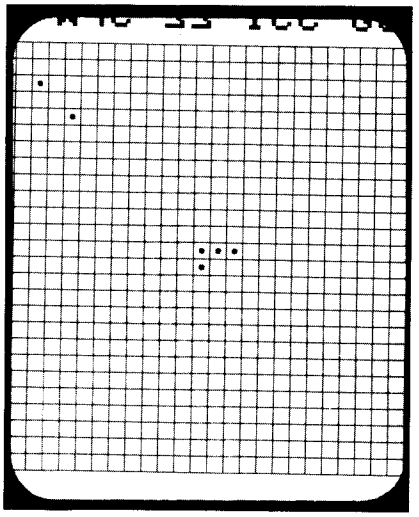

Figure 2-18.
Geometric grid target.

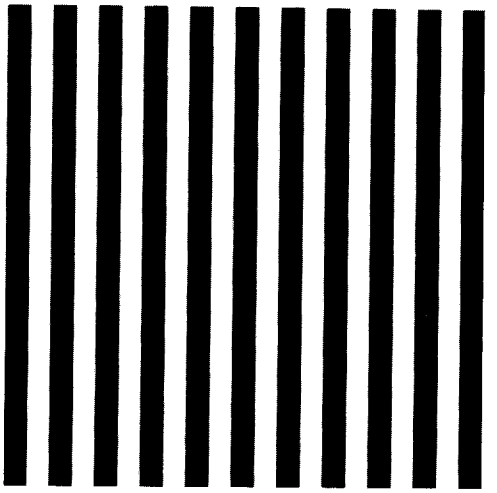

Figure 2-19.
Modulation transfer function
(MTF) target.

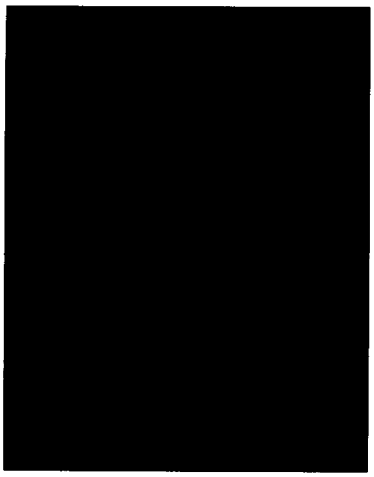

Figure 2-20.
Point response function target.

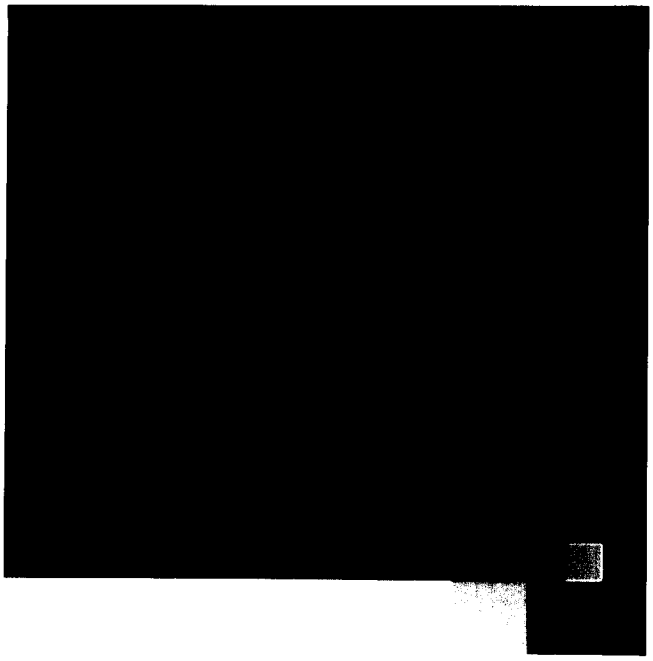

Figure 2-21.
Color reconstruction target.

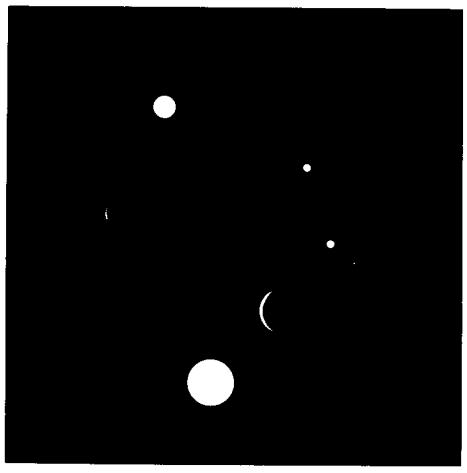

Figure 2-22. Navigation target.

The point-response function target was manufactured[2] according to JPL specifications. Size and coordinates of the 10-μm pinholes were verified at JPL. The resulting positional accuracy is ±2 μm.

The color reconstruction target, designed and computer-generated by JPL's Multimission Image Processing Laboratory, was calibrated to develop a method of color simulation from black and white SSI images. It was used as described in Section IV-A-7.

The navigation target was manufactured at JPL for CCD component-level testing. The Navigation Systems Section at JPL requested images at the subsystem level with the same target. For further information on these test results, see Section IV-D.

E. CALIBRATION ENVIRONMENTS

The SSI subsystem-level calibrations, which utilized the equipment described in Sections II-A through II-D, were performed at two locations:

(1) JPL optical tunnel (bench calibrations).

(2) JPL thermal vacuum chamber (environmental calibrations).

The JPL optical tunnel employs an Askania optical bench, which is aligned with the Fairchild collimator. Figure 2-23 shows a view of the optical tunnel area. The camera with its electronics assembly is mounted on the optical bench and pointed along the optical axis of the Fairchild collimator. The xenon light cannon, which was used for illumination of the collimator targets, is hidden behind the far end (focal/target plane) of the collimator.

Figure 2-24 shows the narrow-angle SSI camera and electronics box assembly setup on the Askania optical bench in the optical tunnel. During subsystem focusing activities, the camera was connected to the Support Equipment (Section II-A) and aligned with the Fairchild collimator for imaging of a resolution target. Component-level optics focal length measurements used the identical setup but without the electronics box assembly and the Support Equipment.

The thermal vacuum chamber #12, which is located in the JPL Environmental Laboratory, is shown in Figure 2-25. Figures 2-26 and 2-27 show the light cannon and GLL collimator positioned directly in front of the chamber window. During calibration, a black velvet cloth was always wrapped around the window to eliminate any outside light and glare. SSI

[2] National Aperture, Tewksbury, MA.

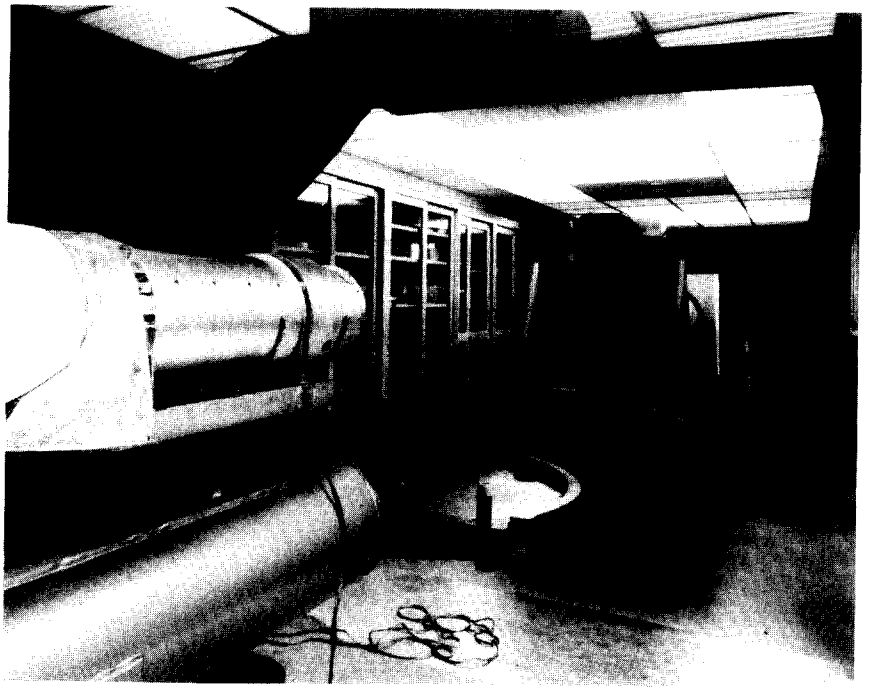

Figure 2-23. General view of the JPL optical tunnel test and calibration area.

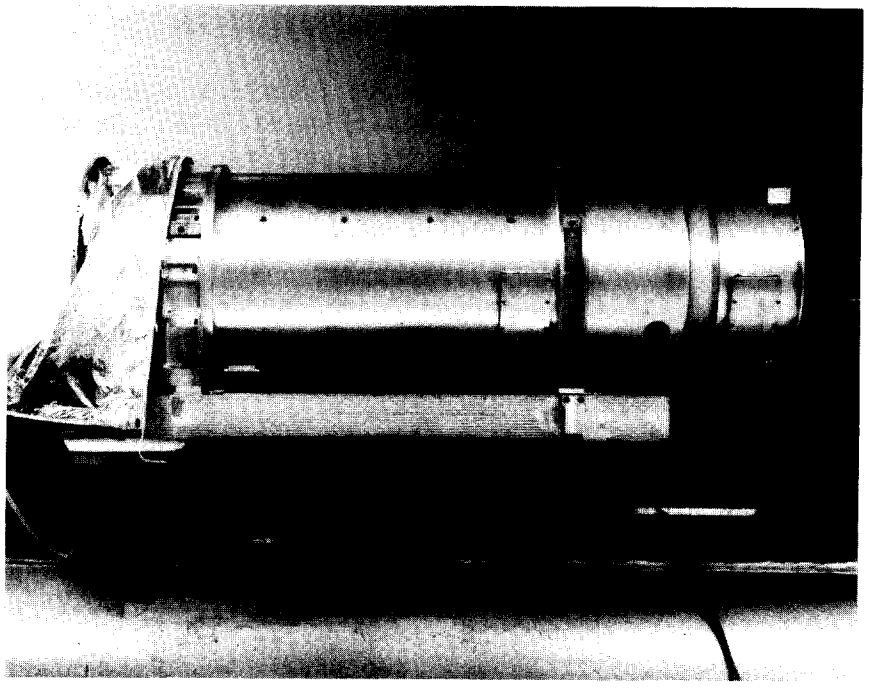

Figure 2-24. SSI camera and electronics box assembly setup on Askania optical bench in optical tunnel.

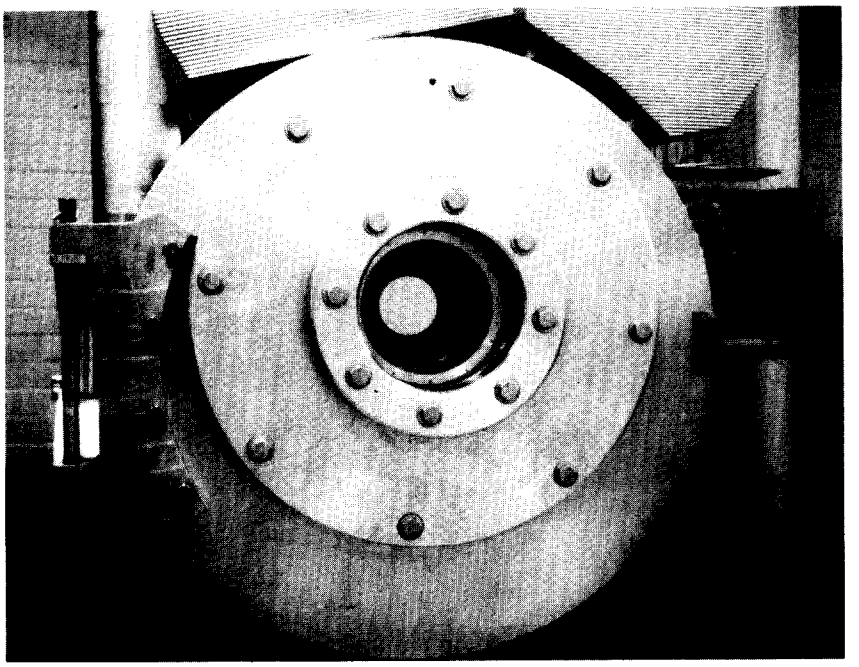

Figure 2-25. Thermal vacuum chamber #12 in JPL Environmental Laboratory.

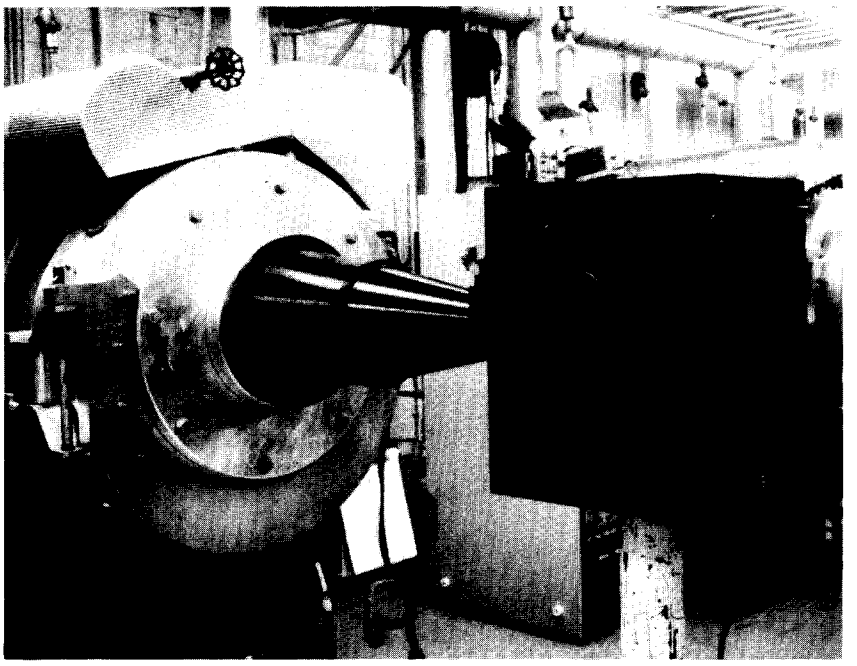

Figure 2-26. Light cannon in front of thermal vacuum chamber window.

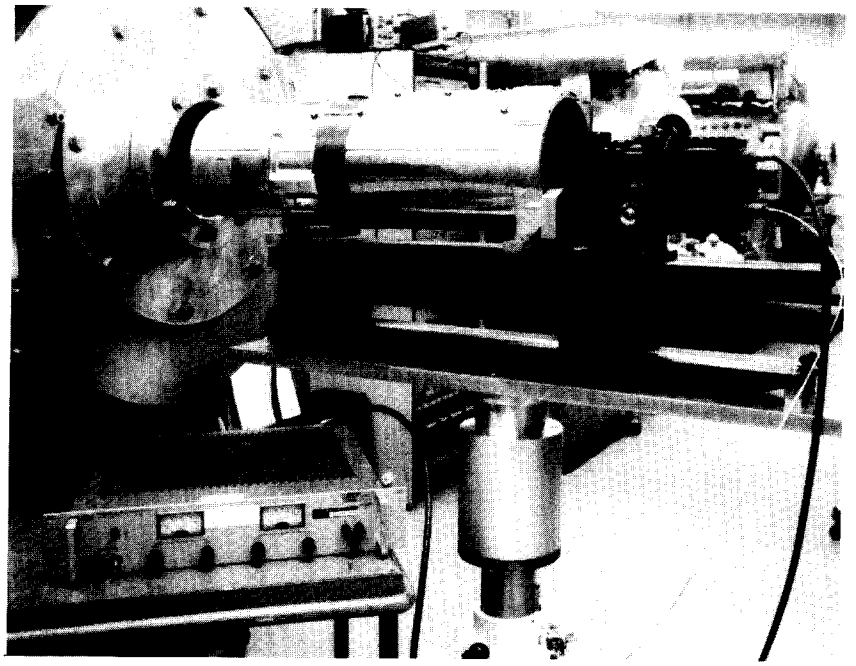

Figure 2-27. GLL collimator in front of thermal vacuum chamber window.

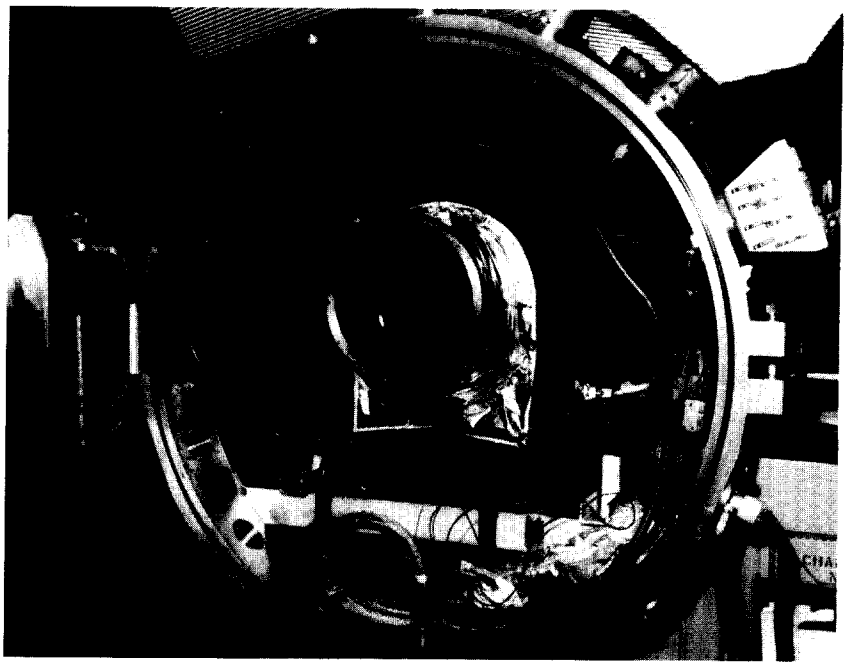

Figure 2-28. SSI camera mounted inside thermal vacuum chamber.

images of the tungsten light cannon set to a low level (~0.8 ftL) were acquired through the clear filter with the room lights both on and off, and the responses were compared to verify that no extraneous room light was reaching the SSI detector. The support equipment was located in a room near the chamber except for the IFU which was located next to the chamber.

The SSI camera was mounted inside the chamber as indicated in Figure 2-28; however, the window center and the camera's optical axis were originally not aligned. The electronics box raised the optical axis of the camera by two inches (as compared to the Voyager camera). Since the cold plate in the chamber was in its lowest position, a new door was made to center the window with the optical axis of the camera. This is shown in Figure 2-25.

The absolute spectral transmission of the chamber window is documented in Figure 2-29 and Table 2-5. The Gamma Scientific Spectroradiometer was used for this measurement. Since it was not possible to dismount the window and ship it to the optical tunnel, the spectroradiometer was moved to the JPL Environmental Laboratory for this test. Because the spectroradiometer is equipped with a silicon detector (which has rapidly decreasing sensitivity toward the blue end of the spectrum), we found it necessary to introduce blue filters into the optical path when making spectral transmission measurements below about 475 nm in order to eliminate any red light that could be scattered internal to the monochrometer and produce spurious signal for measurements in the blue. The xenon light cannon was used as a light source for this measurement in order to achieve adequate signal at blue wavelengths.

Focus checks of the SSI in the chamber initially showed that the focus shifted 0.011 inch when the thermal vacuum chamber wall was cooled from room temperature to -185° C. This effect was traced to a radial temperature gradient in the fused quartz chamber window. This gradient and the resulting focus shift were eliminated for the actual SSI calibration either by turning on the front optics and hood heater or by shielding the window's view of the cold chamber wall with a thermal blanket.

Experience has shown that vibrations in the thermal vacuum chamber can seriously degrade image sharpness. Whenever imaging calibrations were conducted (MTF, point response, color, navigation target, etc.), the vacuum pumps in the chamber were temporarily turned off, the MVM collimator stand was stabilized using lead weights on its base, and all personnel movement in the chamber room was restricted. The degree to which any residual vibrations in the building may have affected calibration image quality is unknown.

Table 2-5. Absolute Spectral Transmission of Thermal Vacuum Chamber Window

λ (nm)	value	λ (nm)	value	λ (nm)	value	λ (nm)	value
370	0.252	540	0.689	730	0.805	920	0.717
375	0.275	545	0.695	735	0.805	925	0.713
380	0.280	550	0.703	740	0.806	930	0.708
385	0.295	555	0.709	745	0.805	935	0.704
390	0.316	560	0.716	750	0.804	940	0.699
395	0.333	565	0.722	755	0.804	945	0.694
400	0.348	570	0.729	760	0.804	950	0.689
405	0.356	575	0.734	765	0.804	955	0.685
410	0.370	580	0.739	770	0.803	960	0.680
415	0.376	585	0.744	775	0.803	965	0.674
420	0.386	590	0.748	780	0.800	970	0.668
425	0.400	595	0.753	785	0.798	975	0.664
430	0.412	600	0.756	790	0.798	980	0.657
435	0.427	605	0.760	795	0.796	985	0.657
440	0.440	610	0.765	800	0.794	990	0.648
445	0.452	615	0.767	805	0.793	995	0.643
450	0.468	620	0.769	810	0.791	1000	0.637
455	0.481	625	0.773	815	0.788	1005	0.633
460	0.497	630	0.776	820	0.782	1010	0.627
465	0.511	635	0.777	825	0.782	1015	0.622
470	0.527	640	0.781	830	0.782	1020	0.617
475	0.541	645	0.784	835	0.779	1025	0.592
480	0.557	650	0.786	840	0.777	1030	0.590
485	0.572	655	0.788	845	0.773	1035	0.586
490	0.587	660	0.791	850	0.769	1040	0.581
495	0.600	665	0.793	855	0.769	1045	0.583
500	0.612	670	0.795	860	0.764	1050	0.587
505	0.627	675	0.797	865	0.762	1055	0.581
510	0.636	680	0.798	870	0.757	1060	0.578
515	0.645	685	0.799	875	0.753	1065	0.572
520	0.655	690	0.800	880	0.748	1070	0.566
525	0.663	695	0.802	885	0.747	1075	0.561
530	0.672	700	0.803	890	0.742	1080	0.557
535	0.680	705	0.803	895	0.738	1085	0.548
		710	0.803	900	0.735	1090	0.547
		715	0.804	905	0.729	1095	0.542
		720	0.805	910	0.726	1100	0.538
		725	0.804	915	0.723		

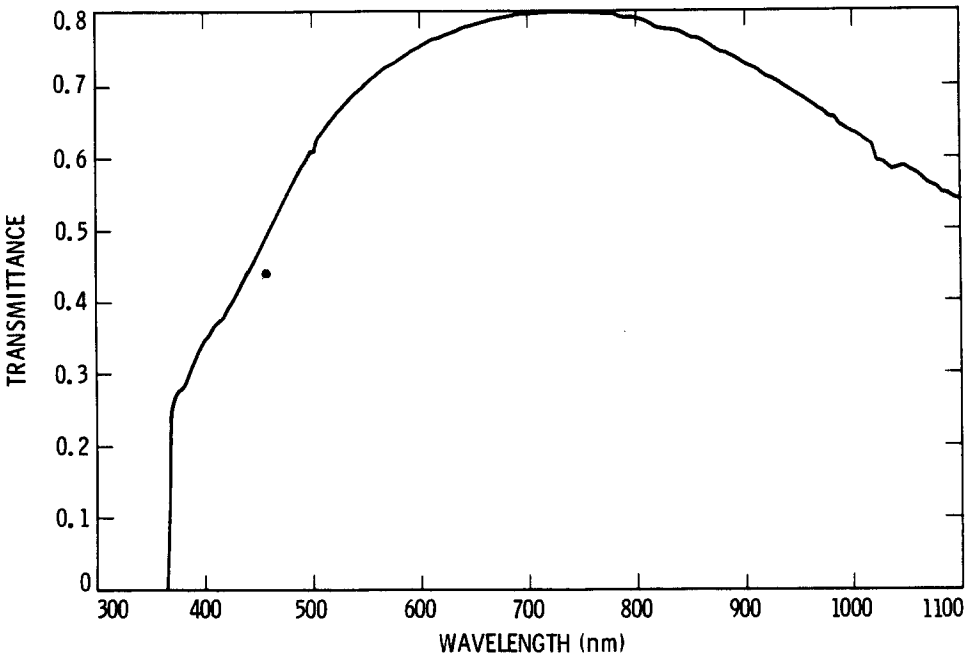

Figure 2-29. Absolute spectral transmission of thermal vacuum chamber window.

REFERENCES

2-1. C. Lebel, Solid State Imaging (SSI) Instrument Calibration Requirements Document, Component Level Calibrations, JPL Document 625-601, Rev. B, June 11, 1982.

2-2. C. Lebel, Solid State Imaging (SSI) Instrument Calibration Requirements Document, Subsystem Level Calibrations, JPL Document 625-606, Rev. A, June 10, 1982.

2-3. GLL SSI Support Equipment, Description and User's Guide, prepared by Support Equipment Group, March 1983.

2-4. Configuration Instruction Manual for Computer-Controlled Digital Drive Spectral/Spatial Scanning System, Gamma Scientific, Inc., September, 1980.

SECTION III

COMPONENT CALIBRATIONS

The Galileo SSI consists of a narrow-angle camera comprising the following four basic parts:

(a) The optics.

(b) The filter wheel/shutter assembly.

(c) The camera head housing the charge-coupled device (CCD).

(d) The electronics assembly (power supply and support electronics).

Figure 3-1 shows the SSI camera fully assembled with its electronic assembly. The optics of the camera is equipped with a sunshade and a deployable transparent optics cover. The SSI narrow-angle camera was built according to a modified design of the Voyager narrow-angle camera (References 3-1 and 3-2).

All components were subjected to a series of engineering acceptance tests, but additional tests and calibrations prior to their integration into the imaging subsystem were made on the optics, filters, shutter and CCD detector. There were two main reasons for these additional calibrations:

(a) It was necessary to verify the compatibility of the manufactured component with the photoscience requirements.

(b) Various radiometric calculations required knowledge of such parameters as spectral characteristics, actual shutter times, etc.

Only results pertaining to the flight SSI camera are documented in this report. However, many component-level calibrations were performed on other cameras and other spare-part components as well. These results were catalogued and filed in case of retrofitting or any other future needs. The assignment of individual components is summarized by their serial numbers as listed in Table 3-1.

All component-level calibration procedures are documented in Reference 3-3 and were based on technical requirements documented in Reference 2-1. They were designed and performed in a way to fully satisfy the specified accuracy criteria.

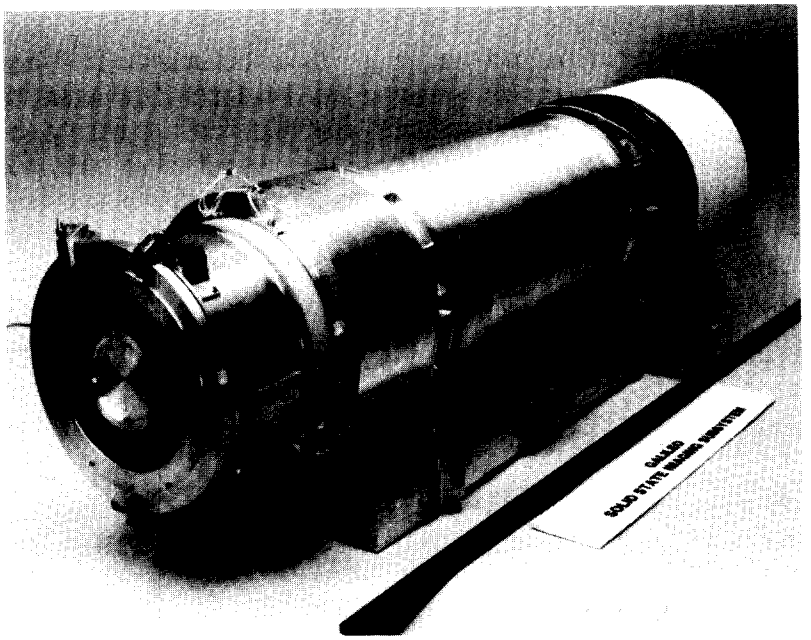

Figure 3-1. Fully assembled SSI camera with electronic assembly.

Table 3-1. Serial numbers of components of the SSI flight unit.

Component	S/N
Optics	2
Shutter	8
CCD	29
Quartz Radiation Plug	1
Deployable Optics Cover	1

A. OPTICS

The narrow-angle camera optics is a 1500-mm focal length all-spherical catadioptric cassegrain telescope consisting of five elements plus an additional quartz window located in the radiation shield between the shutter and the CCD. The f-stop number (f/#) is 8.5. The sunshade on the front of the telescope is intended to screen out scattered light which could cause veiling glare, and to provide an additional baffle effect to eliminate direct light from reaching the CCD. The narrow-angle optics refractive elements were fabricated from T-20 Suprasil II, an extremely stable optical material, and ultralow-expansion materials were used for the mirrors, which resulted in essentially diffraction-limited performance.

The theoretical computer-generated modulation transfer function (MTF) curve of the SSI optics is shown in Figure 3-2 and summarized in Table 3-2. The original requirements for optical quality of the Voyager narrow-angle optics were defined in Reference 3-2 as follows: spatial frequency of at least 36 line pairs/mm (lp/mm) at 50% modulation and 120 lp/mm at 15% modulation. As can be seen from Figure 3-2, these constraints were nearly met for Galileo despite expanding the required wavelength range over which the optics must perform to between 0.4 and 1.1 μm.

1. Spectral Transmission

Spectral transmission of the SSI telescope was measured with the JPL spectroradiometer. The method and the typical test setup are described in detail in Reference 3-3.

The results obtained are documented in Figure 3-3, and they include the effect of center obscuration. The curve is scaled to match the absolute transmission at the effective wavelength of the T-stop number (T/#) measurements described in Section III-A- 2.

The spectroradiometer was operated between 350 and 1100 nm at 5-nm intervals. The accuracy of these spectral measurements is very difficult to measure, but based on past experience, as well as on several comparison tests, it should be better than the ±2% required by Reference 2-1.

Table 3-3 has been included for those who require spectral transmission data in numerical form for computer applications.

Table 3-2. Modulation transfer function (MTF) of the SSI optics.

spatial frequency (lp/mm)	MTF	spatial frequency (lp/mm)	MTF	spatial frequency (lp/mm)	MTF
5	0.917	45	0.395	85	0.237
10	0.835	50	0.369	90	0.216
15	0.753	55	0.350	95	0.197
20	0.672	60	0.334	100	0.183
25	0.594	65	0.319	105	0.173
30	0.529	70	0.303	110	0.165
35	0.476	75	0.285	115	0.156
40	0.429	80	0.262	120	0.143

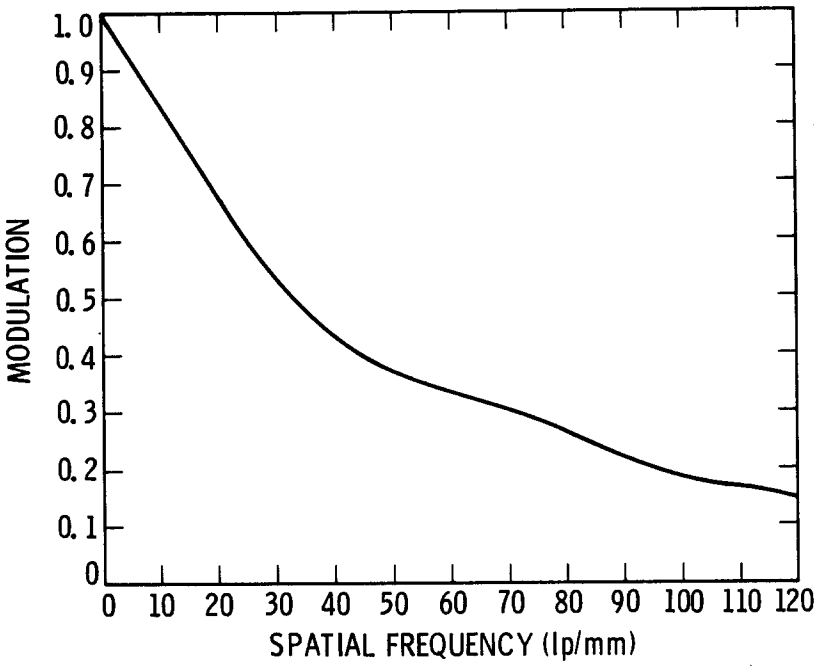

Figure 3-2. Theoretical computer-generated modulation transfer function (MTF) for the SSI optics.

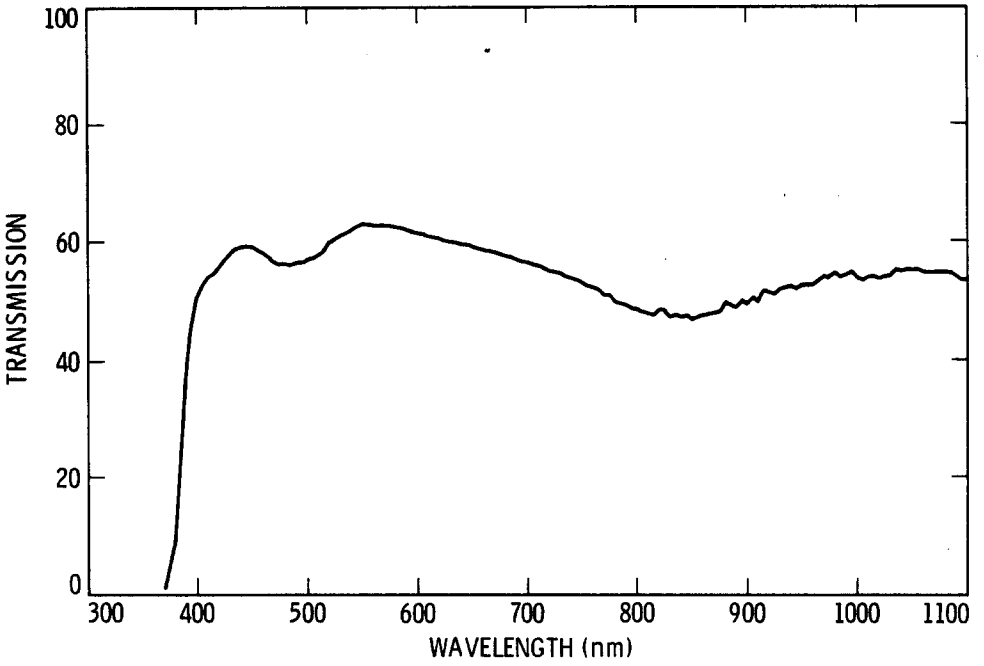

Figure 3-3. Spectral transmission of the SSI telescope optics.

Table 3-3. Spectral transmission of the SSI optics.

λ (nm)	trans (%)	λ (nm)	trans (%)	λ (nm)	trans (%)	λ (nm)	trans. (%)
350	0.00	540	61.94	730	54.67	920	51.26
355	0.00	545	62.56	735	54.09	925	50.98
360	0.00	550	63.03	740	53.79	930	51.79
365	0.00	555	62.99	745	53.52	935	52.12
370	0.00	560	62.88	750	53.05	940	52.33
375	4.49	565	62.87	755	52.47	945	51.88
380	9.36	570	62.86	760	52.27	950	52.52
385	22.91	575	62.75	765	51.90	955	52.50
390	36.86	580	62.50	770	50.93	960	52.62
395	45.14	585	62.38	775	50.91	965	53.16
400	50.44	590	62.13	780	49.71	970	53.97
405	52.54	595	61.78	785	49.42	975	53.85
410	53.96	600	61.56	790	49.20	980	54.66
415	54.62	605	61.40	795	48.65	985	53.77
420	55.75	610	61.14	800	48.48	990	54.21
425	56.98	615	60.97	805	48.05	995	54.83
430	58.04	620	60.61	810	47.81	1000	53.70
435	58.97	625	60.20	815	47.53	1005	53.29
440	59.32	630	60.05	820	48.52	1010	53.88
445	59.46	635	59.87	825	48.45	1015	54.04
450	59.31	640	59.61	830	47.29	1020	53.61
455	58.72	645	59.48	835	47.59	1025	53.95
460	58.21	650	59.17	840	47.23	1030	54.18
465	57.71	655	58.98	845	47.45	1035	55.10
470	57.13	660	58.70	850	46.70	1040	54.91
475	55.63	665	58.49	855	47.17	1045	55.09
480	55.99	670	58.26	860	47.44	1050	55.02
485	55.74	675	57.92	865	47.66	1055	54.98
490	56.25	680	57.68	870	47.90	1060	54.67
495	56.28	685	57.41	875	48.05	1065	54.61
500	56.80	690	56.97	880	49.52	1070	54.64
505	57.27	695	56.62	885	49.23	1075	54.65
510	57.84	700	56.53	890	48.69	1080	54.55
515	58.50	705	56.24	895	49.96	1085	54.56
520	60.04	710	56.03	900	49.33	1090	53.96
525	60.54	715	55.61	905	50.54	1095	53.39
530	61.08	720	55.02	910	49.80	1100	53.36
535	61.47	725	54.94	915	51.63		

2. T-Stop Number

The T-stop number, T/#, of an optical system is a function of its f-stop number, f/#, and its absolute transmission t. The quantities are related by

$$T/\# = (f/\#) / \sqrt{t}$$

The determination of the T/# for an optical system consists of two steps:

1) An ideal lens with 100% transmission yields T/# = f/#. A system can be constructed to give 100% transmission by placing an aperture of known diameter, D, at the light cannon face and erecting an imaginary image plane in front of an integrating-cavity receptor located a distance L from the light cannon face. In these terms, the T/# is given by

$$T/\# = \sqrt{(0.25 + (L/D)^2)}$$

The relative energy collected by the integrating cavity in the image plane is then measured with a photometer coupled to the integrating cavity by a fiber optics bundle. A calibration curve for the light cannon is then constructed by plotting the square root of the relative energy versus the inverse value of the T/#.

2) Next, the telescope is placed between the light cannon and the imaginary image plane, and the relative energy is measured in the image plane. The value of the square root of this relative energy is plotted on the calibration curve, and the T/# of the system is found on the other axis.

The effective wavelength for which this T/# applies can be calculated. The measured T/# then yields the absolute transmission of the optics at this wavelength.

Because the light cannon is not uniformly bright across its face, a correction factor must be applied to the measured relative energy for each aperture used in constructing the calibration curve. The correction factor to the measured relative energy, E(D), is given by

$$\bar{B}(D) = (8/D^2) \int_0^{D/2} R\, B_D(R)\, dR$$

where

$B_D(R)$ = relative light cannon radiance when measured from the location of the integrating cavity

R = distance on the light cannon face from the center

D = aperture diameter

The measured relative energy should thus be scaled by

$$E'(D) = E(D)/\bar{B}(D)$$

Figure 3-4 shows $B_D(R)$ and $RB_D(R)$. The correction factor for light cannon non-uniformity, $\bar{B}(D)$, to the measured relative energy, E(D), is shown in Table 3-4. The T/# and relative energy for each aperture size are shown in Table 3-5 for L = 46 inches. Figure 3-5 shows the resulting calibration curve.

For the optics measurements, the correction factor to the measured relative energy, E, for field flatness and center obscuration of the telescope is given by

$$\bar{B} = \frac{2}{R_2^2 - R_1^2} \int_{R_1}^{R_2} R\, B_f(R)\, dR$$

where

$B_f(R)$ = relative light cannon radiance measured normal to the diffuser

R = distance on the light cannon face from the center

R_1 = radius of the optics' secondary obscuration

R_2 = radius of the optics' entrance aperture

The measured relative energy should be scaled by

$$E' = E/\bar{B}$$

The T/# of the optics is calculated from the value of D for which E'(D) = E'.

Figure 3-6 shows $B_f(R)$ and $RB_f(R)$. The correction factor for the field flatness and center obscuration, $\bar{B}$, as calculated from these curves is

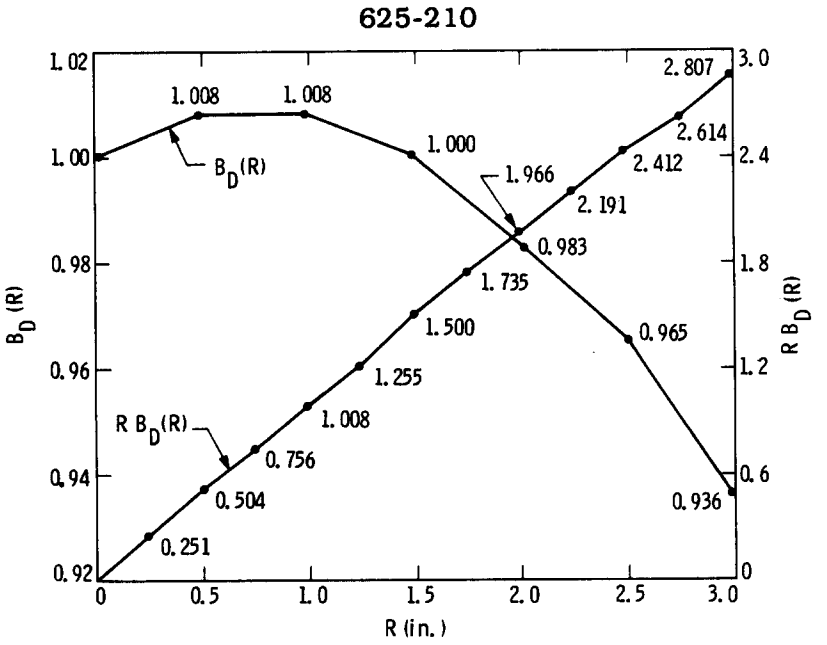

Figure 3-4. Plot of $B_D(R)$, the relative light cannon radiance measured from the location of the integrating cavity, and $RB_D(R)$ vs. R, the distance on the light cannon face from the center.

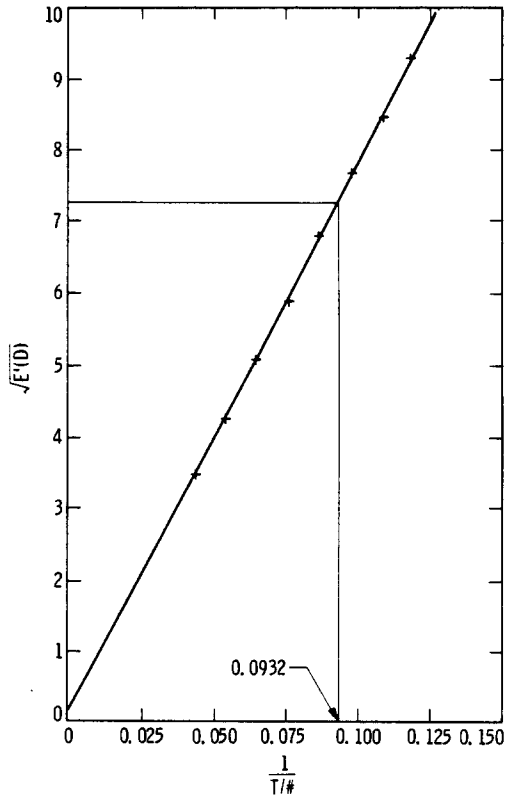

Figure 3-5. Calibration curve for the SSI optics.

Table 3-4. Correction to measured relative energy due to light cannon brightness nonuniformity.

D (in.)	$\int_0^{D/2} RB_D(R)dR$	B(D)	E(D) ± 0.50	E'(D)
2.0	0.504	1.008	12.33	12.23 ± 0.49
2.5	0.787	1.007	18.17	18.04 ± 0.49
3.0	1.131	1.006	26.00	25.84 ± 0.49
3.5	1.535	1.003	34.83	34.73 ± 0.49
4.0	1.998	0.999	45.67	45.72 ± 0.50
4.5	2.518	0.995	57.83	58.12 ± 0.50
5.0	3.093	0.990	70.00	70.71 ± 0.51
5.5	3.721	0.984	84.00	85.37 ± 0.51
6.0	4.399	0.977	99.33	101.67 ± 0.51

Table 3-5. T/# and relative energy for each aperture size.

D (in.)	T/#	1/(T/#)	$\sqrt{E'(D)}$
2.0	23.005	0.044	3.49 ± 0.07
2.5	18.407	0.054	4.25 ± 0.06
3.0	15.342	0.065	5.08 ± 0.05
3.5	13.152	0.076	5.89 ± 0.04
4.0	11.511	0.087	6.76 ± 0.04
4.5	10.234	0.098	7.62 ± 0.03
5.0	9.214	0.109	8.41 ± 0.03
5.5	8.379	0.119	9.24 ± 0.03
6.0	7.683	0.130	10.08 ± 0.03

$\bar{B}$ = 0.969. For the flight optics, the measured relative energy, E, was E = 50.83 ± 0.50. Thus, the scaled relative energy was E' = 52.46 ± 0.52. $\sqrt{E'}$ was therefore 7.24 ±0.04 and, using the calibration curve of Figure 3-5, the T/# = 10.73 ±0.01. The corresponding wavelength for which this T/# applies is given by

$$\lambda_{eff} = \frac{\int L(\lambda)\, T(\lambda)\, P(\lambda)\, \lambda\, d\lambda}{\int L(\lambda)\, T(\lambda)\, P(\lambda)\, d\lambda}$$

where

$L(\lambda)$ = relative light cannon radiance

$T(\lambda)$ = relative optics transmission

$P(\lambda)$ = photopic response

The relative light cannon spectral radiance is given in Section II-B-1, and the spectral transmission of the optics is given in Section III-A-1. The effective wavelength of the T/# measurement is computed to be 575.9 nm. The absolute optics transmission at this wavelength is given by

$$t = ((f/\#)/(t/\#))^2$$

With f/# = 8.5, t = 62.75 ± 0.06 percent. This value of transmission was used to establish the absolute spectral transmission curve for the optics described in Section III-A-1.

3. Focal Length

The focal length of the SSI optics was determined by measuring the X,Y coordinates of selected points on a grid target as imaged in the focal plane of the flight optics. These coordinates were then compared to the

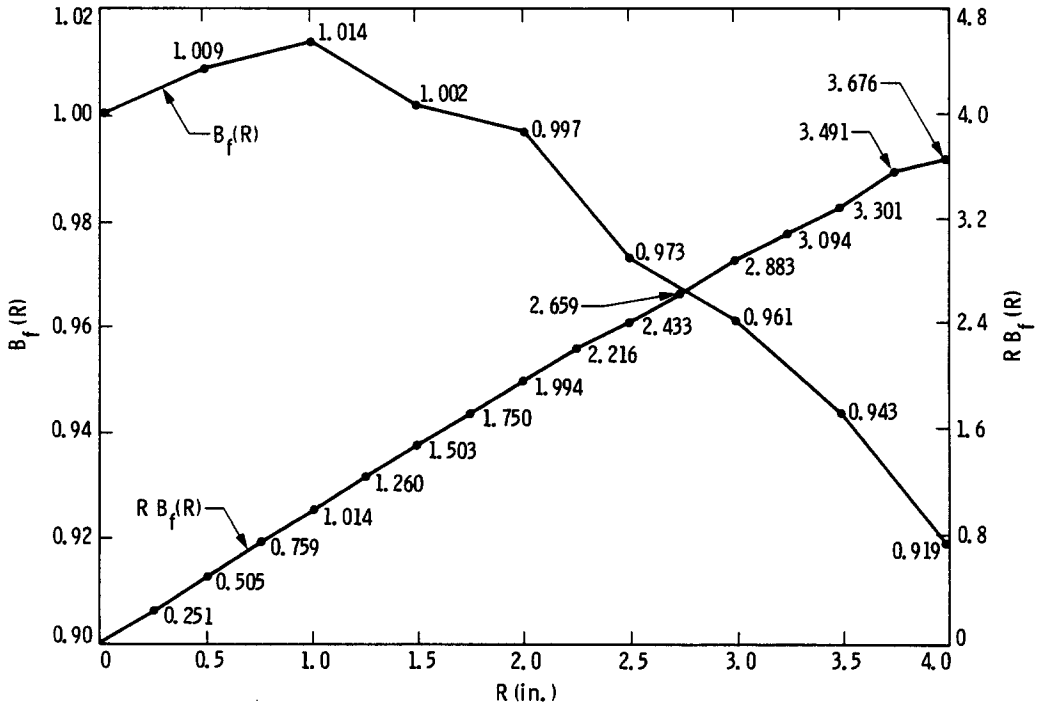

Figure 3-6. Plot of $B_f(R)$, the relative light cannon radiance measured normal to the diffuser, and $RB_f(R)$ vs. R, the distance on the light cannon face from the center.

known coordinates of the target, and a value for the focal length of the optics obtained.

The optics were placed on the Askania bench facing the Fairchild collimator. The optical axis of the optics must be aligned to be parallel with that of the collimator. This was done by positioning a theodolite between the Fairchild and the optics and measuring the direction to a pinhole target in the collimator. The theodolite was then swung 180° horizontally and 90° - n (where n was the offset from 90° in the pinhole measurement) vertically, and an illuminated hole fixed in the focal plane of the optics was centered on these coordinates by pivoting the optics slightly on the Askania bench.

Next, the grid target was placed in the collimator. A traveling microscope in the focal plane of the optics then was used to measure the coordinates of the selected image points three times.

The imaged coordinates were then fit to the known coordinates by rotating, translating and scaling the imaged coordinates in an iterative, least-squares manner. The focal length of the optics was determined from the scaling factor and the known focal length of the Fairchild collimator. The resulting focal length was computed to be 1497.24 ± 0.48 mm.

4. Veiling Glare

The ability of an optical system to keep light from sources outside of the detector field of view from reaching the detector can be characterized by an off-axis attenuation factor, $K(\theta)$, which is defined by

$$K(\theta) = R(\theta)/R(0)$$

where θ = off-axis angle of source

R = total amount of light reaching a detector element (pixel)

The relative throughput of light as a function of off-axis angle to the source was measured for the SSI telescope including the shutter and filter wheel assembly at the low-scatter facility at Utah State University using a point calibration source. A description of this facility is given in Reference 3-4, and Figure 3-7 shows the configuration of the facility. The telescope was mounted on a motor-driven rotating pedestal that reads out azimuth angle. The entrance aperture of the telescope was positioned on the pivot axis of the pedestal to ensure full illumination by the collimator throughout the scan range. The telescope was tested in only one plane assuming

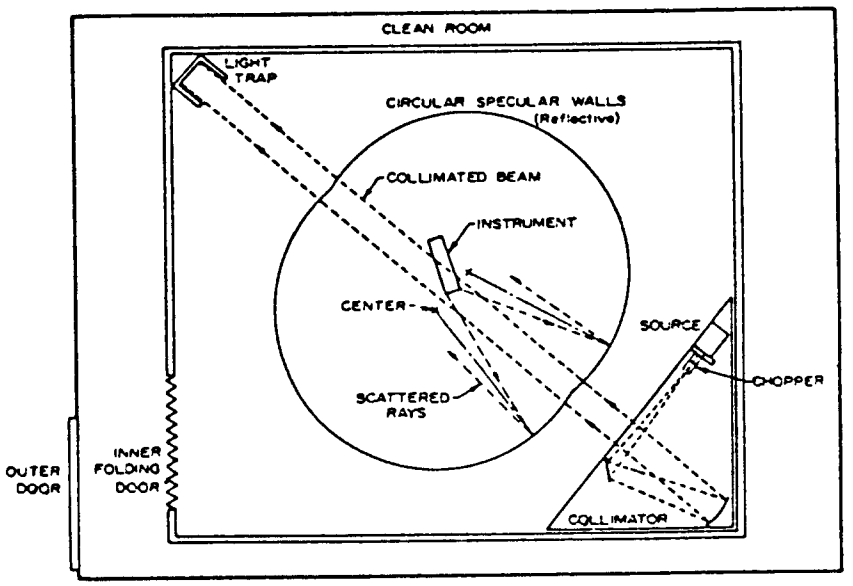

Figure 3-7. Low-scatter facility at Utah State University.

Table 3-6. Relative off-axis response for the SSI optics.

Angle (Deg)	$-\log_{10}$(Rel Response)	Angle (Deg)	$-\log_{10}$(Rel. Response)	Angle (Deg)	$-\log_{10}$(Rel. Response)
0.0	0.0	12.5	6.9	57.5	10.4
0.5	3.5	15.0	6.925	60.0	10.4
1.0	3.9	17.5	7.0	62.5	10.4
1.5	4.975	20.0	7.85	65.0	10.45
2.0	5.0	22.5	7.9	67.5	10.6
2.5	5.2	25.0	7.95	70.0	10.6
3.0	5.6	27.5	7.975	72.5	10.7
3.5	5.75	30.0	8.0	75.0	10.75
4.0	5.825	32.5	8.3	77.5	10.8
4.5	5.975	35.0	8.4	80.0	10.8
5.0	6.0	37.5	8.6	82.5	10.85
5.5	6.2	40.0	8.7	85.0	10.95
6.0	6.25	42.5	8.85	87.5	11.4
6.5	6.45	45.0	8.9	90.0	11.7
7.0	6.55	47.5	8.975		
7.5	6.65	50.0	9.4		
8.0	6.25	52.5	9.9		
10.0	6.8	55.0	10.2		

symmetry about the optical axis. A photomultiplier tube detector was located in the focal plane with a 0.393-in.-diameter aperture stop defining its active area. The image of the source lamp on axis was entirely contained within this "pixel". The field of view of this "pixel" was ±0.19°, which represents the minimum off-axis angle for which the measurement is valid.

Figures 3-8 and 3-9 plot the relative response of the photomultiplier as a function of off-axis angle up to 90° normalized to one on axis. Table 3-6 presents this data in tabular form. The drop in response at about 50° corresponds to where the optics sunshade completely shadows the first optical element of the telescope. The smaller features between 0.5° and 50° result from various specular surfaces, baffle edges and ghost images in the telescope. The minimum reading at 90° is thought to be limited by molecular scattering in the air. The uncertainty in the relative response is estimated to be about 100% and the angular measure is uncertain to about 20%.

To predict the SSI off-axis response using these test data, one must adjust for any differences between the observing conditions and the test conditions. For a point source,

$$K_p(\theta) = (a_S/a_L)\, C(\theta)$$

where

a_S = area of an SSI CCD pixel (2.322576×10^{-6} cm^2)

a_L = area of the calibration "pixel" (0.783 cm^2)

$C(\theta)$ = relative off-axis response curve from calibration (Figures 3-8 and 3-9)

For an extended source (i.e., one that subtends an angle larger than the pixel field of view),

$$K_E(\theta) = (\sigma_S/\sigma_L)\, C(\theta)$$

where

σ_S = solid angle subtended by the source

σ_L = solid angle subtended by the calibration "pixel" (3.5×10^{-5} sr)

The above equations assume that the scattered light reaching the SSI focal plane from the off-axis source during calibration was uniformly spread over the entire area of the calibration "pixel".

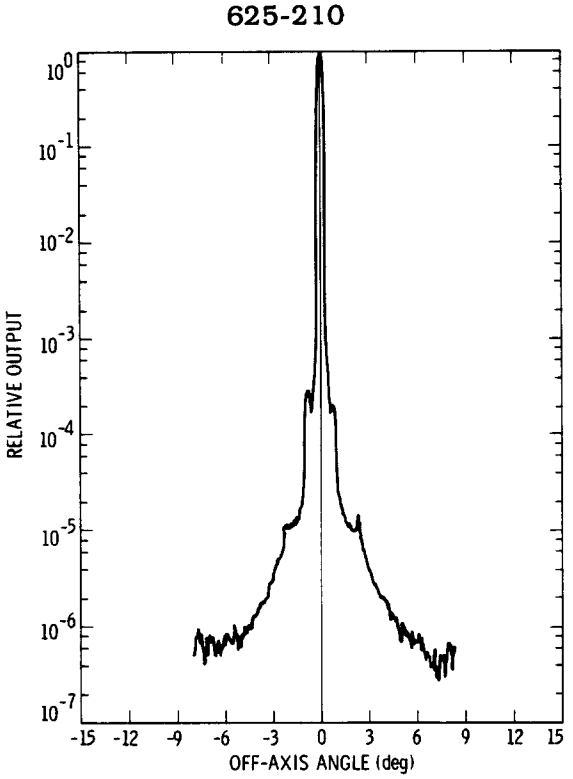

Figure 3-8. Relative off-axis response curve for the SSI optics for angles within 9° of the optical axis.

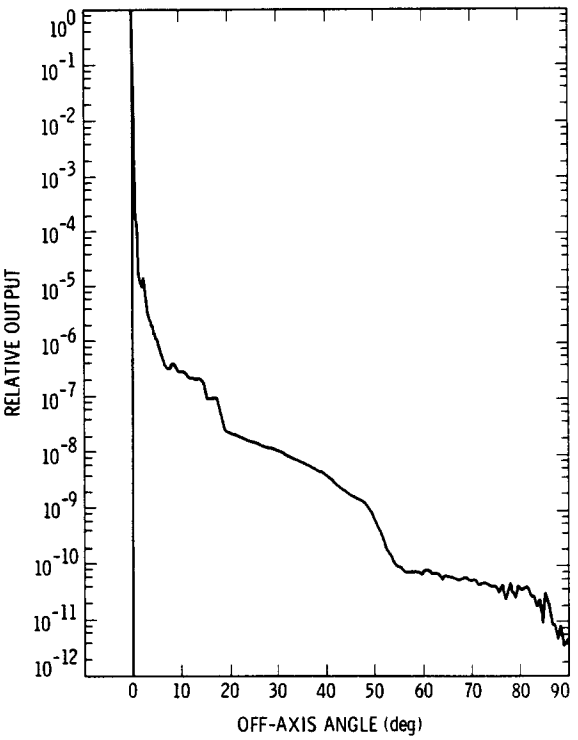

Figure 3-9. Relative off-axis response curve for the SSI optics for off-axis angles up to 90°.

5. Aperture Cover Transmission

The SSI includes a cover containing a quartz annulus over the front aperture of its telescope. The cover is intended to provide contamination protection for the optics. To avoid static charge buildup on the cover, both surfaces are coated with a transparent conductive material, IR-81-E, which causes some loss of transmission in the violet and near-IR. Although the cover is deployable, observations may be made during the early portion of the mission with the cover still in place. Therefore, the transmission characteristics of the cover were measured.

The dimensions of the clear aperture of the cover are 1.75 in. for the inside radius (determined by the secondary mirror obscuration of the telescope) and 2.85 in. for the outside radius. The cover annulus, therefore, increases the optics f/# from 8.5 to 10.4 and reduces the area of the clear aperture of the telescope to about 55% of its value without the cover.

The spectral transmission of the optics cover is shown in Figure 3-10 as measured using a Cary 14 spectrophotometer. No variations in spectral transmission have been observed with location in the annulus. The transmission measurement is accurate to better than ±2% of full scale.

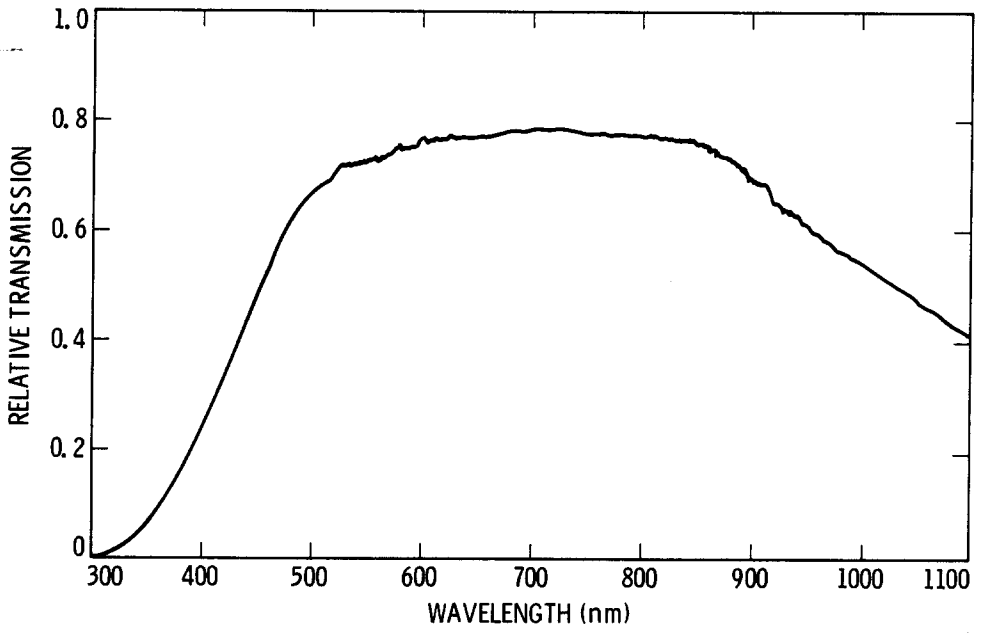

Figure 3-10. Spectral transmission of the optical aperture cover.

6. Quartz Radiation Shield Transmission

To protect the CCD detector from the Jovian charged particle environment, it is desirable to surround the device with a shield of high-atomic-number material. Thus, the SSI camera head includes a 1-cm-thick tantalum shield that encompasses the CCD except for a circular aperture on the optical axis of the instrument. This aperture is filled by a solid, anti-reflection-coated quartz plug to reduce the flux of charged particles that can reach the detector from this direction. Since this plug was not included in the optics transmission measurement, its spectral transmission was measured separately using the Cary 14 spectrophotometer.

The spectral transmission of the quartz plug is shown in Figure 3-11, which is accurate to better than ±2% of full scale.

B. FILTER SPECTRAL TRANSMISSION

The SSI camera is equipped with a filter wheel containing eight spectral filter positions. This wheel can be stepped one through seven positions per imaging frame (depending on the SSI frame rate being used) in the forward direction only. Figure 3-12 shows the filters mounted in order in the filter wheel.

The clear filter was fabricated from T-20 Suprasil fused quartz and coated on both sides with a wideband anti-reflection coating. The spectral filters were manufactured by Barr Associates (7560 Å and 8890 Å) and by Microcoatings, Inc. (<4450 Å, 5600 Å, 6600 Å, 7270 Å and >9680 Å) using various colored glass substrates (from Schott Optical Glass, Inc.) and thin-film interference layers. Spectral transmission data for each filter (at 0^{o} C in a vacuum) are given in Figures 3-13 through 3-20 and Table 3-7. Transmission data at a finer wavelength resolution is provided for the three narrowband filters in Tables 3-8 through 3-10. Calculated filter factors for these filters with respect to the clear filter are listed in Table 3-11 for various source spectra.

The spectral filters were fabricated only from materials that had been verified to be sufficiently resistant to change when subjected to a charged particle radiation environment in excess of that which they will experience at Jupiter (about 50,000 Rad (Si), primarily from electrons with energies of a few MeV). A sample of each filter from the same lot as that used in the flight SSI was also tested for stability under comparable doses. Spectral transmission was measured before and within a few hours after subjecting each filter to successive doses of 30,000, 30,000, and 60,000 Rad (Si) in the JPL Dynamitron (~2-MeV electron source) at room temperature. The only changes observed at a level greater than the transmission measurement

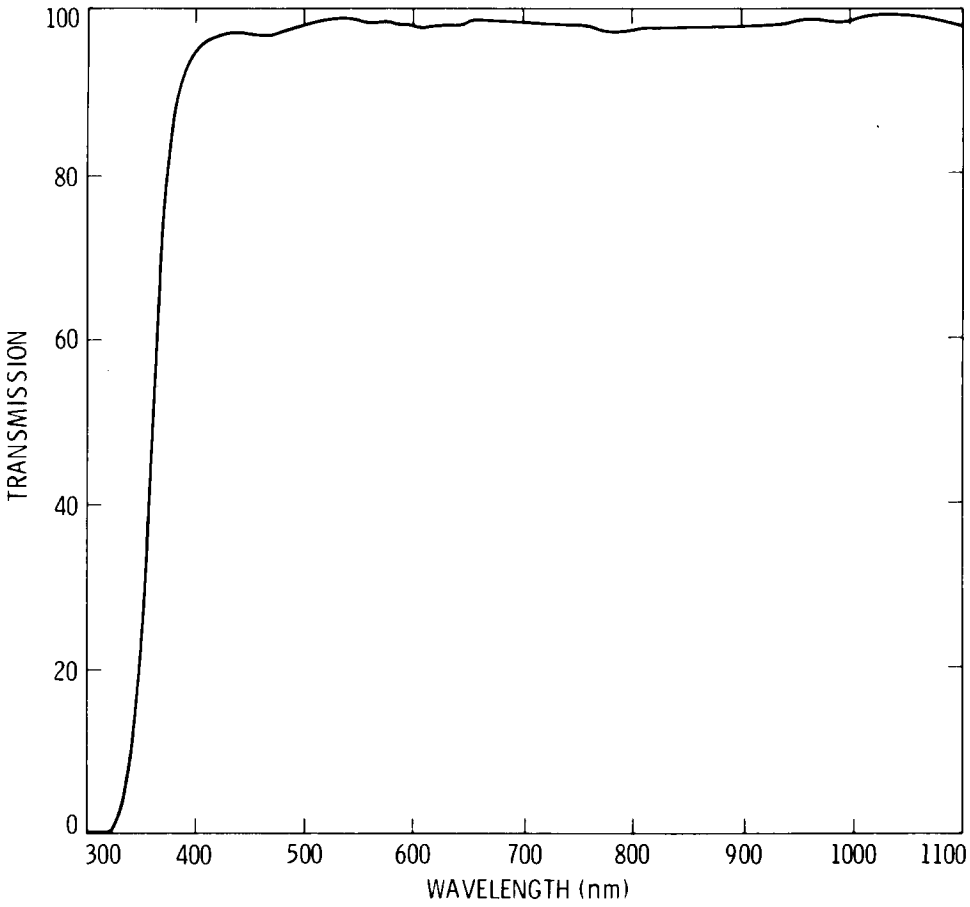

Figure 3-11. Spectral transmission of the quartz radiation shielding plug.

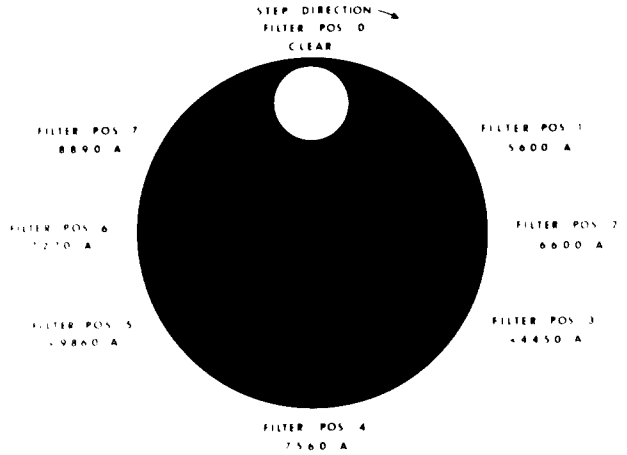

Figure 3-12. SSI filter wheel with filters installed.

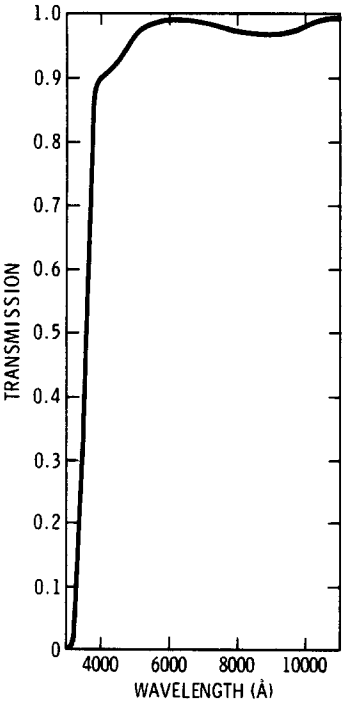

Figure 3-13.
Spectral transmission of the SSI clear filter.

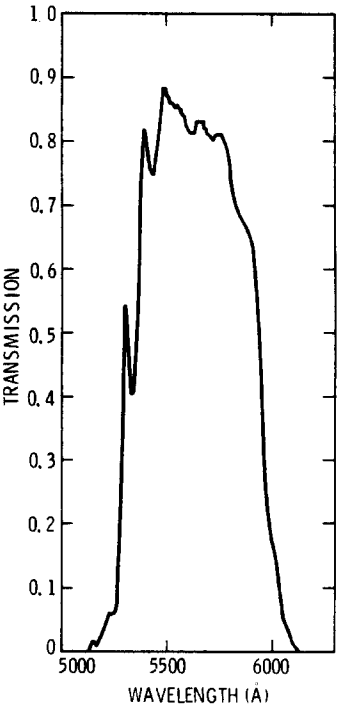

Figure 3-14.
Spectral transmission of the SSI 5600 Å (green) filter.

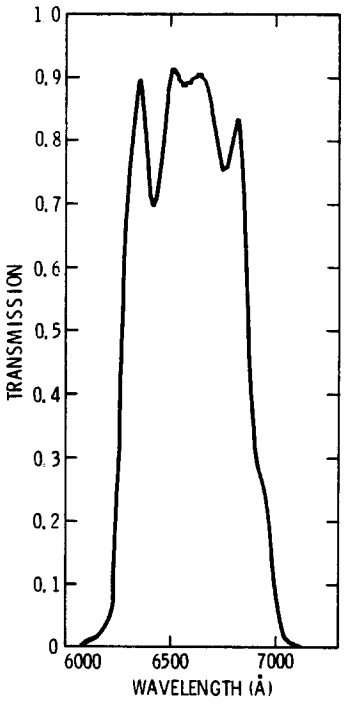

Figure 3-15.
Spectral transmission of the SSI 6600 Å (red) filter.

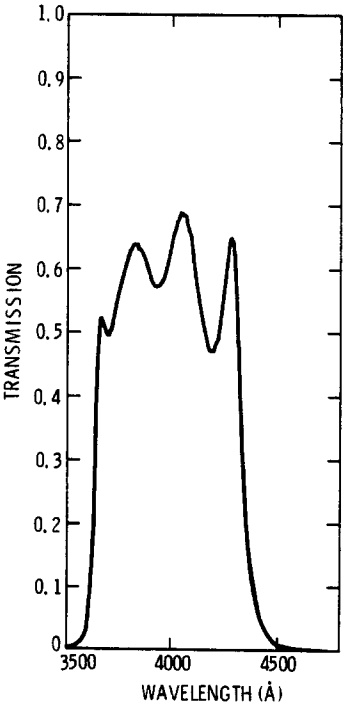

Figure 3-16.
Spectral transmission of the SSI <4450 Å (violet) filter.

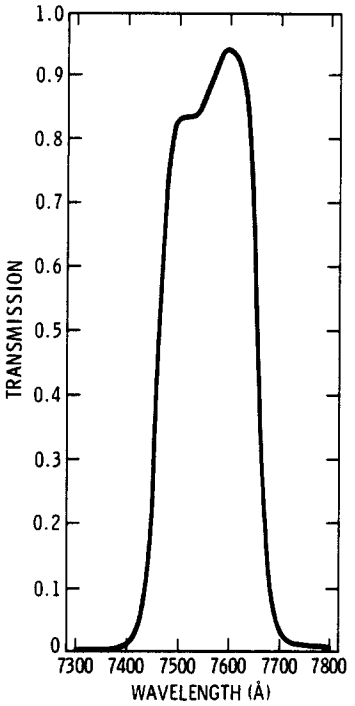

Figure 3-17.
Spectral transmission of the SSI 7560 Å filter.

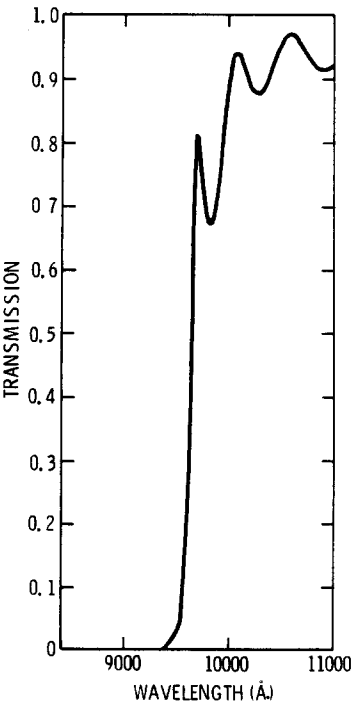

Figure 3-18.
Spectral transmission of the SSI >9680 Å (infrared) filter.

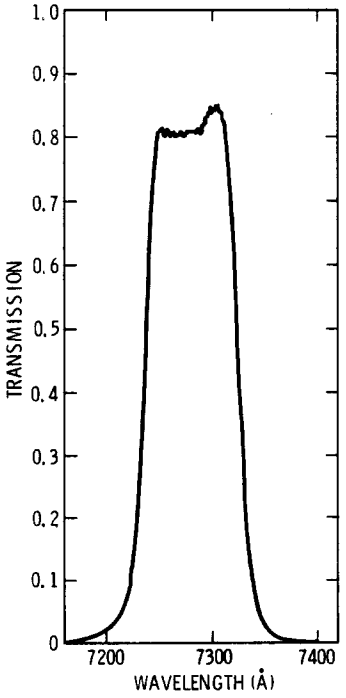

Figure 3-19.
Spectral transmission of the SSI 7270 Å (methane) filter.

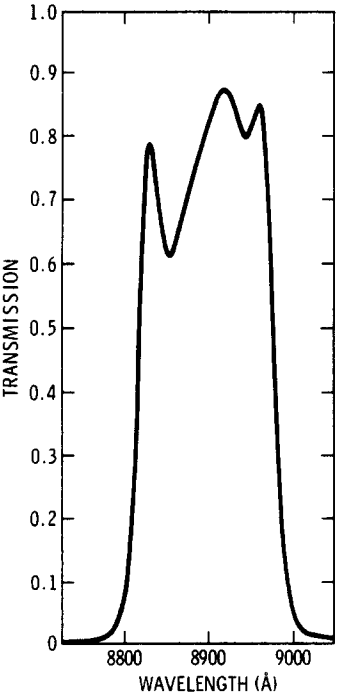

Figure 3-20.
Spectral transmission of the SSI 8890 Å (methane) filter.

Table 3-7. Spectral transmission of the SSI filters at 0° C in vacuum.

λ (nm)	0 clear	1 5600 Å green	2 6600 Å red	3 <4450 Å violet	4 7560 Å	5 >9680 Å	6 7270 Å	7 8890 Å
300	-	-	-	-	-	-	-	-
305	-	-	-	-	-	-	-	-
310	-	-	-	-	-	-	-	-
315	-	-	-	-	-	-	-	-
320	0.0071	-	-	-	-	-	-	-
325	0.0222	-	-	-	-	-	-	-
330	0.053	-	-	-	-	-	-	-
335	0.109	-	-	-	-	-	-	-
340	0.171	-	-	-	-	-	-	-
345	0.240	-	-	-	-	-	-	-
350	0.312	-	-	0.003	-	-	-	-
355	0.387	-	-	0.009	-	-	-	-
360	0.487	-	-	0.053	-	-	-	-
365	0.602	-	-	0.450	-	-	-	-
370	0.696	-	-	0.494	-	-	-	-
375	0.773	-	-	0.558	-	-	-	-
380	0.816	-	-	0.619	-	-	-	-
385	0.859	0.00006	-	0.628	-	-	-	-
390	0.884	0.00006	-	0.583	-	-	-	-
395	0.895	0.00015	-	0.574	-	-	-	-
400	0.908	0.00005	-	0.634	-	-	-	-
405	0.911	0.00004	-	0.685	-	-	-	-
410	0.913	0.00005	-	0.632	-	-	-	-
415	0.916	0.00017	-	0.517	-	-	-	-
420	0.918	0.00100	-	0.468	-	-	-	-
425	0.922	0.00006	-	0.557	-	-	-	-
430	0.926	-	-	0.623	-	-	-	-
435	0.927	-	-	0.234	-	-	-	-
440	0.930	-	-	0.074	-	-	-	-
445	0.934	-	-	0.0273	-	-	-	-
450	0.936	-	-	0.0117	-	-	-	-
455	0.938	-	-	0.0049	-	-	-	-
460	0.940	-	-	0.0021	-	-	-	-
465	0.944	-	-	0.0004	-	-	-	-
470	0.948	-	-	0.0004	-	-	-	-
475	0.952	-	-	0.0004	-	-	-	-
480	0.956	-	-	0.0004	-	-	-	-
485	0.961	-	-	0.0004	-	-	-	-
490	0.965	-	-	0.0004	-	-	-	-
495	0.970	-	-	0.0004	-	-	-	-
500	0.972	-	-	0.00018	-	-	-	-
505	0.977	-	-	0.00011	-	-	-	-
510	0.981	-	-	0.00007	-	-	-	-
515	0.984	0.0133	-	0.00004	-	-	-	-

Table 3-7 (continued).

λ (nm)	0 clear	1 5600 Å green	2 6600 Å red	3 <4450 Å violet	4 7560 Å	5 >9680 Å	6 7270 Å	7 8890 Å
520	0.986	0.0458	-	0.00003	-	-	-	-
525	0.988	0.0735	-	0.00002	-	-	-	-
530	0.990	0.549	-	0.00001	-	-	-	-
535	0.989	0.458	-	0.00001	-	-	-	-
540	0.988	0.820	-	0.00002	-	-	-	-
545	0.987	0.778	-	0.00003	-	-	-	-
550	0.991	0.885	-	0.00007	-	-	-	-
555	0.993	0.865	-	0.00018	-	-	-	-
560	0.994	0.828	-	0.00033	-	-	-	-
565	0.992	0.838	-	0.00053	-	-	-	-
570	0.994	0.816	-	0.00055	-	-	-	-
575	0.988	0.817	0.00007	0.00034	-	-	-	-
580	0.986	0.767	-	0.00012	-	-	-	-
585	0.992	0.689	-	0.00003	-	-	-	-
590	0.996	0.658	-	0.00001	-	-	-	-
595	0.995	0.414	-	0.00001	-	-	-	-
600	0.996	0.187	-	0.00001	-	-	-	-
605	0.996	0.0440	0.0019	0.00001	-	-	-	-
610	0.997	0.0022	0.0100	0.00001	-	-	-	-
615	1.000	-	0.0135	0.00001	-	-	-	-
620	0.997	0.0006	0.0375	0.00001	-	-	-	-
625	0.993	-	0.243	0.00001	-	-	-	-
630	0.995	-	0.726	0.00001	-	-	-	-
635	0.997	-	0.900	0.00001	-	-	-	-
640	0.997	-	0.736	0.00001	-	-	-	-
645	0.995	-	0.748	0.00001	-	-	-	-
650	0.999	-	0.906	0.00001	-	-	-	-
655	0.995	-	0.891	0.00001	-	-	-	-
660	0.991	-	0.895	0.00002	-	-	-	-
665	0.992	-	0.905	0.00003	-	-	-	-
670	0.993	-	0.851	0.00009	-	-	-	-
675	0.992	-	0.754	0.00018	-	-	0.00001	0.00001
680	0.990	-	0.817	0.00038	-	-	0.00001	0.00001
685	0.990	-	0.682	0.00064	-	-	0.00001	0.00001
690	0.990	-	0.328	0.00090	-	-	0.00001	0.00001
695	0.990	-	0.241	0.00100	-	0.00001	0.00002	0.00001
700	0.989	-	0.100	0.00100	-	0.00002	0.00003	0.00001
705	0.989	-	0.0174	0.00095	-	0.00001	0.00006	0.00001
710	0.988	-	0.0047	0.00079	-	-	0.00008	0.00003
715	0.987	-	0.0028	0.00062	-	-	0.00010	0.00001
720	0.986	-	0.0027	0.00049	-	0.00007	0.020	0.00001
725	0.985	-	0.0028	0.00040	-	0.00002	0.811	0.00003
730	0.983	-	-	0.00031	0.000	-	0.840	0.00002
735	0.981	-	0.0001	0.00025	0.003	-	0.0256	0.00001
740	0.981	-	-	0.00039	0.012	0.00002	0.0011	-

Table 3-7 (continued).

λ (nm)	0 clear	1 5600 Å green	2 6600 Å red	3 <4450 Å violet	4 7560 Å	5 >9680 Å	6 7270 Å	7 8890 Å
745	0.981	-	0.00055	0.00033	0.200	0.00001	0.0010	-
750	0.980	-	0.00055	0.00026	0.829	0.00001	0.00006	-
755	0.980	-	0.00065	0.00021	0.854	0.00001	0.00004	-
760	0.978	-	0.00067	0.00020	0.937	0.00001	0.00003	-
765	0.977	-	0.00054	0.00022	0.614	0.00001	0.00002	-
770	0.966	0.00011	0.00039	0.00027	0.0320	0.00001	0.00001	-
775	0.974	-	0.00035	0.00017	0.00500	-	-	-
780	0.973	-	0.00030	0.00016	0.00294	-	-	-
785	0.971	0.00013	0.00030	0.00015	0.00100	-	-	-
790	0.970	-	0.00037	0.00017	0.00049	-	-	-
795	0.961	0.00028	0.00048	0.00019	0.00033	-	0.00001	-
800	0.952	0.00043	0.00047	0.00022	0.00029	-	0.00002	-
805	0.943	0.00041	0.00041	0.00024	0.00013	0.00001	0.00002	-
810	0.943	0.00027	0.00042	0.00028	0.00016	0.00001	0.00002	-
815	0.934	0.00028	0.00043	0.00033	0.00017	0.00001	0.00002	-
820	0.934	0.00050	0.00048	0.00038	0.00016	0.00002	0.00002	-
825	0.925	0.00060	0.00061	0.00042	0.00016	0.00002	0.00001	-
830	0.934	0.00043	0.00095	0.00052	0.00017	0.00002	-	-
835	0.925	0.00010	0.00180	0.00062	0.00018	0.00002	0.00002	-
840	0.916	0.00027	0.00198	0.00070	0.00018	0.00002	0.00003	-
845	0.908	0.00022	0.00193	0.00083	0.00017	0.00003	0.00003	0.00001
850	0.916	0.00028	0.00306	0.00105	0.00017	0.00003	0.00002	0.00001
855	0.934	0.00033	0.00400	0.00130	0.00018	0.00002	0.00002	0.00001
860	0.960	0.00034	0.00650	0.00143	0.00019	0.00002	0.00001	0.00003
865	0.970	0.00032	0.00806	0.00154	0.00019	0.00001	0.00001	0.00009
870	0.970	0.00022	0.00456	0.00159	0.00019	-	0.00001	0.0050
875	0.959	0.00030	0.00106	0.00156	0.00017	0.00004	0.00001	0.0067
880	0.969	0.00040	0.0106	0.00152	0.00016	0.00008	0.00002	0.0850
885	0.970	0.00046	0.0185	0.00143	0.00015	0.00006	0.00004	0.610
890	0.971	0.00050	0.00177	0.00130	0.00013	0.00008	0.00008	0.828
895	0.974	0.00054	0.00041	0.00106	0.00011	0.00006	0.00004	0.808
900	0.974	0.00055	0.00019	0.00087	0.00009	0.00041	0.00002	0.043
905	0.974	0.00055	0.00017	0.00065	0.00007	0.00043	0.00001	0.007
910	0.975	0.00054	0.00033	0.00048	0.00006	0.00061	0.00001	0.003
915	0.976	0.00052	0.00028	0.00035	0.00004	0.00076	0.00002	0.00022
920	0.978	0.00048	0.00011	0.00022	0.00003	0.00100	0.00003	0.00013
925	0.978	0.00039	0.00007	0.00017	0.00002	0.00150	0.00018	0.00009
930	0.978	0.00028	0.00012	0.00016	0.00001	0.00220	0.00018	0.00008
935	0.978	0.00024	0.00015	0.00015	-	0.00359	0.00003	0.00007
940	0.979	0.00020	0.00011	0.00014	-	0.00522	0.00001	0.00006
945	0.980	0.00017	0.00009	0.00013	-	0.0143	0.00001	0.00005
950	0.981	0.00019	0.00021	0.00013	-	0.0318	0.00001	0.00005
955	0.982	0.00024	0.00041	0.00012	-	0.0626	-	0.00005
960	0.983	0.00035	0.00050	0.00010	-	0.235	0.00001	0.00004
965	0.985	0.00046	0.00048	0.00009	-	0.578	0.00001	0.00004

Table 3-7 (continued).

λ (nm)	0 clear	1 5600 Å green	2 6600 Å red	3 <4450 Å violet	4 7560 Å	5 >9680 Å	6 7270 Å	7 8890 Å
970	0.984	0.00061	0.00029	0.00009	-	0.809	0.00001	0.00003
975	0.986	0.00057	0.00021	0.00009	-	0.750	0.00001	0.00003
980	0.987	0.00054	0.00016	0.00010	-	0.680	-	0.00002
985	0.989	0.00052	0.00015	0.00011	-	0.680	-	0.00002
990	0.990	0.00054	0.00016	0.00013	-	0.735	-	0.00002
995	0.991	0.00052	0.00018	0.00014	-	0.813	0.00001	0.00002
1000	0.990	0.00048	0.00019	0.00013	-	0.880	0.00002	0.00001
1005	0.992	0.00050	0.00022	0.00012	-	0.934	0.00001	0.00001
1010	0.994	0.00059	0.00026	0.00011	-	0.941	-	0.00001
1015	0.995	0.00087	0.00028	0.00012	-	0.917	-	0.00001
1020	0.996	0.00109	0.00028	0.00013	-	0.885	0.00001	0.00001
1025	0.996	0.00126	0.00023	0.00015	-	0.878	0.00002	0.00001
1030	0.998	0.00143	0.00013	0.00020	-	0.878	0.00001	0.00001
1035	0.998	0.00158	0.00005	0.00022	-	0.887	0.00001	0.00001
1040	0.998	0.00170	0.00009	0.00023	-	0.909	0.00001	0.00001
1045	0.999	0.00179	0.00017	0.00022	-	0.933	0.00001	0.00001
1050	0.997	0.00189	0.00018	0.00018	-	0.956	-	0.00001
1055	0.997	0.00200	0.00018	0.00017	-	0.970	0.00001	0.00001
1060	0.997	0.00213	0.00022	0.00020	-	0.974	0.00001	0.00002
1065	0.997	0.00250	0.00024	0.00024	-	0.963	0.00001	0.00004
1070	0.997	0.00283	0.00026	0.00033	-	0.953	0.00001	0.00002
1075	0.997	0.00326	0.00033	0.00039	-	0.936	0.00001	0.00001
1080	0.997	0.00367	0.00070	0.00046	-	0.926	0.00002	0.00001
1085	0.996	0.00422	0.00100	0.00054	-	0.914	0.00002	-
1090	0.996	0.00459	0.00200	0.00076	-	0.915	0.00002	-
1095	0.996	0.00509	0.00500	0.00085	-	0.916	0.00002	-
1100	0.996	0.00530	0.00630	0.00100	-	0.919	0.00001	-

accuracy (~2%) were: a) the 5600 Å filter transmission increased 3 - 4 % within the bandpass after the last incremental dose (going from 60,000 to 120,000 Rad total), b) the 6600 Å filter transmission was reduced about 2% in the bandpass and the bandpass shifted about 10 Å longward after the last incremental dose, and c) the 7560 Å filter transmission was reduced by about 2.5 - 3 % after each incremental dose for a total drop of 9% after 120,000 Rad; however, after 18 days at ambient conditions, the transmission had increased again by about 7%.

C. SHUTTER TIMES

The SSI shutter is of the mechanical focal-plane type with two blades: one blade opens the aperture, and the other blade covers it after the desired exposure interval. The exposure time is controlled by the SSI microprocessor, which provides a separate pulse to start each of the two shutter blades.

Table 3-8. Spectral transmission of the SSI 7270 Å filter at 0° C in vacuum.

λ (nm)	trans.	λ (nm)	trans.	λ (nm)	trans.	λ (nm)	trans.
714	0.00000	722	0.07500	730	0.84000	738	0.00200
715	0.00010	723	0.21000	731	0.83500	739	0.00200
716	0.00080	724	0.57000	732	0.62000	740	0.00110
717	0.00250	725	0.81100	733	0.27000	741	0.00100
718	0.00750	726	0.81000	734	0.09000	742	0.00100
719	0.01200	727	0.80500	735	0.02560	743	0.00050
720	0.02000	728	0.80900	736	0.00900	744	0.00000
721	0.03200	729	0.81500	737	0.00400		

Table 3-9. Spectral transmission of the SSI 7560 Å filter at 0° C in vacuum.

λ (nm)	trans.	λ (nm)	trans.	λ (nm)	trans.	λ (nm)	trans.
721	0.00000	736	0.00500	751	0.83500	766	0.53000
722	0.00000	737	0.00600	752	0.84500	767	0.31000
723	0.00000	738	0.00600	753	0.85000	768	0.12000
724	0.00000	739	0.00800	754	0.85250	769	0.09000
725	0.00000	740	0.01200	755	0.85400	770	0.03200
726	0.00000	741	0.09500	756	0.86500	771	0.03000
727	0.00000	742	0.02700	757	0.91000	772	0.01500
728	0.00000	743	0.04200	758	0.94500	773	0.00900
729	0.00000	744	0.11000	759	0.95700	774	0.00900
730	0.00000	745	0.20000	760	0.93700	775	0.00500
731	0.00500	746	0.25000	761	0.95500	776	0.00500
732	0.00500	747	0.50500	762	0.95000	777	0.00400
733	0.00500	748	0.74500	763	0.92000	778	0.00300
734	0.00500	749	0.82000	764	0.83000	779	0.00200
735	0.00300	750	0.82900	765	0.61400	780	0.00294

Table 3-10. Spectral transmission of the SSI 8890 A filter at 0° C in vacuum.

λ (nm)	trans.	λ (nm)	trans.	λ (nm)	trans.	λ (nm)	trans.
870	0.00010	879	0.02687	888	0.75620	897	0.75620
871	0.00010	880	0.08500	889	0.79600	898	0.37810
872	0.00010	881	0.19900	890	0.82700	899	0.09950
873	0.00010	882	0.47760	891	0.85073	900	0.03800
874	0.00010	883	0.78108	892	0.86267	901	0.02574
875	0.00200	884	0.65670	893	0.81590	902	0.00792
876	0.00200	885	0.60700	894	0.79103	903	0.00495
877	0.00299	886	0.61690	895	0.80500	904	0.00198
878	0.01592	887	0.64675	896	0.84078	905	0.00099

Table 3-11. Filter factors and effective wavelengths for SSI filters (based on component calibrations).

source spectrum		filter clear	green	red	violet	7560Å	>9680Å	7270Å	8890Å
gray	FF	1.000	8.113	7.145	22.36	36.97	138.2	59.31	150.0
	λ_{eff}	642.1	563.3	660.4	410.4	756.4	992.7	727.5	890.0
solar	FF	1.000	6.760	7.055	22.90	45.43	275.0	68.22	239.3
	λ_{eff}	618.1	562.9	659.4	412.2	756.3	991.1	727.5	890.0
Jupiter	FF	1.000	6.058	6.716	26.49	44.90	690.8	108.8	1895.
NTrZ	λ_{eff}	608.7	562.8	659.3	413.4	756.1	991.4	727.8	890.0
Jupiter	FF	1.000	5.932	6.253	35.32	43.00	628.4	101.5	1416.
EQ	λ_{eff}	617.4	563.2	659.3	414.6	756.0	991.4	727.8	889.9
Jupiter	FF	1.000	6.129	6.546	30.33	43.23	361.5	75.72	420.3
SPH	λ_{eff}	615.5	563.0	659.3	413.8	756.2	991.3	727.6	889.9
Io	FF	1.000	6.734	5.980	78.49	37.60	237.2	57.11	205.4
"reddest"	λ_{eff}	645.2	563.9	659.7	421.0	756.3	991.0	727.5	889.9
Io	FF	1.000	6.956	6.263	44.23	39.38	248.4	59.81	215.2
average	λ_{eff}	636.6	563.6	659.7	416.6	756.3	991.0	727.5	889.9
Io	FF	1.000	7.377	6.734	23.67	42.33	267.1	64.31	231.3
"whitest"	λ_{eff}	623.3	563.3	659.7	413.3	756.3	991.0	727.5	889.9
Europa	FF	1.000	6.571	6.616	35.31	42.85	270.4	64.33	231.6
leading	λ_{eff}	627.9	563.0	659.5	414.5	756.3	990.7	727.5	889.9
Europa	FF	1.000	6.517	6.561	41.36	42.49	268.2	63.80	229.7
trailing	λ_{eff}	629.7	563.0	659.5	415.4	756.3	990.7	727.5	889.9
Ganymede	FF	1.000	6.739	6.533	33.54	42.71	271.1	62.79	230.3
	λ_{eff}	628.7	563.4	659.5	413.9	756.2	990.7	727.5	889.9
Callisto	FF	1.000	6.660	6.677	33.80	41.29	254.5	64.56	217.1
	λ_{eff}	629.3	563.1	659.4	414.2	756.3	990.8	727.5	890.0
Moon	FF	1.000	7.035	6.102	82.07	35.36	254.0	53.68	182.8
	λ_{eff}	652.3	563.9	660.0	419.5	756.4	990.2	727.5	889.9
Venus	FF	1.000	6.245	6.210	83.21	40.46	341.8	59.29	230.6
	λ_{eff}	638.2	563.3	659.5	420.7	756.4	989.4	727.5	889.9

Each shutter assembly has a different response to commands because of differing frictional forces and other influences. The actual exposure and shading data were obtained at -15, -9, 0, +6, +16 and +26° C.

A shutter test fixture illuminated five diodes with collimated light for measurements of shutter characteristics. The five diodes were equally spaced at 3.15 mm. The true times obtained for a commanded exposure of 2.5, 25.0 and 97.5 ms are summarized in Table 3-12. Twenty measurements were obtained for each diode at each commanded exposure time and each temperature. The uncertainties given in Table 3-12 are the standard deviations over all 20 measurements at each of the 5 diodes. As can be seen, the true shutter times are shorter than the commanded time, but what is even more important is that the difference is consistently systematic. The frame-wide average shutter offset value does not appear to vary in any systematic way with the commanded exposure time. It does, however, vary systematically with temperature, the offset being somewhat larger at +16° C, +6° C and also possibly at -15° C than at the other temperatures. These systematic shutter time offsets, listed in Table 3-13, were also determined at the subsystem level during radiometric reciprocity calibrations (see Section IV-A-2 for full details).

The shutter shading characteristics are shown in Figures 3-21 through 3-26. Although the shutter offset values at a given diode position do vary with temperature, the variation in offset across the diodes (i.e., the shading) stays fairly constant except at the edge of the frame which is exposed first (i.e., the top edge of an SSI image). Here the offset increases systematically as the temperature of the shutter decreases. At the expected flight operating temperature of about 8° C, the shutter offset should be the greatest at the top of an image with progressively less offset (i.e., longer exposure) as one moves toward the bottom of an image. However, the subsystem-level measurements of shutter offset showed the opposite trend (see Section IV-A-2). Note that only three of the five diodes lie within the active SSI CCD format (shown in Figures 3-21 through 3-26), although the average shutter times in Tables 3-12 and 3-13 are based on all five diodes. The accuracy of several repeated measurements at a given diode location was less than 0.14 ms (1 σ), with the largest variations occurring at the extreme temperatures. At the +6° C temperature (closest to the expected flight temperature), the variation was less than 0.04 ms, within the ± 40 µs accuracy requirement of Reference 2-1.

The shutter blades do bounce at the completion of an exposure, which causes an additional amount of light to pass through below the bottom edge of the detector. Tests indicated that this additional exposure will never

Table 3-12 SSI component-level shutter times (frame-wide averages).

commanded shutter time	2.5 ms	25.0 ms	97.5 ms
actual shutter times (ms)			
-15° C	1.661 ± 0.126	24.196 ± 0.094	96.690 ± 0.062
-9° C	1.761 ± 0.093	24.265 ± 0.061	96.738 ± 0.057
0° C	1.814 ± 0.061	24.264 ± 0.058	96.779 ± 0.052
+6° C	1.760 ± 0.048	24.182 ± 0.046	96.688 ± 0.042
+16° C	1.695 ± 0.046	24.178 ± 0.037	96.634 ± 0.045
+26° C	1.767 ± 0.061	24.312 ± 0.043	96.702 ± 0.038

Table 3-13. SSI component-level shutter time offsets (frame-wide averages).

commanded shutter time	2.5 ms	25.0 ms	97.5 ms
shutter time offset (ms)			
-15° C	0.840	0.804	0.810
-9° C	0.739	0.735	0.762
0° C	0.686	0.736	0.722
+6° C	0.740	0.818	0.812
+16° C	0.805	0.822	0.866
+26° C	0.733	0.688	0.798

occur less than 0.1 inch from the CCD pixel array over a temperature range of -20° C to +25° C. The results and analysis of the subsystem-level radiometric tests verify this result (see Section IV-A-2).

D. CCD

The detector used in the SSI is an 800 x 800 picture element array, virtual-phase charge-coupled device (CCD) manufactured by Texas Instruments, Inc. The photosensitive material is a thin wafer of silicon upon which an array of polysilicon electronic gates is deposited for use in controlling signal charge collection and transfer. The active image area is 12.192 x 12.192 mm. Each pixel is 15.24 μm square. The device is illuminated from the front side (i.e., the side on which the

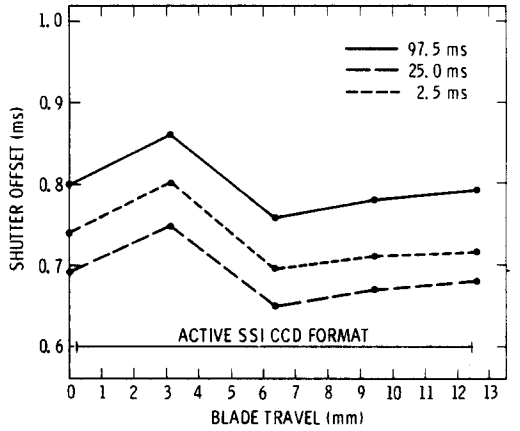

Figure 3-21.
Shutter time offsets
at +26° C.

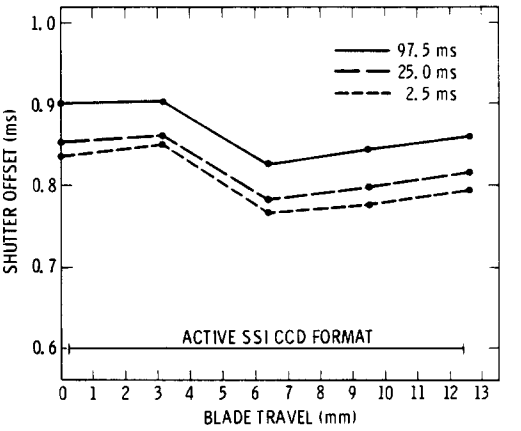

Figure 3-22.
Shutter time offsets
at +16° C.

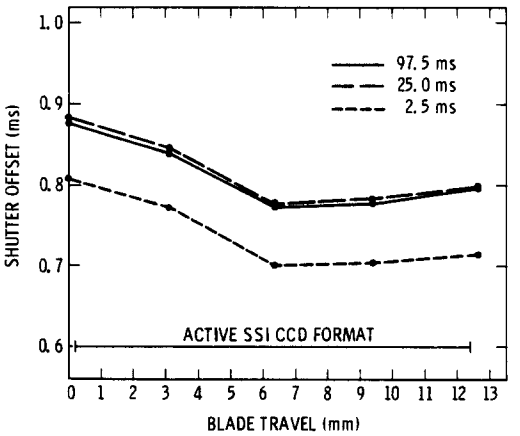

Figure 3-23.
Shutter time offsets
at +6° C.

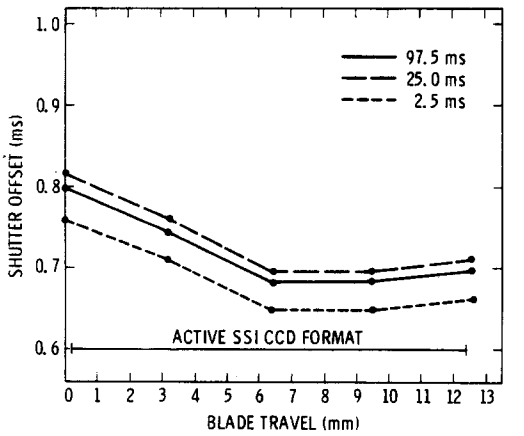

Figure 3-24.
Shutter time offsets
at 0° C.

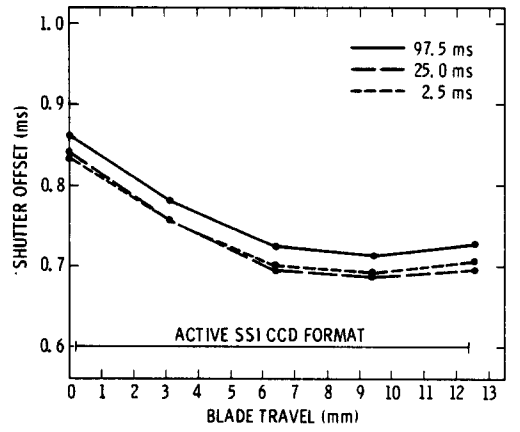

Figure 3-25.
Shutter time offsets
at -9° C.

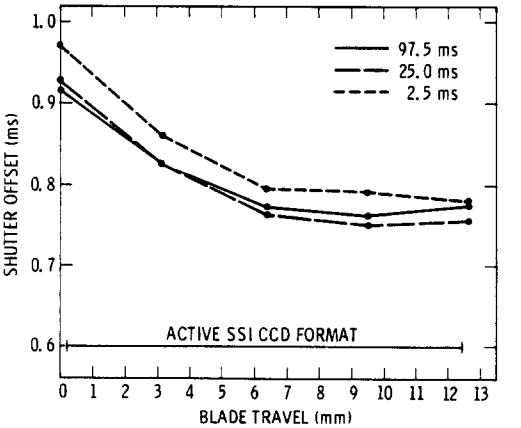

Figure 3-26.
Shutter time offsets
at -15° C.

gates are deposited). The CCD chip is mounted in a package with an anti-reflection-coated quartz window in front of it. For more details on the SSI CCD, see References 3-5 and 3-6.

1. Spectral Response

The absolute quantum efficiency (signal electrons out/incident photon) was measured for the flight CCD in its package. QE was measured over the wavelength band from 375 to 1100 nm in steps of 25 nm. The CCD was cooled to a temperature of -70° C for these measurements (the nominal flight temperature was subsequently lowered to -110° C). A monochrometer was used to illuminate the CCD at each selected wavelength, and an image was acquired using the JPL Virtual-Phase Sensor Test Set. The image data numbers (DN) were converted to signal electrons/pixel by subtracting the zero-exposure offset DN value and multiplying by a previously established system gain constant (e-/DN). The amount of light falling on the CCD was determined by placing a calibrated photodiode detector at the same distance from the monochrometer output as the CCD and recording its response at each wavelength. QE was then calculated by

$$QE = \frac{CRhc}{Dat\lambda}$$

where

C = calibrated photodiode sensitivity (amps/watt)
R = CCD output (e-/pixel)
h = Planck's constant (watt-sec^2)
c = speed of light (cm/sec)
D = calibrated photodiode output per unit area (amps/cm^2)
a = area of pixel (cm^2/pixel)
t = CCD exposure time (sec)
λ = wavelength of incident light (cm-photon)

Note: hc/λ = energy associated with a photon of wavelength λ.

Visual examination of the near-monochromatic images revealed only a few isolated pixels whose response versus wavelength differed significantly from that of the average across the entire array. Therefore we present QE data only for the average of four 65 x 59 pixel areas selected to avoid any anomalous blemishes on the array. This average QE is plotted versus wavelength in Figure 3-27 and listed in Table 3-14. The values given are estimated to be accurate to ±6% absolute for wavelengths of 425 nm or greater. The value of QE at one wavelength relative to that at another should be accurate to ±4% above 425 nm. Below 425 nm, the accuracy of the QE measurement degrades due to decreasing sensitivity of the calibrated

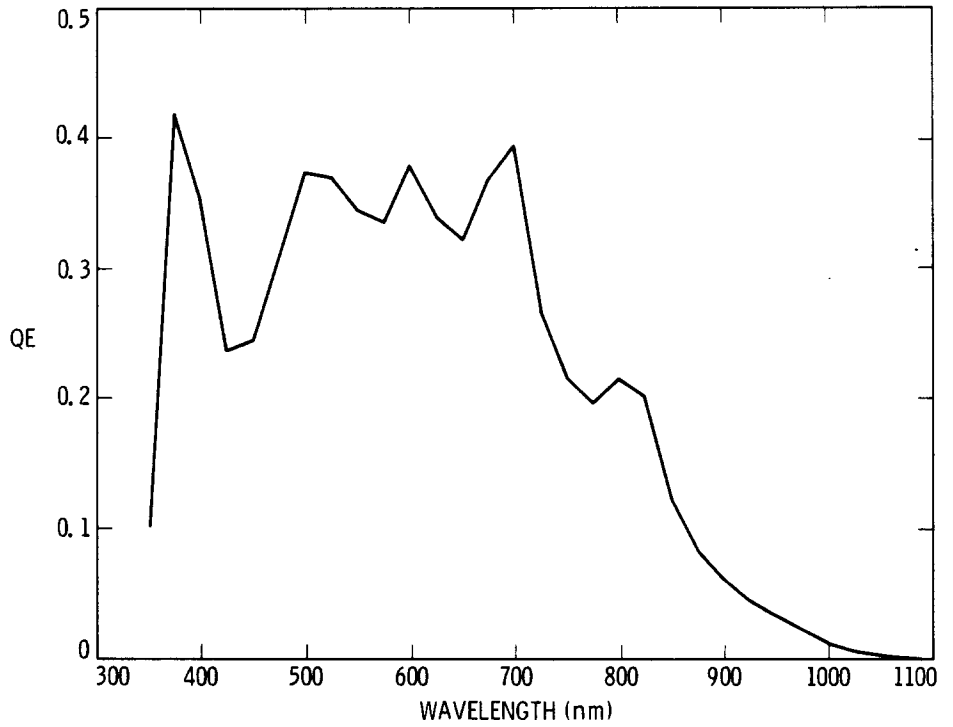

Figure 3-27. Quantum efficiency (QE) of the SSI CCD as measured at -70° C.

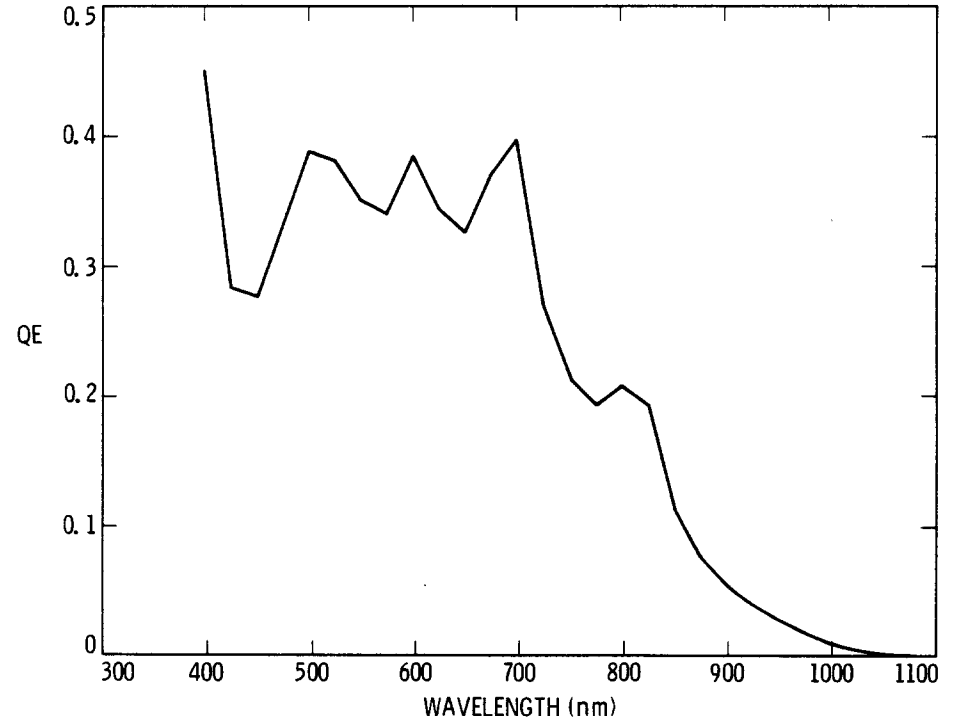

Figure 3-28. Quantum efficiency (QE) of the SSI CCD corrected for difference between calibration temperature (-70° C) and nominal flight temperature of -110° C.

Table 3-14. CCD Quantum Efficiency (QE) Measured at -70° C.

λ (nm)	QE	λ (nm)	QE
350	0.1	750	0.216
375	0.42	775	0.196
400	0.352	800	0.215
425	0.236	825	0.202
450	0.245	850	0.123
475	0.310	875	0.0828
500	0.374	900	0.0611
525	0.371	925	0.0460
550	0.345	950	0.0335
575	0.335	975	0.0220
600	0.379	1000	0.0123
625	0.340	1025	0.0055
650	0.322	1050	0.00198
675	0.368	1075	0.00074
700	0.393	1100	0.000082
725	0.268		

Table 3-15. CCD Quantum Efficiency (QE) Corrected for -110° C.

λ (nm)	QE	λ (nm)	QE
400	0.451	750	0.214
425	0.283	775	0.193
450	0.277	800	0.208
475	0.333	825	0.193
500	0.389	850	0.115
525	0.382	875	0.0762
550	0.352	900	0.0550
575	0.341	925	0.0405
600	0.385	950	0.0285
625	0.345	975	0.0180
650	0.327	1000	0.0094
675	0.372	1025	0.0039
700	0.397	1050	0.00125
725	0.269	1075	0.00038
		1100	0.000028

photodiode and output of the monochrometer source. Short wavelength QE accuracies are estimated to be ±25% at 400 nm, ±200% at 375 nm, and meaningless at 350 nm.

Two effects cause the QE of the virtual-phase CCD to change with temperature. First, the bandgap of silicon increases as temperature decreases. This reduces QE at wavelengths beyond the red because fewer of these lower-energy photons will interact with sufficient energy to release a signal electron. Second, the absorption coefficient of the polysilicon gate material decreases as temperature decreases. This enhances the QE at wavelengths shortward of blue because fewer of these photons get absorbed in the gate material and therefore will penetrate to interact in the silicon wafer where their signal charge can be collected. Since the planned flight temperature of the CCD is lower by 40° C than that at which QE calibration data were obtained, the QE curve must be adjusted to account for the temperature-induced effects described above if we wish to have a better estimate of the actual CCD QE curve under flight conditions. Our best estimate of such a corrected QE curve is given in Figure 3-28 and Table 3-15. The uncertainties in this curve are obviously larger in the blue and red/near-IR than for the directly measured QE curve. Uncertainties are estimated to be ±35% at 400 nm, ±20% between 400 and 500 nm and between 800 and 1000 nm, and ±40% above 1000 nm.

2. Full-Well Capacity

The individual pixels in the CCD array are able to collect and/or properly transfer only a limited number of signal electrons at a time. This limit is called the full-well capacity of the pixel. For the virtual-phase CCD, the full well is limited by the number of signal electrons that can be transferred properly rather than by the number that can be held in a pixel without spillover (blooming) occurring during signal integration. The full-well limit of every pixel was determined by acquiring flat-field images at progressively longer exposure times so as to generate signal levels just below, at, and above the various full-well limits of the pixels in the array.

Two techniques were used in analyzing these data to determine the full-well capacity of the device. The first technique, which establishes an average full-well level for a given area on the array, involves use of the photon transfer curve. The photon transfer curve is a plot of r.m.s. noise (after correcting for pixel-to-pixel sensitivity variations) versus mean signal level over a specified area on the array. A photon transfer curve for a typical area on the SSI CCD is shown in Figure 3-29. The curve is plotted in units of DN. Three principal regions of interest are apparent in this curve. At low signal levels the noise level is determined by the intrinsic CCD read noise. At intermediate signal levels, the curve is dominated by signal shot noise due to photon statistics, and is characterized by a line of slope 1/2 since the noise is proportional to the square root of the signal level. This

straight line also yields the system gain constant (conversion from DN to signal electrons). For a shot-noise-limited system, $n = \sqrt{s}$ in electrons where n = noise and s = signal. Converting both signal and noise to units of DN as are plotted in Figure 3-29 yields the equation $g = s/n^2$, where s and n are now in units of DN and g = system gain constant (e-/DN). At high signal levels, a break point occurs in the plot where noise actually decreases. This break point signifies the device full-well capacity. Above this signal level, charge begins to spill from one pixel to another during image readout, resulting in an averaging of charge between the pixels and an apparent reduction in the shot noise component.

Photon transfer curves were computed and analyzed for full-well levels for 100 20 x 20 areas spread across the CCD array. Full-well limits ranged between 111,000 e- and 122,000 e- for areas near the top of the array (where charge packets must be transferred through relatively few pixel locations during readout) and between 102,000 e- and 111,000 e- for areas near the bottom of the array.

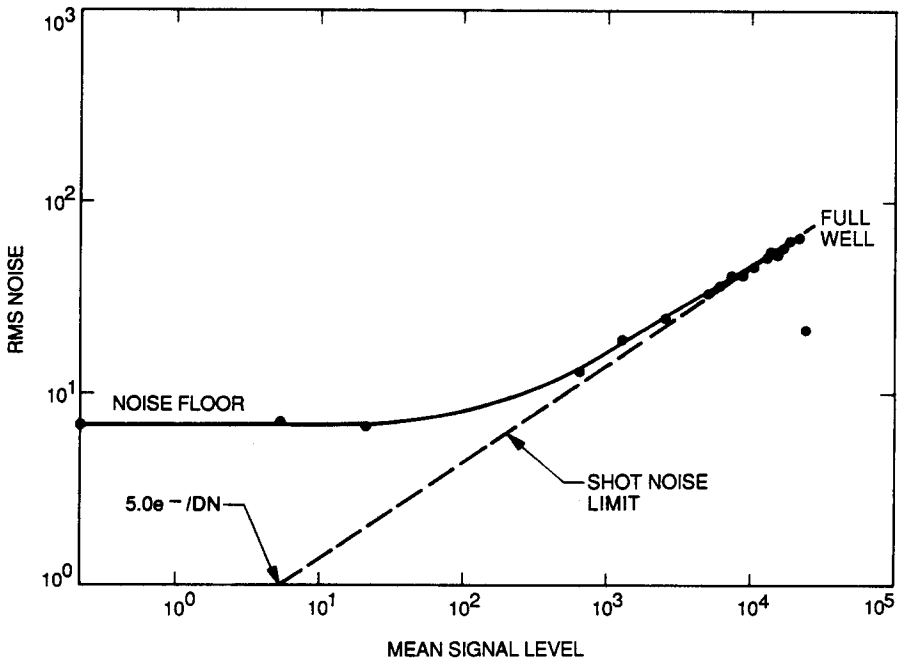

Figure 3-29. Photon transfer curve for a region of the SSI CCD.

The second technique, which can establish the full-well limit of any given pixel, involves producing plots of the signal level along a line near the bottom of the frame and visually examining the flat-field images for exposures near and over the full-well signal level. Flat-field images, such as that of Figure 3-30, show that there are a few isolated pixels with full-well limits much lower than the average (see columns 269, 466, 520, 578 and 594, for example). These pixels also limit the amount of charge that can be properly read out for all pixels below them in their columns. Line traces of the signal in line 796, such as shown in Figure 3-31, allow estimation of the limiting signal level for each column for any pixel on or above that line. As the signal level reaches the level of full well for more pixels, the image begins to smear near the bottom center of the array, as shown in Figure 3-32, and the random noise level in this area decreases, as shown in the line trace of Figure 3-33. Further increases in exposure result in Figures 3-34 and 3-35. Using these data, a full-well limit can be established that will retain proper charge transfer for all columns except those few having much lower than average full-well levels. This technique yields a value of about 108,000 e- for the SSI CCD, which is consistent with the value found for the bottom of the frame using the photon transfer technique. Exposures which generate more signal electrons than this will result in smearing out of image detail.

The SSI CCD can be operated in a mode in which the charge from 2 x 2 blocks of pixels is summed on the detector during readout to enhance the signal-to-noise ratio and shorten the frame readout time. The full-well limit of these "summed" pixels was also investigated using flat-field images and line traces. As can be seen from Figure 3-36, the limiting mechanism for full well in this mode is the same as that when the CCD is operated normally. Thus, the full-well limit in the summation mode is simply four times that without summation, i.e., 432,000 e- per summed pixel.

3. Blooming

If signal charge is generated in the CCD that exceeds the full-well capacity, charge can spill over (or bloom) from one pixel to adjacent pixels. This effect was characterized by imaging the blooming target (see Section II-D) at exposure levels of approximately 1, 2, 5, 10 and 50 times full well. A sufficient number of dark frames were acquired after each exposure to guarantee that all charge generated had been transferred out of the array prior to the next exposure.

Images were acquired with the CCD clock voltages controlled in three different modes denoted inverted, non-inverted, and blemish protection.

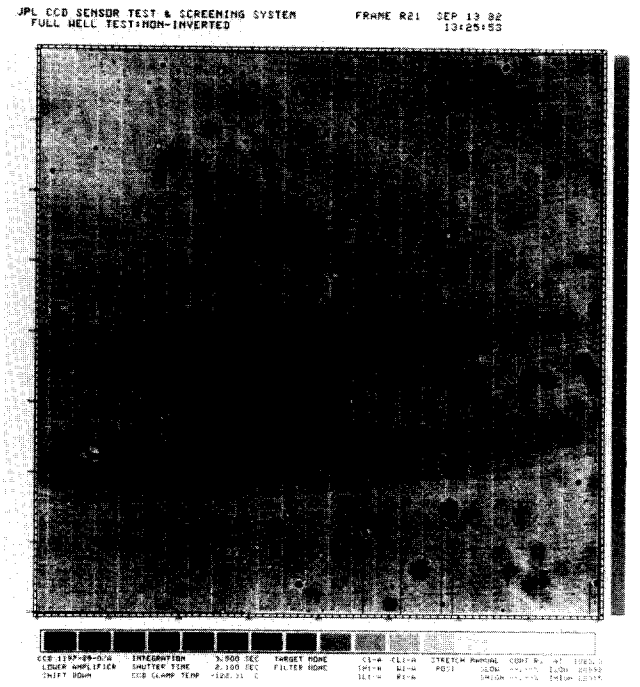

Figure 3-30. Flat-field image showing isolated pixels with unusually low full-well limits.

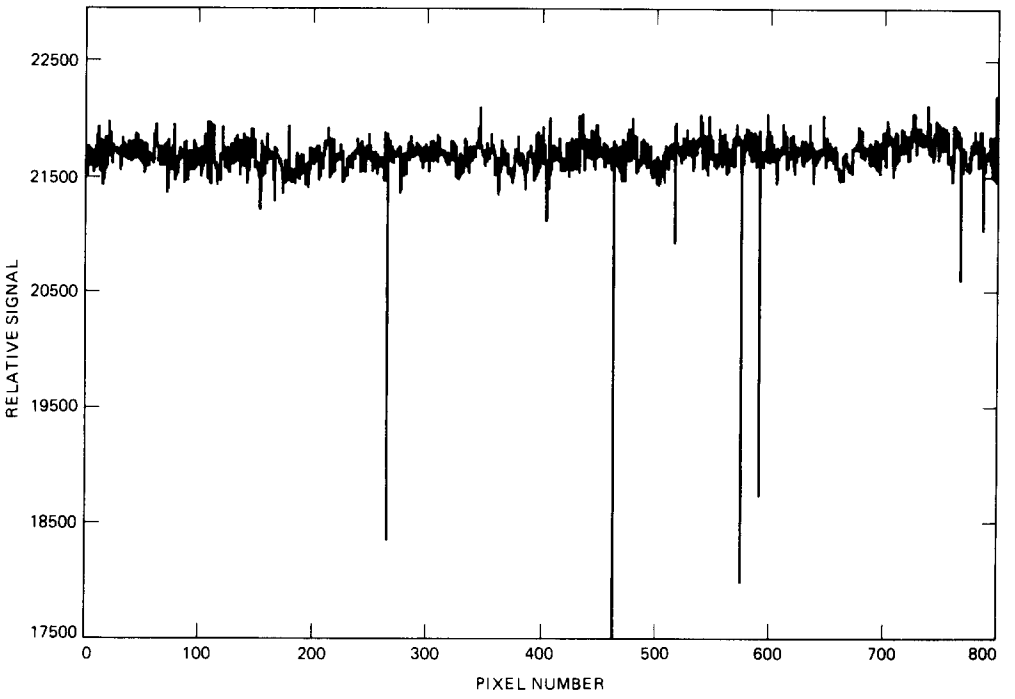

Figure 3-31. Line trace of signal in line 796 of image in Figure 3-30.

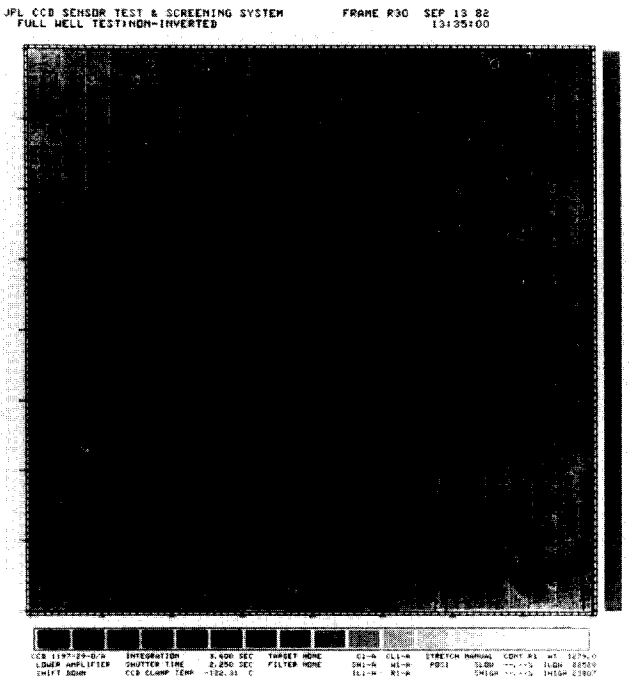

Figure 3-32. Flat-field image at higher exposure than Figure 3-30.

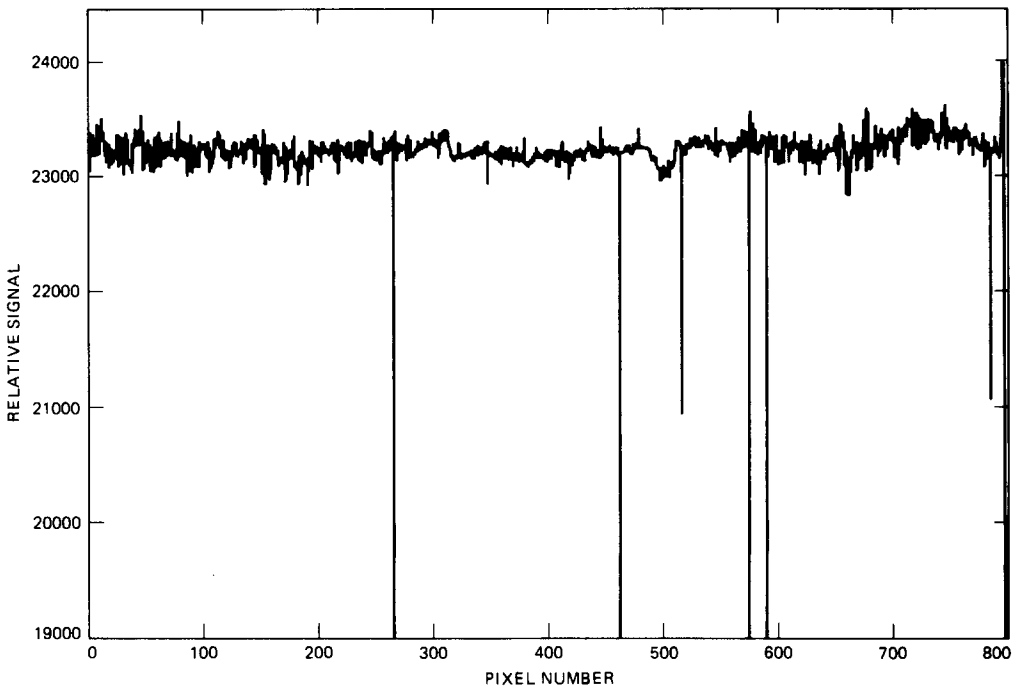

Figure 3-33. Line trace of signal from image in Figure 3-32.

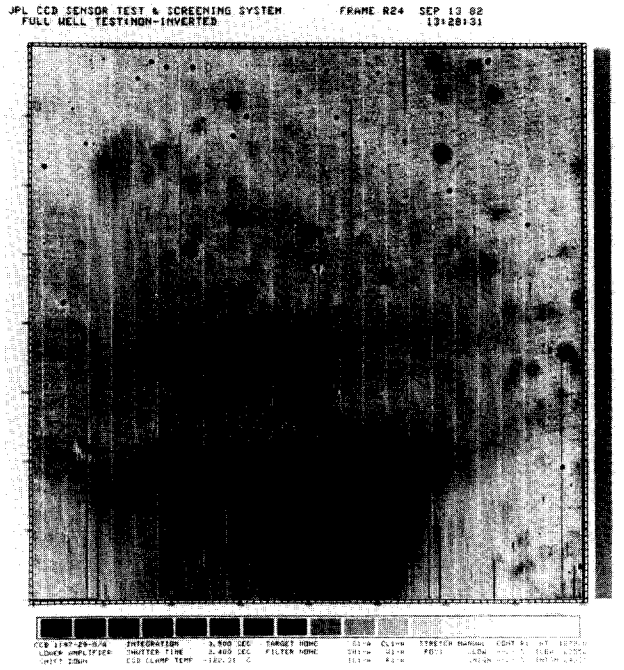

Figure 3-34. Flat-field image at still higher exposure.

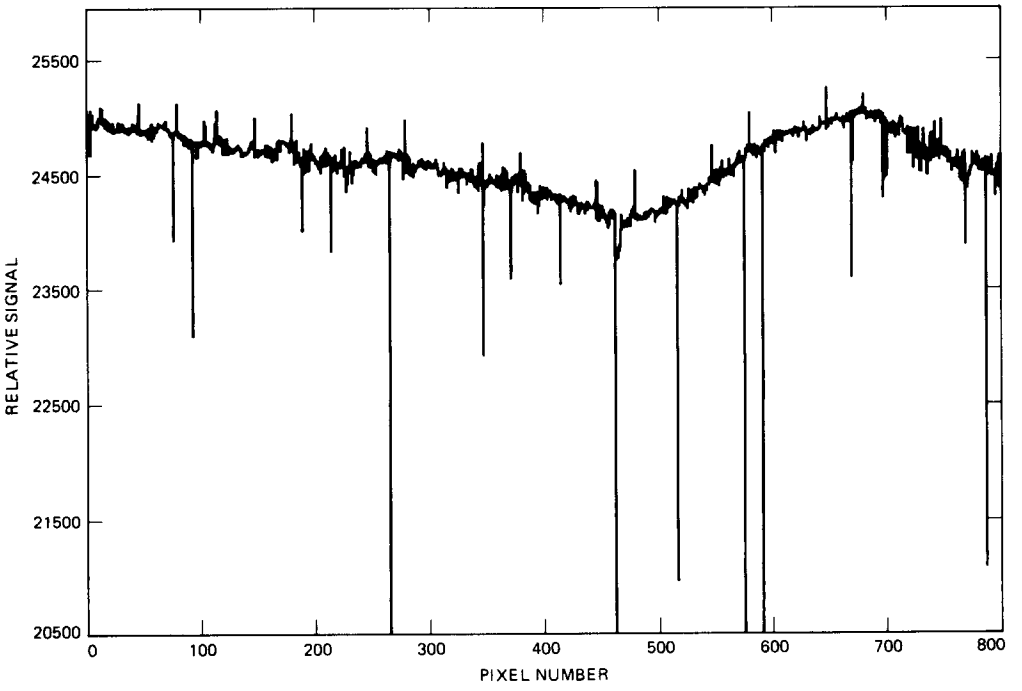

Figure 3-35. Line trace of signal from image in Figure 3-34.

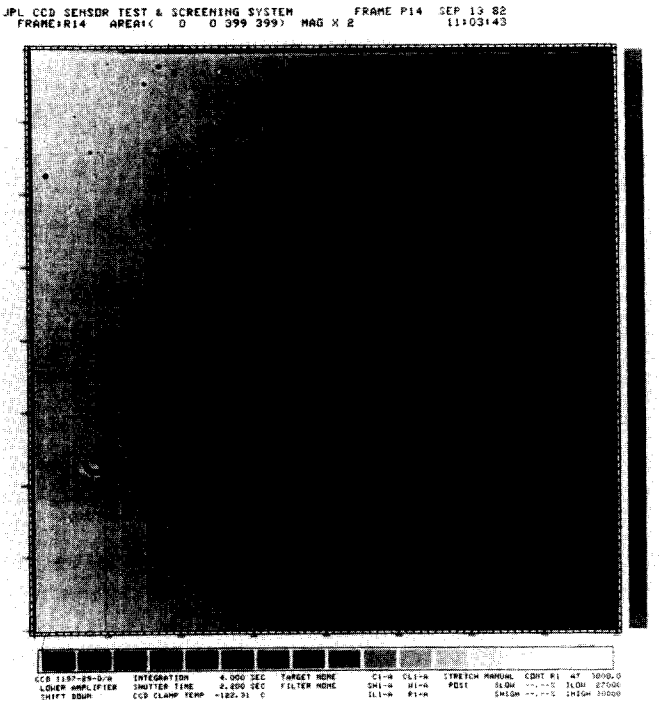

Figure 3-36. Flat-field image taken in 2 x 2 pixel summation mode.

The only difference between the inverted and non-inverted modes is in the value of the negative voltage of the clocks used to shift the charge along the parallel columns of pixels in the array. The non-inverted mode is the normal flight mode. It generates somewhat more thermal dark current but significantly less "spurious" charge than the inverted mode. In the blemish protection mode, the parallel clocks are held at their positive voltage level during image integration as opposed to holding them negative as is normally done. In this way, the potential levels in the active array are shifted lower relative to that of the transfer gate, which then forms an effective barrier to keep any over-full-well charge generated in the columns due to overexposure or the formation of a catastrophic blemish from spilling over into the serial register during integration.

The CCD blooming characteristics are the same in all three modes as long as the above-full-well charge does not reach the serial register of the device. As long as this is true, charge does not spread between columns since the channel stops fabricated into the device define the columns with sufficient potential barriers to prevent this. Above-full-well charge will spread only within a column. The data show that the spreading is restricted to the "down-column" direction as long as the charge is less than about five

times full well. The spreading occurs during the charge transfer process and is due to the above-full-well charge not being completely transferred out of a pixel site but rather being left behind and mixed with subsequent charge packets as they are transferred through this pixel site. This effect is illustrated in Figure 3-37, which shows an image at about the full-well level, and in Figure 3-38, at about five times full well, both in the normal non-inverted mode.

Above about five times full well, the potential wells along the columns are no longer able to control the charge packets during the clock transitions. Charge in excess of this level will spread instantaneously with the first clock transition both up and down the column until all pixels adjacent to the original charge location contain about five times their full-well level. After this, the charge lag described in the previous paragraph will take place during the remainder of the image readout. Figure 3-39 illustrates this behavior for an image exposed to about ten times full well. Notice that the charge in the half-circle has spread up the columns somewhat while a much longer tail trails below the nominal image location due to charge lag. If the tail extends to line 800, the remaining charge will be read out at the beginning of the next frame read out. For the SSI, this normally occurs during the image prepare cycle when multiple erasures of the CCD take place.

Once above-full-well charge blooms to the serial register, the behavior of the device becomes much more complicated and depends on the CCD clocking mode being used. Figures 3-40 and 3-41 show exposures to 50 times full well in the non-inverted and blemish protection modes. Notice that lateral charge spreading can occur in the serial register for the first lines read out at the top of the frame. The CCD baseline stabilization circuit, which automatically adjusts for changes in the CCD offset level by sensing the charge in the 25-pixel extended region of the serial register, can also be misled by charge blooming along the serial direction. This is apparent in the blemish protection mode. This mode was not intended to control blooming for overexposed images, but rather serves to control the effects of any blemish which might arise in the device which would produce high levels of charge continuously in a single column.

4. Residual Image

The calibration requirements of Reference 2-1 called for examining the possible residual image in an unexposed frame due to a previous frame exposed to as much as 50 times full well. This was done at the CCD component level. Improved understanding of the virtual-phase CCD subsequent to publication of Reference 2-1 indicates that a more sensitive test for residual image would be to examine pixels in a column below

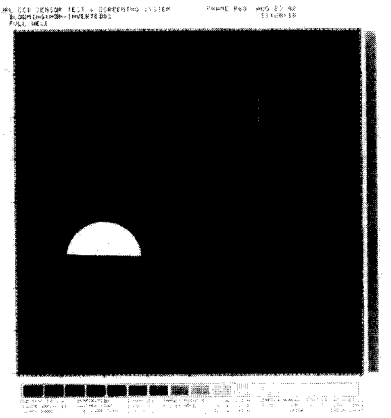

Figure 3-37. Image of the CCD blooming target exposed to approximately the full-well level.

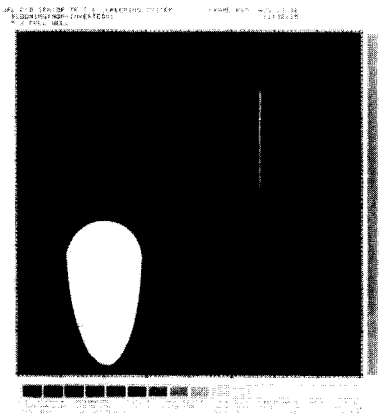

Figure 3-38. Image of the CCD blooming target exposed to about five times the full-well level.

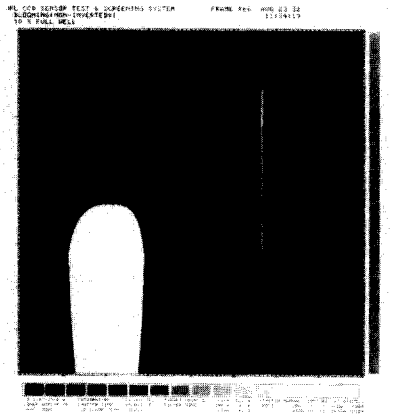

Figure 3-39. Image of the CCD blooming target exposed to about ten times the full-well level.

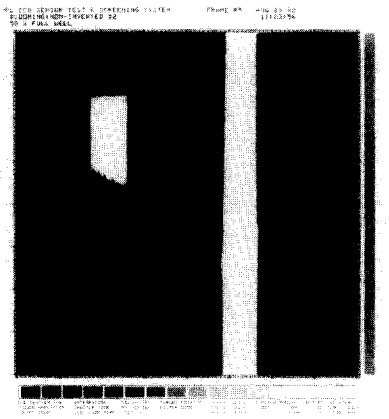

Figure 3-40. Image of the CCD blooming target exposed to 50 times the full-well level in the non-inverted mode.

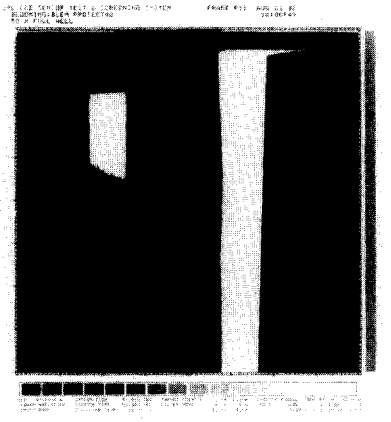

Figure 3-41. Image of the CCD blooming target exposed to 50 times the full-well level in the blemish-protection mode.

a (possibly bloomed) exposed area for a residual charge tail. Finally, during the initial calibration of the SSI subsystem in 1983, another form of residual image was discovered which only appeared in exposed frames. All types of residual image will be discussed here.

Images of the residual-image and slant-bar targets were acquired at exposures of 1/2, 1, 2, 5, 10 and 50 times full well. Zero-exposure frames were acquired immediately after each exposure, and the signal levels for the previously exposed areas were examined. In no case was any difference in dark-frame signal observed as a result of the preceding overexposure for any of the three CCD operating modes.

No data were acquired and processed specifically to search for a

residual charge tail within a frame containing an overexposed area. In fact, such a tail does not really fall into the category of residual image. However, the front side silicon dioxide/silicon interface charge trapping mechanism observed to produce residual image in other types of CCDs also appears to act in a less drastic way in the SSI virtual-phase CCD to produce a faint charge tail when the device is operated in the non-inverted or blemish-protection mode. Such tails were observed unintentionally in some of the blooming data that were contrast-enhanced in such a way as to make the tails visible. Figures 3-42 through 3-44 show an unenhanced image of the blooming target exposed to 50 times full well in the non-inverted mode along with two successive zero-exposure frames. The first (unenhanced) shows the charge left over from the exposed frame that had not yet been transferred out. The second is highly contrast-enhanced (~100 times) and shows a subtle lighter band of residual charge in the columns that were overexposed (112 - 290 and 562 - 569). Figures 3-46 and 3-47 show two zero-exposure frames (contrast-enhanced ~100 times) acquired immediately after a 50-times-over-full-well image acquired in the blemish-protection mode (Figure 3-45). Below the leftover charge being read out in the first dark frame (columns 470 - 560) appears a faint tail of residual charge. This tail is no longer visible in the following dark frame. No tail is visible in columns 160 - 255 below the saturated area even in the first dark frame. Since the SSI prepare cycle includes multiple high-speed erasures prior to acquiring each image (except in the on-chip summation mode), any residual charge tail should normally not extend beyond the initial overexposed frame.

The type of residual image detected during initial subsystem calibrations has been denoted "residual bulk image". It is evidenced only in frames acquired at wavelengths beyond about 700 nm. The mechanism by which this type of residual image is generated is as follows. Recall that the VP CCD is a front-side-illuminated device, and the silicon wafer is not thinned. From the front side, light with wavelengths longward of about 7000 Å will penetrate the CCD wafer to a depth beyond the shallow (~10 μm) high-resistivity epitaxial layer of silicon and into the low-resistivity substrate. Signal electrons are then created within the substrate. Some fraction of these signal electrons will diffuse into the epitaxial layer and will be collected in the potential wells of the pixels. However, at the boundary between the epitaxial region and the substrate, interface states exist which can trap some of the signal electrons generated in the substrate before they reach the potential well. These electrons are then lost as collected signal, thereby reducing the effective quantum efficiency of the detector. At the -110°C operating temperature of the SSI CCD, a trapping site that becomes filled can remain filled for an extended period of time, typically from a few seconds to several days or more, in some cases. To the extent that the trapping sites remain filled, the effective quantum efficiency for subsequent

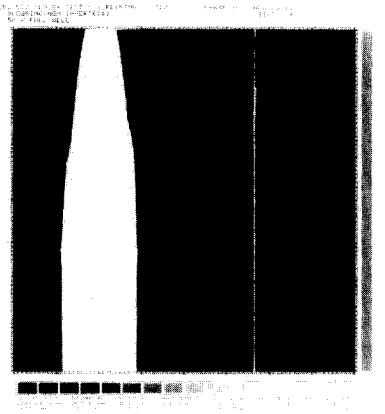

Figure 3-42. Unenhanced image of the CCD blooming target exposed to 50 times the full-well level in the non-inverted mode.

Figure 3-43. Unenhanced zero-exposure frame acquired following image in Figure 3-42.

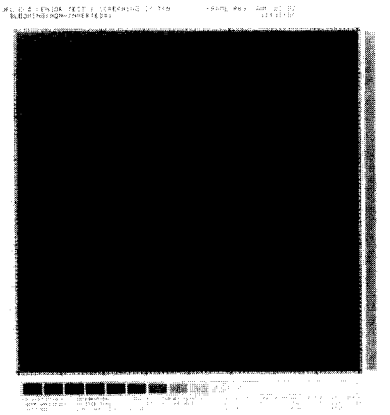

Figure 3-44. Highly contrast-enhanced (~100 times) zero-exposure frame acquired following image in Figure 3-43.

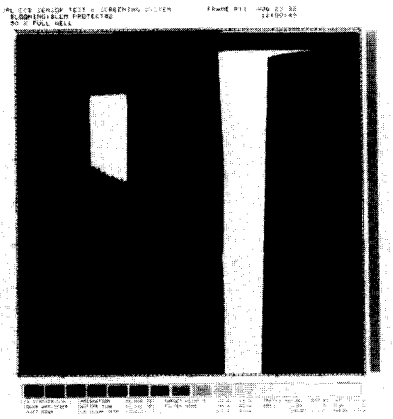

Figure 3-45. Image of the CCD blooming target exposed to 50 times the full-well level in the blemish-protection mode.

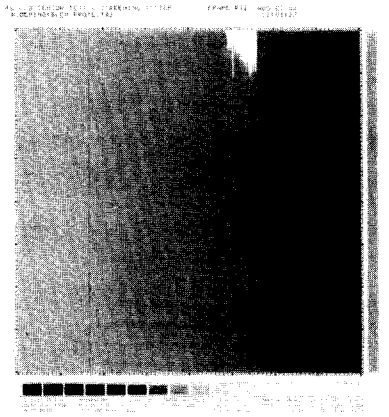

Figure 3-46. Highly contrast-enhanced (~100 times) zero-exposure frame acquired following image in Figure 3-45.

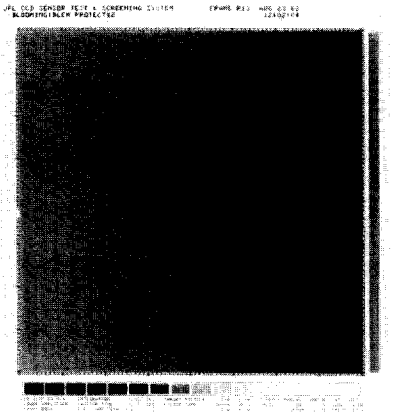

Figure 3-47. Highly contrast-enhanced (~100 times) zero-exposure frame acquired following image in Figure 3-46.

images will be increased, since less trapping of newly generated signal from the substrate will occur.

Near-IR images will tend to result in more traps being filled beneath those pixels where a scene is bright since more photons are generated in the bulk in these areas and more trapping sites are filled. Therefore, subsequent near-IR images will be formed on a detector with non-uniform QE, and a flat-field image will show up with a ghost image from the earlier near-IR frame. Figure 3-48 shows a flat-field image acquired at a wavelength of about 1 μm containing the residual image of a slant bar target acquired immediately before it, also at 1 μm. Although the contrast in the residual image in this case is quite low (~1 %), QE changes of up to 30% can occur at 1 μm due to residual bulk image.

In order to provide stable near-infrared quantum efficiency at the highest possible level and to eliminate residual bulk image, the SSI has incorporated the capability to saturate the CCD with near-infrared light (~9000 Å) from small LEDs prior to each exposure. This saturation is followed by multiple high-speed erasures of the CCD to remove all traces of its signal prior to exposure of the next image. This light-flood technique will normally be used in flight except in the SSI summation mode in which it is not possible due to the short prepare cycle in this mode.

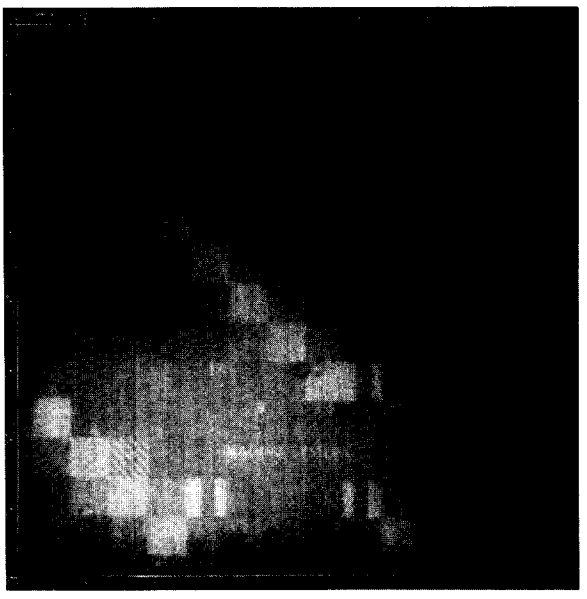

Figure 3-48. Flat-field image acquired at ~1-μm wavelength showing residual image of slant-bar target imaged immediately before at same wavelength.

5. Interference Fringes

Imaging of narrow-wavelength-band sources with the CCD detector can conceivably introduce a pattern of light and dark contours in the image due to interference occurring within the layers of the device that vary in thickness across the array. The interference fringing in the SSI virtual-phase CCD was characterized by taking flat-field images of six emission line sources at wavelengths ranging between 4330 Å and 9701 Å in both the normal full-resolution mode and the 2 x 2 pixel summation mode.

An example of the result is shown in Figure 3-49 for 6699 Å light in the full-resolution mode (contrast enhanced ~13 times). At other wavelengths, the fringing pattern is the same, but the fringe spacing varies proportionately with wavelength. No differences are seen in the summation mode.

The number of fringes seen across the array indicates a variation in spacing between the reflecting surfaces of the interference layer of somewhere between 2 and 9 μm depending on the index of refraction of the layer material. This amount of non-parallelism is too large for any of the potential layers in the CCD device itself (the thickest layer is the polysilicon gate structure, and it is only ~0.5 μm thick). In addition, the position of the light source was found to greatly affect the contrast level of the fringes. Moving the source closer to the CCD reduced contrast. Figure 3-50 shows the fringing at 6699 Å (contrast enhanced ~40 times) with the source moved in from about 5 ft. away (as for Figure 3-49) to about 11 inches away. This contrast reduction also indicates that the interference is occurring in a thick layer. The most likely candidate is the space between the CCD surface and the window of its package.

When the light source was moved in to a distance of only 7 inches from the CCD, no interference fringes were observed at all (see Figure 3-51, contrast enhanced ~40 times). Therefore, the CCD layers are shown to be regular in thickness across the array to better than one fringe.

Since the CCD-to-window fringing is seen to be a function of source distance, the actual fringing possible in the SSI depends on the optics f/#, i.e., the angular size of the incoming light cone. Figure 3-49 was obtained at a source distance which matched the SSI f/8.5 light cone. The contrast level of the fringes in this case is about 1%.

The SSI spectral filters' bandpasses are all far too broad to cause interference fringing when imaging a broad-band source. The only way any fringing could be observed would be with sources containing narrow emission or absorption bands (< 3 Å wide).

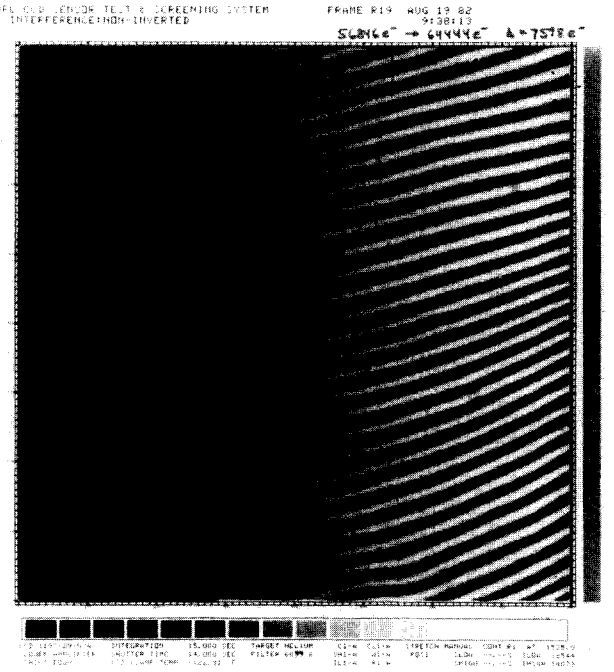

Figure 3-49. Contrast-enhanced (~13 times) flat-field image of 6699 Å emission line source 5 ft. away in full-resolution mode.

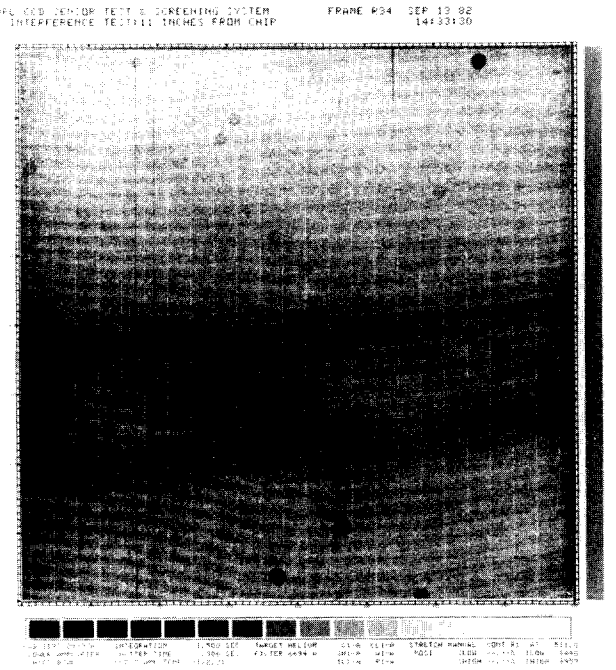

Figure 3-50. Contrast-enhanced (~40 times) flat-field image of 6699 Å emission line source 11 in. away in full-resolution mode.

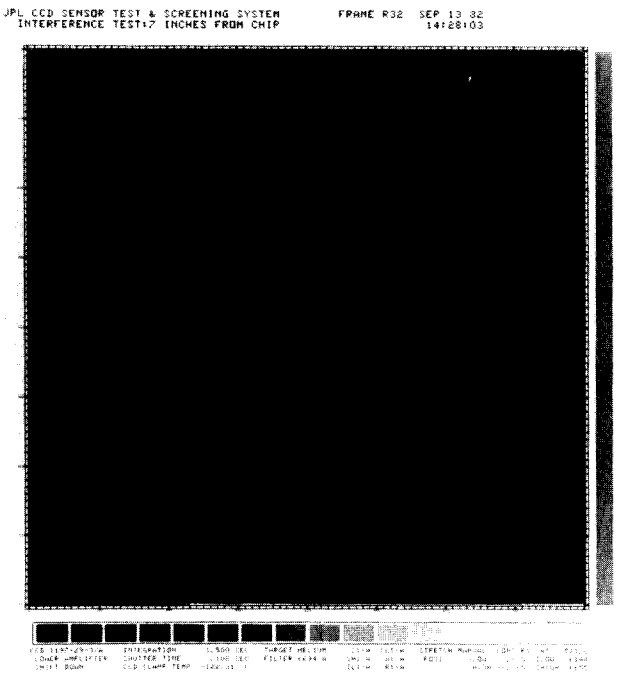

Figure 3-51. Contrast-enhanced (~40 times) flat-field image of 6699 Å emission line source 7 in. away in full-resolution mode.

REFERENCES

3-1. MJS77-ISS Flight Equipment, Detail Specification For Narrow-Angle Optical System, JPL Specification No. ES510993, 19 November 1975.

3-2. ISS-MJS77 Flight Equipment, Design Requirements For Narrow-Angle Optical Subsystem, JPL MJS77-2036-1, 14 August 1974.

3-3. C. Lebel, Solid State Imaging (SSI) Instrument Calibration Procedure Document, Component Level Calibrations, JPL Document 625-602, Rev. B, 11 June 1982.

3-4. J. C. Kemp and C. L. Wyatt, "Terrestrial Measurements of the Performance of High Rejection Optical Baffling Systems", Optical Engineering, Vol. 16, pp. 412-416, July-August, 1977.

3-5. James R. Janesick, J. Hynecek, and M. Blouke, A Virtual-Phase Imager for Galileo, SPIE Vol. 290 -- Solid-State Imagers for Astronomy, Cambridge, Massachusetts, June, 1981.

3-6. K. Klaasen, M. Clary, and J. Janesick, Charge-Coupled Device Camera for the Galileo Jupiter Orbiter Spacecraft, SPIE Vol. 493 -- The National Symposium and Workshop on Optical Platforms, Huntsville, Alabama, June, 1984.

SECTION IV

SUBSYSTEM CALIBRATIONS

The SSI subsystem has a variety of commandable operating modes. Selection of a given mode can affect some of the calibration parameters that apply to the SSI data. The commandable mode options are as follows:

1. Frame rate -- there are four available frame times; 2 1/3 sec, 8 2/3 sec, 30 1/3 sec and 60 2/3 sec. The 2 1/3-sec mode involves summing 2 x 2 blocks of pixels on the CCD and is primarily intended to be used only to enhance image signal-to-noise ratios in the intense radiation environment close in to Jupiter. No CCD erasure occurs during the image prepare cycle in this mode.

2. Gain state -- there are four available gain states, which spread the available 8 bits of encoding over different fractions of the CCD full-well capacity. The lowest gain state is intended for use only in the 2 x 2 pixel summation mode. Gain is controlled by two switches having ratios of approximately 4.8:1 and 10:1. The four possible combinations of states for these gain switches define the four available gain states.

3. Exposure mode -- there are two exposure modes. In the normal mode, exposure times between 4 1/6 msec and 800 msec can be commanded (except in the 2 1/3-sec summation mode where the maximum is 400 msec). In the extended exposure mode, two frame times are required to obtain one image; the first frame time has its readout inhibited so as to allow the shutter to be kept open longer while the second frame time has its prepare cycle inhibited followed by image readout at the normal time. The maximum extended exposure duration depends on frame rate as follows: 2 1/3-sec rate -- 1.6 sec; 8 2/3-sec rate -- 6.4 sec; 30 1/3-sec rate -- 25.6 sec; and 60 2/3-sec rate -- 51.2 sec.

4. Data compression -- the SSI includes an optional data compressor which encodes the differences in signal level between adjacent pixels in a line rather than the absolute signal level itself for each pixel and thereby reduces the average number of data bits per pixel from the standard 8 to 3.24. The compression can be done in either of two ways. In the information-preserving mode, the signal level differences are encoded exactly beginning at pixel 1 of each line and proceeding to the right along the line. If the differences are great enough, the total bit allocation of 2592 bits/line may be used up prior to reaching the end of the line. In that case, the data from the remainder of the

line is discarded. In the non-information-preserving (or rate-controlled) mode, if exact encoding of the signal differences would exceed 2592 bits for a given line, the least-significant bit in the most active 64-pixel block in the line is truncated. This truncation is repeated again and again until the 2592-bit allocation is met or until every block has had 3 least-significant bits truncated. If truncation of 3 bits is still not sufficient to meet the allocation, pixels are dropped from the right-hand end of the line until the allocation is met. Data compression is not available in the 2 1/3-sec summation mode, and the 30 1/3-sec mode is always compressed.

5. Light flood -- flooding of the CCD with near-IR light followed by high-speed erasure of the resulting saturated signal during each prepare cycle is available in all but the 2 1/3-sec summation mode. This light flood maximizes and stabilizes the near-IR quantum efficiency of the detector and thereby eliminates any residual image (see Section III-D-4).

6. Parallel clock state -- the CCD negative parallel-clock voltage can be selected to result in the clocked well being either inverted or non-inverted (see Reference 3-5). The non-inverted mode is the expected flight mode since, although the thermal dark current is slightly higher than in the inverted mode, the CCD "spurious" charge level is lower.

7. Blemish protection -- the polarity of the CCD parallel clock voltage used during image integration can be selected. The expected flight mode is to have blemish protection off (i.e., parallel clock voltage negative during integration). The blemish-protection mode might prove useful should a blemish develop in the detector array that continuously generates large amounts of charge. This mode will tend to keep such charge from spilling over into the serial register during the interval between line shifts thereby ruining data from many other columns in the array and causing a shift in the offset control level.

The SSI signal chain includes a baseline stabilization circuit. This circuit samples the signal level in the first 25 unexposed pixels of the 825-pixel serial register and automatically forces this signal level to a preset, near-zero level. This technique stabilizes the zero-exposure offset level in the presence of any variations in the background dark charge level or clock pulse feed-through distortions.

Calibrations of the SSI subsystem were conducted in June, 1983; April, 1984; and May, 1985. The 1983 data revealed several problems in the instrument which were subsequently corrected: residual bulk image was

corrected by implementing CCD light flood, the baseline stabilization circuit timing was modified to make it active during the prepare cycle of the summation mode as well as the other modes, a spectral filter centered at 7450 Å that had poor optical quality was replaced by one centered at 7560 Å, changes were made to the analog-to-digital converter (ADC) clock frequency and grounding to improve the encoding accuracy by reducing unevenness in the widths of the DN bins, and a software patch was implemented to correct the failure to output line 800. Although these problems were corrected for the 1984 calibration, one new problem arose with the data compressor. A bad solder joint on one memory chip resulted in the compressed data being incorrect for the last 32-pixel sub-block of each even-numbered image line. This problem was corrected prior to the 1985 calibration. Subsystem-level data presented in this report will be restricted to that acquired in 1985 with some discussion of any time-variable performance as appropriate.

A. RADIOMETRIC CALIBRATIONS

1. Background

The response of CCD detectors has been shown to be very linear with exposure. Assuming a linear detector, the SSI response at any pixel ij can be modeled by the equation

$$DN_{ij} = \frac{t\,\Omega\,a_{ij}}{g\,C} \int S\,T\,F\,I\,P\,d\lambda + DN_{0ij} \qquad (1)$$

where

DN_{ij} = the output data number of pixel ij
g = gain state ratio factor
t = exposure time (sec)
C = constant high-gain conversion factor (e-/pixel/DN)
Ω = solid angle of optics (sr)
a_{ij} = area of CCD pixel ij (cm^2/pixel)
S = average CCD spectral sensitivity (e-/photon)
T = spectral transmission of the optics
F = spectral transmission of the filter
I = spectral radiance of the scene (watts/cm^2/sr/nm)
P = λ(nm)/1.9862 x 10^{-16} (photons/watt-sec)
λ = wavelength (nm)
DN_{0ij} = zero-exposure output data number for pixel ij

Making radiometric measurements with the SSI requires inverting this equation to solve for scene radiance, I. Without knowing the spectral shape of the radiance curve a priori, we assume that the radiance is constant over a given filter bandpass and solve for

$$I_f = \frac{(DN - DN_0)\, g\, C}{t\, \Omega\, a \int S\, T\, F\, P\, d\lambda}$$

Alternatively, for solar-illuminated scenes such as the SSI will normally image, we can solve for the reflectance of the scene assuming it is constant over the filter bandpass. Reflectance, R, is related to radiance by

$$I(\lambda) = \frac{H(\lambda)\, R(\lambda)}{\pi} \qquad \text{or} \qquad R(\lambda) = \frac{\pi\, I(\lambda)}{H(\lambda)}$$

where $H(\lambda)$ = the solar irradiance incident on the reflecting surface at wavelength λ. Thus,

$$R_f = \frac{(DN - DN_0)\, \pi\, g\, C}{t\, \Omega\, a \int S\, T\, F\, H\, P\, d\lambda}$$

The unknowns in the above equations are DN_0, g, t, C, a_{ij}, $S(\lambda)$, Ω, $T(\lambda)$ and $F(\lambda)$. In this section, we will address the determination of the first five of these parameters as well as the integrals over wavelength. The individual spectral curves were determined at the component level (Section III-A, B and D). In this section, we will only discuss small adjustments to the component-level curves required to make the SSI spectral response model match the radiometric calibration data more closely. We will also discuss the uncertainties in the determination of these parameters along with some noise or error sources.

2. Reciprocity and Hysteresis

The reciprocity of the SSI camera represents a measure of its radiometric consistency; i.e., a fully reciprocal system produces a constant video-signal output when the exposure, which is a function of the changing scene brightness and shutter time, remains constant. An ideal camera should also be free of hysteresis; i.e., its response should not depend at all on its past exposure history. Three data sets were acquired to check these characteristics for the SSI. A reciprocity test was conducted by taking a series of images with reciprocal changes in the light source intensity and the commanded shutter time. Three frames were acquired at each of 10 exposure times going from shortest to longest and then back down to the shortest again. Two additional hysteresis tests were conducted. In one, the light cannon brightness was held constant and images were acquired at nine exposure levels, first progressively increasing the exposure and then progressively decreasing it again. In the second, the exposure time was held constant, and the light cannon level was varied. Four brightness levels

were used, first increasing then followed by decreasing brightness. Three images were also acquired at each exposure level for the hysteresis tests. All tests used the clear filter and were conducted at three instrument temperatures (-10°, +8° and +18° C, referenced to the rear optics).

Historically, the major cause of lack of reciprocity in our imaging systems has been shutter offset, i.e., the actual exposure time is less than the commanded time by a fixed amount. For such a case, the output DN level, DN, would be given by

$$DN - DC = L\,(t_C - t_{OS})\,A$$

where

DC = DN of a zero-exposure frame
L = light source brightness (ftL)
t_C = commanded exposure time (msec)
t_{OS} = shutter offset (msec)
A = camera sensitivity (DN/ftL/msec)

The effect of a shutter-time offset would be strongest for the shortest shutter times, gradually becoming insignificant for longer shutter times. Therefore, only commanded shutter times from 4 1/6 msec to 100 msec were used in the reciprocity test while the light cannon brightness was varied between 62.2 ftL and 2.87 ftL. Because of uncertainties in the light cannon calibration curve at the time of the test, the actual brightnesses used were not exactly reciprocals of the commanded shutter times, the variation being about ±7%. Since the actual shutter times differ from those commanded, however, the lack of true reciprocity between the light cannon brightness and the commanded shutter times does not compromise the test results as long as the SSI response is linear.

The unknowns in the above equation are t_{OS} and A. L is assumed known to within small, randomly distributed errors. The solution for t_{OS} and A is overdetermined. Therefore, a least-squares fit to all the data is the appropriate method of solution, with weighting applied by assigning an assumed constant error in the measured DN value. Solutions were obtained for 256 25 x 25 pixel areas spread evenly across the CCD array. DC was subtracted on a pixel-by-pixel basis from each frame, and the multiple frames at each exposure level were averaged to reduce random noise. The final light cannon calibration curve was used to derive the actual brightness levels used.

Inspection of the best-fit t_{OS} values across the array showed a smooth ramp increase from the top to the bottom. To characterize this top-to-bottom variation, a plot of all t_{OS} values as well as the average for t_{OS} along lines across the images (for the selected areas) was generated versus image

line number. These plots are shown in Figures 4-1 through 4-3 for the three different instrument temperatures. These plots show an almost exponential increase in t_{os} with line number from the top to the bottom of the images, consistent with the movement of the shutter blades vertically from top to bottom of the image. The scatter in the values of t_{os} at a given line number is an indication of the accuracy of the t_{os} determination, which is estimated to be better than ±0.01 msec. The slight "hook" in the t_{os} vs. line number plot at low line numbers for -10° C data may be showing the effects of frictional forces at low temperature. The sensitivity, A, does not show any particular spatial distribution.

The variation in shutter offset with line number is in the opposite sense from the shutter offset variations measured at the component level (see Section III-C). In addition, the absolute value of the offset is somewhat larger (1.327 msec at +8° C for subsystem data vs. 0.644 msec at +6° C for component data at the center of the frame).

To determine whether a shutter offset correction alone will yield a reciprocal system, the quantity $(DN - DC)/L(t_c - t_{os})$ must be examined. For a fully reciprocal system, this quantity will be a constant for all values of L and t_c. Figure 4-4 plots this quantity versus t_c along with the uncorrected quantity, $(DN - DC)/Lt_c$ for the +8° C case averaged over the various areas in the array. Note that the shutter offset correction results in almost perfect reciprocity (to within ±1%, which is as good as the relative light cannon brightness is known). This result also confirms that the SSI response is indeed linear.

Proper radiometric calibration of the SSI requires a line-dependent shutter offset correction. This has been incorporated in the MIPL radiometric calibration programs GALSOS and GALGEN. Determination of the shutter offset characteristics in flight will be an important post-launch objective.

The hysteresis tests showed no measurable hysteresis in the SSI. These tests were conducted with the SSI light flood turned on so as to eliminate the effects of any residual bulk image. Only the data from the 1984 calibration at +10° C have been analyzed. For the test with a fixed light cannon setting, differences in the mean DN - DC levels in a 50 x 50 pixel area for identical exposures on the ascending and descending legs were never greater than 0.06 DN in gain state 3 (~200 e-/DN). For the test with a fixed exposure time, differences were also less than 0.06 DN (0.07%) in this gain state for all light cannon settings except the lowest (~0.8 ftL), for which the difference was 0.5 DN (~3%, which is consistent with the repeatability of setting the light cannon brightness for this low level).

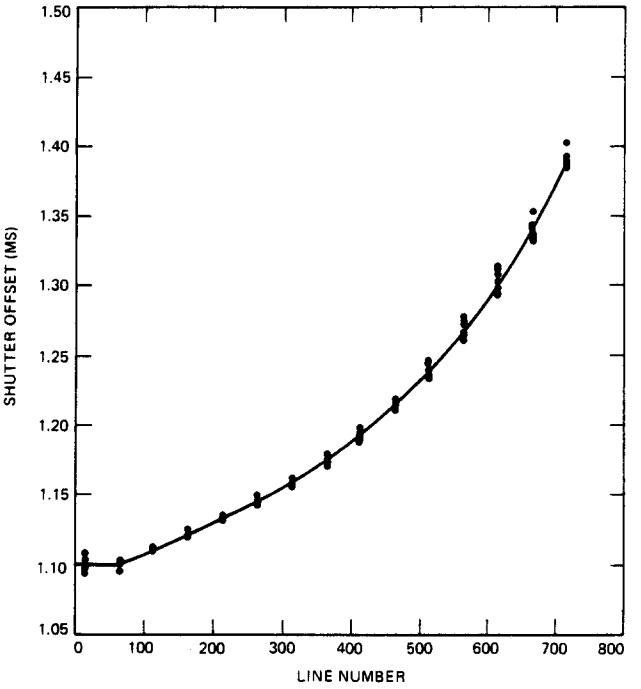

Figure 4-1. Shutter offset t_{os} vs. image line number at instrument temperature of -10° C.

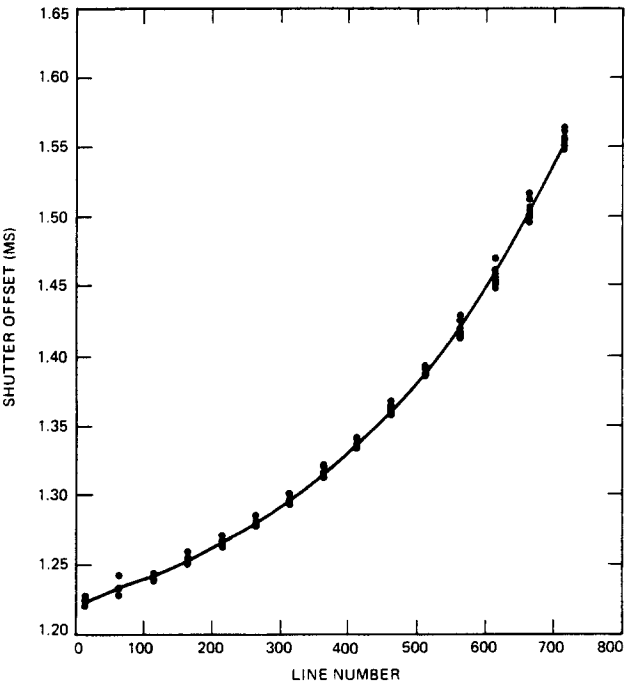

Figure 4-2. Shutter offset t_{os} vs. image line number at instrument temperature of +8° C.

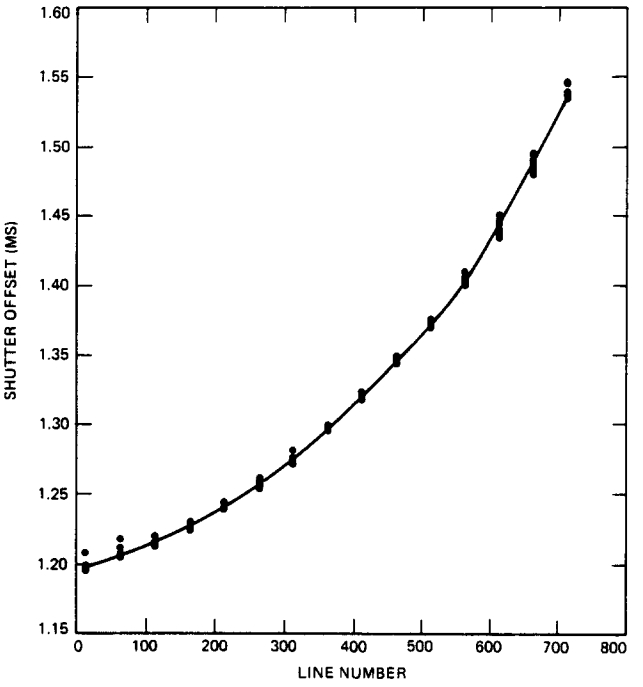

Figure 4-3. Shutter offset t_{os} vs. image line number at instrument temperature of +18° C.

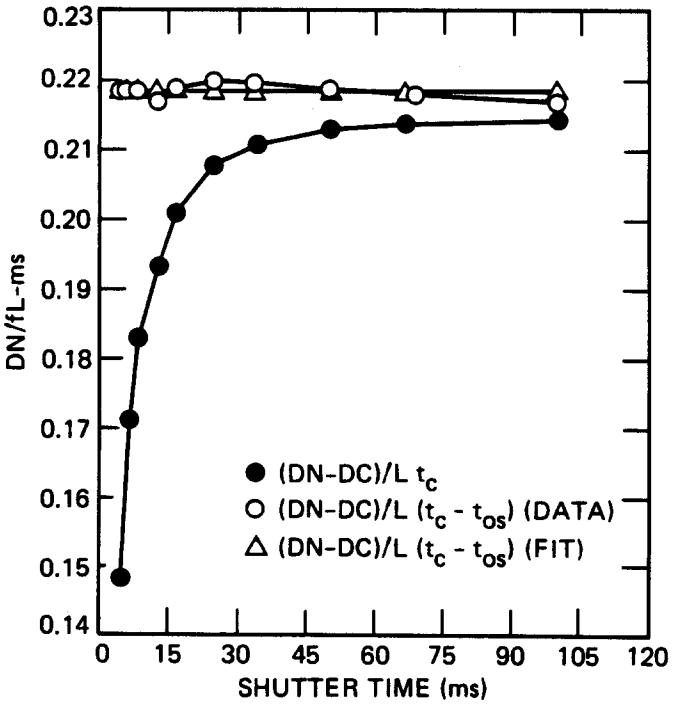

Figure 4-4. The quantities (DN - DC)/Lt_c and (DN - DC)/L(t_c - t_{os}) vs. shutter time (see text for definitions of symbols).

3. Flat-Field Light Transfer

a. Purpose

The purpose of the flat-field light transfer calibration is to determine the absolute response of each SSI picture element as a function of exposure to a known calibration source. Determination of this response characteristic is required for all combinations of variables that might affect it -- spectral filter, gain state, exposure level, 2 x 2 pixel summation mode, instrument temperature, data compression, CCD parallel clock voltage level, and use of the blemish protection mode. In addition, those pixels whose response cannot be reliably calibrated must be identified.

b. Method

The response characteristics of each SSI pixel in a given camera configuration can be examined by taking a set of flat-field images starting with zero exposure and increasing the exposure until the full-scale signal level is reached. A total of 10 exposure levels were used for each configuration tested. The calibrated light cannon was used for the flat-field source, and its brightness level was kept constant for each 10-level light-transfer data set acquired. Multiple images (typically 3 or more) were obtained at each exposure level and were later averaged to reduce random noise effects.

Light transfer data sets were acquired for each flight filter in each gain state, the lowest gain state being used in conjunction with the 2 x 2 pixel summation mode, at three instrument temperatures, -10^{o} C, $+8^{o}$ C and $+18^{o}$ C. In addition, summation-mode data sets were acquired through the green filter in the three higher gain states. Finally, three clear-filter sets were obtained in gain state 2 (~440 e-/DN) for (a) inverted CCD parallel clocks, (b) data compressor on, and (c) blemish protection mode.

Figures 4-5 through 4-12 show examples of contrast-enhanced flat-field images acquired as part of the light transfer data sets. Various filters and use of the summation mode are shown. The dark circular "donuts" are shadows of small dust specks located on various optical surfaces near the CCD. The smallest donuts are from specks on the inside of the CCD package window, intermediate-size donuts are from dust specks on the outside of this window, and the largest donuts are from specks on the inside of the quartz radiation plug. The dust specks are smaller than about 60 μm in diameter, and some changes in their locations have been observed between the component CCD testing and the 1983, 1984 and 1985 SSI subsystem calibrations. The darkening in the corners of the images is due to vignetting by the filter aperture. The light vertical columns spaced every 33 pixels are

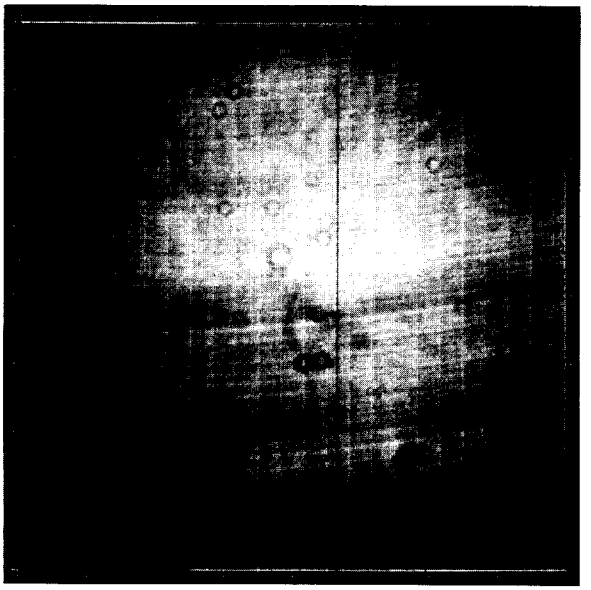

Figure 4-5
Contrast-enhanced flat-field image acquired for light transfer data using the <4450 Å filter, 60 2/3-sec frame rate and gain state 2.

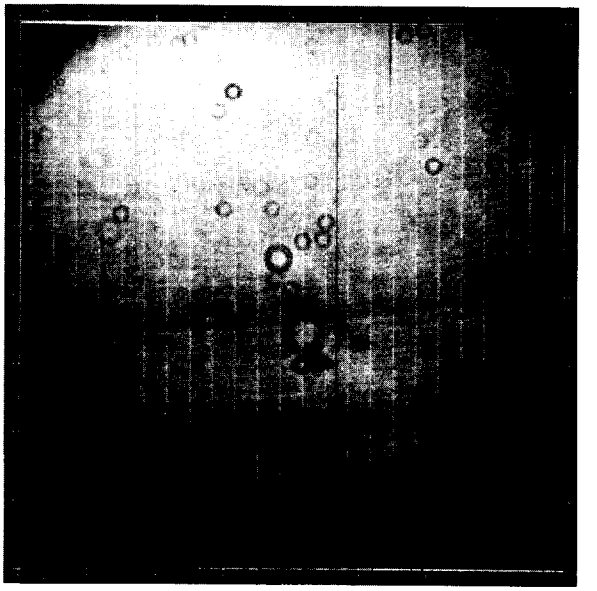

Figure 4-6.
Contrast-enhanced flat-field image acquired for light transfer data using the 6600 Å filter, 8 2/3-sec frame rate and gain state 2.

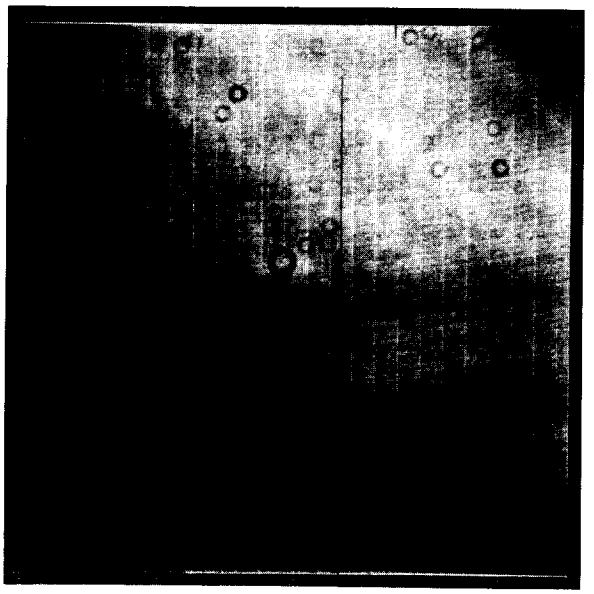

Figure 4-7.
Contrast-enhanced flat-field image acquired for light transfer data using the 7560 Å filter, 8 2/3-sec frame rate and gain state 2.

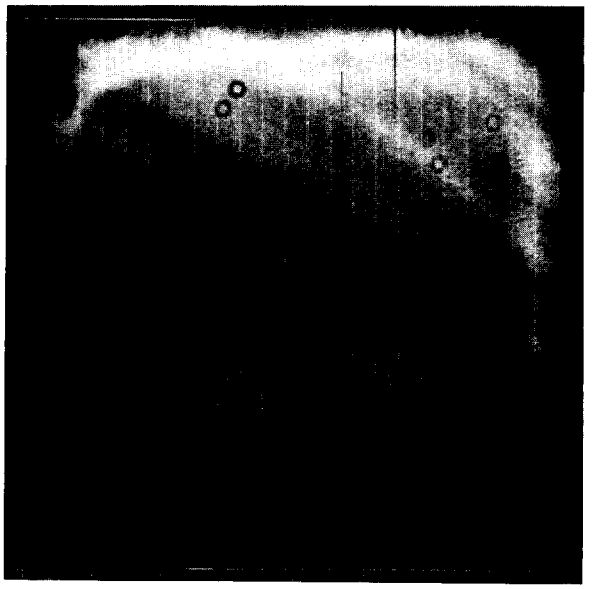

Figure 4-8.
Contrast-enhanced flat-field image acquired for light transfer data using the >9680 Å filter, 8 2/3-sec frame rate and gain state 2.

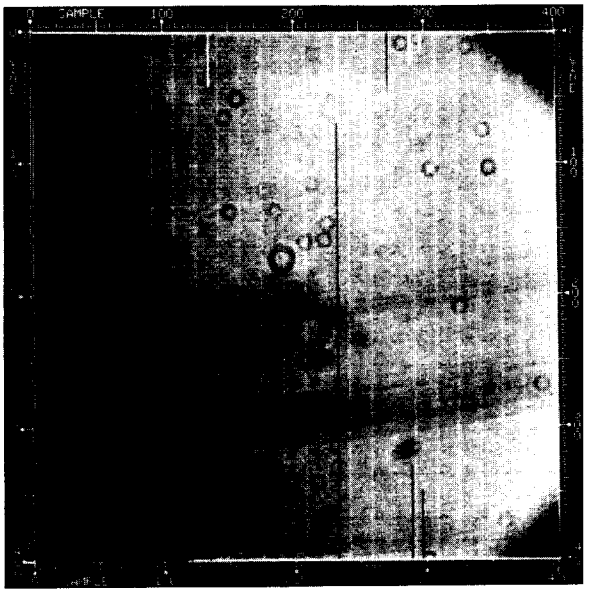

Figure 4-9
Contrast-enhanced flat-field image acquired for light transfer data using the 5600 Å filter, summation mode, 2 1/3-sec frame rate and gain state 1.

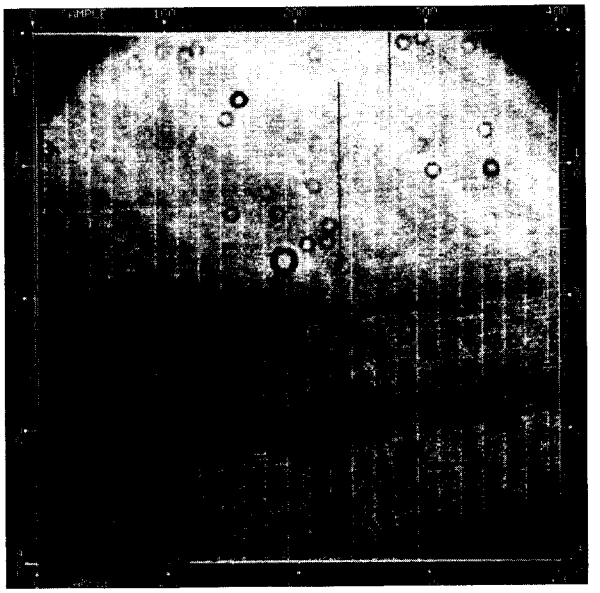

Figure 4-10.
Contrast-enhanced flat-field image acquired for light transfer data using the clear filter, summation mode, 2 1/3-sec frame rate and gain state 1.

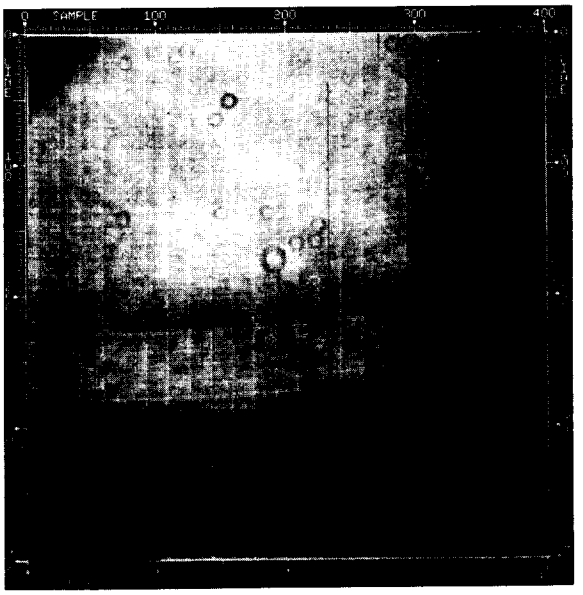

Figure 4-11
Contrast-enhanced flat-field image acquired for light transfer data using the 7270 Å filter, summation mode, 2 1/3-sec frame rate and gain state 1.

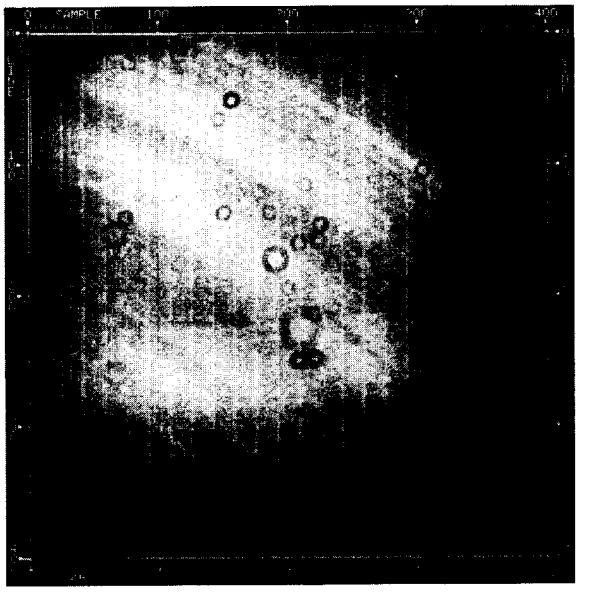

Figure 4-12.
Contrast-enhanced flat-field image acquired for light transfer data using the 8890 Å filter, summation mode, 2 1/3-sec frame rate and gain state 1.

due to increased pixel area in these columns resulting from the step-and-repeat photolithographic techniques used in fabricating the CCD.

c. Gain State Factors

The high-gain state conversion factor, C, from signal electrons/pixel to DN can be determined by the photon transfer curve technique (see Section III-D-2). This method is applicable for systems whose noise levels are governed by photon statistics (i.e., shot-noise limited). The SSI meets this requirement at high signal levels in its highest gain state (gain state 4). Figure 4-13 plots random noise in DN versus mean signal level in DN over a typical area of the SSI CCD using the highest gain state. The random noise level, n, in units of electrons is related to signal, s, in electrons by the equation

$$n = \sqrt{n_o^2 + s}$$

where the s term represents the square of the signal shot noise (equal to $\sqrt{s}$) and n_o is the inherent system readout noise floor. Writing this equation in units of DN using the constant C we have

$$N = \sqrt{N_0^2 + S/C}$$

where N, N_0 and S are the noise and signal terms in units of DN. Solving for C gives

$$C = \frac{S}{N^2 - N_0^2}$$

The result of this calculation for the SSI is C = 43.8 e-/DN in the highest gain state. The uncertainty in this value is estimated to be ±10%. Although this uncertainty is quite large, it should be kept in mind that the determination of the absolute SSI sensitivity does not depend on accurate knowledge of C by itself. The SSI sensitivity is determined directly in units of DN/unit brightness, and knowledge of the absolute values of the intermediate parameters such as C or S is not terribly important as long as the calibration of the overall subsystem radiometric sensitivity is accurate. An SSI spectral response model that produces a best fit to the entire calibration data set yields a value of C = 42.3 ± 2.7 e-/DN in the highest gain state.

The gain state ratio factors, g, have been measured in several different ways. The most straightforward measurement involves simply ratioing the mean DN - DN_0 for the same pixel area of two frames for which only the gain state has been varied. The number of such frame pairs available ranged between 2 and 27 for the various gain ratios at each temperature. No

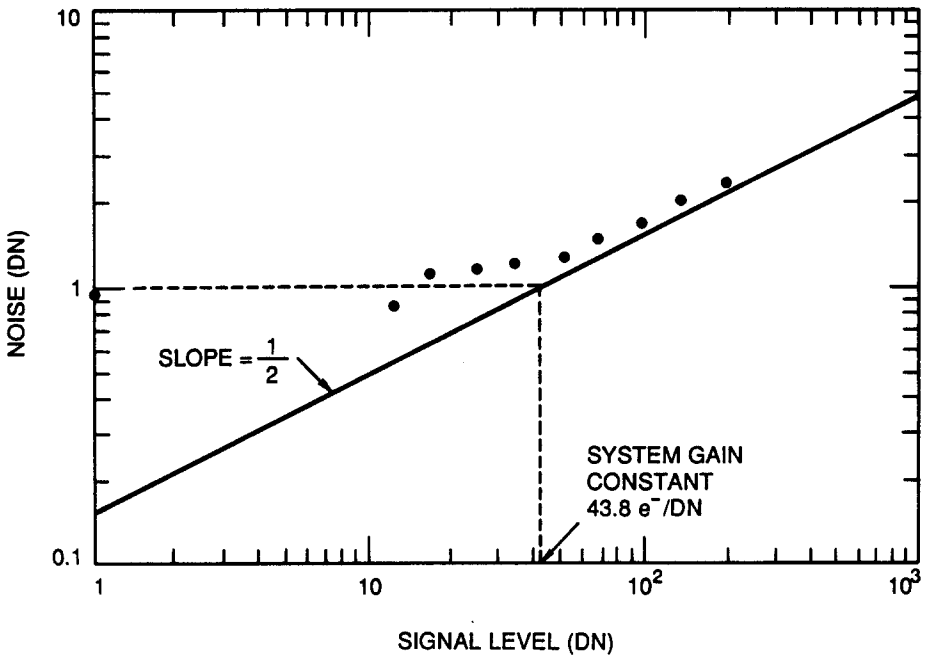

Figure 4-13. Random noise in DN versus mean signal level in DN over a typical area of the SSI CCD using the highest gain state.

differences in gain ratio with temperature were apparent within the measurement accuracy (typically better than 1% standard deviation, 3% worst case). Combining the data for all temperatures yielded the gain ratios listed in Column A of Table 4-1. The summation mode gain ratio includes not only a factor of 4 due to summation of the charge from 2 x 2 blocks of pixels but also a factor of 1.313 due to use of slightly different timing in the signal sampling circuit in this mode.

A second approach to determining the gain ratios involved performing least-squares linear fits to the mean DN level versus exposure (ftL-ms) for 256 20 x 20 pixel areas for light transfer data sets acquired at the same temperature and filter position but using different gain states and ratioing the slopes of the light transfer functions. This was done only for the red filter data. The major error source in this approach is the accuracy of the light cannon brightness calibration since typically different light cannon settings are used for the different gain states. Assuming a 1% uncertainty in light cannon brightness, again no temperature dependence for the gain ratios is found. Combining the results for all temperatures, the ratios are given in Column B of Table 4-1. These values are consistent with those determined by the first method although the uncertainties are greater.

Table 4-1. Gain State Ratio Factors

gain state	A	B	C
1	47.184 ± 0.274	46.379 ± 0.540	47.139
2	9.824 ± 0.037	9.721 ± 0.096	9.835
3	4.803 ± 0.021	4.771 ± 0.030	4.793 ± 0.018
4	1	1	1
2 x 2 summation	0.1904 ± 0.0023	0.1871 ± 0.0046	0.1896 ±0.0025
gain state	D	E	F
1	47.639 ± 0.805	47.075 ± 0.184	47.091 ± 0.123
2	9.900 ± 0.138	9.797 ± 0.027	9.809 ± 0.019
3	4.812 ± 0.046	4.805 ± 0.013	4.799 ± 0.0088
4	1	1	1
2 x 2 summation	0.1871 ± 0.0039	0.1887 ± 0.00077	0.1888 ± 0.00068

A third approach involved ratioing the mean values of the best-fit light transfer function slopes determined on a pixel-by-pixel basis (see subsection g below) for data sets with the same filter and a temperature of $+8^{o}$ C. For pairs which also used the same light cannon setting, the ratios are as listed in Table 4-1, Column C. The uncertainties listed are the standard deviations of the values obtained when more than one ratio was available for a given gain state pair. When pairs with different light cannon settings are included, the ratios and uncertainties are as given in Column D.

A least-squares adjustment to all camera and light cannon radiometric parameters to best match the entire 8^{o} C radiometric calibration data set resulted in the gain ratios of Column E in Table 4-1.

The weighted means of the gain ratio values determined in these various ways are listed in Column F of Table 4-1 and represent the best determination of the SSI gain switch ratios. The uncertainties in these ratios are only about 0.2% except for the summation mode gain effect, which has an uncertainty of about 0.4%.

d. Filter Factors

Filter factors are the ratios of the exposure times required to yield the same system response to a given source in a given gain state using one of the SSI spectral filters as using the clear filter. From equation (1), we see that the filter factor for filter n, f_n, is given by

$$f_n = \frac{t_n}{t0} = \frac{\int S\,T\,F_0\,I\,P\,d\lambda}{\int S\,T\,F_n\,I\,P\,d\lambda}$$

where the zero subscripts refer to the clear filter. These factors vary with the spectral content of the scene being imaged.

The filter factors for the calibration source (tungsten light cannon viewed through the thermal vacuum chamber window) were determined in several different ways. The most straightforward measurement involves simply ratioing the mean DN - DN_0 for the same pixel area of two frames for which only the filter has been varied. Unfortunately, no frame pairs including the clear filter were acquired under these conditions. However, by letting the gain state also vary, frame pairs involving the clear filter do exist. Using the gain ratios computed above allows filter factors with respect to the clear filter to be computed. The gain state ratio uncertainties are small enough that no systematic errors in the computed filter factors were apparent due to gain-ratio adjustments. Even allowing for gain differences, pairs of frames relating each filter directly to the clear filter are not available. However, each filter can be related back to clear indirectly by using chains of ratios between other filters. The computed filter factors have uncertainties of about ±2%. They do vary systematically with SSI temperature as shown in Table 4-2.

A second approach to determining calibration-source filter factors was to ratio the best-fit DN/exposure slopes for 256 20 x 20 pixel areas for light transfer data sets acquired at the same temperature but different filter positions. This was done only for data acquired in gain state 2 (~440 e-/DN). The light cannon setting was different for the clear, red and 7270 Å filters than for the others, and so an adjustment for the relative source

Table 4-2. Thermal-vacuum calibration filter factors from DN - DN_0 ratios for a single area.

filter	position #	-10° C	+8° C	+18° C
clear	0	1.000	1.000	1.000
green	1	13.40	13.52	13.92
red	2	5.325	5.390	5.482
violet	3	590.6	599.0	618.3
7560 Å	4	20.65	20.61	21.35
> 9680 Å	5	63.97	65.21	67.83
7270 Å	6	40.37	40.94	42.25
8890 Å	7	73.30	73.14	75.72

brightness is required to derive filter factors with respect to clear. The resulting filter factors are given in Table 4-3. The estimated uncertainties are ±2%. These values agree with those computed by the first method to within 3%.

A third approach involved ratioing the means of the best-fit light transfer function slopes determined on a pixel-by-pixel basis for data sets acquired at an SSI temperature of $+8^{o}$ C at the same light cannon setting. Adjustments were made for differing gain states. The results are given in Table 4-4 along with their standard deviations.

A least-squares adjustment to all SSI and light cannon radiometric parameters to best match the entire calibration data set results in the filter factors given in Table 4-5. Table 4-6 lists the SSI filter factors computed from the best-fit SSI spectral response model for some other source spectra of interest. The effective wavelength of the system response to each source spectrum is also given for each filter position. Effective wavelength is defined as

$$\lambda_{eff} = \frac{\int STFIP\lambda\, d\lambda}{\int STFIP\, d\lambda}$$

e. Linearity

Although the SSI response was expected to be linear, this was checked for different SSI configurations. A linear response function was fit to the average response over a 50 x 50 pixel area for each light transfer data set acquired for each filter, temperature and gain state combination. The best-fit shutter offset correction was made. Solutions minimized in a least-squares sense the errors in absolute DN. No weighting was applied since for most SSI data the noise is dominated by quantization error and is therefore independent of signal level (see Section IV-A-6). The typical r.m.s. error in the fits was about 0.11 DN for non-summation-mode data with a typical maximum error of about 0.20 DN. The largest r.m.s. error (non-summation) was 0.28 DN and the largest error was 0.45 DN. For the summation mode over the same area (25 x 25 summed pixels), the typical r.m.s. error in the fits was about 0.25 DN with a typical maximum error of about 0.45 DN. The largest summation-mode r.m.s. error was 0.61 DN, and the largest error was 1.22 DN. The goodness of the fits showed no variation with gain state, filter or temperature.

The residual errors from a linear fit to the response function do not reveal any systematic departures from true linearity with one exception

Table 4-3. Thermal-vacuum calibration filter factors from ratios of sensitivities averaged over 256 20 x 20 pixel areas.

filter	position #	-10° C	+8° C	+18° C
clear	0	1.000	1.000	1.000
green	1	13.62	13.67	13.94
red	2	5.336	5.365	5.456
violet	3	601.5	598.7	619.0
7560 Å	4	20.71	20.49	21.67
> 9680 Å	5	64.26	64.40	69.81
7270 Å	6	40.68	40.60	43.65
8890 Å	7	73.05	72.82	78.28

Table 4-4. Thermal-vacuum calibration filter factors at +8° C based on ratios of pixel-by-pixel sensitivity values.

filter	position #	mean	σ
clear	0	1.000	0.00
green	1	13.519	0.058 = 0.43 %
red	2	5.352	0.019 = 0.36 %
violet	3	597.7	3.53 = 0.59 %
7560 Å	4	20.508	0.031 = 0.15 %
> 9680 Å	5	64.38	0.27 = 0.43 %
7270 Å	6	40.69	0.22 = 0.55 %
8890 Å	7	72.88	0.29 = 0.40 %

Table 4-5. Thermal-vacuum calibration filter factors at +8° C from least-squares fit to entire calibration data set.

filter	position #	mean	σ
clear	0	1.000	0.00
green	1	13.50	0.053 = 0.39 %
red	2	5.369	0.021 = 0.40 %
violet	3	595.5	1.21 = 0.20 %
7560 Å	4	20.46	0.079 = 0.39 %
> 9680 Å	5	64.36	0.26 = 0.41 %
7270 Å	6	40.44	0.19 = 0.48 %
8890 Å	7	72.90	0.21 = 0.29 %

discussed below. Figures 4-14 through 4-25 show examples of typical residuals (in both DN and percent) of mean response versus relative exposure for various gain states, filters and summation mode. These residuals are from linear fits to the average response over 256 20 x 20 pixel areas distributed over the CCD array and are generally somewhat larger than those from the fit to the single 50 x 50 pixel area discussed in the previous

Table 4-6. Filter factors and effective wavelengths for SSI filters (based on best-fit spectral response model).

source spectrum		filter clear	green	red	violet	7560Å	>9680Å	7270Å	8890Å
gray	FF	1.000	7.776	7.071	16.25	35.86	111.5	68.14	132.5
	λ_{eff}	633.1	558.9	671.5	401.6	760.4	987.8	734.3	887.4
solar	FF	1.000	6.477	7.178	17.94	44.59	220.0	80.04	211.0
	λ_{eff}	611.0	558.6	670.5	404.2	760.3	986.2	734.2	887.3
Jupiter	FF	1.000	5.793	6.877	21.59	44.49	497.4	94.19	1477.
NTrZ	λ_{eff}	602.8	558.5	670.4	405.4	760.1	983.0	734.7	885.3
Jupiter	FF	1.000	5.674	6.381	29.26	42.64	460.1	89.75	1136.
EQ	λ_{eff}	612.1	558.9	670.4	406.5	760.1	983.5	734.6	885.7
Jupiter	FF	1.000	5.860	6.676	24.72	42.73	282.7	81.06	369.1
SPH	λ_{eff}	609.7	558.7	670.3	405.7	760.1	985.7	734.4	887.2
Io	FF	1.000	6.420	5.938	69.34	36.26	186.2	65.87	178.1
"reddest"	λ_{eff}	640.7	559.6	670.7	412.1	760.3	986.0	734.2	887.3
Io	FF	1.000	6.630	6.246	37.61	41.95	195.8	69.28	187.3
average	λ_{eff}	631.4	559.2	670.7	408.7	760.3	986.0	734.2	887.3
Io	FF	1.000	7.056	6.770	19.37	41.33	212.2	75.10	203.0
"whitest"	λ_{eff}	616.8	558.8	670.7	406.1	760.3	986.0	734.2	887.3
Europa	FF	1.000	6.252	6.651	28.99	41.70	213.6	74.84	202.5
leading	λ_{eff}	622.3	558.7	670.6	406.8	760.3	985.7	734.2	887.3
Europa	FF	1.000	6.189	6.585	34.48	41.28	211.5	74.09	200.5
trailing	λ_{eff}	624.4	558.7	670.6	407.8	760.3	985.7	734.2	887.3
Ganymede	FF	1.000	6.444	6.571	27.08	41.61	214.4	73.08	201.4
	λ_{eff}	622.9	559.1	670.6	406.2	760.3	985.7	734.2	887.3
Callisto	FF	1.000	6.346	6.738	27.47	40.14	201.5	75.12	189.8
	λ_{eff}	623.5	558.8	670.6	406.4	760.3	985.8	734.2	887.3
Moon	FF	1.000	6.697	5.985	72.29	33.42	198.1	61.38	157.1
	λ_{eff}	647.8	559.6	671.2	413.0	760.3	985.2	734.2	887.2
Venus	FF	1.000	5.929	6.209	77.65	38.57	266.2	68.71	199.0
	λ_{eff}	634.1	559.0	670.7	414.5	760.2	984.4	734.2	887.2

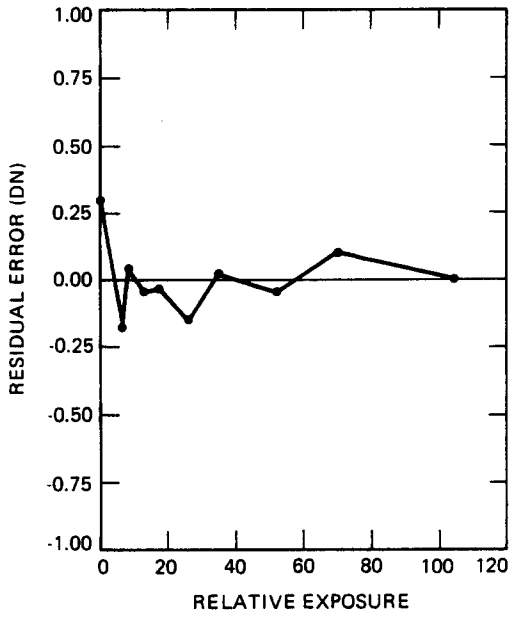

Figure 4-14.
Residuals in DN from linear fits to the mean response vs relative exposure for the red filter and gain state 4.

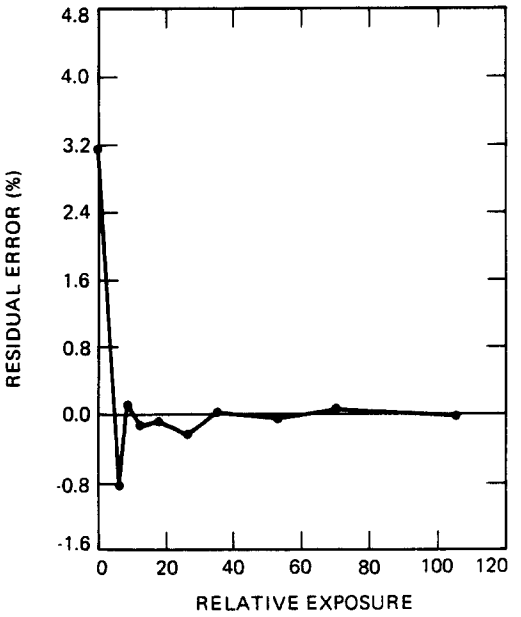

Figure 4-15.
Residuals in percent from linear fits to the mean response vs. relative exposure for the red filter and gain state 4.

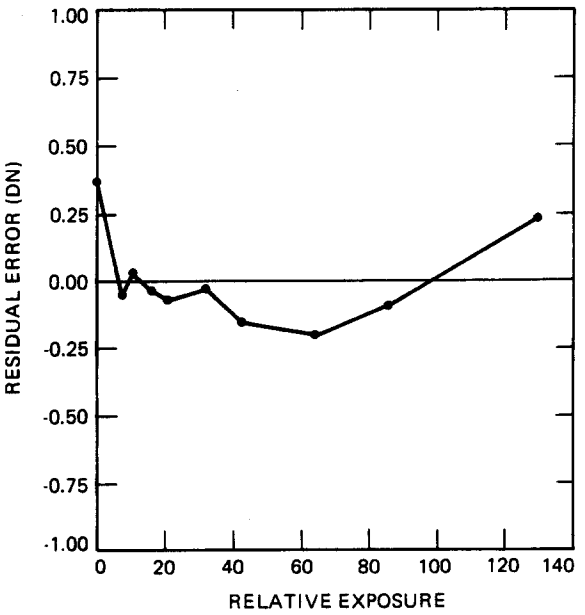

Figure 4-16.
Residuals in DN from linear fits to the mean response vs relative exposure for the red filter and gain state 3.

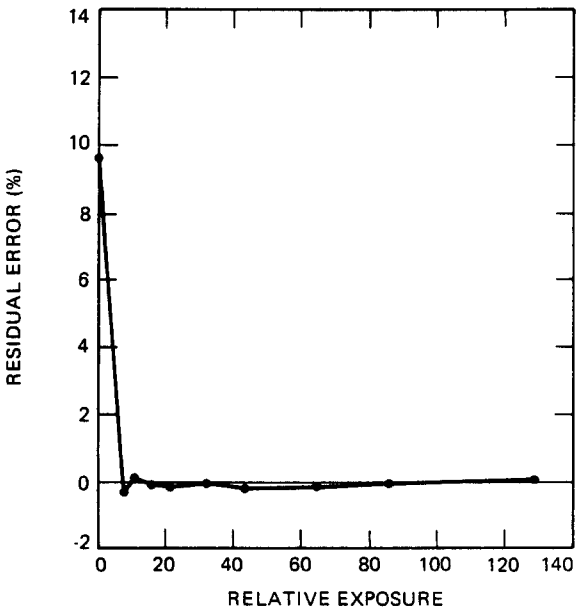

Figure 4-17.
Residuals in percent from linear fits to the mean response vs. relative exposure for the red filter and gain state 3.

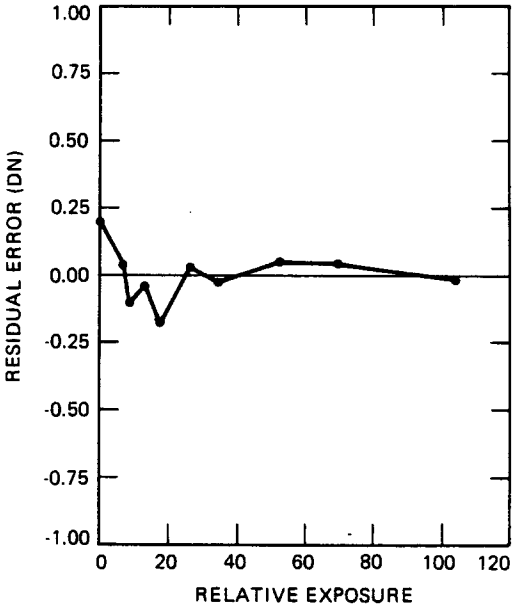

Figure 4-18.
Residuals in DN from linear fits to the mean response vs relative exposure for the red filter and gain state 2.

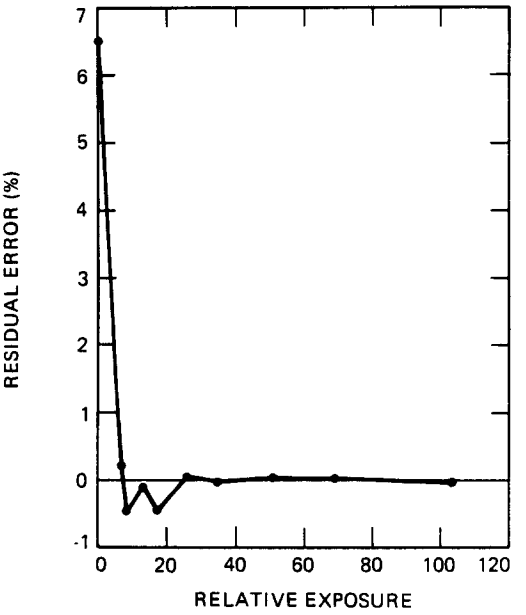

Figure 4-19.
Residuals in percent from linear fits to the mean response vs. relative exposure for the red filter and gain state 2.

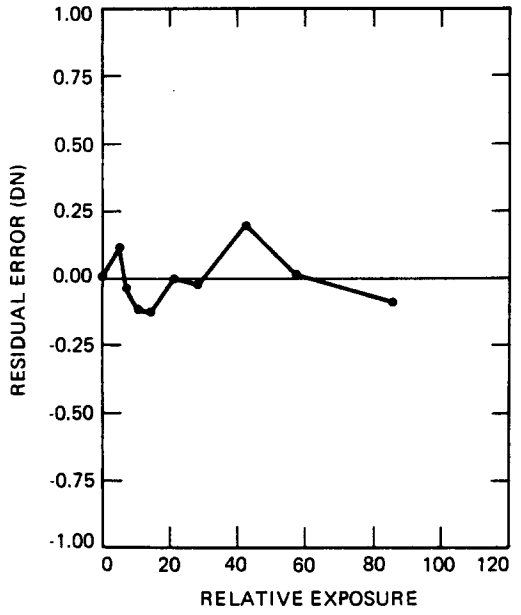

Figure 4-20.
Residuals in DN from linear fits to the mean response vs. relative exposure for the red filter, summation mode and gain state 1.

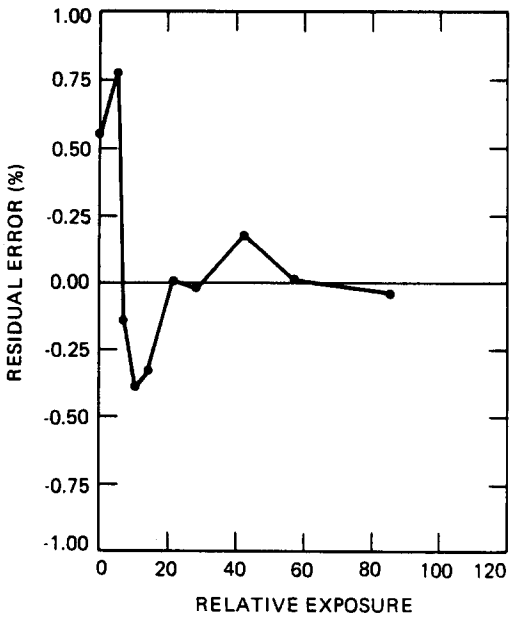

Figure 4-21.
Residuals in percent from linear fits to the mean response vs. relative exposure for the red filter, summation mode and gain state 1.

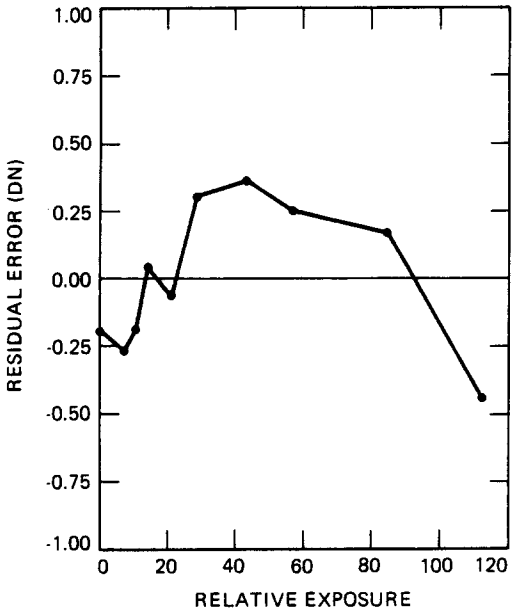

Figure 4-22.
Residuals in DN from linear fits to the mean response vs relative exposure for the violet filter and gain state 2

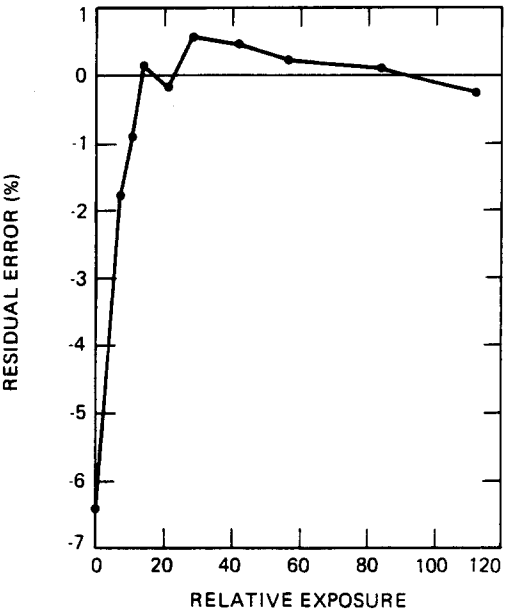

Figure 4-23.
Residuals in percent from linear fits to the mean response vs. relative exposure for the violet filter and gain state 2.

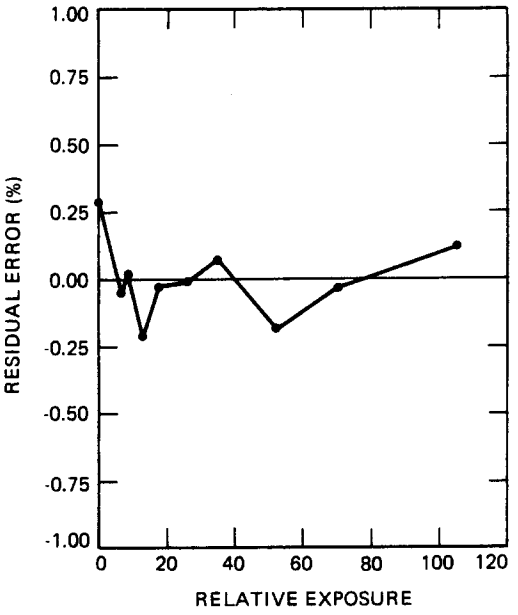

Figure 4-24.
Residuals in DN from linear fits to the mean response vs relative exposure for the >9680 Å filter and gain state 2

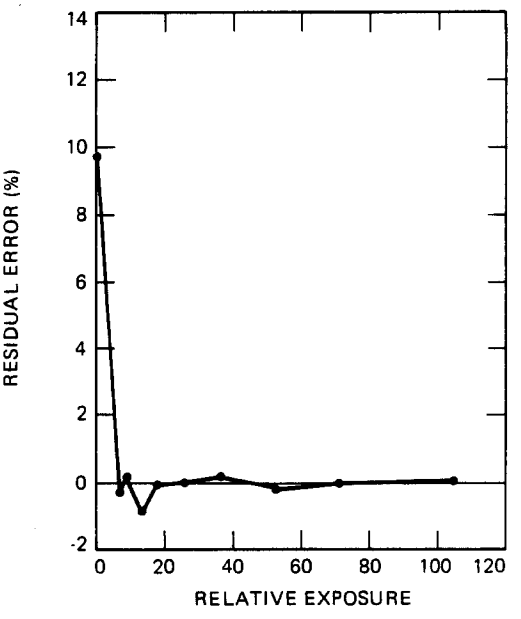

Figure 4-25.
Residuals in percent from linear fits to the mean response vs. relative exposure for the >9680 Å filter and gain state 2.

paragraph. The residuals are randomly distributed with exposure level. The percentage errors are typically less than 1% except for the offset level (zero exposure). The offset uncertainty is discussed in more detail in Section IV-A-5 below. Various sources of noise in the image data are discussed in Section IV-A-6.

The generally larger residuals in the summation mode are a result of several factors -- the random noise level in the original data is larger (see Section IV-A-6 below), the CCD area over which the response was computed contains four times fewer pixels (25^2 vs. 50^2), and since there is no CCD light flood in the summation mode, the effects of CCD residual bulk image are present in summation mode light transfer data. The effects of residual bulk image are seen in the data from the two longest wavelength filters where its changes to CCD quantum efficiency are the greatest. The >9680 Å filter has the largest residuals to a linear fit, and the 8890 Å filter also has above-average residuals. The residuals in these filters show a systematic pattern in which the actual SSI response is less than the value from the linear fit for mid-range signal levels but becomes greater than the linear fit value at the highest signal level. This pattern is consistent with the way CCD quantum efficiency changes due to residual bulk image for the imaging sequence used to acquire summation-mode light transfer data.

The light transfer data sets generally start with a minimum signal level of about 12 DN above the offset. In terms of signal electrons, the minimum signal level examined is about 500 electrons/pixel for the gain state 4 cases. For very low-light-level science objectives (e.g., Jovian aurorae and ring), the SSI linearity at signal levels below 500 e- is of concern. Therefore, one light transfer data set was acquired in 1983 for signals in the range of about 50 - 200 electrons. An analysis of these data shows linear response to about the same confidence level as for the higher signal levels (r.m.s. error of 0.08 DN, maximum error of about 0.13 DN, and maximum percent error of about 1.4%).

Single light transfer data sets were acquired through the clear filter in gain state 2 with the data compressor on in each of its modes, with the CCD parallel clock voltages set to the inverted mode, and in the blemish protection mode. No loss of linearity was observed in any of these SSI configurations.

The conclusions regarding response linearity given above apply to the average response over a 25 x 25 or 50 x 50 pixel area. As will be discussed further in Section IV-A-3g, departures from linearity are observed for selected columns at signal levels below 2500e- and in the summation mode.

f. Sensitivity

Although knowledge of the conversion factor, C, coupled with calibration of the other SSI components, is sufficient to compute the SSI sensitivity to any known scene spectral radiance by Equation (1), the accuracy to which these components, and C in particular, are determined individually is not adequate to meet the science requirements. These requirements demand an end-to-end subsystem sensitivity determination. This is accomplished by using the light transfer data to compute the response in DN/exposure time for a known, well-calibrated source, i.e., the light cannon. The shape of the light cannon spectral output is known, and its absolute brightness at the center of its diffuser at any iris setting is measured in units of ftL. This brightness level can be scaled to the average level over the annulus visible to the SSI (i.e., 0.960 of the value at the center of the diffuser for the tungsten light cannon and 0.934 for the xenon cannon) and converted to an equivalent brightness level in ftL for the spectrum as modified by the thermal vacuum chamber window transmission properties. Thus, we can specify the SSI response in DN/ftL-msec to the known calibration source spectrum. The results for the clear filter in gain state 2 averaged over 256 20 x 20 pixel areas are as follows:

temperature (deg. C)	-10	+8	+18
sensitivity (DN/ftL-msec)	0.1580	0.1539	0.1595

The average sensitivity values for other filters or gain states can be derived using the gain ratios and calibration source filter factors given above. The sensitivities for each filter are plotted versus temperature in Figures 4-26 through 4-33 for the 256-area averages in gain state 2.

The SSI sensitivity to the tungsten light cannon in the green filter at the expected flight temperature (+8^{0} to +10^{0} C) has remained constant over the 1983, 1984 and 1985 calibrations to within ±4% (which is equivalent to the estimated absolute accuracy of the NBS-traceable luminance standard used to calibrate the light cannon). However, the response to the tungsten light cannon at other wavelengths (in units of DN/ftL-msec) has appeared to drift over the years. Violet response has decreased about 8% from 1983 to 1985 while response in wavelengths longward of green has systematically and progressively increased (the response in the >9680 Å filter has increased by about 26% from 1983 to 1985). A part of the increased long-wavelength sensitivity is due to the addition of light flood between 1983 and 1984 to correct the residual bulk image problem. Changes in the shape of the light cannon spectral output could result in such apparent drifts (since response is given per unit of foot-Lamberts, which only characterizes the

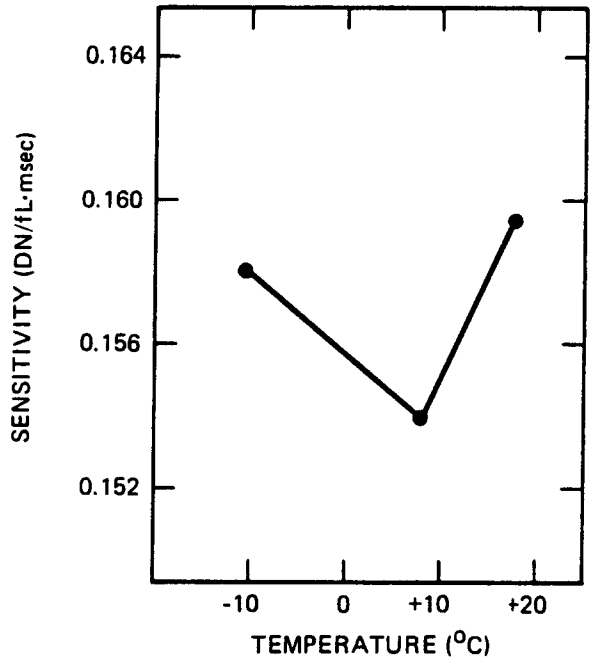

Figure 4-26.
Sensitivity for the clear filter vs. temperature in gain state 2.

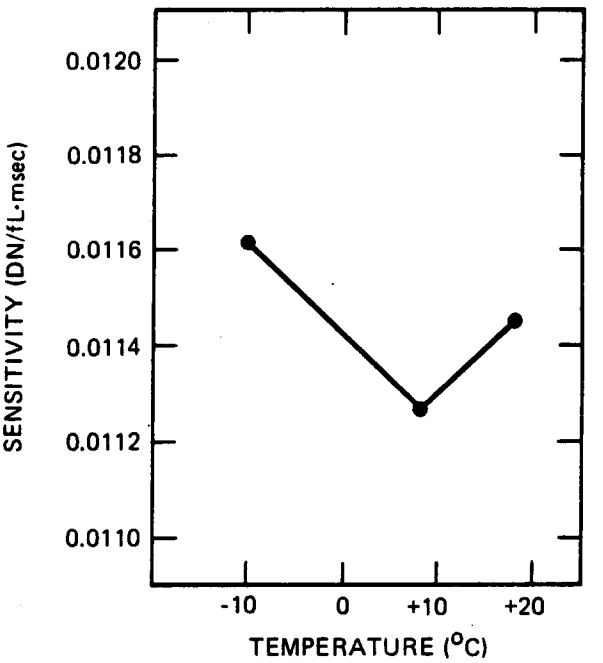

Figure 4-27.
Sensitivity for the green filter vs. temperature in gain state 2.

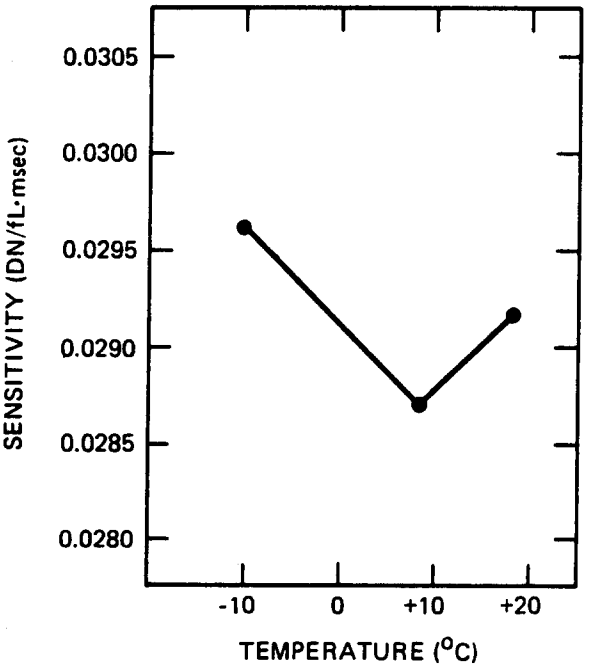

Figure 4-28.
Sensitivity for the red filter vs. temperature in gain state 2.

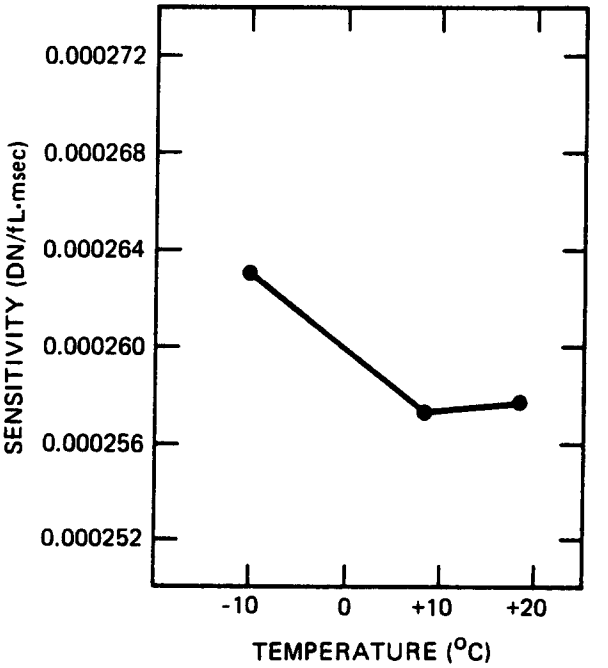

Figure 4-29.
Sensitivity for the violet filter vs. temperature in gain state 2.

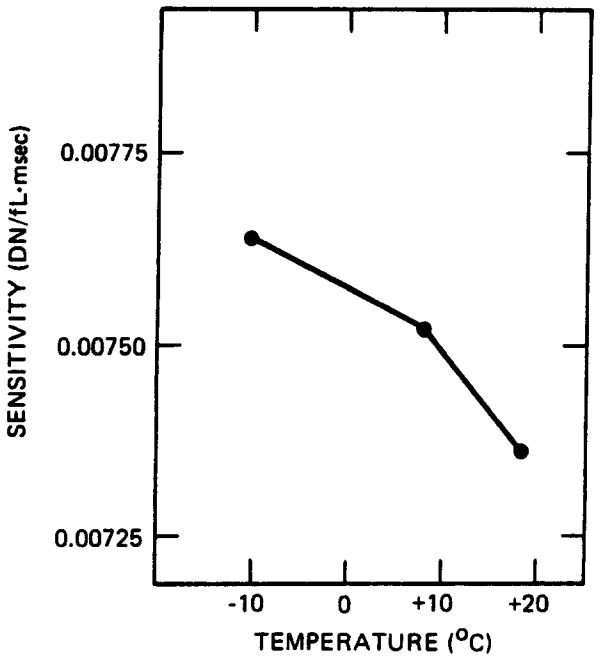

Figure 4-30.
Sensitivity for the 7560 Å filter vs. temperature in gain state 2.

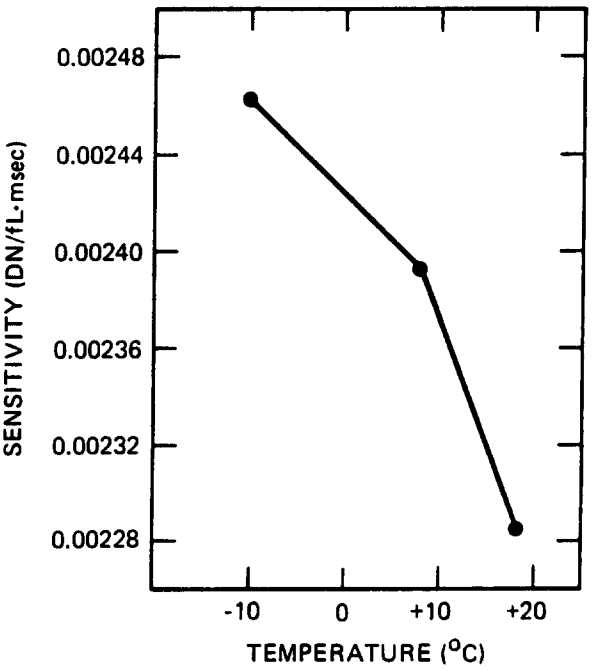

Figure 4-31.
Sensitivity for the >9680 Å filter vs. temperature in gain state 2.

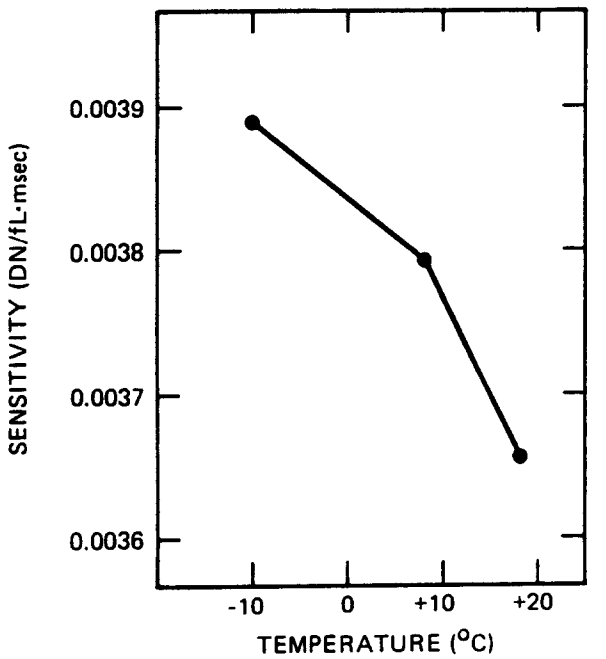

Figure 4-32.
Sensitivity for the 7270 Å filter vs. temperature in gain state 2.

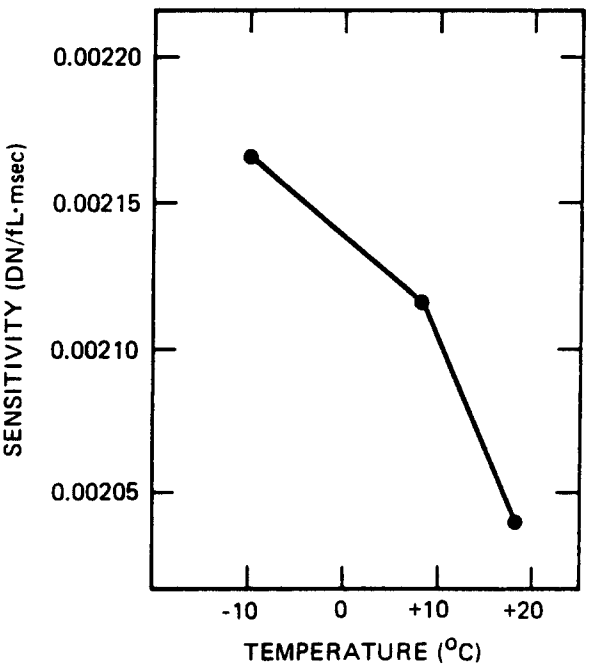

Figure 4-33.
Sensitivity for the 8890 Å filter vs. temperature in gain state 2.

visible output); however, measurements of the light cannon spectrum over the years show changes different from the drifts in the calculated SSI response (violet 5% down, red 4% up, 1 μm 27% down) particularly at the longest wavelengths between 1983 and 1984. Even if the 1983 data are ignored, there does appear to be a progressive increase in the near-IR response of the SSI between 1984 and 1985 (20% for the >9680 Å filter). Possible causes of such a drift include shifts in filter bandpasses, changes in CCD quantum efficiency, and/or errors in calibration of the light cannon spectral radiance.

The average sensitivity across the entire array derived from pixel-by-pixel fits to the 1985 light transfer data sets at +8° C temperature are given in Table 4-7 for each filter. Best-fit adjustments of all SSI and calibration source parameters to match the entire 8° C radiometric calibration data set results in sensitivities as given in Table 4-8. The uncertainties listed are a measure of the precision of the sensitivity measurements (i.e., the internal consistency of the entire 8° C calibration data set). The absolute calibration accuracy is not this good since the systematic error in knowledge of the luminance reference standard used is about ±4%.

Switching the SSI configuration to use data compression or blemish protection has no measurable effect on sensitivity. However, inverting the CCD causes an apparent increase in sensitivity of about 2%.

For scientific studies, it is desirable to express SSI sensitivity in radiometric rather than photometric units, particularly since the SSI spectral range extends beyond the visible. It is also necessary to consider sources with spectra different from our calibration source. Two alternative ways of defining SSI radiometric sensitivity have been adopted: (1) for scenes whose radiance comes solely from reflected sunlight, express sensitivity in units of DN per unit of surface reflectivity, or (2) for scenes that are self-radiating, express sensitivity in units of DN per unit radiance (watts/cm^2/sr/nm). In each case, since the spectrum of the surface reflectivity or source radiance is unknown a priori, it is assumed to be constant over the bandpass of the filter used. The measured reflectivity or radiance then applies at the effective wavelength of the SSI for that filter assuming a solar spectrum for surface reflectivity or a flat spectrum for source radiance. These effective wavelengths were listed in Table 4-6.

To convert from units of calibration source ftL to units of surface reflectivity, the following expression is used:

$$\frac{\pi \int S\,T\,F\,I_{cal}\,P\,d\lambda}{A \int K\,I_{cal}\,d\lambda \int S\,T\,F\,H\,P\,d\lambda} \qquad \left(\frac{\text{reflectivity units}}{\text{calibration source ftL}}\right)$$

625-210

Table 4-10. Mean values and standard deviations of GALGEN-produced slopes and offsets.

filter	gain	slope (ftL-msec/DN)	σ		offset (DN)	σ
clear	1 (sum)	8.532	0.081	(0.9 %)	2.825	0.205
	2	9.339	0.098	(1.0 %)	2.817	0.224
	3	4.556	0.0475	(1.0 %)	3.538	0.281
	4	0.9532	0.0128	(1.3 %)	8.897	0.828
green	1 (sum)	116.4	1.57	(1.4 %)	2.686	0.214
	2	130.0	1.93	(1.5 %)	2.891	0.209
	2 (sum)	23.79	0.340	(1.4 %)	4.036	0.449
	3	62.28	0.891	(1.4 %)	3.507	0.299
	3 (sum)	11.49	0.188	(1.6 %)	6.276	1.087
	4	12.94	0.218	(1.7 %)	8.872	0.805
	4 (sum)	2.413	0.066	(2.7 %)	20.149	4.006
red	1 (sum)	45.32	0.623	(1.4 %)	2.602	0.218
	2	49.95	0.711	(1.4 %)	2.781	0.236
	3	24.66	0.363	(1.5 %)	3.455	0.321
	4	5.121	0.0868	(1.7 %)	8.789	0.803
violet	1 (sum)	2058.*	74.0	(3.6 %)	2.692	0.251
	2	5707	148.6	(2.6 %)	3.257#	0.444
	3	2789	74.12	(2.7 %)	3.797#	0.573
	4	580.3	16.86	(2.9 %)	8.730	0.784
7560 Å	1 (sum)	178.8	2.84	(1.6 %)	2.652	0.217
	2	195.1	3.17	(1.6 %)	2.814	0.215
	3	93.15	1.53	(1.7 %)	3.484	0.295
	4	19.48	0.380	(2.0 %)	8.835	0.803
>9680 Å	1 (sum)	583.8	8.41	(1.4 %)	2.453	0.252
	2	612.0	9.19	(1.5 %)	2.719	0.221
	3	295.1	4.31	(1.5 %)	3.531	0.311
	4	61.47	1.21	(2.0 %)	8.760	0.783
7270 Å	1 (sum)	359.3	5.48	(1.5 %)	2.609	0.200
	2	376.0	5.73	(1.5 %)	2.755	0.237
	3	190.7	2.99	(1.6 %)	3.462	0.283
	4	38.92	0.620	(1.6 %)	8.826	0.668
8890 Å	1 (sum)	658.6	11.51	(1.7 %)	2.586	0.194
	2	694.4	11.86	(1.7 %)	2.764	0.163
	3	332.1	5.68	(1.7 %)	3.315	0.350
	4	69.67	1.20	(1.7 %)	8.860	0.644

(*) xenon light cannon (#) 60 2/3-sec mode, extended exposures

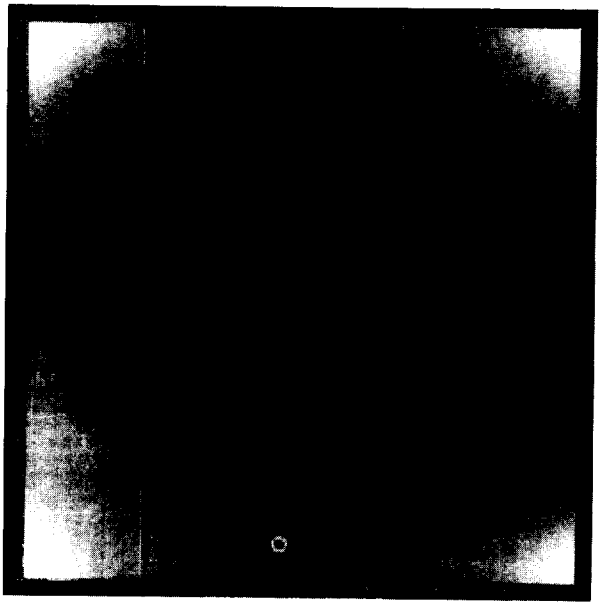

Figure 4-34.
Slope term image for
gain state 4, violet filter.
slope range = 549.1 - 646.4

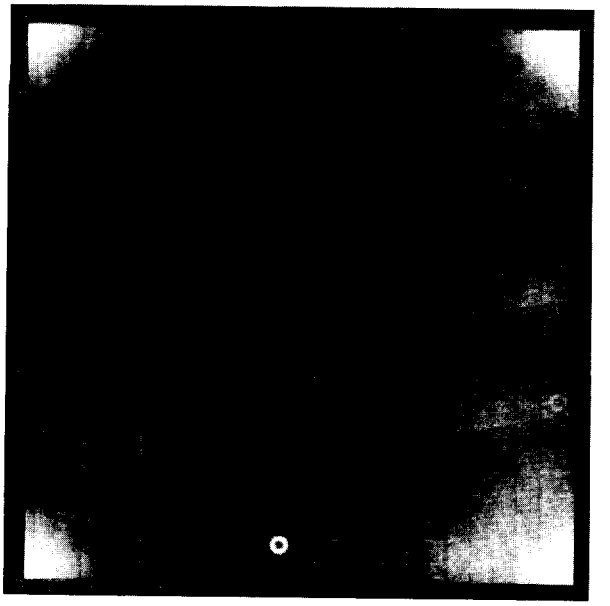

Figure 4-35.
Slope term image for
gain state 4, 7270 Å filter.
lope range = 37.56 - 41.30

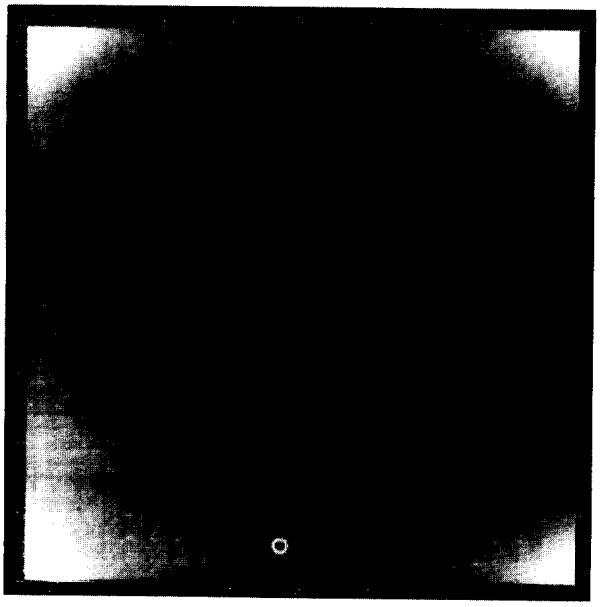

Figure 4-36.
Slope term image for
gain state 3, violet filter.
slope range = 2667. - 3100.

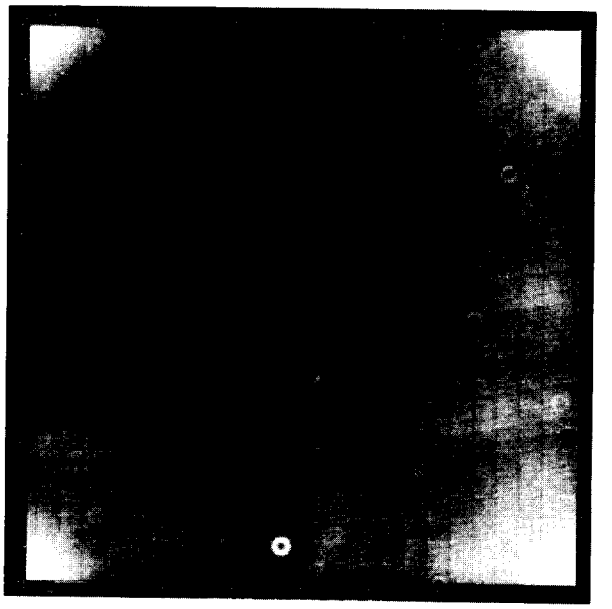

Figure 4-37.
Slope term image for
gain state 3, 7270 Å filter.
slope range = 183.7 - 202.3

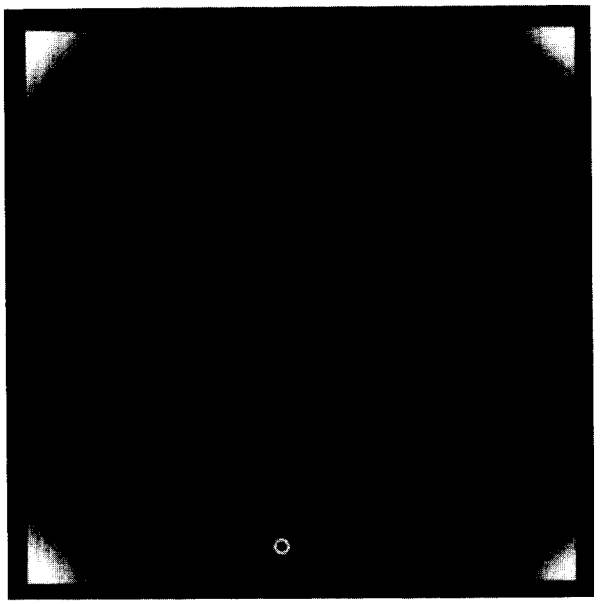

Figure 4-38.
Slope term image for
gain state 2, clear filter.
slope range = 9.085 - 9.797

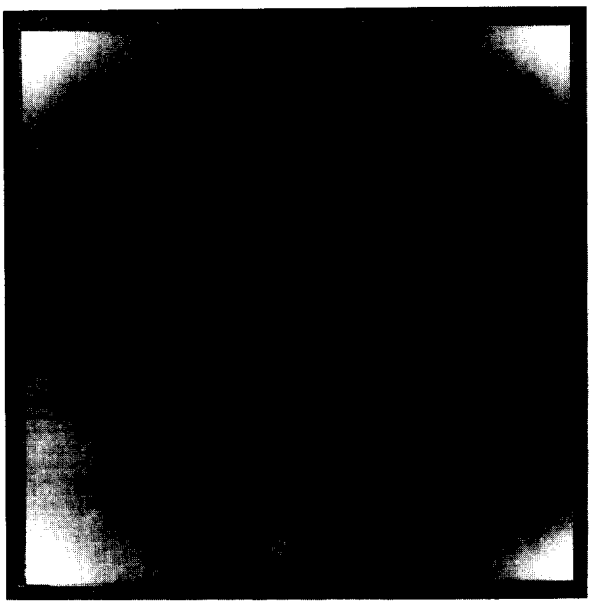

Figure 4-39.
Slope term image for
gain state 2, violet filter.
slope range = 5466. - 6345.

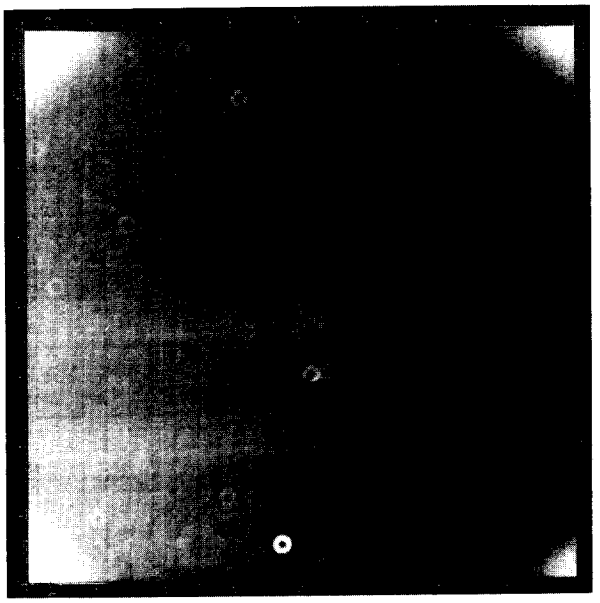

Figure 4-40.
Slope term image for
gain state 2, green filter.
slope range = 125.8 - 138.0

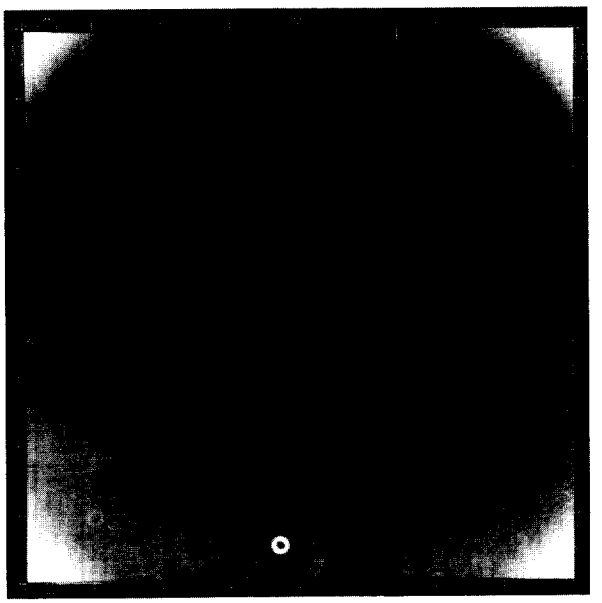

Figure 4-41.
Slope term image for
gain state 2, red filter.
slope range = 48.63 - 53.40

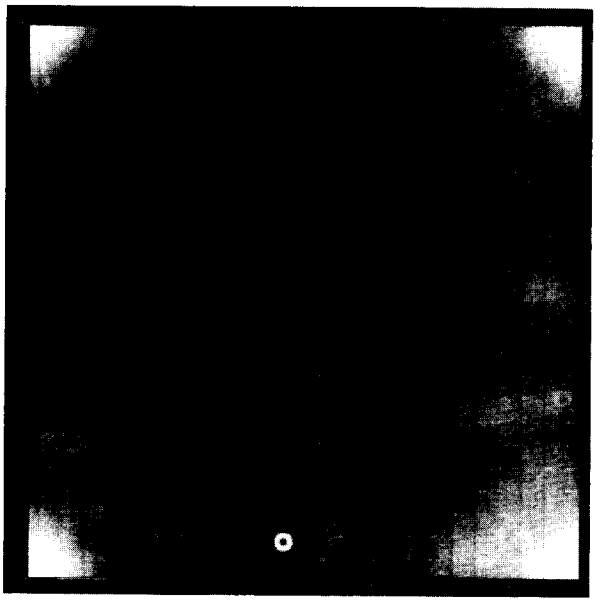

Figure 4-42.
Slope term image for
gain state 2, 7270 Å filter.
slope range = 361.9 - 398.7

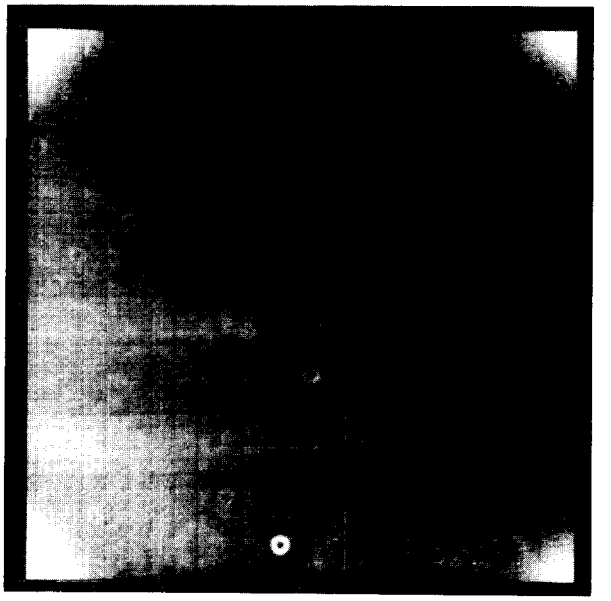

Figure 4-43.
Slope term image for
gain state 2, 7560 Å filter.
slope range = 186.8 - 205.7

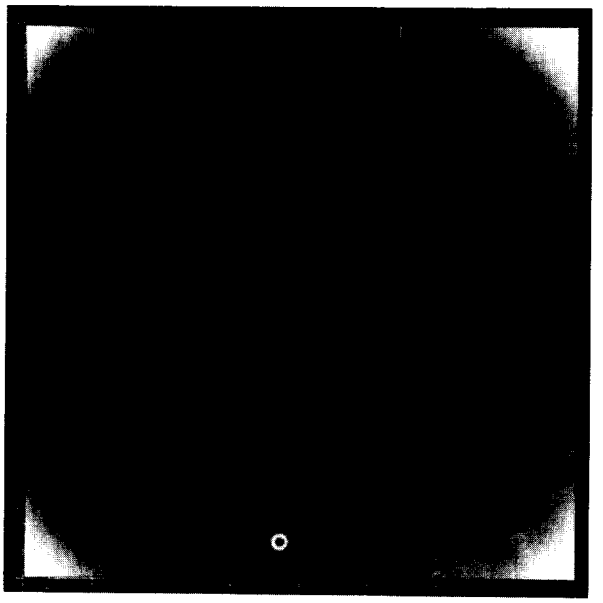

Figure 4-44.
Slope term image for
gain state 2, 8890 Å filter.
slope range = 675.0 - 749.6

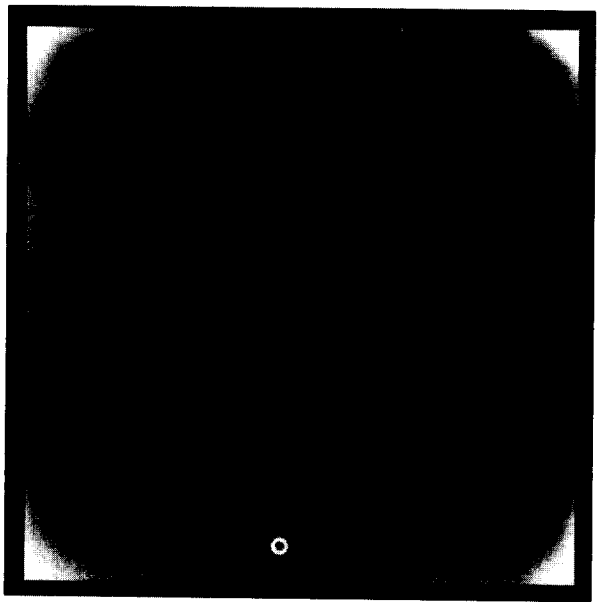

Figure 4-45.
Slope term image for
gain state 2, >9680 Å filter.
slope range = 592.0 - 652.8

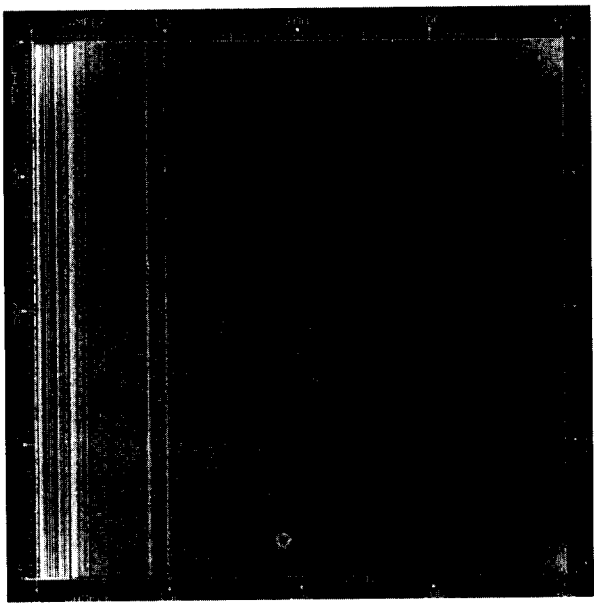

Figure 4-46.
Slope term image for
gain state 4, green filter,
and summation mode.
slope range = 2.212 - 2.664

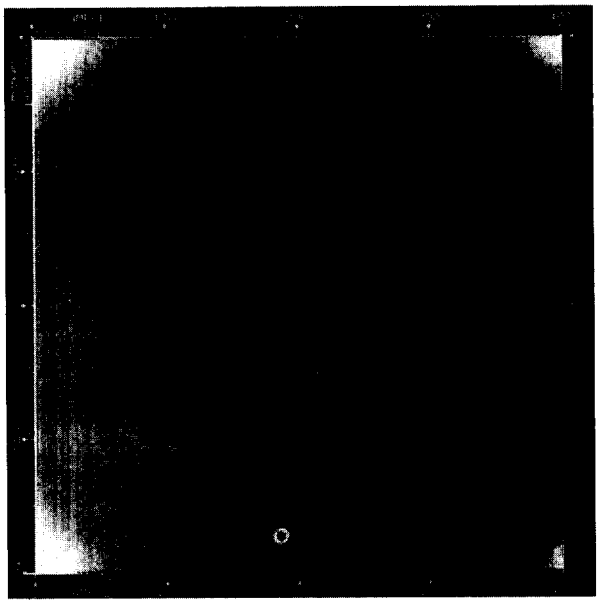

Figure 4-47.
Slope term image for
gain state 3, green filter,
and summation mode.
slope range = 11.12 - 12.19

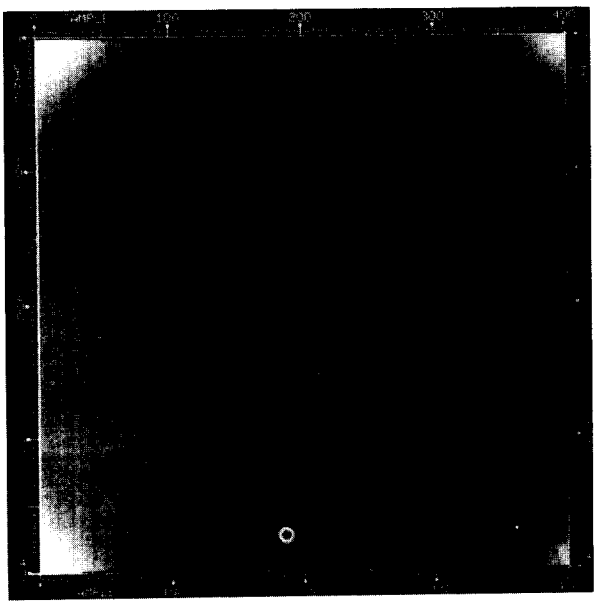

Figure 4-48.
Slope term image for
gain state 2, green filter,
and summation mode.
slope range = 23.14 - 25.27

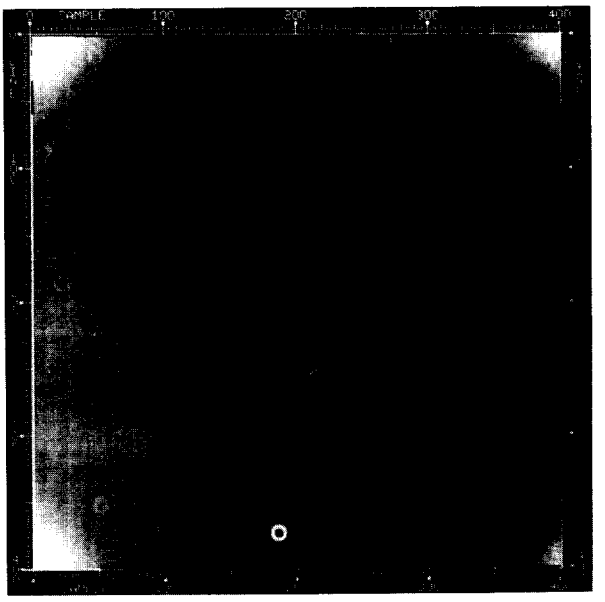

Figure 4-49.
Slope term image for
gain state 1, green filter,
and summation mode.
slope range = 113.1 - 123.1

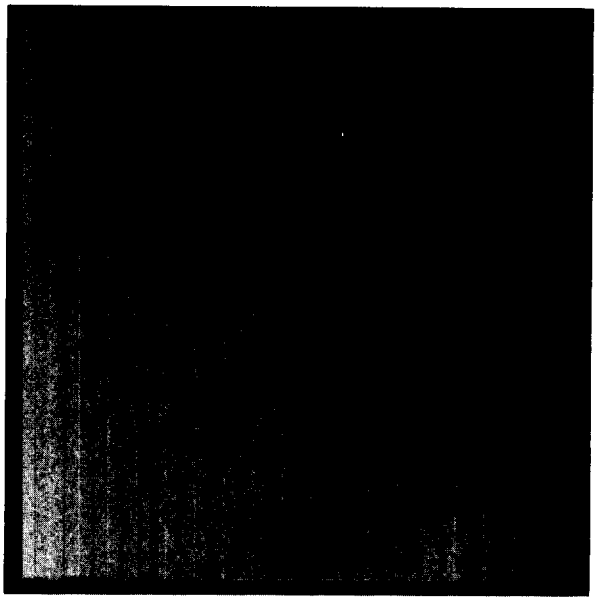

Figure 4-50.
Offset term image for
gain state 4, red filter.
offset range = 6.38 - 10.8

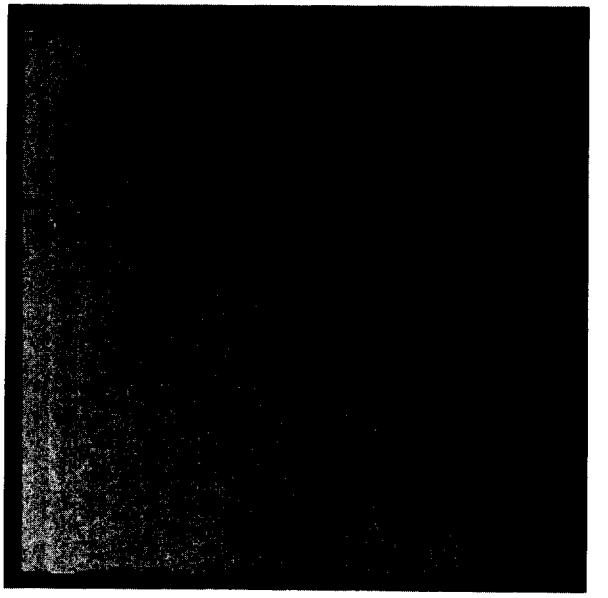

Figure 4-51.
Offset term image for
gain state 3, green filter.
offset range = 2.61 - 4.42

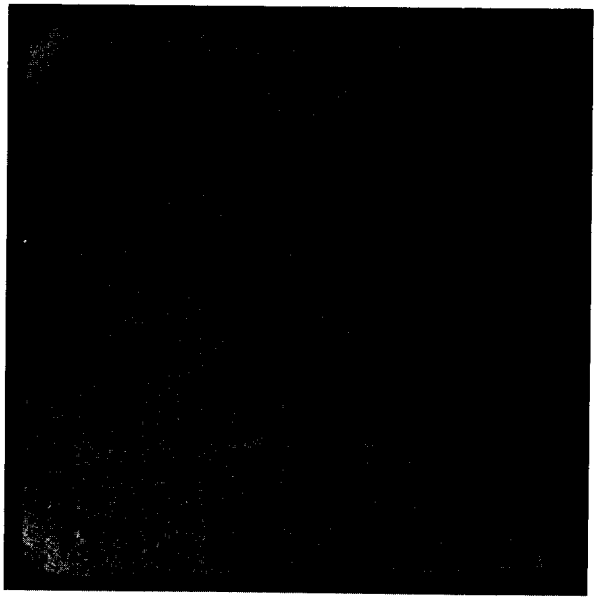

Figure 4-52.
Offset term image for
gain state 2, clear filter.
offset range = 2.12 - 3.42

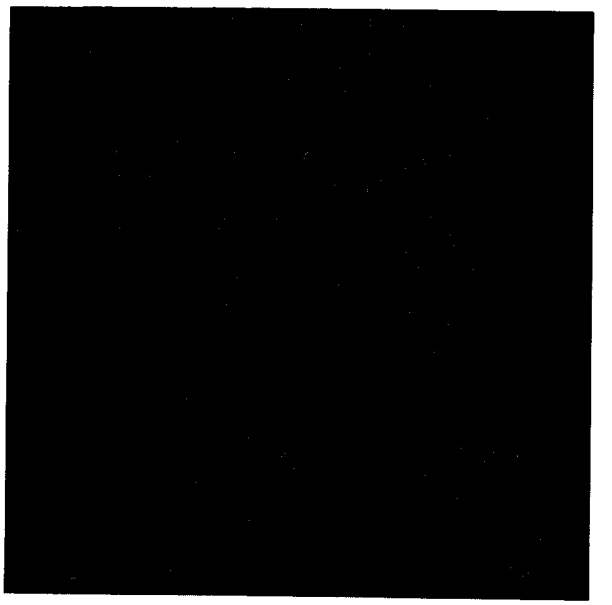

Figure 4-53.
Offset term image for
gain state 2, violet filter.
offset range = 2.28 - 4.62

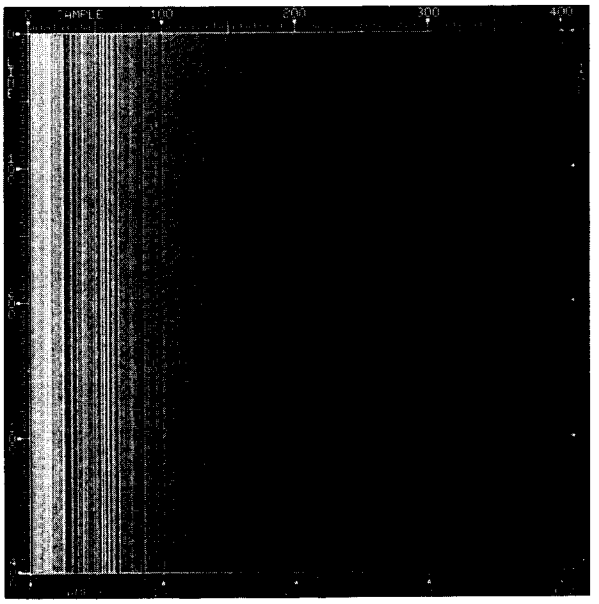

Figure 4-54.
Offset term image for
gain state 4, green filter,
and summation mode.
offset range = 12.9 - 32.2

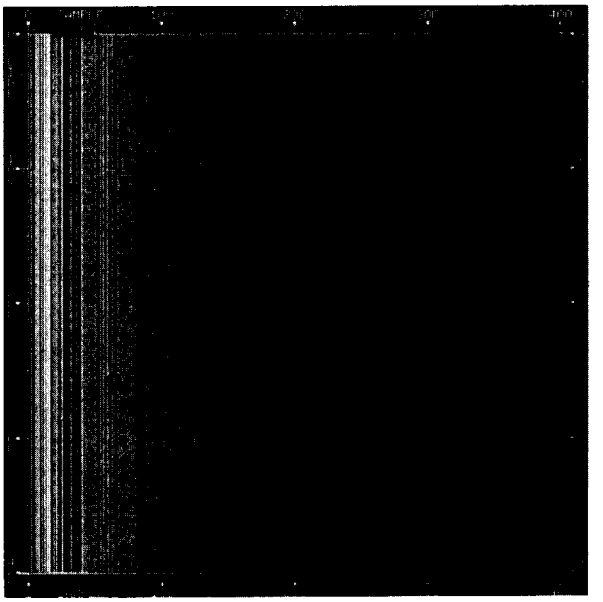

Figure 4-55.
Offset term image for
gain state 3, green filter,
and summation mode.
offset range = 3.88 - 9.82

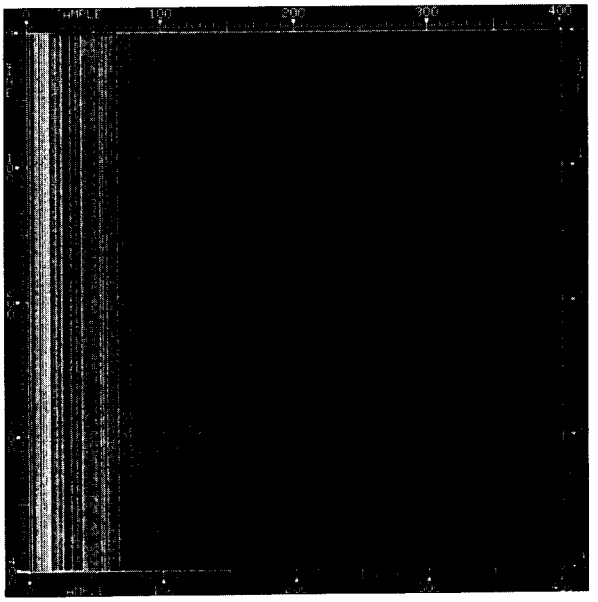

Figure 4-56.
Offset term image for
gain state 2, green filter,
and summation mode.
offset range = 2.77 - 5.95

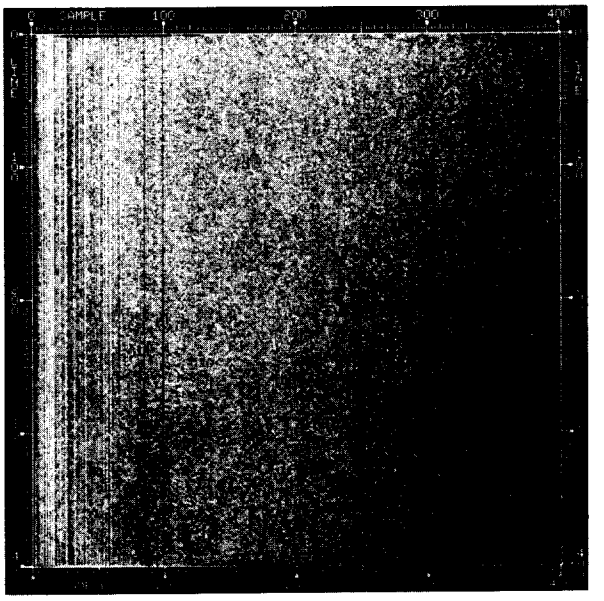

Figure 4-57.
Offset term image for
gain state 1, green filter,
and summation mode.
offset range = 2.02 - 3.24

The slope, offset and blemish files from GALGEN and BLEMGEN are used by the program GALSOS to calibrate SSI images into units proportional to the scene brightness. GALSOS also interpolates over any blemishes or pixels whose signal level exceeds their full-well limit using the signal levels of neighboring pixels to perform the interpolation. Figures 4-58 through 4-99 show several examples of flat field images before and after calibration. Various exposure levels, gain states, filters and use of the summation mode are included. Note that the calibration totally corrects for the dust speck "donuts", the corner vignetting and the step-and-repeat pattern, leaving an extremely flat field. The remaining random noise level is discussed in Section IV-A-6 below. The range of exposure values in the resulting images are listed below each picture.

In the summation mode, the linear calibration leaves a pattern of vertical striations in the first 100 or so columns. These are most noticeable in the highest gain state (Figures 4-76 through 4-81). Investigation of these striations has shown that they are generated in the CCD, probably during the parallel-to-serial register transfer of charge. The location and amplitude of the striations vary with the applied CCD clock drive voltages. Switching the CCD negative parallel clock voltage to the inverted level, for example, strongly affects the striation pattern.

Since the linear calibration does not remove these striations, the pattern must either involve a nonlinear response function or be time-variable. Variability in the pattern was examined by comparing 50-line averages from identical frames taken a few seconds apart, a year apart, and at different instrument temperatures. The amplitude (peak-to-peak) of the striations in the raw data in gain state 4 is about ±12 DN for a mean signal level of 70 DN and is about ±48 DN for a mean signal level of 210 DN. Differencing two frames taken several seconds apart reduces the amplitude to less than ±1 DN. For two frames taken a year apart, the differenced amplitude is about ±2 DN. For two frames taken at the opposite extremes of the SSI temperature range (-20° C to +18° C), the amplitude in the differenced frames is about ±3 DN. Thus, the striation pattern is shown to be quite stable with time for a given temperature and only slightly variable with instrument temperature. The striations are therefore due to slight response nonlinearities in these columns.

The level of nonlinearity in the striations is shown in Table 4-11. Consideration was given to using a piecewise-linear calibration function for summation-mode data in order to correct for the striations. Such functions were derived and used to correct frames at various exposure levels in all four gain states. Figures 4-100 through 4-107 show a comparison of the calibrated frames using linear and piecewise-linear functions for a mid-level signal in various gain states. The frames in each pair have been contrast-enhanced identically. The striations are completely removed by the piecewise linear approach; however, because the linear function was derived by fitting all 10 exposure levels from a light transfer data set while the

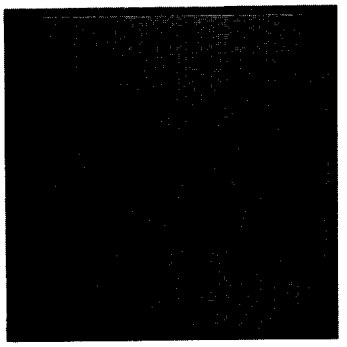

Figure 4-58.
Raw flat-field image for
gain state 2, clear filter,
and 33 1/3-msec exposure.
DN range = 14 - 16

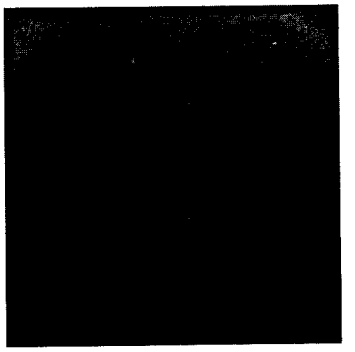

Figure 4-59.
Calibrated flat-field image for
gain state 2, clear filter,
and 33 1/3-msec exposure.
range = 107 - 121 ftL-msec

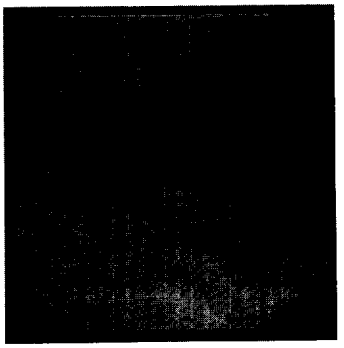

Figure 4-60.
Raw flat-field image for
gain state 2, clear filter,
and 133 1/3-msec exposure.
DN range = 51 - 55

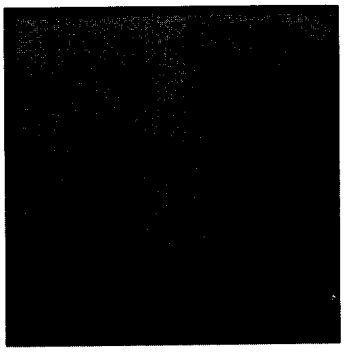

Figure 4-61.
Calibrated flat-field image for
gain state 2, clear filter,
and 133 1/3-msec exposure.
range = 458 - 477 ftL-msec

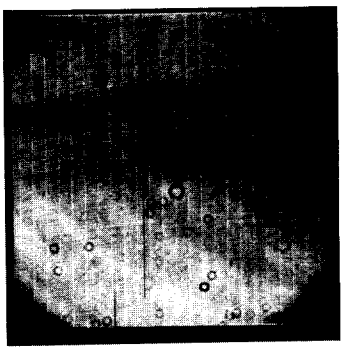

Figure 4-62.
Raw flat-field image for
gain state 2, clear filter,
and 533 1/3-msec exposure.
DN range = 200 - 209

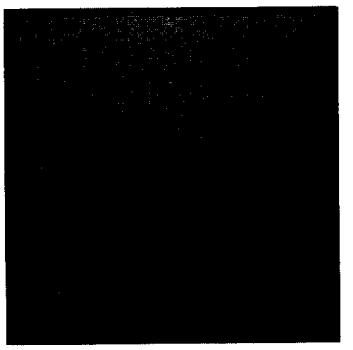

Figure 4-63.
Calibrated flat-field image for
gain state 2, clear filter,
and 533 1/3-msec exposure.
range = 1863 - 1909 ftL-msec

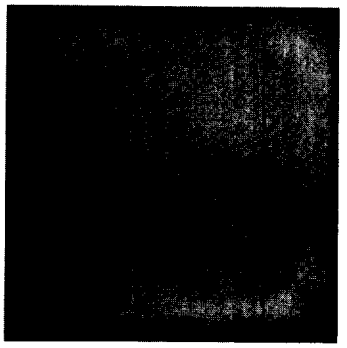

Figure 4-64.
Raw flat-field image for
gain state 3, >9680 Å filter,
and 266 2/3-msec exposure.
DN range = 14 - 18

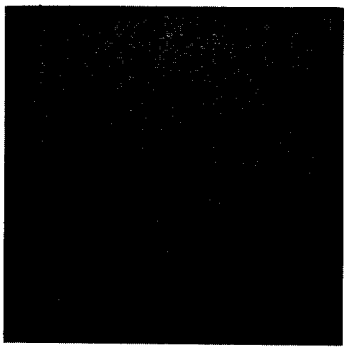

Figure 4-65.
Calibrated flat-field image for
gain state 3, >9680 Å filter,
and 266 2/3-msec exposure.
range = 3342 - 4119 ftL-msec

Figure 4-66.
Raw flat-field image for
gain state 3, >9680 Å filter,
and 1066 2/3-msec exposure.
DN range = 53 - 58

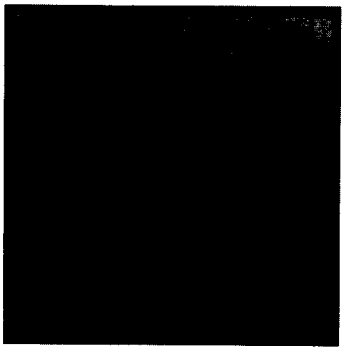

Figure 4-67.
Calibrated flat-field image for
gain state 3, >9680 Å filter,
and 1066 2/3-msec exposure.
range = 14801 - 15754 ftL-msec

Figure 4-68.
Raw flat-field image for
gain state 3, >9680 Å filter,
and 4266 2/3-msec exposure.
DN range = 204 - 216

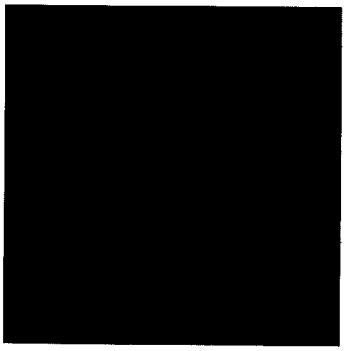

Figure 4-69.
Calibrated flat-field image for
gain state 3, >9680 Å filter,
and 4266 2/3-msec exposure.
range = 60140 - 62040 ftL-msec

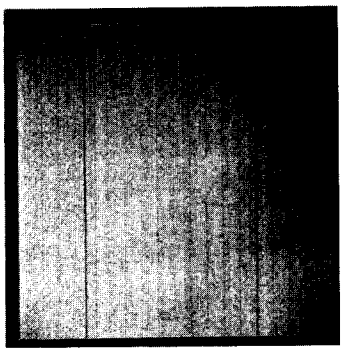

Figure 4-70.
Raw flat-field image for
gain state 4, <4450 Å filter,
and 200-msec exposure.
DN range = 17 - 22

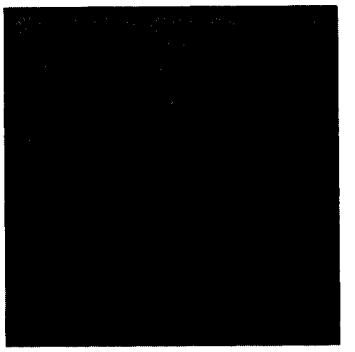

Figure 4-71.
Calibrated flat-field image for
gain state 4, <4450 Å filter,
and 200-msec exposure.
range = 5131 - 7878 ftL-msec

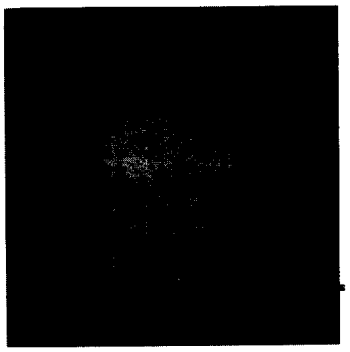

Figure 4-72.
Raw flat-field image for
gain state 4, <4450 Å filter,
and 800-msec exposure.
DN range = 50 - 58

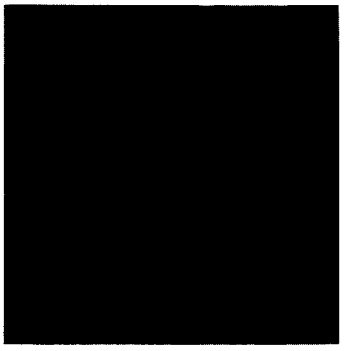

Figure 4-73.
Calibrated flat-field image for
gain state 4, <4450 Å filter,
and 800-msec exposure.
range = 24292 - 28444 ftL-msec

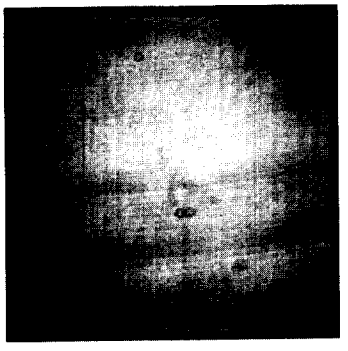

Figure 4-74.
Raw flat-field image for
gain state 4, <4450 Å filter,
and 3200-msec exposure.
DN range = 179 - 199

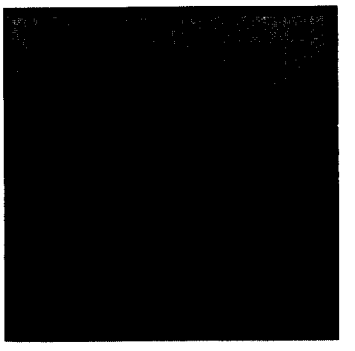

Figure 4-75.
Calibrated flat-field image for
gain state 4, <4450 Å filter,
and 3200-msec exposure.
range = 101340 - 110410 ftL-msec

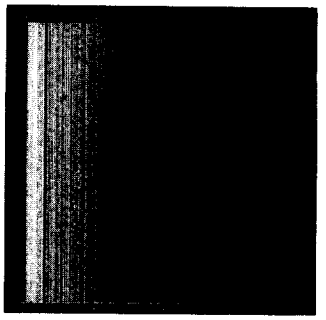

Figure 4-76.
Raw flat-field image for gain state 4, green filter, summation mode, and 33 1/3-msec exposure.
DN range = 24 - 40

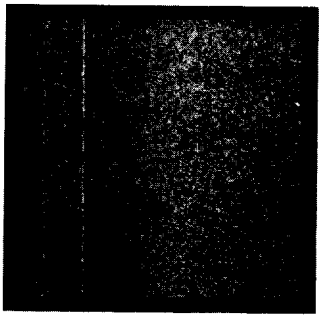

Figure 4-77.
Calibrated flat-field image for gain state 4, green filter, summation mode, and 33 1/3-msec exposure.
range = 17 - 36 ftL-msec

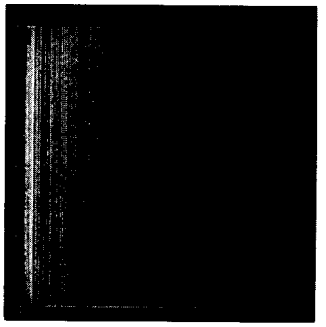

Figure 4-78.
Raw flat-field image for gain state 4, green filter, summation mode, and 33 1/3-msec exposure.
DN range = 24 - 40

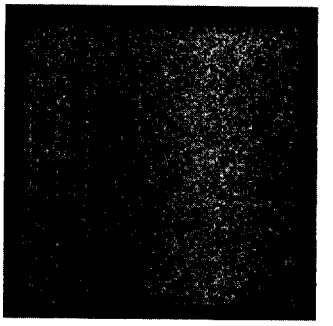

Figure 4-79.
Calibrated flat-field image for gain state 4, green filter, summation mode, and 33 1/3-msec exposure.
range = 17 - 36 ftL-msec

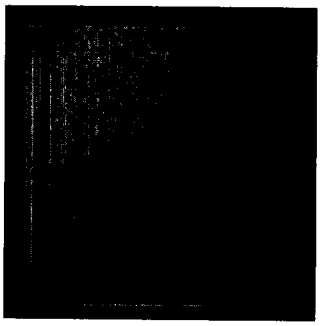

Figure 4-80.
Raw flat-field image for gain state 4, green filter, summation mode, and 533 1/3-msec exposure.
DN range = 187 - 209

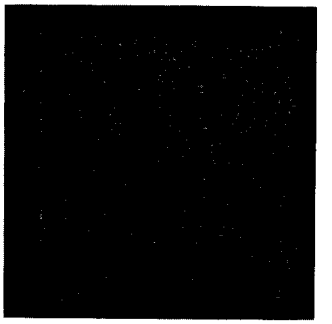

Figure 4-81.
Calibrated flat-field image for gain state 4, green filter, summation mode, and 533 1/3-msec exposure.
range = 408 - 449 ftL-msec

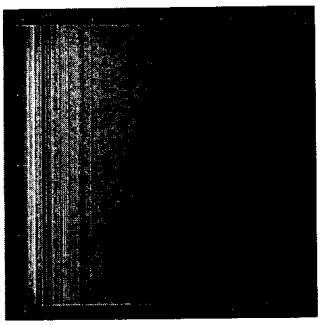

Figure 4-82.
Raw flat-field image for gain state 3, green filter, summation mode, and 50-msec exposure.
DN range = 16 - 21

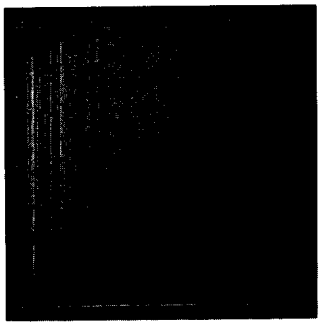

Figure 4-84.
Raw flat-field image for gain state 3, green filter, summation mode, and 200-msec exposure.
DN range = 53 - 59

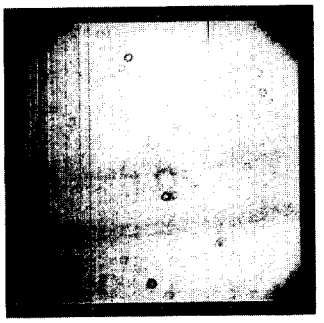

Figure 4-86.
Raw flat-field image for gain state 3, green filter, summation mode, and 800-msec exposure.
DN range = 199 - 210

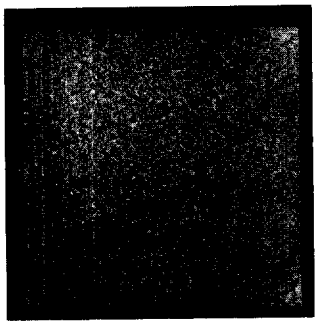

Figure 4-83.
Calibrated flat-field image for gain state 3, green filter, summation mode, and 50-msec exposure.
range = 119 - 155 ftL-msec

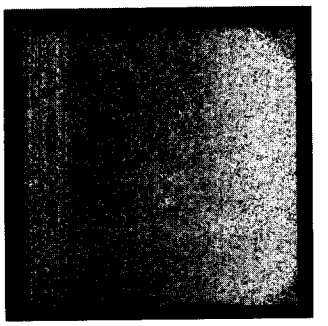

Figure 4-85.
Calibrated flat-field image for gain state 3, green filter, summation mode, and 200-msec exposure.
range = 548 - 590 ftL-msec

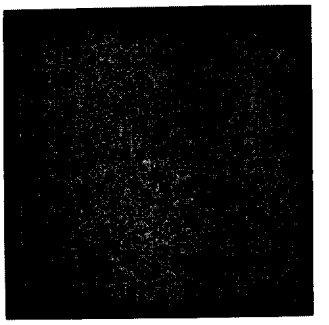

Figure 4-87.
Calibrated flat-field image for gain state 3, green filter, summation mode, and 800-msec exposure.
range = 2242 - 2351 ftL-msec

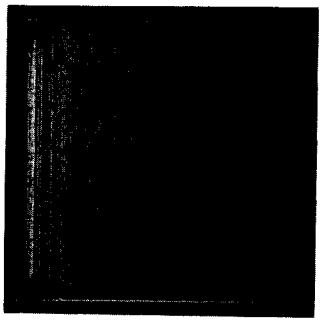

Figure 4-88.
Raw flat-field image for gain state 2, green filter, summation mode, and 100-msec exposure.
DN range = 14 - 18

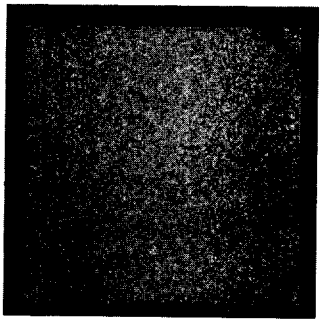

Figure 4-89.
Calibrated flat-field image for gain state 2, green filter, summation mode, and 100-msec exposure.
range = 257 - 305 ftL-msec

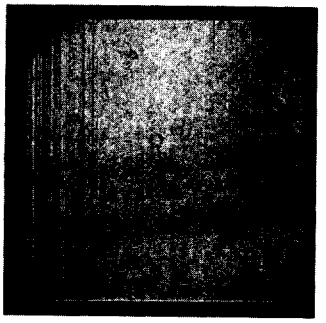

Figure 4-90.
Raw flat-field image for gain state 2, green filter, summation mode, and 400-msec exposure.
DN range = 50 - 54

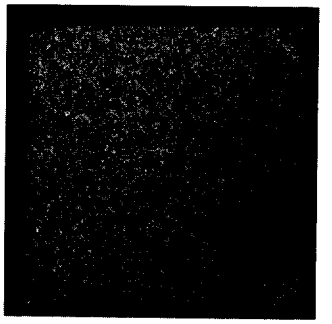

Figure 4-91.
Calibrated flat-field image for gain state 2, green filter, summation mode, and 400-msec exposure.
range = 1118 - 1176 ftL-msec

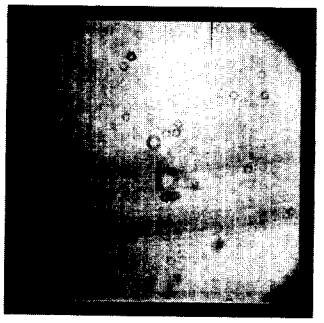

Figure 4-92.
Raw flat-field image for gain state 2, green filter, summation mode, and 1600-msec exposure.
DN range = 191 - 201

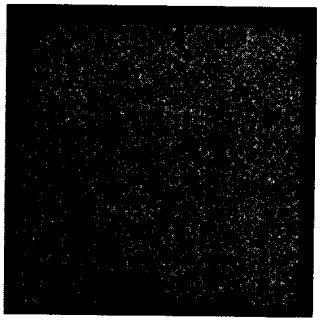

Figure 4-93.
Calibrated flat-field image for gain state 2, green filter, summation mode, and 1600-msec exposure.
range = 4520 - 4657 ftL-msec

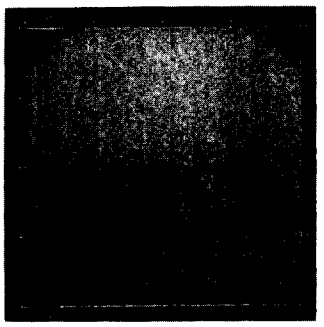

Figure 4-94.
Raw flat-field image for gain state 1, green filter, summation mode, and 50-msec exposure.
DN range = 15 - 18

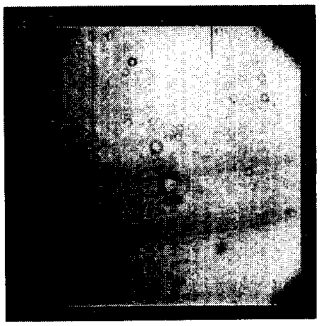

Figure 4-96.
Raw flat-field image for gain state 1, green filter, summation mode, and 200-msec exposure.
DN range = 57 - 61

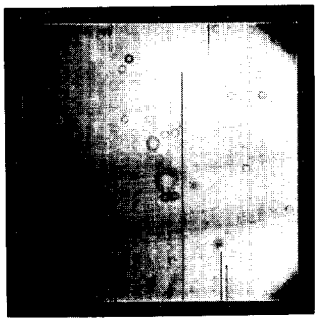

Figure 4-98.
Raw flat-field image for gain state 1, green filter, summation mode, and 800-msec exposure.
DN range = 221 - 233

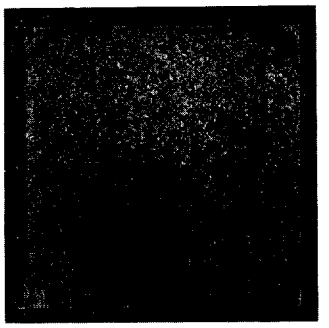

Figure 4-95.
Calibrated flat-field image for gain state 1, green filter, summation mode, and 50-msec exposure.
range = 1502 - 1695 ftL-msec

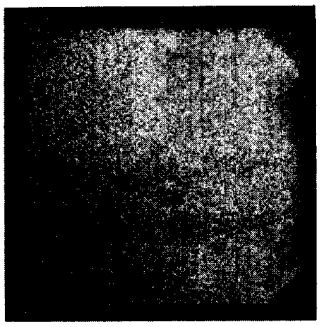

Figure 4-97.
Calibrated flat-field image for gain state 1, green filter, summation mode, and 200-msec exposure.
range = 6455 - 6668 ftL-msec

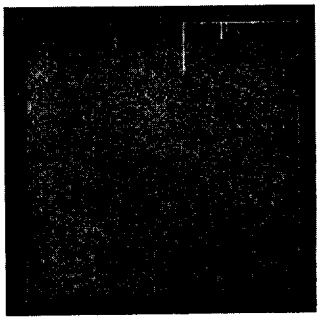

Figure 4-99.
Calibrated flat-field image for gain state 1, green filter, summation mode, and 800-msec exposure.
range = 26035 - 26471 ftL-msec

Table 4-11. Summation-mode nonlinearity in columns 1 - 100.

gain state	mean DN - DN_O level	maximum DN error	approx. r.m.s. DN error
4	4	4.5	0.8
4	177	3.4	1.2
3	49	1.1	0.3
3	201	1.1	0.4
2	48	0.3	0.1
2	194	0.6	0.2
1	50	0.3	0.1
1	202	0.3	0.1

piecewise-linear function was derived using only pairs of adjacent points, calibration using the linear function results in noticeably less random noise in the output image (between 0.6 and 0.9 of that in the piecewise-linear outputs). Therefore, the plan is to use a linear calibration function for summation-mode data despite the residual striations that might remain in high-gain images. Piecewise-linear functions will also be derived and will be available for use if desired in special circumstances.

Calibrated flat-field images with low signal levels in the highest gain state (see Figure 4-71) show selected columns that are less well-calibrated than the average (columns around 170, 198 and 610, for example). These apparent nonlinearities do not appear for signal levels above 2500e-. Since, except for column 170, these columns are not classified as blemishes, the maximum departures from linear response must be less than 6 DN and in most cases are only about 1 DN.

The GALGEN slope files for light transfer data sets acquired in different gain states through the same filter at the same light cannon setting were ratioed to determine gain ratios. The results are displayed in Figures 4-108 through 4-113 and tabulated in Table 4-12. The standard deviations are derived over the array of pixels. The variations are primarily due to random errors in the slope determinations resulting from the noise inherent in the original calibration images. These slope errors range from about 0.5% to 1% as the gain increases in the full-resolution mode and from about 0.5% to about 2% as the gain increases in the summation mode. The gain ratio in the summation mode also exhibits some spatial variability in the striation columns, particularly in the higher gain states.

The slope files for gain state 2 were also ratioed for each filter to that of the red filter. The results are displayed in Figures 4-114 through 4-120.

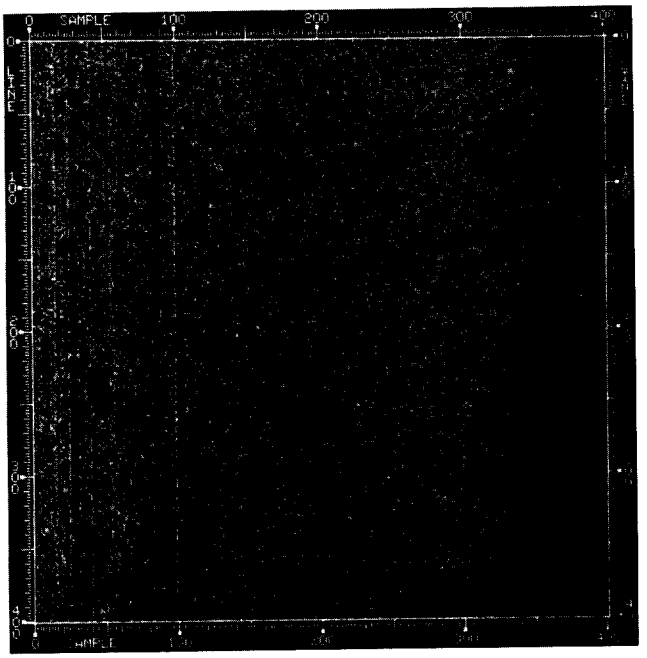

Figure 4-100.
Summation mode frame in gain state 4 calibrated using linear calibration function.

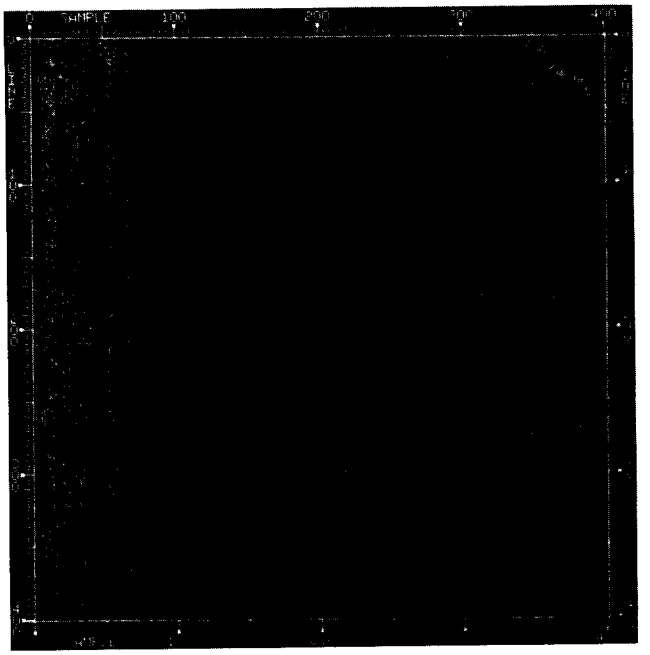

Figure 4-101.
Summation mode frame in gain state 4 calibrated using piecewise linear calibration function.

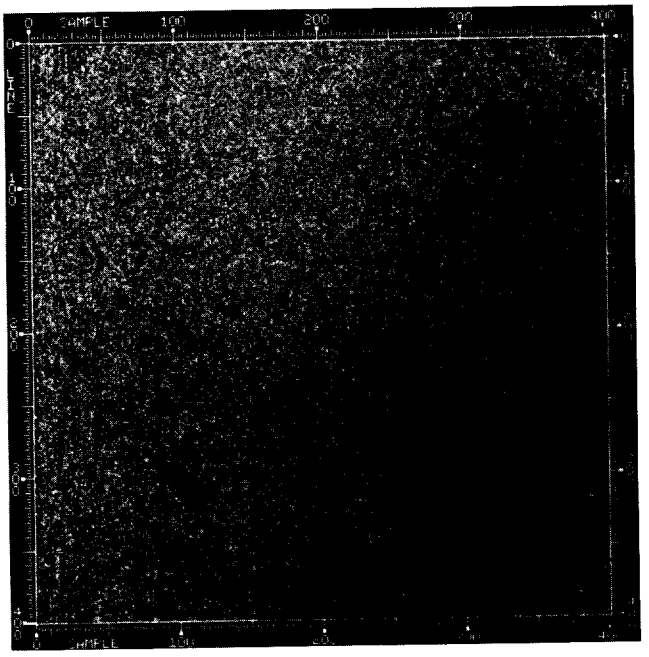

Figure 4-102.
Summation mode frame in gain state 3 calibrated using linear calibration function.

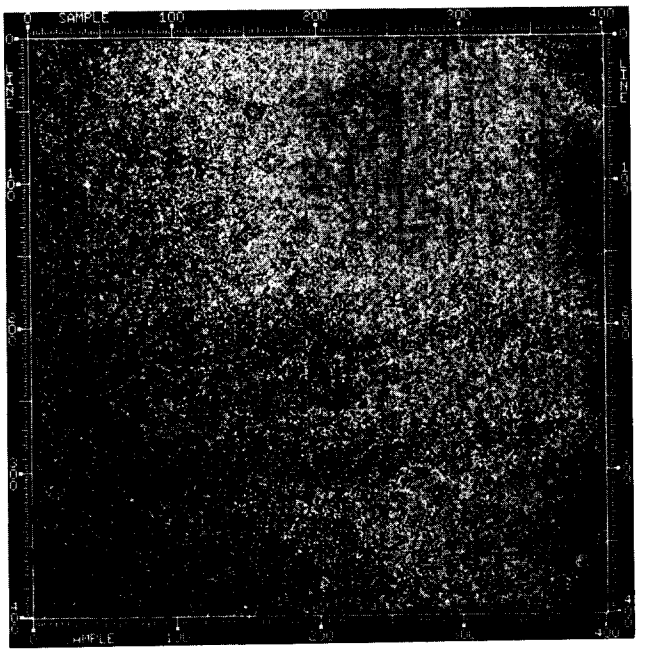

Figure 4-103.
Summation mode frame in gain state 3 calibrated using piecewise linear calibration function.

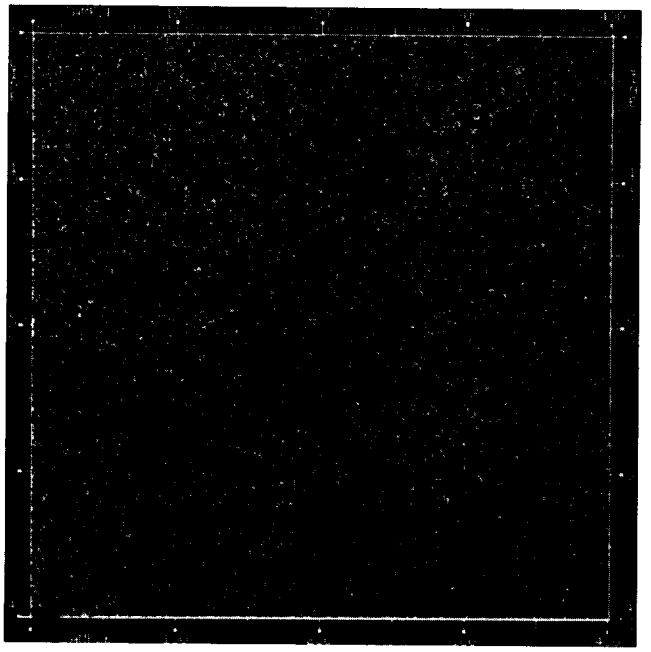

Figure 4-104.
Summation mode frame in gain calibrated using linear calibration function.

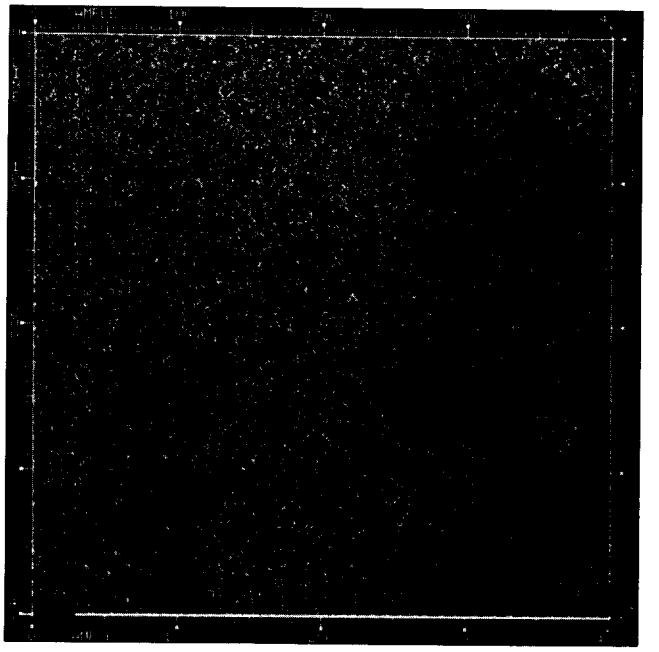

Figure 4-105.
Summation mode frame in gain state 2 state 2 calibrated using piecewise linear calibration function.

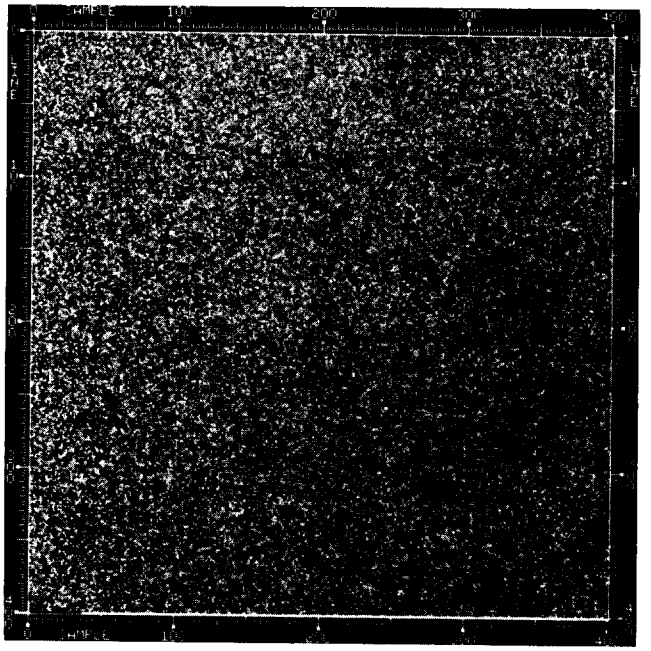

Figure 4-106.
Summation mode frame in gain calibrated using linear calibration function.

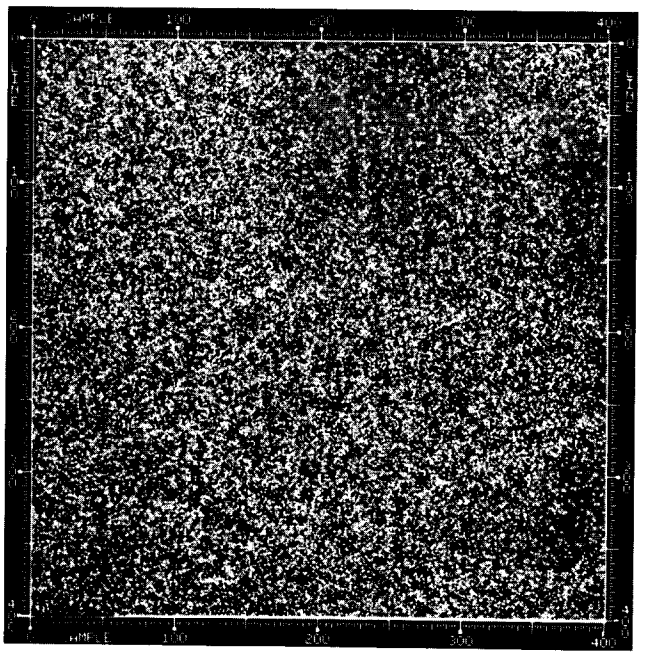

Figure 4-107.
Summation mode frame in gain state 1 state 1 calibrated using piecewise linear calibration function.

Table 4-12. Spatial variations in gain ratios.

gain ratio	filter	mean	standard deviation across array (%)
4:1	violet	4.806	1.5
10:1	violet	9.841	1.5
4:1 summation	green	4.900	0.61
10:1 summation	green	9.880	2.26
summation (gain 3)	green	0.1823	0.55
summation (gain 2)	green	0.1839	2.57

Table 4-13. Spatial variation in filter factors.

filter	filter factor with respect to red filter	standard deviation in filter factor across array
clear	0.1869	0.00165 (0.88 %)
green	2.526	0.0330 (1.31 %)
violet	111.7	1.95 (1.74 %)
7560 Å	3.832	0.0422 (1.10 %)
>9680 Å	12.03	0.126 (1.05 %)
7270 Å	7.603	0.0668 (0.88 %)
8890 Å	13.62	0.129 (0.94 %)

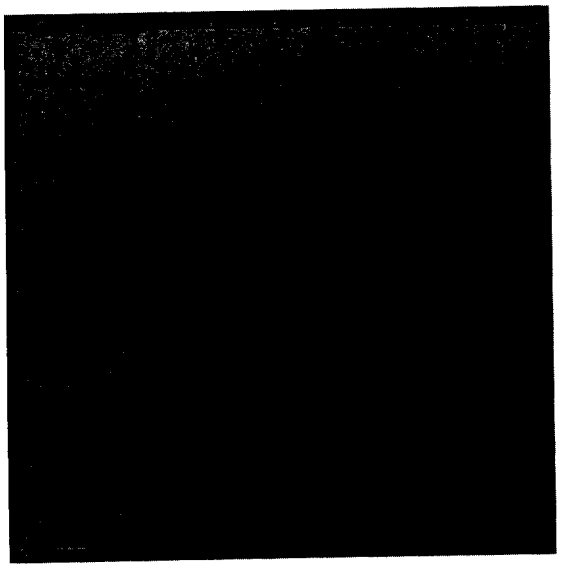

Figure 4-108.
Gain state 3/4 ratios from ratios of GALGEN slopes.

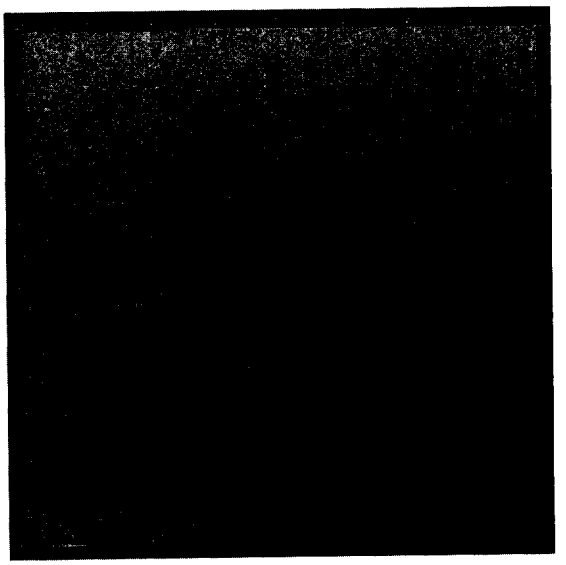

Figure 4-109.
Gain state 2/4 ratios from ratios of GALGEN slopes.

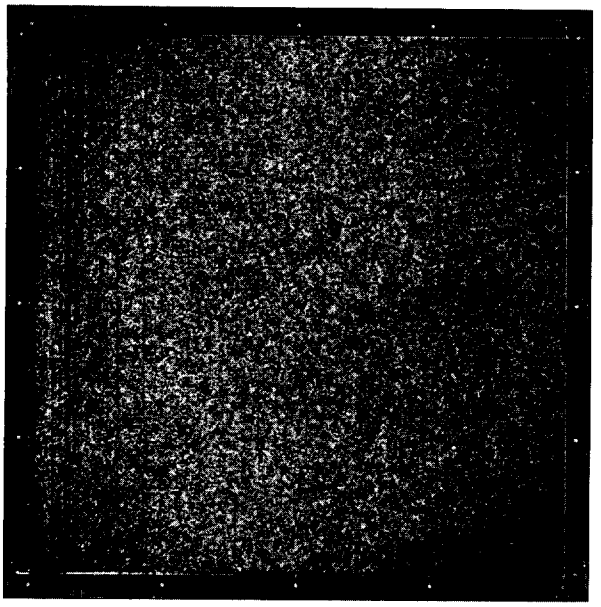

Figure 4-110.
Summation mode gain state
1/2 ratios from
ratios of GALGEN slopes.

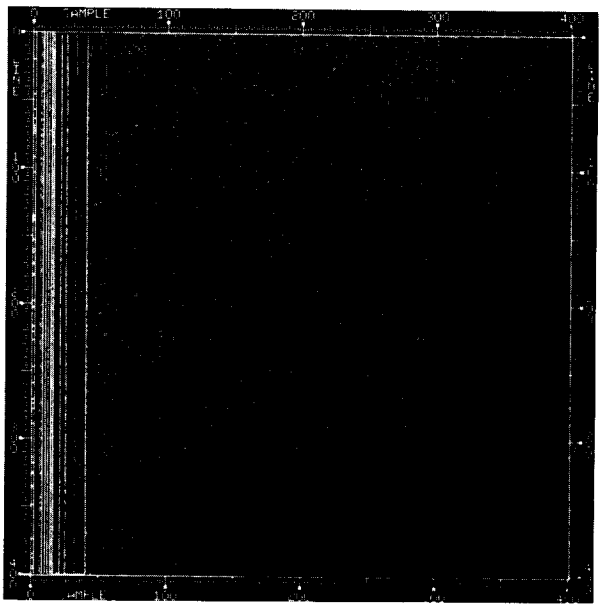

Figure 4-111.
Summation mode gain state
2/4 ratios from
ratios of GALGEN slopes.

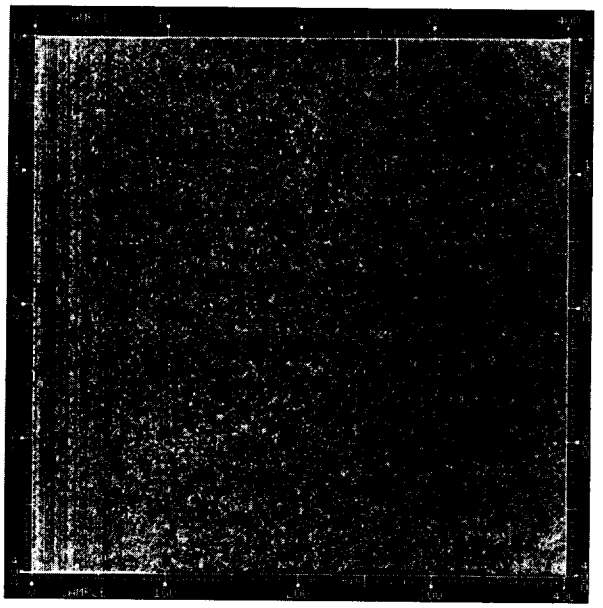

Figure 4-112.
Summation/normal gain
state 3 ratios from
ratios of GALGEN slopes.

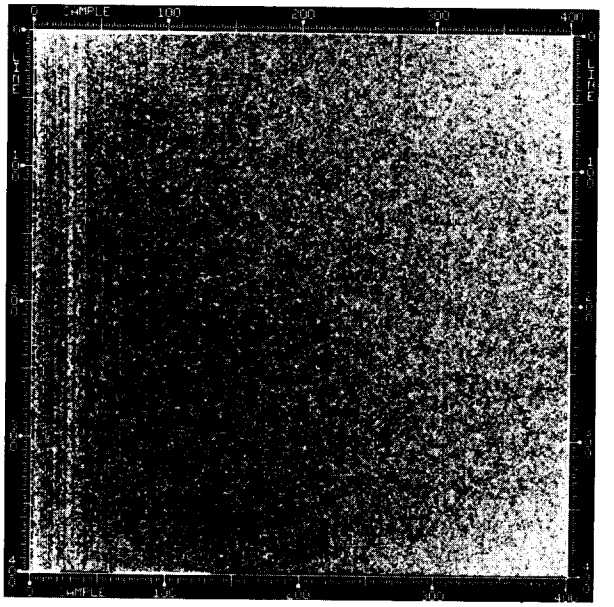

Figure 4-113.
Summation/normal gain
state 2 ratios from
ratios of GALGEN slopes.

The variability across the array is given in Table 4-13 along with the average filter factors with respect to red. The variations are due primarily to variations in the CCD quantum efficiency as a function of wavelength at different locations across the array.

Figures 4-121 through 4-134 display the array of maximum DN errors and r.m.s. DN errors produced by GALGEN for each combination of gain state and summation mode available. No significant differences with filter position were evident. The pixels having unacceptably nonlinear fits as defined by their residual errors are primarily concentrated in lines 1, 2, 799 and 800 and in columns 1 and 2 of the CCD array. Column 170 also exhibits unacceptably nonlinear behavior in gain state 4.

Figures 4-135 through 4-141 show the locations of all pixels defined as blemishes by BLEMGEN for each combination of gain state and summation mode. Again, no variation with filter position was observed. Most blemishes are due to excessive charge collection in pixels located along the edge of the CCD array. In gain state 4 in the full-resolution mode, column 170 is classified as a blemish because of its nonlinear response, and in gain states 1 and 2, several columns exhibit low-full-well response. Although GALGEN can detect and characterize low-full-well pixels so that this information can be inserted in the blemish file by BLEMGEN, it is limited in how accurately it can do this characterization. The frames included in the light transfer data sets have quite large gaps between their mean DN levels, and most data sets do not include data above about 200 DN. In addition, the amount of signal contained in low-full-well pixels that are saturated is not a constant level but does increase somewhat with the mean signal level of the frame. Therefore, more accurate determinations of the threshold saturation levels of the low-full-well pixels were obtained by examining pixel listings of various flat-field frames in the area of each low-full-well pixel at signal levels near and slightly above those pixels' saturation points. Table 4-14 lists the low-full-well pixel locations and the maximum charge level they will reliably transfer. The blemish files have been edited to incorporate these more accurate saturation thresholds. Figures 4-142 through 4-145 show a set of flat-field images acquired just below and above the mean full-well level for the CCD. The locations of the low-full-well pixels are obvious. Saturation of large numbers of pixels occurs starting at about 235 DN in gain state 2 near the bottom center of the array. No saturation is observed in any of the other gain states at less than 255 DN.

Figure 4-98 shows an example of a summation-mode flat-field image taken immediately after a near-full-well summation-mode image. Note that several columns having low-full-well pixels contain high levels of charge beginning at the top of the frame and extending part-way down the column.

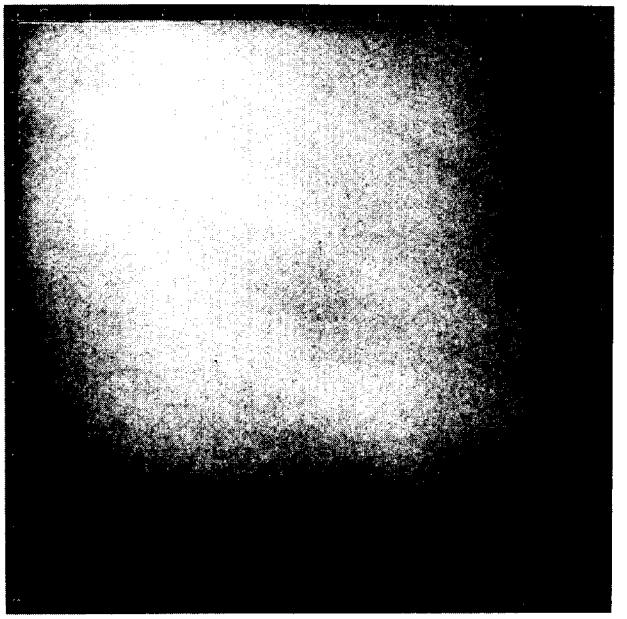

Figure 4-114.
GALGEN slope ratios of
the clear filter to the
red filter in gain state 2.

Figure 4-115.
GALGEN slope ratios of
the green filter to the
red filter in gain state 2.

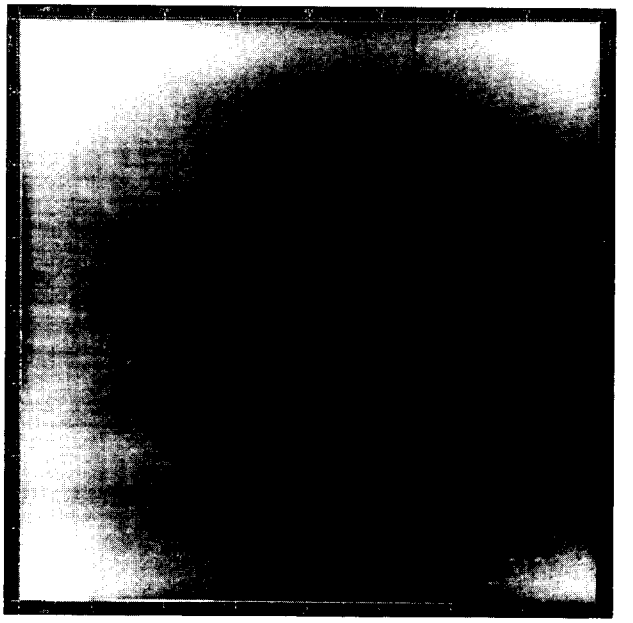

Figure 4-116.
GALGEN slope ratios of
the violet filter to the
red filter in gain state 2.

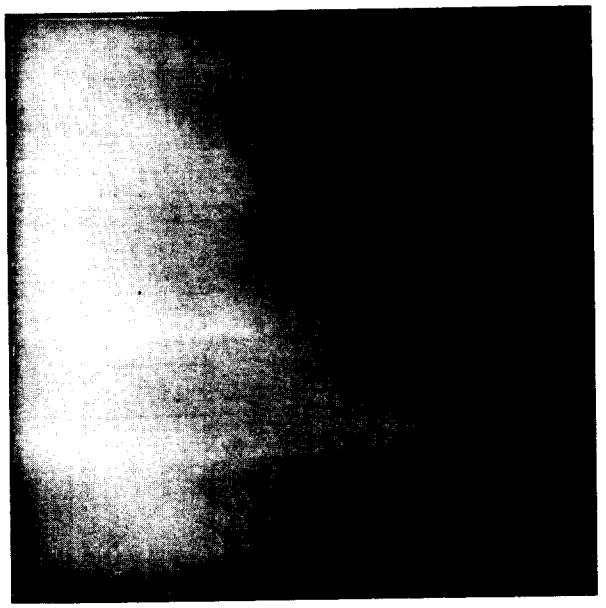

Figure 4-117.
GALGEN slope ratios of the 7560 Å filter to the red filter in gain state 2.

Figure 4-118.
GALGEN slope ratios of the >9680 Å filter to the red filter in gain state 2.

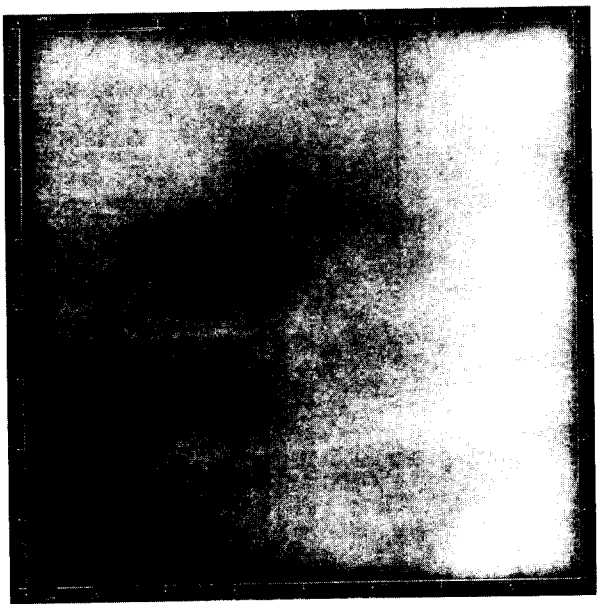

Figure 4-119.
GALGEN slope ratios of the 7270 Å filter to the red filter in gain state 2.

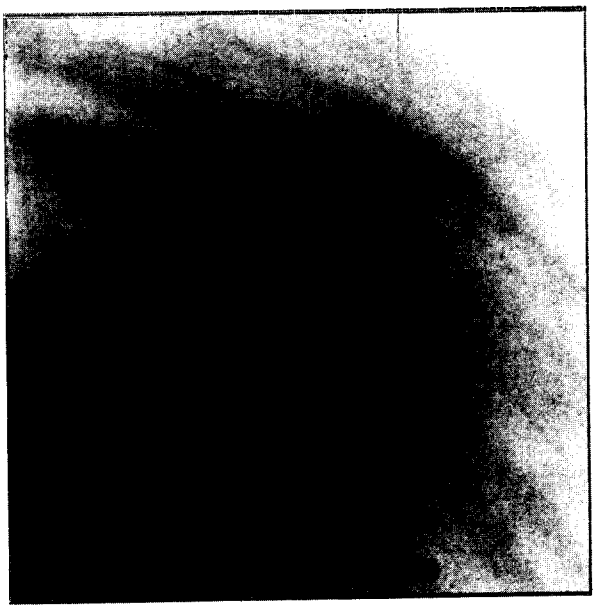

Figure 4-120.
GALGEN slope ratios of the 8890 Å filter to the red filter in gain state 2.

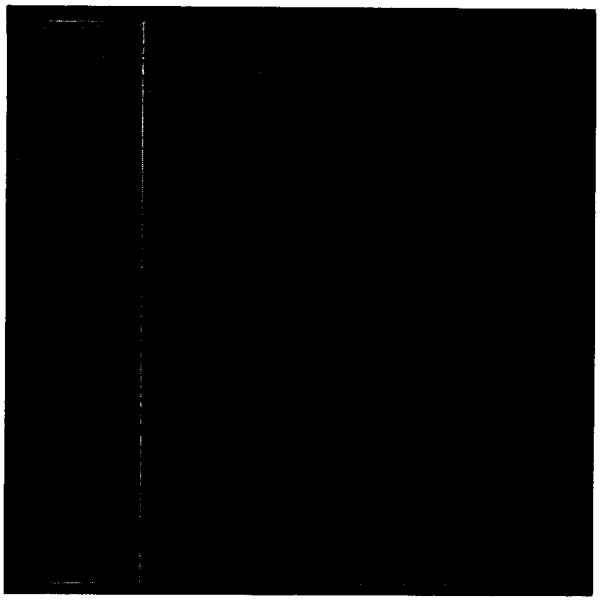

Figure 4-121.
Maximum DN errors produced by GALGEN for gain state 4, normal mode.

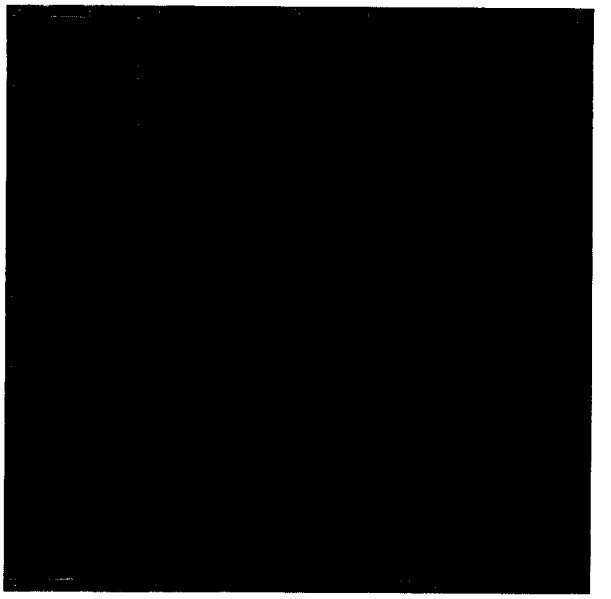

Figure 4-122.
r.m.s. DN errors produced by GALGEN for gain state 4, normal mode.

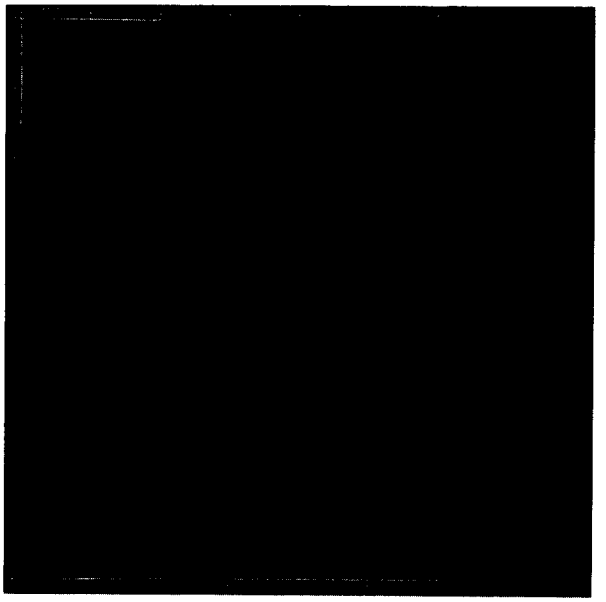

Figure 4-123.
Maximum DN errors produced by GALGEN for gain state 3, normal mode.

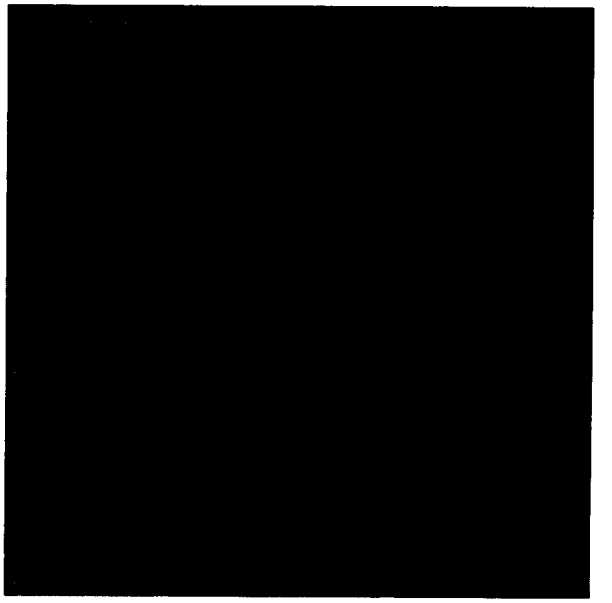

Figure 4-124.
r.m.s. DN errors produced by GALGEN for gain state 3, normal mode.

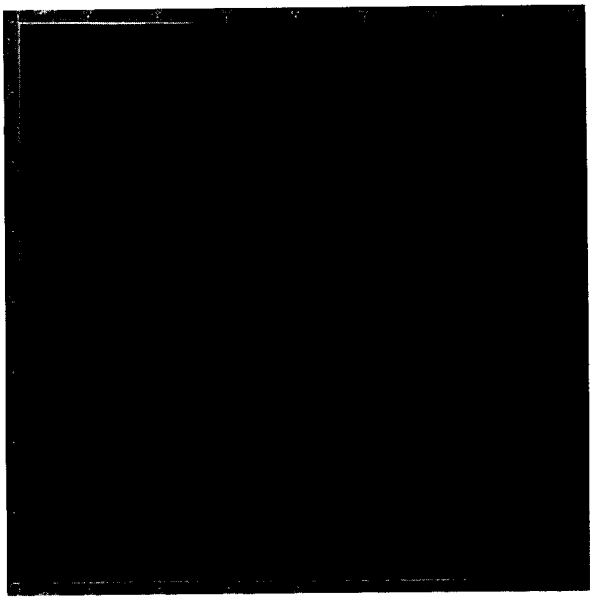

Figure 4-125.
Maximum DN errors produced
by GALGEN for gain state 2,
normal mode.

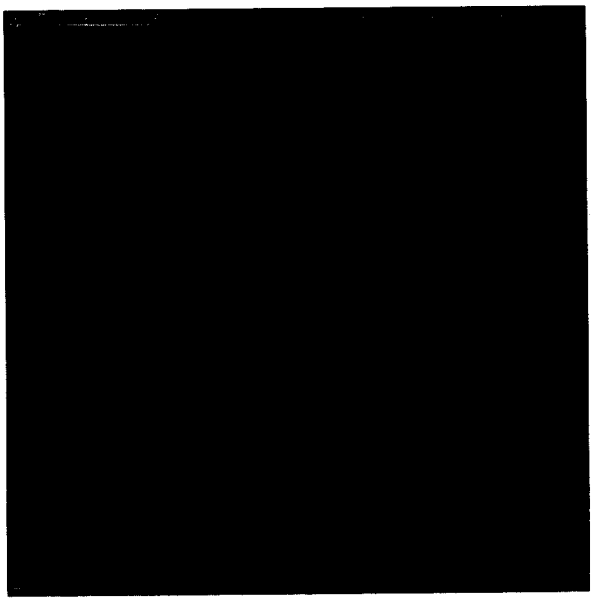

Figure 4-126.
r.m.s. DN errors produced
by GALGEN for gain state 2,
normal mode.

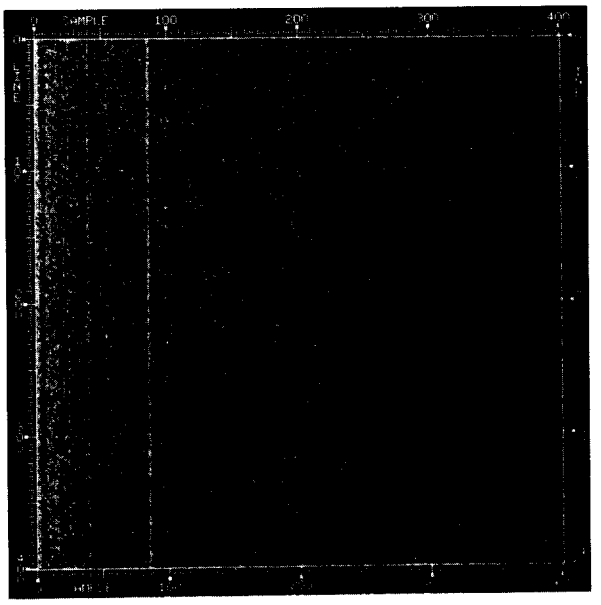

Figure 4-127.
Maximum DN errors produced
by GALGEN for gain state 4,
summation mode.

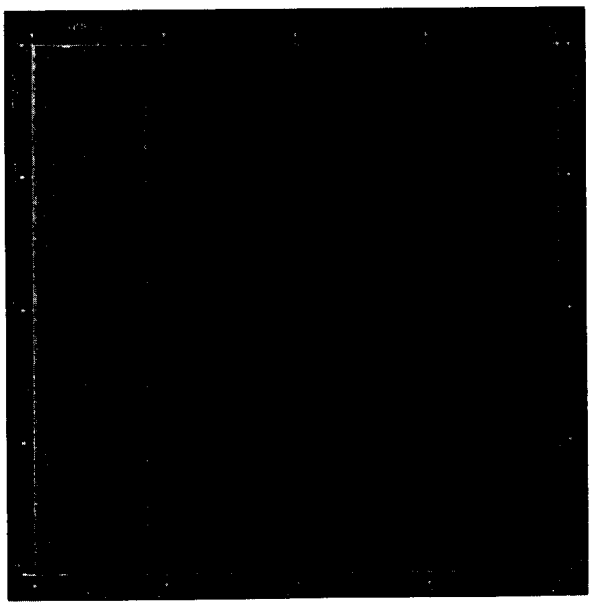

Figure 4-128.
r.m.s. DN errors produced
by GALGEN for gain state 4,
summation mode.

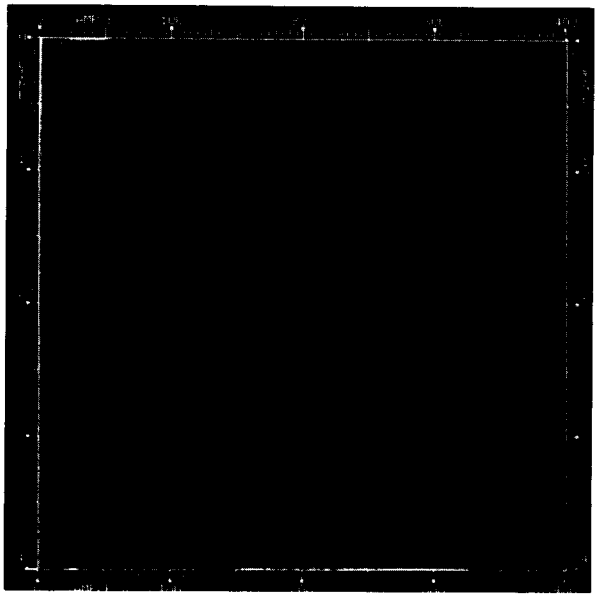

Figure 4-129.
Maximum DN errors produced by GALGEN for gain state 3, summation mode.

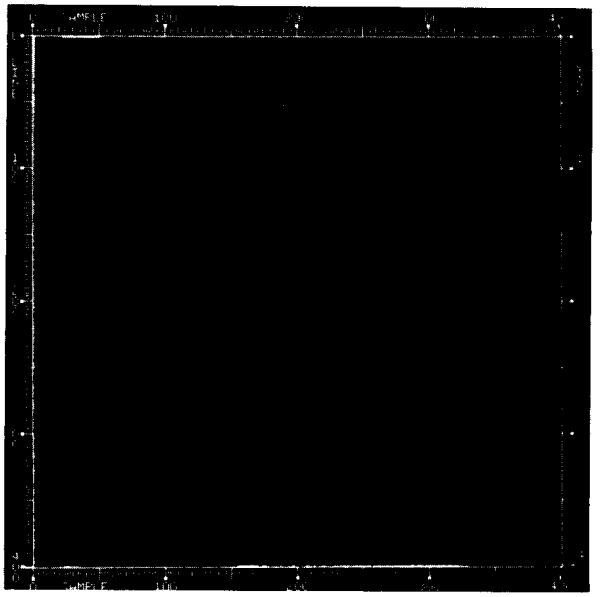

Figure 4-130.
r.m.s. DN errors produced by GALGEN for gain state 3, summation mode.

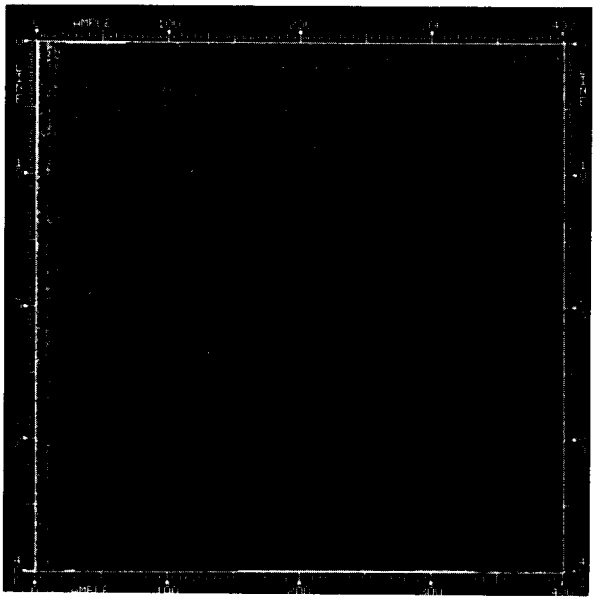

Figure 4-131.
Maximum DN errors produced by GALGEN for gain state 2, summation mode.

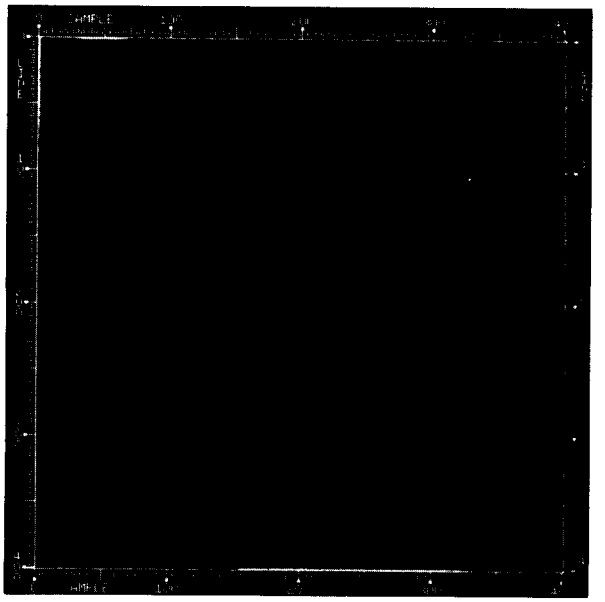

Figure 4-132.
r.m.s. DN errors produced by GALGEN for gain state 2, summation mode.

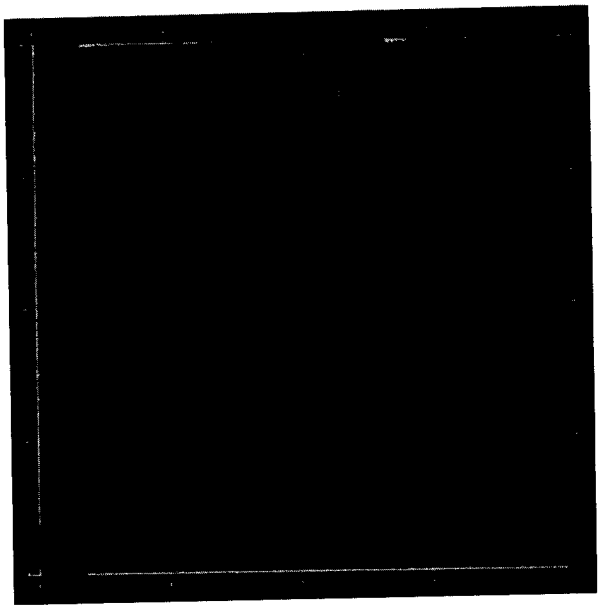

Figure 4-133.
Maximum DN errors produced by GALGEN for gain state 1, summation mode.

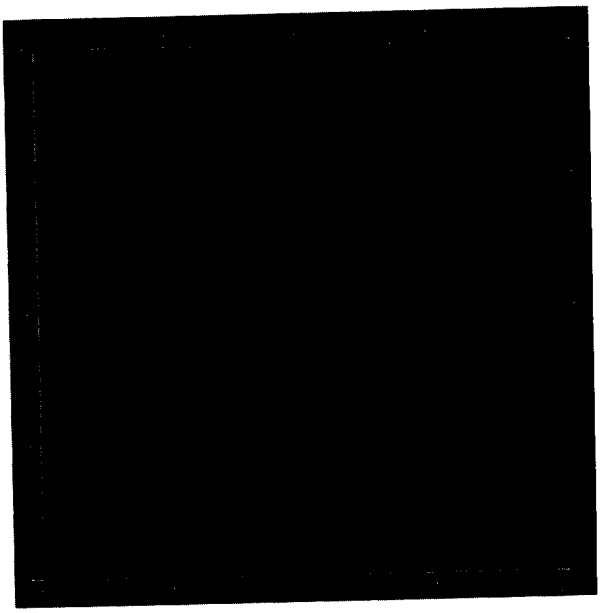

Figure 4-134.
r.m.s. DN errors produced by GALGEN for gain state 1, summation mode.

Table 4-14. Low-full-well pixel characteristics.

gain state 2				summation gain state 1			
column	row	e-	1985 DN	column	row	e- (#)	1985 DN
96	389	90000	219	48	195	90000	241
269	420	62000	153	135	211	62000	169
351	679	88000	215	176	340	88000	237
466	75	32000	80(*)	233	38	37000	101
520	668	78000	191	260	334	82000	220
578	659	64000	156	289	330	67000	180
594	696	70000	172	297	348	71000	192
673	743	83000	204	337	372	82000	220
790	754	80000	195	395	377	84000	226

(*) 161 DN in gain state 3
(#) e- per original unsummed pixel

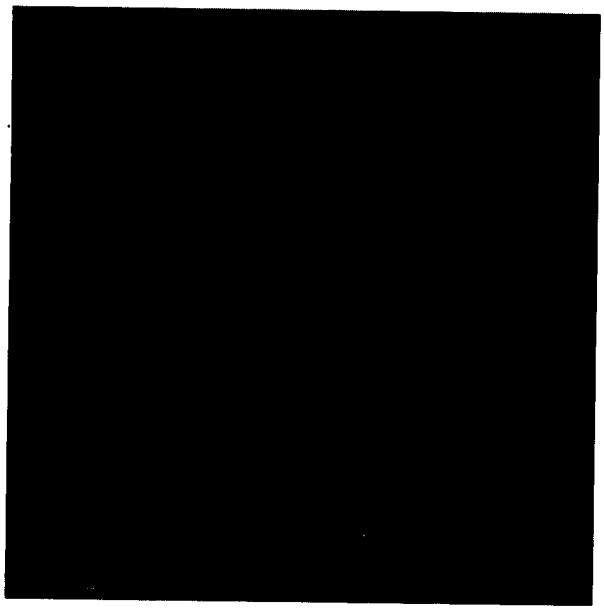

Figure 4-135.
Blemish location image for
gain state 4, clear filter.

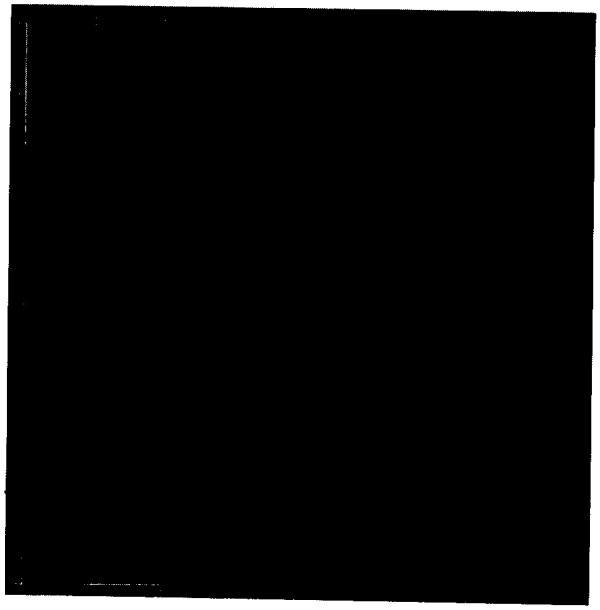

Figure 4-136.
Blemish location image for
gain state 3, clear filter.

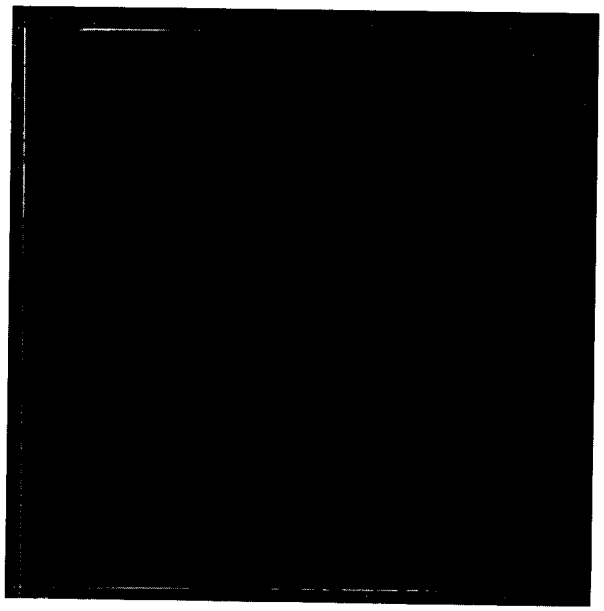

Figure 4-137.
Blemish location image for
gain state 2, clear filter.

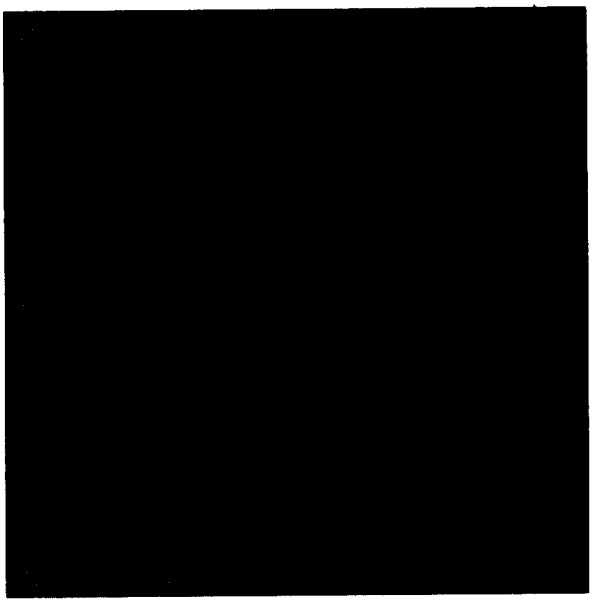

Figure 4-138.
Blemish location image for gain state 4, green filter, and summation mode.

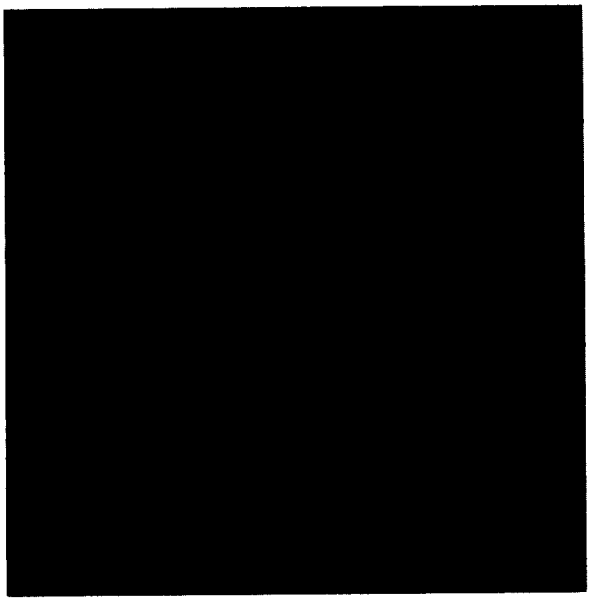

Figure 4-139.
Blemish location image for gain state 3, green filter, and summation mode.

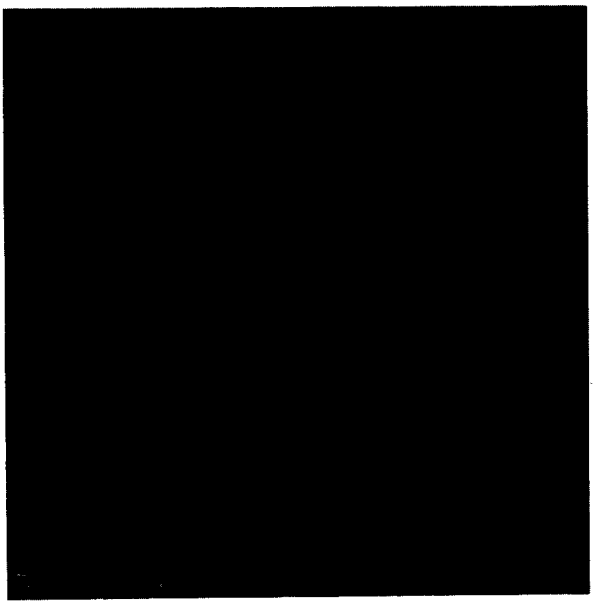

Figure 4-140.
Blemish location image for gain state 2, green filter, and summation mode.

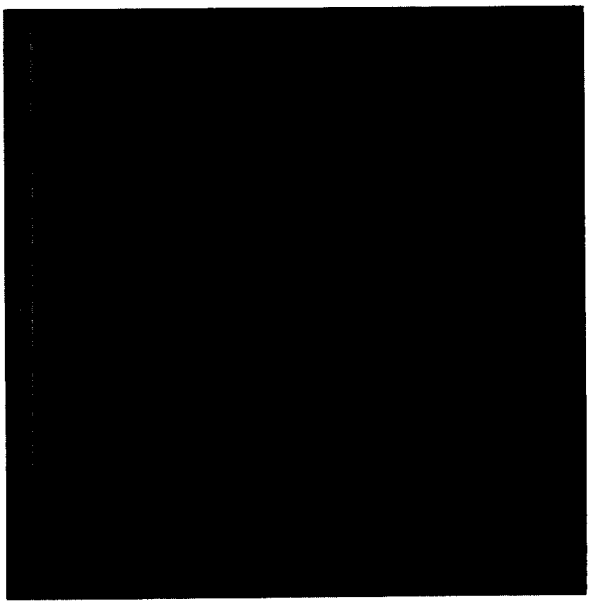

Figure 4-141.
Blemish location image for gain state 1, green filter, and summation mode.

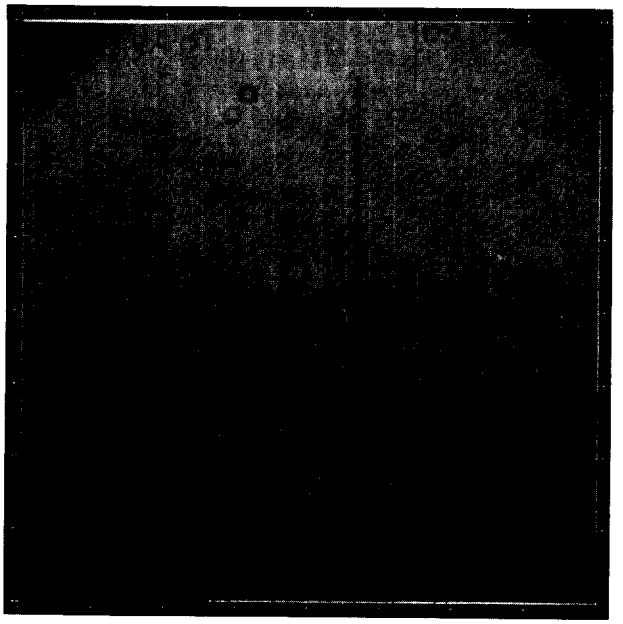

Figure 4-142.
Flat-field image acquired at a mean signal level of 225 DN in gain state 2.

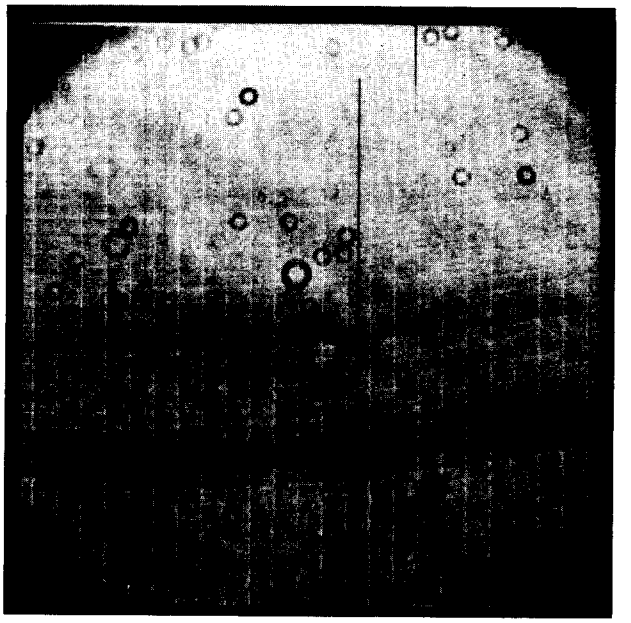

Figure 4-143.
Flat-field image acquired at a mean signal level of 235 DN in gain state 2.

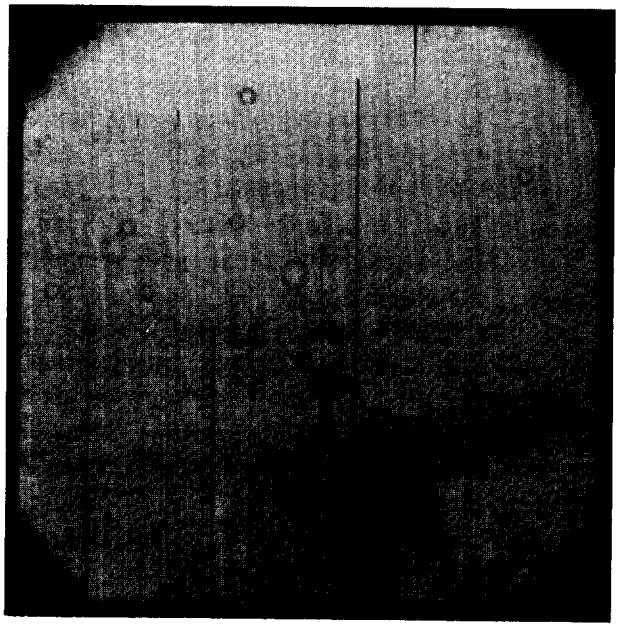

Figure 4-144.
Flat-field image acquired at a mean signal level of 245 DN in gain state 2.

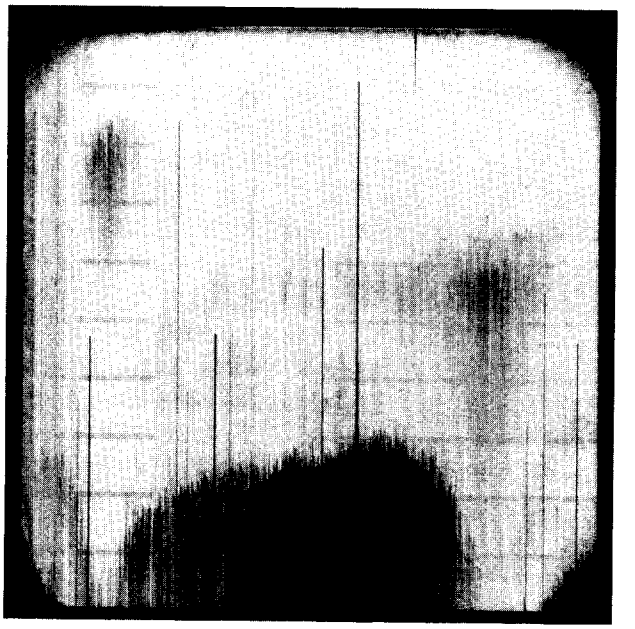

Figure 4-145.
Flat-field image acquired at a mean signal level of 250 DN in gain state 2.

This charge is leftover charge from the previous frame that could not be completely transferred out because of the low-full-well pixels. Since the summation mode has no CCD erasure between frames, this leftover charge is not read out until the next frame readout. Such occurrences of charge spillover were removed from the light transfer data sets prior to construction of GALGEN calibration files.

Clear-filter light transfer data sets were acquired in gain state 2 with the CCD clock voltages at the inverted level, with the blemish-protection mode on, and with the data compressor on in both information-preserving and non-information-preserving modes. Ratios of the GALGEN slope files in these cases to that of the normal SSI mode show no significant differences. Figures 4-146 and 4-147 show flat-field images at signal levels of about 210 DN in each data-compressed mode. In the information-preserving mode, lines are occasionally truncated because the DN differences from pixel to pixel are too large to be encoded in the available number of bits/line. Truncation occurs at signal levels as low as about 170 DN for flat fields. In the non-information-preserving mode, truncation of the least-significant bit in the most active 64-pixel block in each line will occur for flat-field signals above this level. This effect may be observed in Figure 4-146 for columns 1-64 as a pattern with slightly increased coarseness in the horizontal direction.

The calibration source brightness used for each light transfer data set is a required input to GALGEN since the outputs are in units of ftL-msec/DN for slope and ftL for offset. Table 4-15 lists the calibration source brightnesses input to GALGEN for each data set. These brightnesses were the best estimates of the true brightness at the time GALGEN was initially run. They represent the light cannon brightness at the center of its diffuser. In actuality, the source as seen by the SSI includes the effects of the thermal vacuum chamber window transmission and the light cannon brightness falloff away from the center of the diffuser. In addition, a best-fit adjustment of all SSI and light cannon variables to match the entire radiometric calibration data set results in slightly different calibration source brightness levels. Table 4-15 also lists the final best estimate of true calibration source brightness levels. The uncertainty in the actual calibration source brightness is the limiting factor in the accuracy of the SSI radiometric calibration and is estimated to be about ± 4% with respect to the NBS-traceable luminance standard used. The output files from GALGEN must be scaled to correct them to the better estimates of brightness levels. The sensitivity values given in Section IV-A-3f above already include the adjustments for the final best-estimate calibration source brightness levels.

Table 4-15. Calibration source brightness levels (ftL) at 8° C.

(a) assumed for initial GALGEN runs

filter	gain/mode 2	3	4	1/sum	2/sum	3/sum	4/sum
clear	3.54	0.802	0.802	3.54			
green	32.9	14.3	3.54	32.9	2.87	2.87	0.802
red	14.3	14.3	2.87	12.3			
violet	32.9	32.9	32.9	302.0*			
7560 Å	32.9	12.3	3.54	32.9			
> 9680 Å	32.9	14.3	3.54	67.1			
7270 Å	12.3	32.9	14.3	67.1			
8890 Å	32.9	12.3	14.3	67.1			

(b) best estimates as seen by SSI

filter	gain/mode 2	3	4	1/sum	2/sum	3/sum	4/sum
clear	2.470	0.563	0.563	2.470			
green	22.48	9.972	2.470	22.48	2.018	2.018	0.563
red	9.972	9.972	2.018	8.648			
violet	22.48	22.48	22.48	203.7*			
7560 Å	22.48	8.648	2.470	22.48			
> 9680 Å	22.48	9.972	2.470	44.18			
7270 Å	8.648	22.48	9.972	44.18			
8890 Å	22.48	8.648	9.972	44.18			

(*) for xenon light cannon

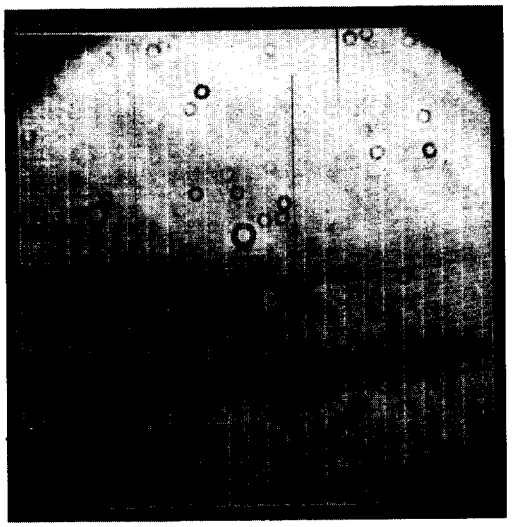

Figure 4-146.
Flat-field image at a signal level of about 210 DN in the rate-controlled data compression mode.

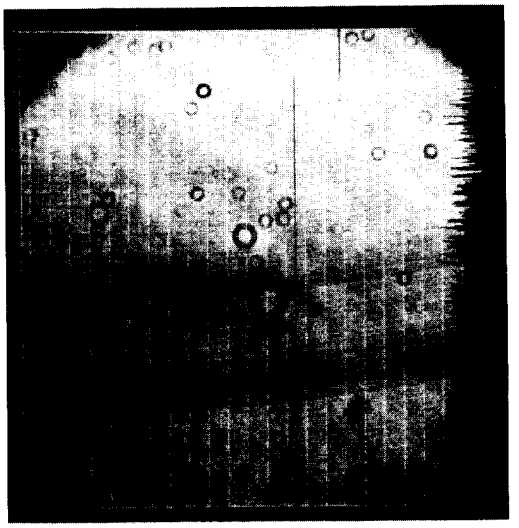

Figure 4-147.
Flat-field image at a signal level of about 210 DN in the information-preserving data compression mode.

As was noted in Sections IV-A-3d and f, the SSI spectral response varies with temperature. GALGEN files have been produced only for the expected flight temperature, +8° C. Light transfer data sets exist at -10° C and +18° C as well; should the SSI temperature in flight differ significantly from that expected, revised calibration files will have to be produced.

4. Spectral Response Math Model

The SSI response to the light cannon sources during calibration as computed using Equation (1) with the component-level data for the S, T, F and I spectral curves did not match the actual SSI response observed in the calibration images themselves and given in Table 4-8. Therefore, in order to create an SSI spectral response math model that more nearly matched the measured instrument performance, adjustments were made to the component level data. A weighted-least-squares fit to the calibration data was derived by changing slightly the CCD spectral QE curve (S) shape and scale, the optics spectral transmission curve (T) scale and central wavelength, the filter transmission curves (F) scales and central wavelengths, and the light source spectral radiance curves (I) shape and scale as well as adjusting the conversion factor from e^- to DN (C) slightly. Held constant at their component-level values were the widths of the filter bandpasses and the spectral transmission of the thermal vacuum chamber window. The calibration data that were matched consisted of the SSI

response to the tungsten light cannon through all 8 filters, the response to the xenon light cannon through the violet filter, the response to the MTF target in the MVM collimator through all 8 filters, and the response to 43 selected squares of the color target in the MVM collimator through 5 filters. Although the MTF and color targets have fairly large uncertainties in their spectral radiances since they were not as well calibrated as the light cannons, the use of the additional different color spectra they provide help to constrain the least-squares solution.

Table 4-16 gives the ratio of the SSI response to the light cannons as computed using Equation (1) to that actually observed in the calibration data for both the original component-level spectral curves and for the adjusted curves resulting from the least-squares fit. With the adjustments, the SSI spectral response math model yields results that match the calibration results to within 1%. Figures 4-148 through 4-154 compare the component-level spectral curves for the CCD QE, optics transmission, filter transmission, the light source radiances, and the overall system spectral response to the adjusted curves from the least-squares fit. The adjusted values for the overall system response are also provided in tabular form in Table 4-17. The CCD QE had to be increased significantly (about 25%) to provide a fit to the calibration data; however, it is not unrealistic that the component-level calibration of the absolute QE could have been in error by this amount. Several of the filter transmission curves had to be changed noticeably - transmission increased by 8% to 17% for the violet, 8890 Å, and >9680 Å filters and decreased 6% to 10% for the clear, green, red, and 7270 Å filters. Bandpass shifts also were implied -- 6 to 14 nm shortward for the clear, violet, and >9680 Å filters and 7 to 11 nm longward for the red and 7270 Å filters. The tungsten cannon and MVM collimator radiances appeared to be lower than expected in the near-IR. And finally, the high-gain conversion factor from e^- to DN dropped about 4%.

Table 4-16. Computed/Actual Response to Light Cannons.

filter	component model	new spectral response model
clear	0.86	1.006
violet	0.79	0.994
green	0.80	0.999
red	0.76	1.001
7270 Å	0.92	0.988
7560 Å	0.79	1.005
8890 Å	0.74	0.996
>9680 Å	0.69	1.010
violet (xenon)	0.78	0.992

The SSI spectral response math model that resulted from this study certainly does not represent a unique solution to the problem of fitting the calibration results. However, it is felt to be a significant improvement over the model that results from simply using the component calibration data unchanged. Therefore, the revised model was used for calculating the conversion factors from source ftL to units of radiance and reflectivity. Until an improved model can be derived, it also will be used for calculating the predicted SSI response to targets imaged in flight.

5. Zero-Exposure Offset

Knowledge of the zero-exposure DN level in each SSI imaging mode is critical for achieving an accurate radiometric calibration. Besides the zero-exposure frames taken as part of the various light transfer data sets, additional zero-exposure frames were acquired for the many SSI modes (93 out of a total of 104 possible combinations of frame time, gain state, normal or extended exposure mode, CCD clock voltage level, and use of blemish protection) in which light transfer data were not acquired. These frames were normally obtained at three SSI temperatures each year -- 1983, 1984

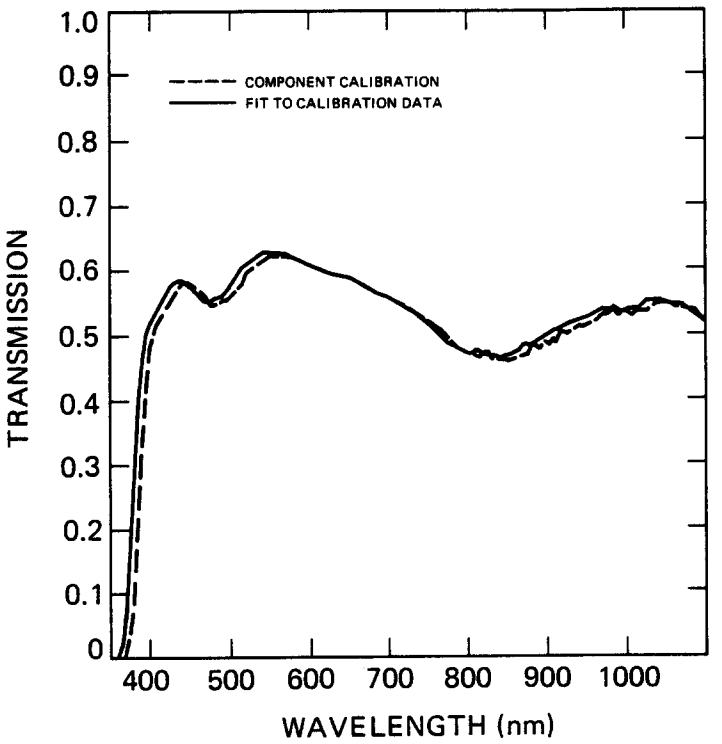

Figure 4-148. SSI optics transmission component-level data before and after adjustment for best fit to 1985 instrument calibration data.

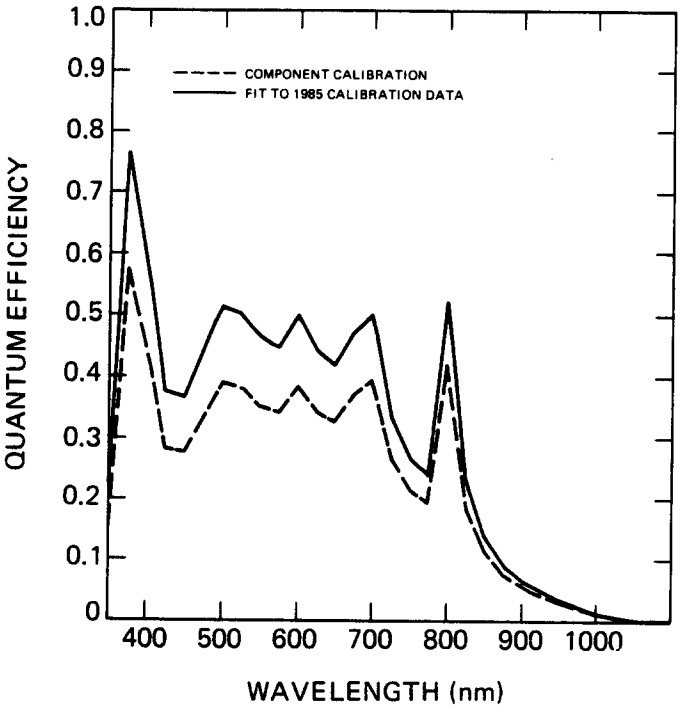

Figure 4-149. CCD quantum efficiency component-level data before and after adjustment for best fit to 1985 instrument calibration data.

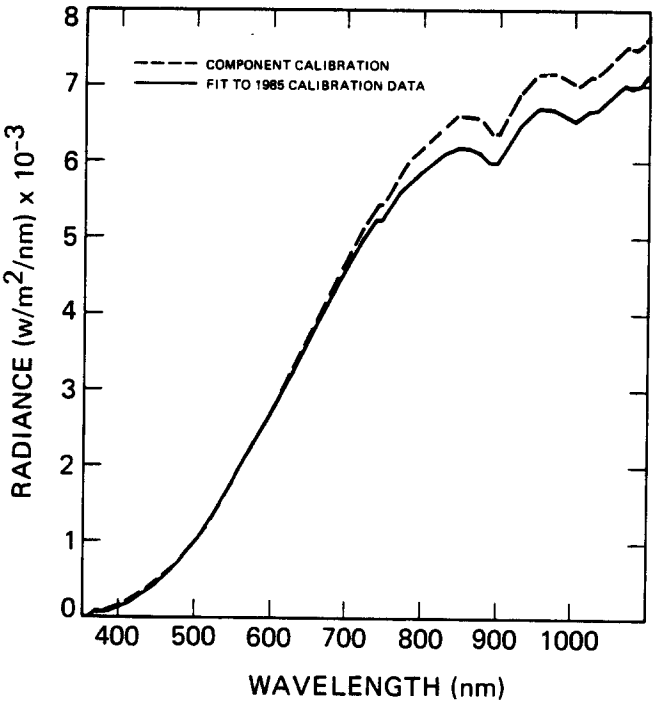

Figure 4-150. Tungsten light cannon spectral radiance component-level data before and after adjustment for best fit to 1985 instrument calibration data.

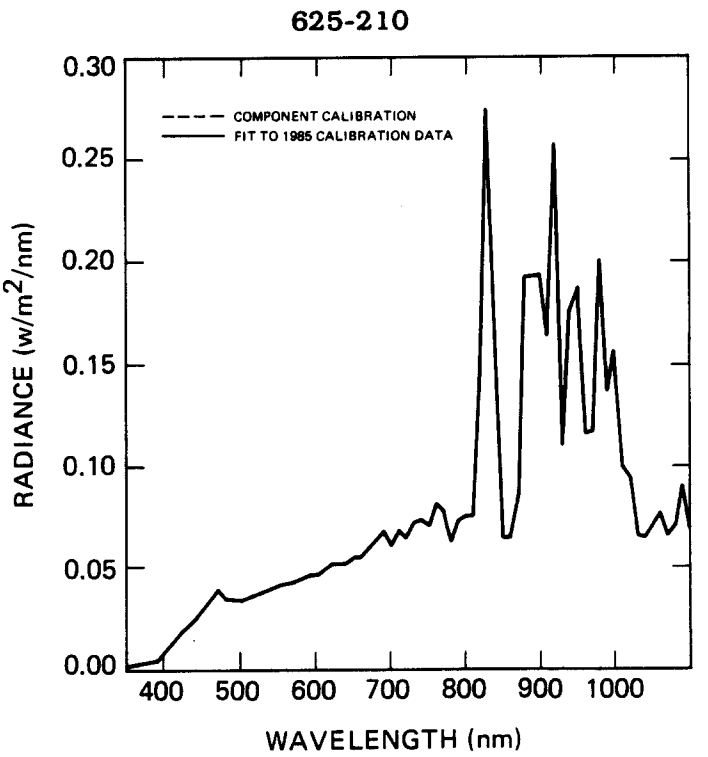

Figure 4-151. Xenon light cannon spectral radiance component-level data before and after adjustment for best fit to 1985 instrument calibration data.

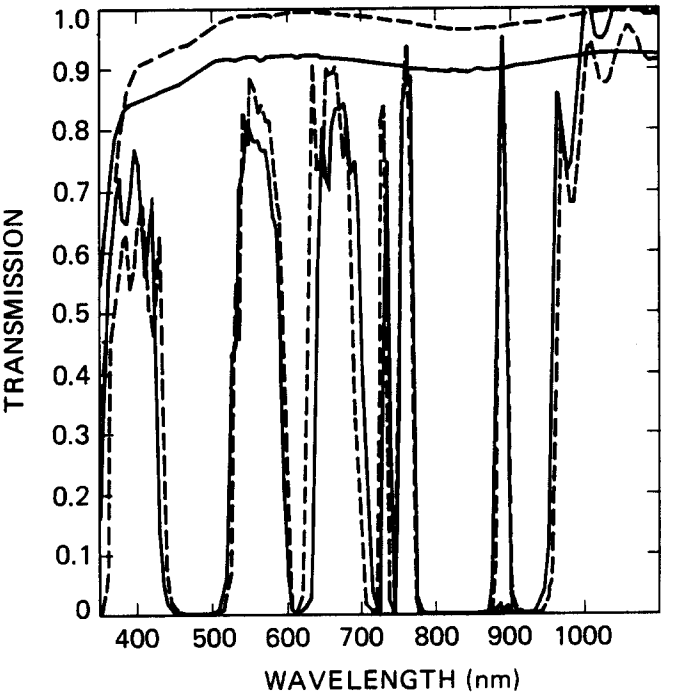

Figure 4-152. SSI filter transmission component-level data before and after adjustment for best fit to 1985 instrument calibration data.

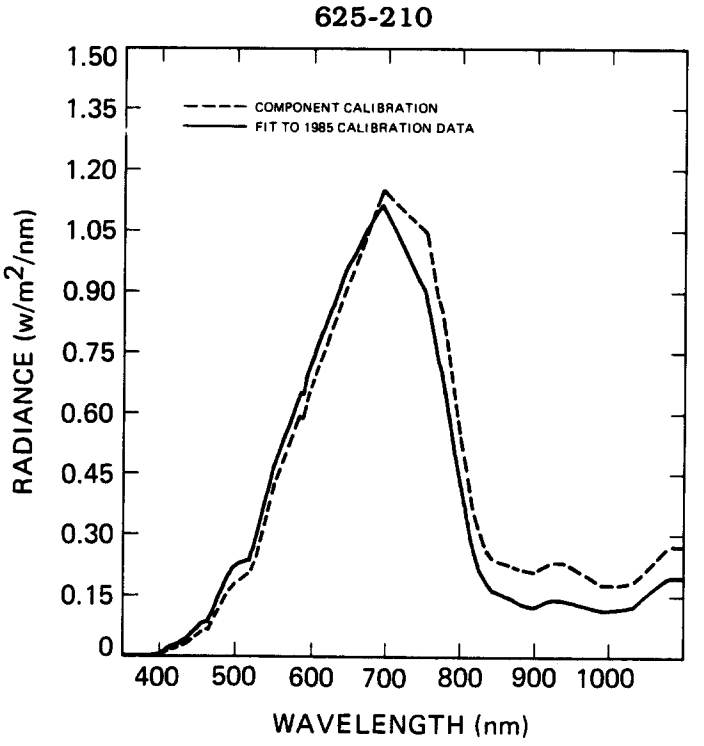

Figure 4-153. MVM collimator spectral radiance component-level data before and after adjustment for best fit to 1985 instrument calibration data.

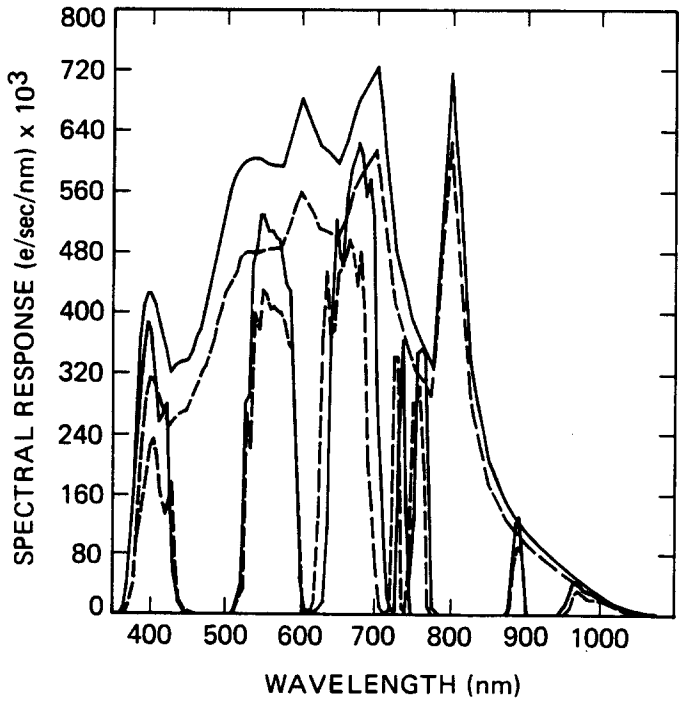

Figure 4-154. SSI spectral response from component-level data before and after adjustment for best fit to 1985 instrument calibration data.

Table 4-17. SSI subsystem spectral response, adjusted for best fit to 1985 instrument calibration data (e-/sec/nm x 10^3).

λ	filter								
(nm)	none	clear	violet	green	>9680Å	red	7270Å	7560Å	8890Å
350	.0000	.0000	.0000	.0000	.0000	.0000	.0000	.0000	.0000
355	.0000	.0000	.0000	.0000	.0000	.0000	.0000	.0000	.0000
360	.0000	.0000	.0000	.0000	.0000	.0000	.0000	.0000	.0000
365	19.00	14.16	11.75	.0000	.0000	.0000	.0000	.0000	.0000
370	63.65	49.99	43.93	.0000	.0000	.0000	.0000	.0000	.0000
375	188.4	153.1	135.7	.0000	.0000	.0000	.0000	.0000	.0000
380	331.5	274.2	217.0	.0166	.0000	.0000	.0000	.0000	.0000
385	432.4	362.6	280.1	.0259	.0000	.0000	.0000	.0000	.0000
390	486.8	410.9	344.5	.0584	.0000	.0000	.0000	.0000	.0000
395	503.8	426.3	387.9	.0302	.0000	.0000	.0000	.0000	.0000
400	500.8	425.0	374.9	.0200	.0000	.0000	.0000	.0000	.0000
405	479.6	408.1	306.9	.0240	.0000	.0000	.0000	.0000	.0000
410	456.0	389.5	254.5	.0638	.0000	.0000	.0000	.0000	.0000
415	432.0	370.4	262.6	.3413	.0000	.0000	.0000	.0000	.0000
420	403.9	346.9	279.8	.0889	.0000	.0000	.0000	.0000	.0000
425	373.2	321.6	156.2	.0037	.0000	.0000	.0000	.0000	.0000
430	379.9	328.8	55.67	.0000	.0000	.0000	.0000	.0000	.0000
435	384.2	333.4	18.95	.0000	.0000	.0000	.0000	.0000	.0000
440	386.3	335.9	7.513	.0000	.0000	.0000	.0000	.0000	.0000
445	385.7	335.9	3.182	.0000	.0000	.0000	.0000	.0000	.0000
450	384.5	336.0	1.342	.0000	.0000	.0000	.0000	.0000	.0000
455	401.1	352.0	.4051	.0000	.0000	.0000	.0000	.0000	.0000
460	417.5	368.0	.1294	.0000	.0000	.0000	.0000	.0000	.0000
465	429.1	379.8	.1330	.0000	.0000	.0000	.0000	.0000	.0000
470	446.9	397.5	.1385	.0000	.0000	.0000	.0000	.0000	.0000
475	469.0	419.0	.1454	.0000	.0000	.0000	.0000	.0000	.0000
480	494.0	443.5	.1531	.0000	.0000	.0000	.0000	.0000	.0000
485	516.1	464.7	.1600	.0000	.0000	.0000	.0000	.0000	.0000
490	540.1	488.4	.1080	.0000	.0000	.0000	.0000	.0000	.0000
495	569.0	516.8	.0626	.0000	.0000	.0000	.0000	.0000	.0000
500	599.1	546.0	.0419	.0000	.0000	.0000	.0000	.0000	.0000
505	609.9	557.2	.0244	.0000	.0000	.0000	.0000	.0000	.0000
510	627.1	574.1	.0188	6.346	.0000	.0000	.0000	.0000	.0000
515	639.8	586.9	.0128	23.81	.0000	.0000	.0000	.0000	.0000
520	648.5	594.8	.0065	41.51	.0000	.0000	.0000	.0000	.0000
525	655.8	600.9	.0066	282.5	.0000	.0000	.0000	.0000	.0000
530	655.9	600.4	.0066	292.1	.0000	.0000	.0000	.0000	.0000
535	656.7	602.7	.0197	462.9	.0000	.0000	.0000	.0000	.0000
540	657.4	604.9	.0329	484.3	.0000	.0000	.0000	.0000	.0000
545	654.3	602.8	.0720	530.5	.0000	.0000	.0000	.0000	.0000
550	648.3	596.6	.1426	527.9	.0000	.0000	.0000	.0000	.0000
555	648.0	596.9	.2268	507.2	.0000	.0000	.0000	.0000	.0000
560	648.8	595.4	.2725	508.5	.0000	.0000	.0000	.0000	.0000

Table 4-17 (continued).

λ (nm)	filter none	clear	violet	green	>9680Å	red	7270Å	7560Å	8890Å
565	649.4	594.0	.2078	499.3	.0000	.0000	.0000	.0000	.0000
570	647.7	594.7	.1036	496.0	.0000	.0000	.0000	.0000	.0000
575	645.5	595.4	.0387	469.8	.0000	.0000	.0000	.0000	.0000
580	663.5	612.3	.0133	437.6	.0000	.0000	.0000	.0000	.0000
585	681.2	628.9	.0068	423.9	.0000	.0000	.0000	.0000	.0000
590	699.0	645.5	.0070	301.3	.0000	.0000	.0000	.0000	.0000
595	718.7	664.2	.0072	154.7	.0000	.0000	.0000	.0000	.0000
600	738.3	684.0	.0074	49.06	.0000	.0000	.0000	.0000	.0000
605	725.4	671.2	.0072	6.841	.0000	.0000	.0000	.0000	.0000
610	711.8	656.1	.0071	.2776	.0000	.0000	.0000	.0000	.0000
615	696.7	642.4	.0070	.3205	.0000	.9196	.0000	.0000	.0000
620	683.3	631.3	.0068	.0752	.0000	5.050	.0000	.0000	.0000
625	670.0	619.4	.0067	.0000	.0000	7.900	.0000	.0000	.0000
630	664.9	613.8	.0066	.0000	.0000	19.46	.0000	.0000	.0000
635	660.8	611.4	.0066	.0000	.0000	117.3	.0000	.0000	.0000
640	656.3	606.2	.0066	.0000	.0000	368.9	.0000	.0000	.0000
645	652.5	600.2	.0065	.0000	.0000	522.1	.0000	.0000	.0000
650	647.3	595.2	.0065	.0000	.0000	471.8	.0000	.0000	.0000
655	665.8	612.9	.0200	.0000	.0000	464.3	.0000	.0000	.0000
660	684.9	630.1	.0479	.0000	.0000	554.5	.0000	.0000	.0000
665	703.1	645.7	.0914	.0000	.0000	589.0	.0000	.0000	.0000
670	721.7	662.5	.1804	.0000	.0000	604.0	.0000	.0000	.0072
675	740.4	679.6	.3258	.0000	.0000	625.4	.0000	.0000	.0074
680	749.6	688.0	.4797	.0000	.0000	607.0	.0075	.0000	.0075
685	758.4	695.7	.5764	.0000	.0000	553.2	.0076	.0000	.0076
690	770.1	706.2	.6161	.0000	.0000	577.2	.0077	.0000	.0077
695	781.6	716.2	.5940	.0000	.0000	524.7	.0078	.0000	.0078
700	792.3	725.2	.5229	.0000	.0000	311.5	.0079	.0000	.0158
705	740.5	677.2	.3925	.0000	.0000	182.7	.0148	.0000	.0222
710	686.7	627.3	.2953	.0000	.0000	87.85	.0275	.0000	.0137
715	635.8	579.9	.2162	.0000	.0636	23.14	.0445	.0000	.0064
720	585.7	533.1	.1523	.0000	.0000	4.387	.0469	.0000	.0117
725	533.0	484.8	.1119	.0000	.0000	1.642	6.189	.0000	.0160
730	510.8	464.6	.1379	.0000	.0000	1.302	243.2	.0000	.0102
735	489.3	444.7	.1321	.0000	.0000	1.272	365.0	.2789	.0049
740	466.6	424.0	.1027	.0000	.0000	.3173	132.4	2.217	.0000
745	444.1	402.9	.0799	.0000	.0000	.0311	3.921	21.29	.0000
750	421.6	382.0	.0674	.0000	.0000	.0084	.3921	135.9	.0000
755	412.2	373.8	.0618	.0000	.0000	.1566	.1443	348.0	.0000
760	399.1	359.6	.0718	.0000	.0000	.2036	.0160	351.4	.0000
765	389.6	351.6	.0740	.0312	.0000	.2260	.0117	345.7	.0000
770	377.4	340.0	.0528	.0076	.0000	.2340	.0076	192.8	.0000
775	366.7	329.9	.0440	.0000	.0000	.1980	.0037	9.995	.0000
780	453.9	409.3	.0590	.0454	.0000	.1816	.0000	2.120	.0000

Table 4-17 (continued).

λ (nm)	none	clear	violet	green	filter >9680Å	red	7270Å	7560Å	8890Å
785	539.5	486.1	.0809	.0108	.0000	.1834	.0000	1.408	.0000
790	625.8	563.3	.1064	.1314	.0000	.1815	.0000	.5758	.0000
795	711.3	638.5	.1351	.2703	.0000	.1992	.0000	.3343	.0000
800	797.3	717.0	.1754	.3110	.0000	.2631	.0080	.2631	.0000
805	710.5	637.2	.1776	.1989	.0000	.2984	.0071	.1847	.0000
810	634.0	569.6	.1775	.1648	.0000	.2790	.0127	.0888	.0000
815	552.2	493.8	.1767	.2374	.0000	.2209	.0110	.0884	.0000
820	458.0	411.5	.1741	.2473	.0000	.1786	.0092	.0779	.0000
825	370.3	332.3	.1703	.1592	.0000	.1481	.0074	.0592	.0000
830	341.2	305.9	.1808	.0512	.0000	.1501	.0034	.0546	.0000
835	312.9	279.3	.1940	.0688	.0000	.1690	.0000	.0532	.0000
840	281.7	251.3	.2169	.0620	.0000	.2282	.0028	.0507	.0000
845	252.9	225.5	.2403	.0632	.0000	.3744	.0051	.0455	.0025
850	225.3	202.1	.2456	.0676	.0000	.4078	.0068	.0383	.0022
855	212.0	190.7	.2502	.0678	.0000	.3859	.0042	.0360	.0042
860	198.6	178.8	.2443	.0596	.0000	.5144	.0040	.0358	.0139
865	184.9	165.6	.2292	.0407	.0000	.6507	.0018	.0351	.0203
870	173.6	156.1	.2101	.0469	.0174	.9514	.0017	.0330	.2222
875	159.3	143.3	.1832	.0573	.0159	1.142	.0016	.0303	8.489
880	149.7	135.0	.1571	.0629	.0150	.7663	.0015	.0254	62.86
885	143.2	129.3	.1289	.0659	.0143	.2634	.0014	.0229	121.2
890	135.0	121.9	.0999	.0675	.0270	1.026	.0040	.0202	129.0
895	128.1	115.7	.0730	.0653	.0512	1.972	.0077	.0166	60.49
900	119.4	108.0	.0501	.0621	.0597	.6841	.0060	.0131	3.952
905	115.6	104.7	.0347	.0590	.0809	.0821	.0023	.0104	1.312
910	110.4	100.1	.0232	.0541	.0994	.0254	.0011	.0077	.0850
915	103.6	93.97	.0156	.0477	.1244	.0166	.0010	.0062	.0352
920	98.24	89.07	.0118	.0373	.1768	.0265	.0010	.0039	.0128
925	92.87	84.26	.0111	.0260	.2600	.0251	.0019	.0028	.0093
930	88.23	80.13	.0097	.0203	.3794	.0124	.0097	.0018	.0079
935	82.73	75.21	.0083	.0157	.6701	.0066	.0132	.0008	.0066
940	78.00	70.99	.0078	.0125	1.576	.0078	.0055	.0000	.0047
945	73.18	66.67	.0058	.0124	3.125	.0095	.0015	.0000	.0044
950	68.04	62.09	.0054	.0150	7.559	.0075	.0007	.0000	.0041
955	63.70	58.12	.0051	.0198	21.52	.0057	.0006	.0000	.0032
960	59.59	54.44	.0048	.0244	40.98	.0101	.0000	.0000	.0030
965	54.79	50.12	.0044	.0301	47.16	.0186	.0006	.0000	.0022
970	50.21	46.02	.0050	.0271	39.86	.0226	.0005	.0000	.0020
975	44.88	41.18	.0045	.0229	33.06	.0202	.0004	.0000	.0014
980	40.78	37.45	.0041	.0200	30.63	.0130	.0004	.0000	.0008
985	37.04	34.01	.0037	.0185	30.26	.0082	.0000	.0000	.0007
990	32.55	29.92	.0033	.0160	29.25	.0052	.0000	.0000	.0006
995	28.03	25.82	.0028	.0129	27.12	.0039	.0000	.0000	.0006
1000	23.99	22.12	.0022	.0113	24.31	.0036	.0002	.0000	.0002

Table 4-17 (continued).

λ (nm)	filter none	clear	violet	green	>9680Å	red	7270Å	7560Å	8890Å
1005	21.40	19.76	.0019	.0116	21.68	.0034	.0002	.0000	.0002
1010	18.55	17.14	.0019	.0143	18.27	.0033	.0002	.0000	.0000
1015	15.79	14.60	.0017	.0155	15.11	.0032	.0000	.0000	.0000
1020	13.03	12.06	.0020	.0150	12.39	.0030	.0000	.0000	.0000
1025	10.31	9.544	.0019	.0135	9.834	.0027	.0001	.0000	.0000
1030	8.976	8.312	.0016	.0130	8.677	.0023	.0001	.0000	.0000
1035	7.597	7.027	.0014	.0119	7.530	.0018	.0001	.0000	.0000
1040	6.199	5.731	.0009	.0103	6.304	.0009	.0001	.0000	.0000
1045	4.762	4.402	.0007	.0083	4.950	.0003	.0000	.0000	.0000
1050	3.334	3.082	.0005	.0062	3.507	.0002	.0000	.0000	.0000
1055	2.873	2.656	.0005	.0057	3.023	.0004	.0000	.0000	.0000
1060	2.420	2.237	.0006	.0055	2.518	.0004	.0000	.0000	.0001
1065	1.960	1.812	.0006	.0051	2.015	.0003	.0000	.0000	.0001
1070	1.490	1.376	.0005	.0044	1.506	.0003	.0000	.0000	.0000
1075	1.019	.9406	.0004	.0034	1.018	.0002	.0000	.0000	.0000
1080	.8254	.7622	.0004	.0032	.8175	.0002	.0000	.0000	.0000
1085	.6319	.5836	.0004	.0027	.6266	.0002	.0000	.0000	.0000
1090	.4444	.4104	.0003	.0021	.4414	.0002	.0000	.0000	.0000
1095	.2554	.2359	.0002	.0013	.2536	.0002	.0000	.0000	.0000
1100	.0700	.0646	.0000	.0004	.0695	.0001	.0000	.0000	.0000

and 1985. In most cases, multiple frames were acquired in succession for each SSI configuration.

Table 4-18 lists the mean DN level and the standard deviation across the frame for zero-exposure frames acquired in 1985 at the expected flight temperature of +8° C. The CCD clock voltages were normal and blemish protection was not used for these frames. Where multiple frames were available in a given configuration, they were averaged to reduce random noise. Variations in frame time and use of the extended exposure mode have only small effects on the offset level (maximum change with frame time of 1.3 DN in gain state 4, typical changes of <0.1 DN in other gains; maximum change with extended exposure mode of 1.1 DN in gain state 4, typical changes of < 0.2 DN in other gains). Changes with gain state and use of the summation mode are more significant.

Figures 4-155 through 4-164 show contrast-enhanced photographs of averaged zero-exposure frames for various gain states and use of the summation mode. The full-resolution, gain state 4 frames show bright and dark columns spaced 42 pixels apart. These are due to a 2400-Hz coherent noise source and are discussed in more detail in Section IV-A-6. The column striations in the first 100 columns of summation-mode frames are also apparent. A gradual left-to-right shading pattern is also seen in the summation-mode frames. As the gain is decreased, the offset becomes more uniform since the variations become smaller than the DN step size. The pattern of the thermal dark current, which is very small, only becomes apparent when extended exposure frames in gain state 4 are compared to normal frames.

Switching the CCD clock voltages to the inverted level and/or using the blemish protection mode drastically affects the zero-exposure offset because in these modes the amount of thermal dark current and spurious charge generated in the CCD array is greatly increased. In these modes, the use of the extended-exposure mode has very little effect on offset. The frame time used only makes a difference when the blemish-protection mode is used. Longer readout periods increase the amount of spurious charge generated in this case, and the offset level increases (but this effect is much smaller than that caused by the switch to blemish protection itself). Table 4-19 lists the frame-wide mean offset levels from 1984 for different frame rates and gain states using the normal exposure mode with the CCD clock voltages at the inverted level and/or blemish protection being used. Note that in gain state 4 in the summation mode, use of the inverted clock voltages in the blemish-protection mode causes the offset level to reach 255 DN. Figures 4-165 through 4-167 show contrast-enhanced offset frames in gain state 4 for the 60 2/3-sec frame rate with inverted clock voltages and/or blemish protection used. Inverted clock voltages increase spurious

Table 4-18. Mean DN level and standard deviation for zero-exposure frames acquired in 1985 at the expected flight temperature of +8° C.

frame rate (sec)	gain state	mean	std. dev.
60 2/3	4	10.10	0.97
	3	3.74	0.45
	2	3.06	0.26
30 1/3	4	9.64	0.97
	3	3.65	0.49
	2	3.02	0.24
8 2/3	4	9.03	0.92
	3	3.82	0.26
	2	3.00	0.12
2 1/3	4	20.61	3.97
	3	6.35	1.21
	2	3.59	0.28
	1	2.50	0.38

Table 4-19. 1984 mean offsets (DN) with inverted CCD clock voltages (INV) and/or use of blemish protection (BPM).

frame rate (sec)	gain state	BPM	INV	INV + BPM
60 2/3	4	23.4	25.4	104.0
	3	6.1	6.4	23.0
	2	4.3	4.5	12.4
30 1/3	4	21.9	25.2	98.4
	3	5.8	6.5	21.8
	2	4.2	4.6	11.9
8 2/3	4	19.2	25.2	86.9
	3	5.5	6.7	19.6
	2	4.0	4.5	10.8
2 1/3	4	67.6	115.5	255.0
	3	16.0	26.3	81.7
	2	8.5	13.5	40.3
	1	3.7	4.6	10.2

charge production during CCD readout when the voltages are rapidly switched from the normally positive level to their negative level and back. This introduces a right-to-left shading pattern of spurious charge. In the blemish-protection mode, the CCD clocks are normally held negative during readout, and the charge is shifted by rapidly switching to the positive level

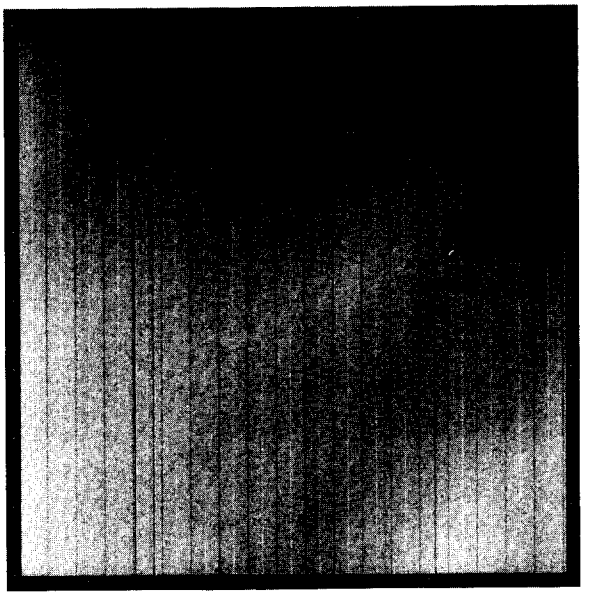

Figure 4-155.
Contrast-enhanced zero-exposure frame for 60 2/3-sec frame rate and gain state 4.

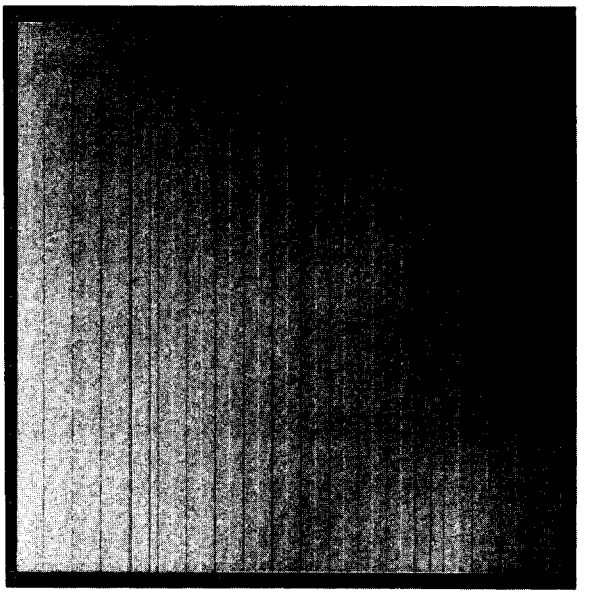

Figure 4-156.
Contrast-enhanced zero-exposure frame for 8 2/3-sec frame rate and gain state 4.

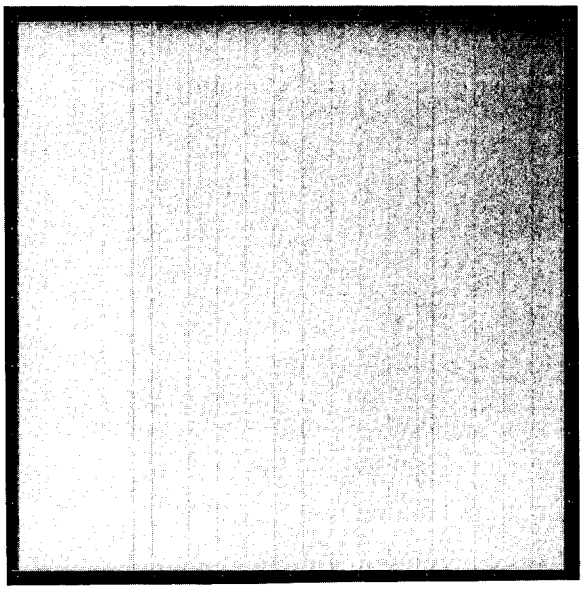

Figure 4-157.
Contrast-enhanced zero-exposure frame for 8 2/3-sec frame rate and gain state 3.

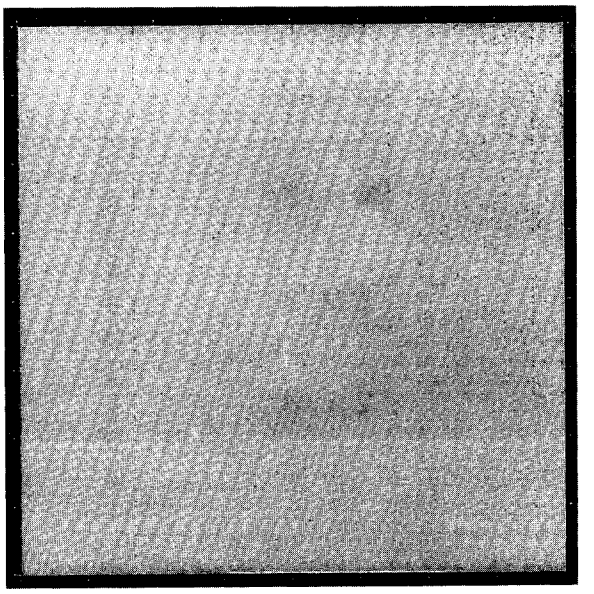

Figure 4-158.
Contrast-enhanced zero-exposure frame for 8 2/3-sec frame rate and gain state 2.

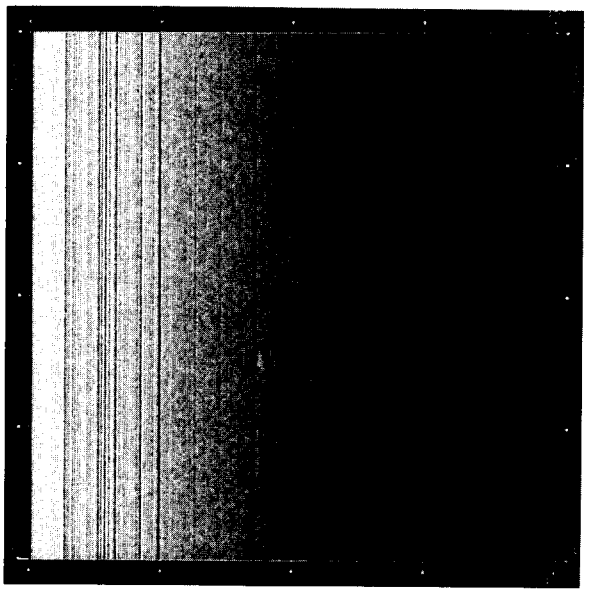

Figure 4-159.
Contrast-enhanced zero-exposure frame for 2 1/3-sec frame rate and gain state 4.

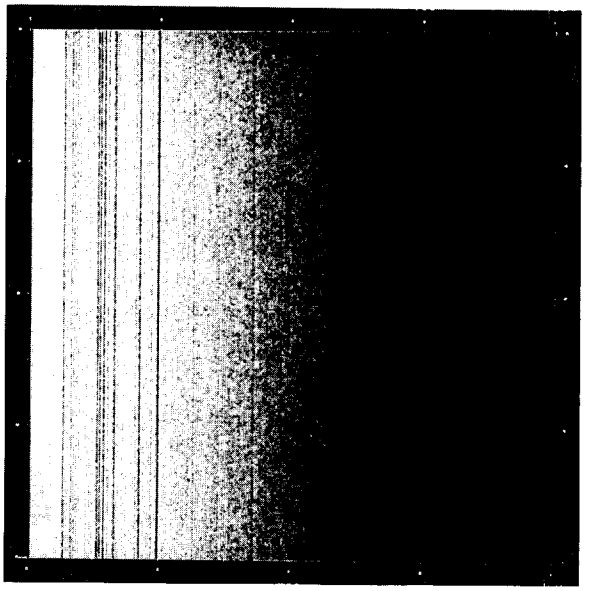

Figure 4-160.
Contrast-enhanced zero-exposure frame for 2 1/3-sec frame rate and gain state 3.

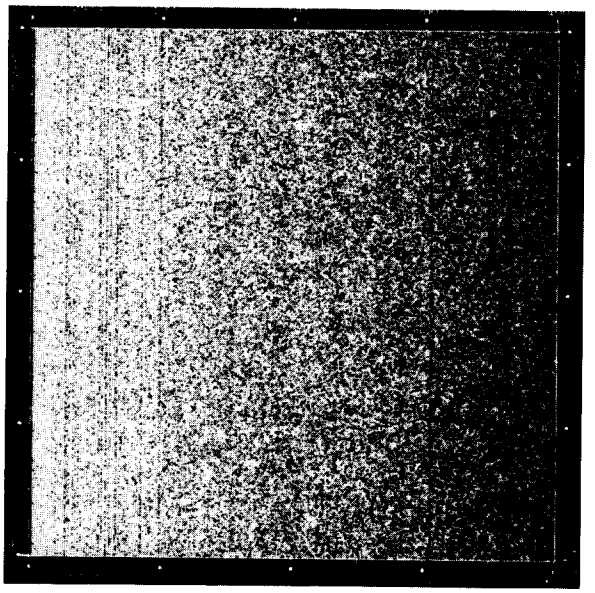

Figure 4-161.
Contrast-enhanced zero-exposure frame for 2 1/3-sec frame rate and gain state 2.

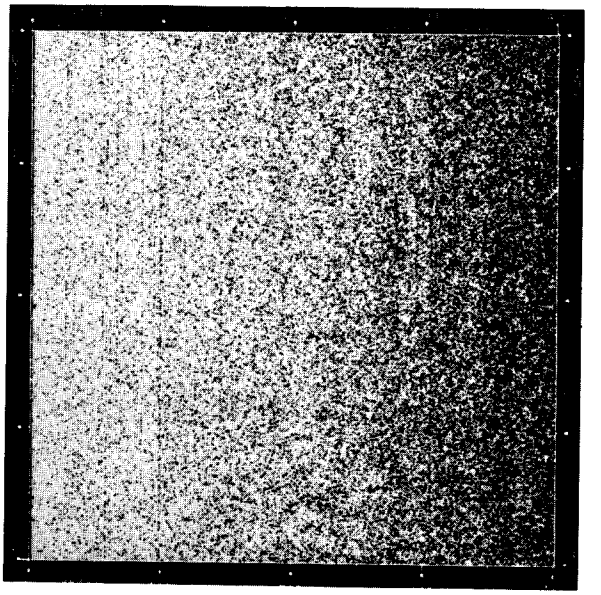

Figure 4-162.
Contrast-enhanced zero-exposure frame for 2 1/3-sec frame rate and gain state 1.

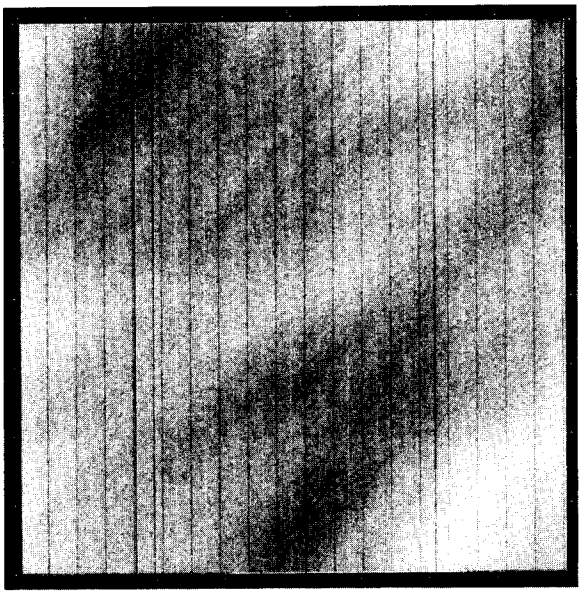

Figure 4-163.
Contrast-enhanced zero-exposure frame for 60 2/3-sec frame rate, gain state 4 and extended exposure mode.

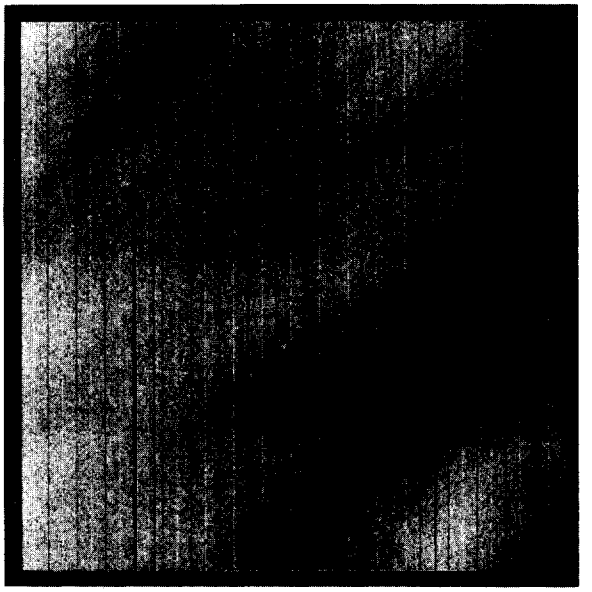

Figure 4-164.
Contrast-enhanced zero-exposure frame for 8 2/3-sec frame rate, gain state 4 and extended exposure mode.

and back during readout. While the clocks are negative, thermal dark current is collected in the CCD potential wells much more rapidly than when they are positive. Therefore, thermal dark current buildup is much greater when blemish protection is used, and this introduces an upper-right-to-lower-left shading pattern of dark current charge. In addition, isolated pixels that generate higher-than-average dark current become visible as "dark spikes" in this mode.

Use of the data compressor has no apparent effects on the offset.

Changes in instrument temperature do cause changes in the offset level. Changes over time have also been observed. Figures 4-168 through 4-170 show the offset level in each gain state versus temperature determined four different ways: (a) mean DN over a 50 x 50 pixel area, (b) offset from linear fit to light transfer data for the same 50 x 50 pixel area, (c) mean offset from linear fit to light transfer data for 256 20 x 20 pixel areas spread across the CCD array, and (d) mean offset from GALGEN linear fit to light transfer data. The error bars shown give an indication of the uncertainty in the measurement and its variability with time over periods of up to a few days. The offset is stable to within about 0.1 DN over this period. Data are

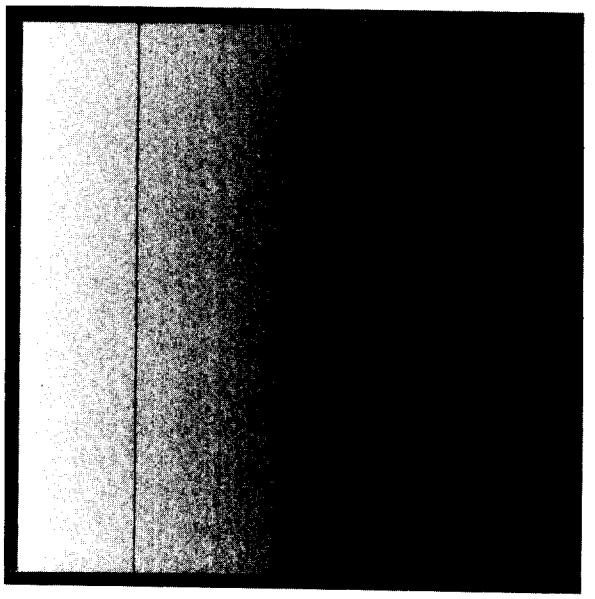

Figure 4-165.
Contrast-enhanced offset frames in gain state 4 for the 60 2/3-sec fame rate with inverted clock voltages.

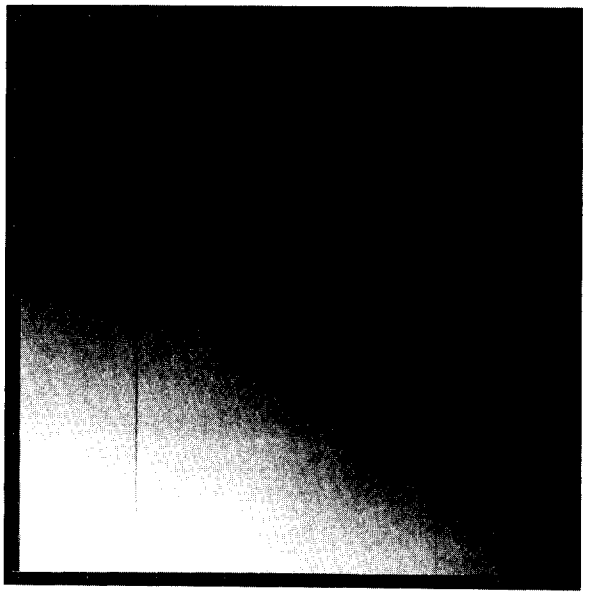

Figure 4-166.
Contrast-enhanced offset frames in gain state 4 for the 60 2/3-sec frame rate with blemish protection.

Figure 4-167.
Contrast-enhanced offset frames in gain state 4 for the 60 2/3-sec frame rate with inverted clock voltages and blemish protection.

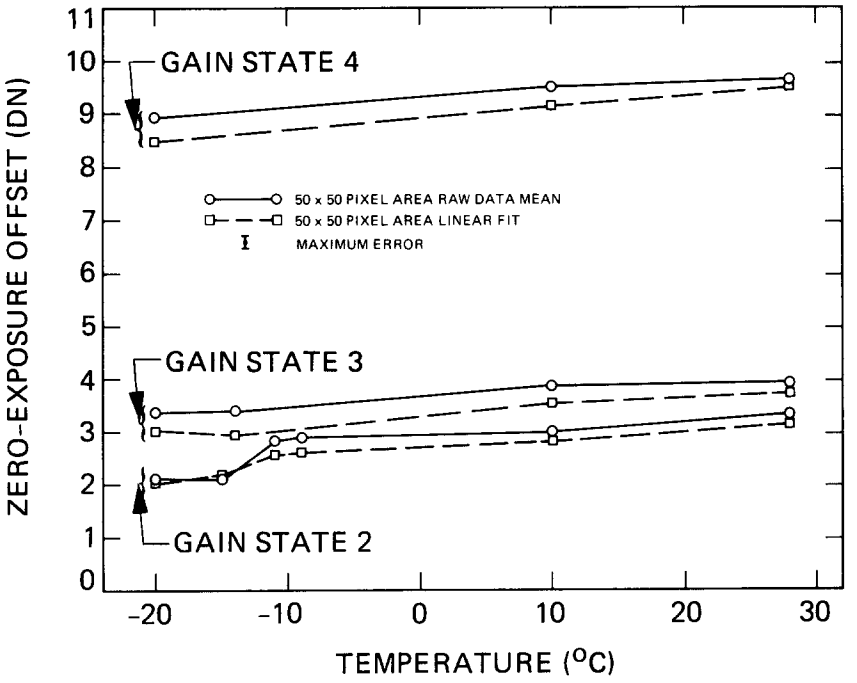

Figure 4-168. Offset level in gain states 2, 3, and 4 versus temperature from 1984 data.

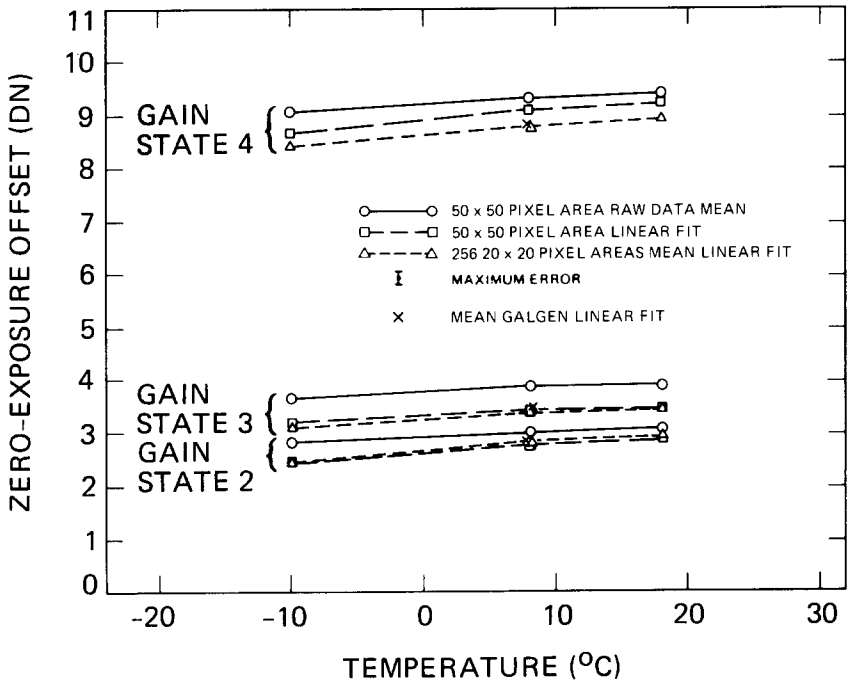

Figure 4-169. Offset level in gain states 2, 3, and 4 versus temperature from 1985 data.

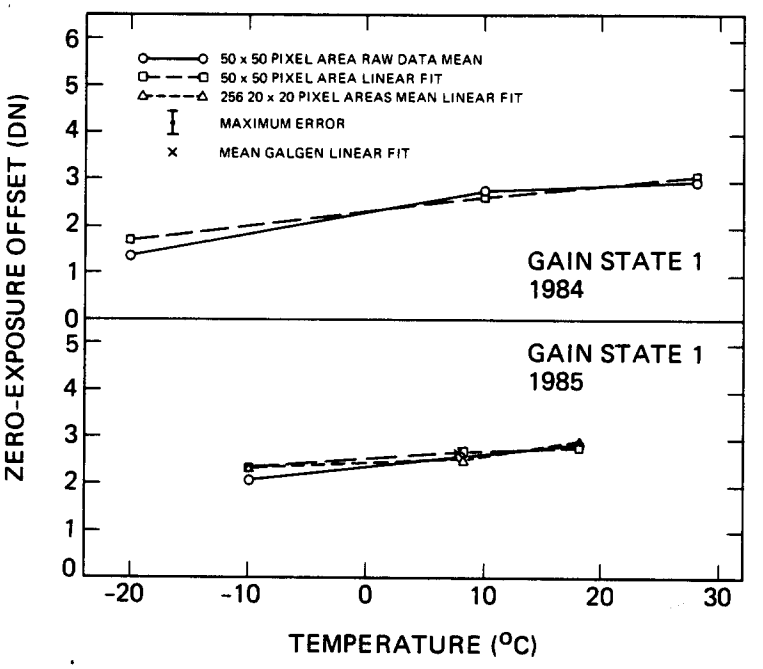

Figure 4-170. Offset level in gain state 1 versus temperature from 1984 and 1985 data.

plotted for both 1984 and 1985, which shows the amount of change over a period of one year. The offset level increases with temperature at a rate of roughly 0.02 DN/°C.

The plots in Figures 4-168 through 4-170 compared to the data in Table 4-18 show that the offsets computed from linear fits to the light transfer data are generally lower than the raw zero-exposure DN level by a few tenths of a DN for the data acquired in the 8 2/3-sec mode (this is not the case in the summation mode). This effect can be seen also in the plots of residual errors in the linear fits shown in Figures 4-14 through 4-25. It is not observed in the few light transfer data sets acquired using the 60 2/3-sec frame time. The raw offset data could be in error by between 0.5 and 1 DN due to digitization errors in the SSI analog-to-digital converter (see Section IV-A-6 below). However, it seems unlikely that the mismatch with the linear-fit offsets in all 18 8 2/3-sec cases examined (1984 and 1985, 3 gain states, 3 temperatures) would have the same sign. It is possible that the SSI response is slightly nonlinear at low signal levels, although the level of error in DN would be expected to decrease as the gain decreases if this were the case, and the low-light-level linearity test discussed in Section IV-A-3e above shows no evidence of this (in fact, the offset residual in this case has the opposite sign). Nor does low-level nonlinearity explain why the summation-mode offsets derived from the linear fits agree well with the raw zero-exposure offsets. It has been decided that, until this difference is understood, SSI flight data will be calibrated using the GALGEN linear-fit

offsets rather than using averages of zero-exposure frames, at least for those SSI configurations in which light transfer data sets were acquired.

Comparison of the GALGEN offset files shown in Figures 4-50 through 4-57 to the corresponding zero-exposure frames in Figures 4-155 through 4-164 shows that they match well in their spatial distributions.

6. Noise Characteristics

To study the SSI noise and the possible effects of instrument temperature and data compressor use on it, the following dark frames were analyzed:

(a) From 1983, images at -10° C, +10° C and +18° C including both full-resolution images (gain states 2, 3 and 4) and summation-mode images (gain state 1), with the data compressor both off and on in both its rate-controlled and information-preserving modes.

(b) From 1984, full-resolution images at temperatures of +28° C, +10° C and -20° C in each of the three highest gain states (2, 3 and 4); summation-mode images at +10° C in these gain states and at +28° C in gain state 1.

(c) From 1985, full-resolution images in gain state 4 with the data compressor off at both the nominal temperature and two off-nominal temperatures, and with the data compressor on in the rate-controlled mode at nominal temperature; also summation mode images at nominal temperature.

The noise analysis procedure employed Fourier analysis techniques to separate coherent (periodic) noise from random noise in SSI images. The analysis was applied to 512 x 512 pixel subsets of 800 x 800 pixel dark frames (256 x 256 pixel subsets for 400 x 400 pixel summation-mode images). The images were not radiometrically calibrated for this part of the noise study (temperature and data compressor effects); however, the low spatial frequency (shading) effects were removed by applying a high-pass filter using a 51 x 51 pixel moving average filter window. The filtered output was multiplied by a factor of 20 to enhance the contrast of the relatively low-amplitude noise data over the background. A two-dimensional fast Fourier transform (FFT) was generated from the filtered image. This converted the data from the spatial domain to the frequency domain and provided a convenient method for separating the coherent noise from the random noise. The coherent noise was interactively removed from the FFT,

in which it appears in the form of sharp spikes or irregularly shaped features transposed on either side of the axes. The FFT with the coherent noise removed represents the transform of the random noise data. An inverse Fourier transform converted it back to the spatial domain, resulting in an image that constitutes the random noise component of the original image. An image of the coherent noise component was produced by pixel-by-pixel subtraction of the random noise image from the original filtered image. One-dimensional power spectrum plots of the images were also generated, and statistical data (means and standard deviations) were obtained. The latter require dividing by the scale factor of 20 applied during the initial filtering.

The analysis revealed no variation in noise characteristics as a result of changing the SSI temperature. In addition, the test frames generated in 1983 and 1985 did not show any apparent effect of the data compressor on noise. Regardless of temperature, the standard deviations for the two compressor modes and the compressor-off state are approximately equal in a given gain state. Table 4-20 lists the statistical information obtained from selected typical dark current frames from the 1984 and 1985 data, in both their raw and filtered forms, and their random and coherent components. The cases shown are 1984 data taken at $+10^{0}$ C in both the full-resolution and summation modes, in each of the available gain states. Also included for comparison are two gain state 4 images obtained in 1985. Figures 4-171 through 4-184 show the image data from the noise analysis of the 1984 dark frame images. Included for each are four sub-images representing the filtered image (a), the two-dimensional FFT (b), the coherent noise component (c), and the random noise component (d). Also included are three histograms of the filtered, coherent and random images respectively, and a corresponding one-dimensional power spectrum plot for the coherent noise in the horizontal direction.

The table shows that in general, the standard deviations in DN increase as the gain state is increased. This holds for all types of images (raw, filtered, random and coherent). In all but three cases (the gain states 3 and 4 summation-mode frames), the standard deviations of the filtered and random images are close to that of the raw image. In the remaining cases, the standard deviation for the raw image appears abnormally high relative to the filtered and random images, a fact accounted for by the relatively high amount of low-spatial-frequency left-to-right shading in the zero-exposure frames in gain states 3 and 4 in the summation mode. In all cases, the standard deviation of the coherent image is significantly lower than that of the random image. A comparison of corresponding images from 1984 and 1985 shows a high level of reproducibility and absence of systematic changes between the 1984 and 1985 calibration runs.

Table 4-20. Noise statistics of selected uncalibrated zero- exposure frames (units are DN).

year	temp. (°C)	gain	mode	raw mean	raw std. dev.	filtered mean	filtered std. dev.	random mean	random std. dev.	coherent mean	coherent std. dev.
1984	+10	4	NORM	9.22	1.03	127.50	0.99	127.50	0.94	128.00	0.26
1984	+10	3	NORM	3.85	0.36	127.48	0.36	127.48	0.35	128.00	0.05
1984	+10	2	NORM	3.02	0.16	127.36	0.16	127.36	0.16	128.00	0.02
1984	+10	4	SUM	21.24	3.04	127.46	1.69	127.46	1.54	128.00	0.62
1984	+10	3	SUM	6.65	1.24	127.50	0.79	127.50	0.77	128.00	0.19
1984	+10	2	SUM	4.09	0.29	127.51	0.26	127.48	0.25	128.03	0.06
1984	+10	1	SUM	2.78	0.42	127.52	0.41	127.52	0.41	127.99	0.04
1985	+8	4	NORM	9.10	1.04	127.49	1.01	127.49	0.95	128.00	0.31
1985	+8	4	SUM	20.58	2.99	127.45	1.68	127.43	1.51	128.02	0.66

The identifiable coherent noise component appears in the coherent image (e.g., Figure 4-171(c)) as a series of vertical stripes with 42-pixel spacing. Ideally the stripes are alternately above and below the background level every 21 pixels, half the full period. This feature is typical of the zero-exposure images studied, although it is most prominent in the higher gain states, and in several frames the stripes do not appear across the entire coherent image. This noise component also is visible as the leftmost prominent spike, with a spatial frequency of 0.0238 cycles/pixel (corresponding to 42 pixels/cycle), in the horizontal power spectrum plot of the coherent noise image (e.g., Figure 4-172). Harmonics derived from this noise component appear as prominent spikes at spatial frequencies that are integer multiples of the primary frequency, with the odd multiples appearing much more prominently than the even. This effect was also consistent through all frames used in the noise analysis study. The spatial frequency of this noise combined with the pixel sampling rate of 100,800 pixels/sec implies a temporal frequency of 2400 Hz, corresponding to the primary AC power supply frequency of the SSI support equipment (which is a simulation of the S/C power supply). This noise source is smaller in magnitude than the random component and typically has a magnitude of less than 1 DN, even in the highest gain state, so it is not considered to be a significant problem.

The noise values given in Table 4-20 include the effects of blemishes, CCD spatial sensitivity variations and digitization errors. Since these have the effect of increasing the noise measurements, the Table 4-20 measurements should be taken as upper bounds on the true noise. The effects of blemishes and shading were minimized by the selection of a relatively blemish-free region of the complete image and the application of a high-pass filter to removing shading. Bit errors in the digital data due to

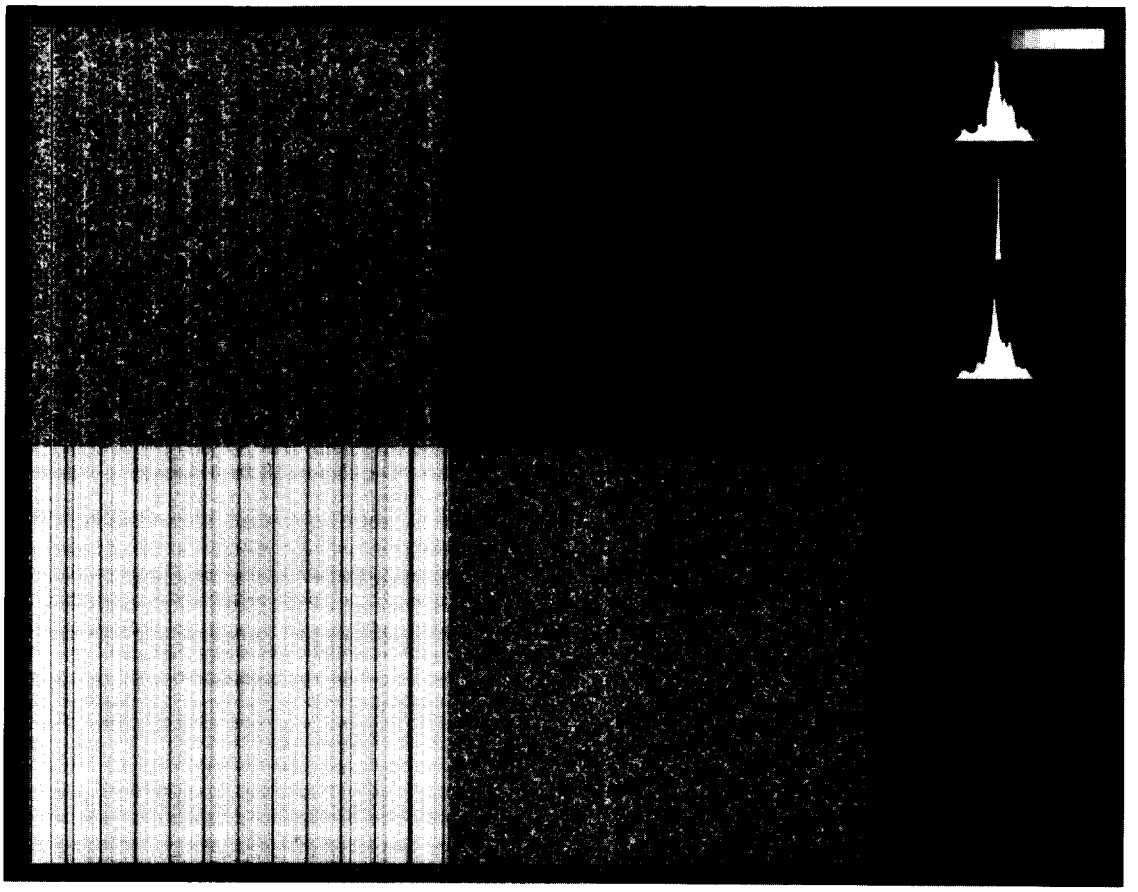

Figure 4-171. Noise analysis data for an uncalibrated dark frame image at 10° C in gain state 4, normal mode.

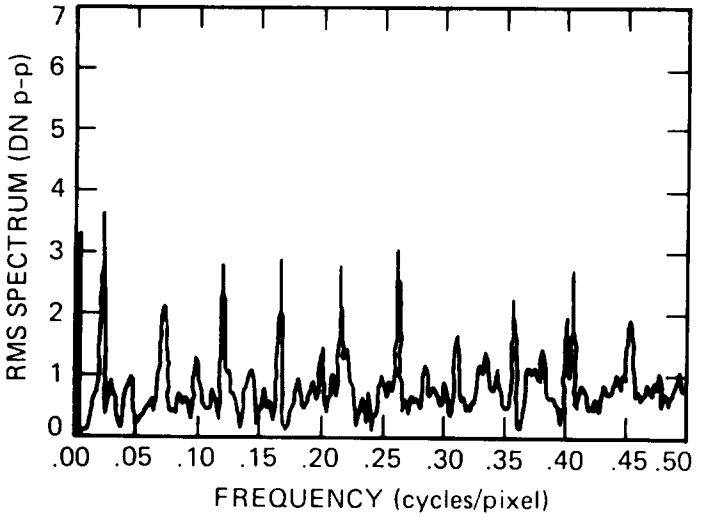

Figure 4-172. One-dimensional power spectrum plot for the horizontal coherent noise component of the image in Figure 4-171.

Figure 4-173. Noise analysis data for an uncalibrated dark frame image at 10° C in gain state 3, normal mode.

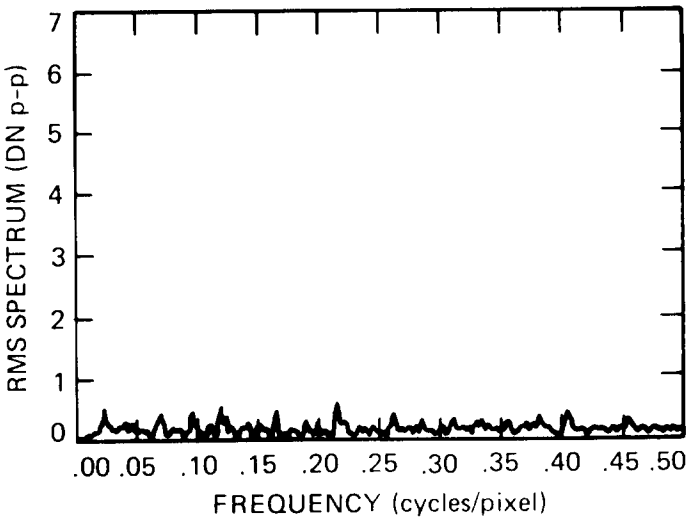

Figure 4-174. One-dimensional power spectrum plot for the horizontal coherent noise component of the image in Figure 4-173.

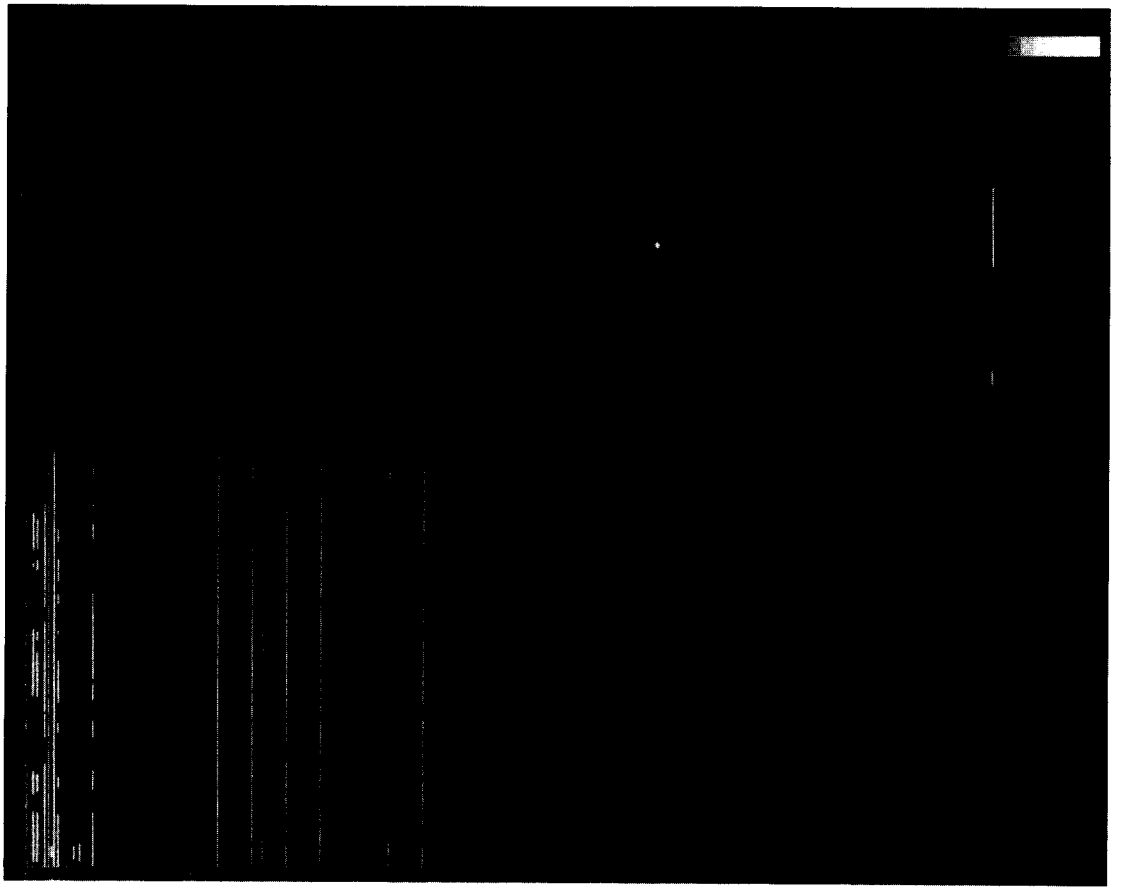

Figure 4-175. Noise analysis data for an uncalibrated dark frame image at 10° C in gain state 2, normal mode.

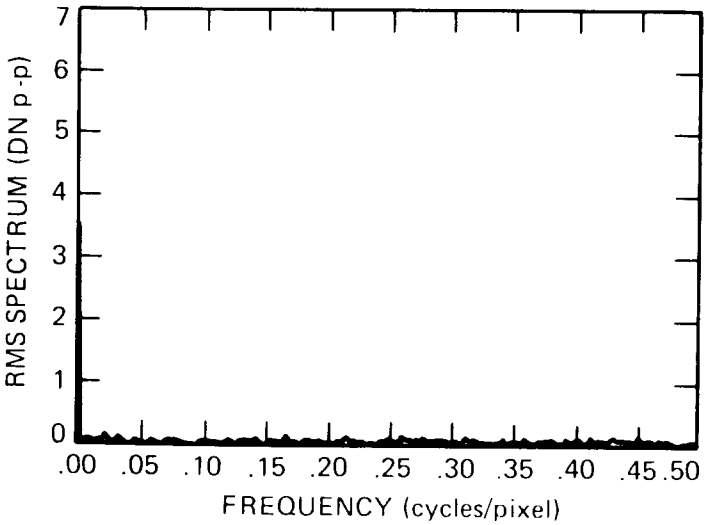

Figure 4-176. One-dimensional power spectrum plot for the horizontal coherent noise component of the image in Figure 4-175.

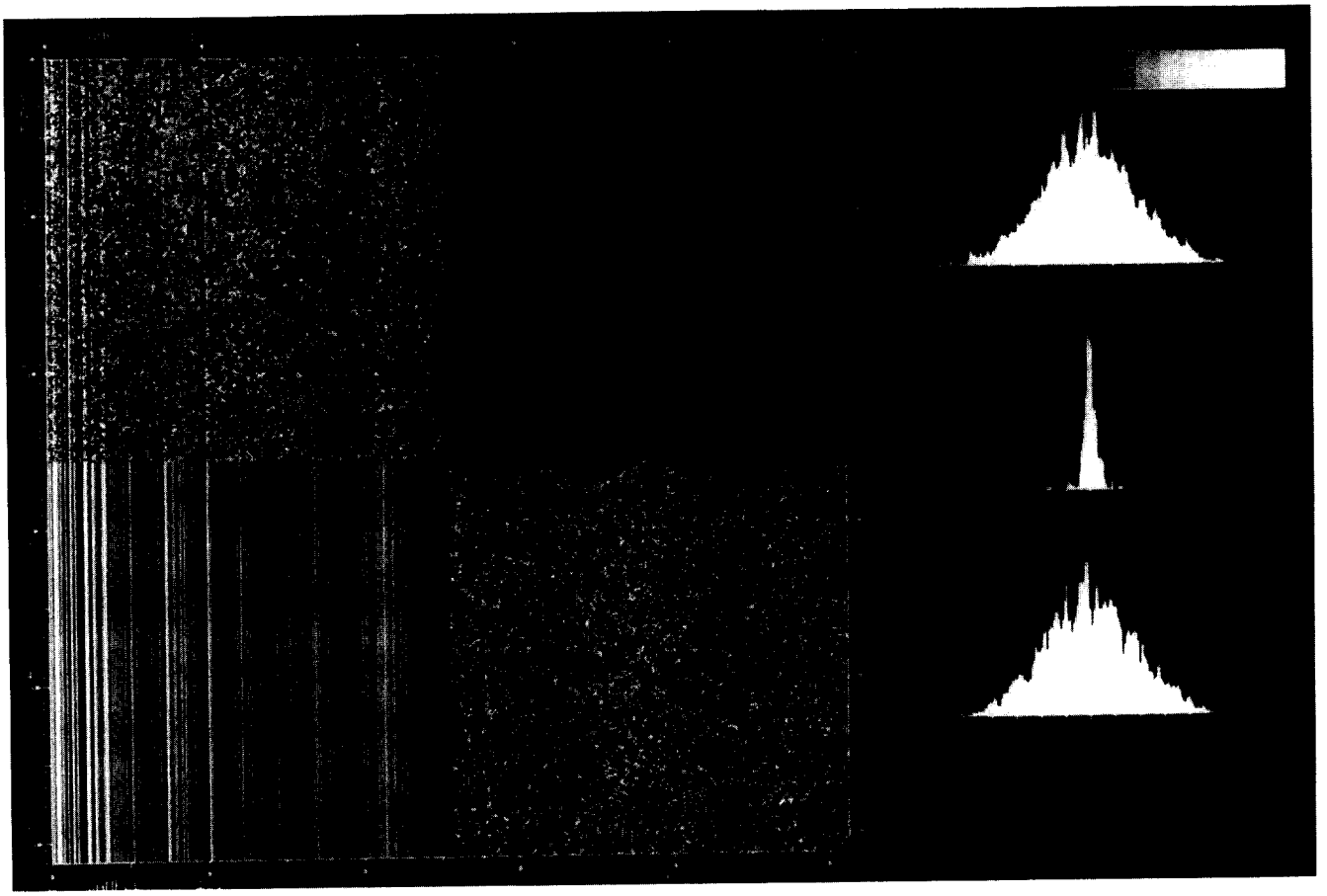

Figure 4-177. Noise analysis data for an uncalibrated dark frame image at 10^{0} C in gain state 4, summation mode.

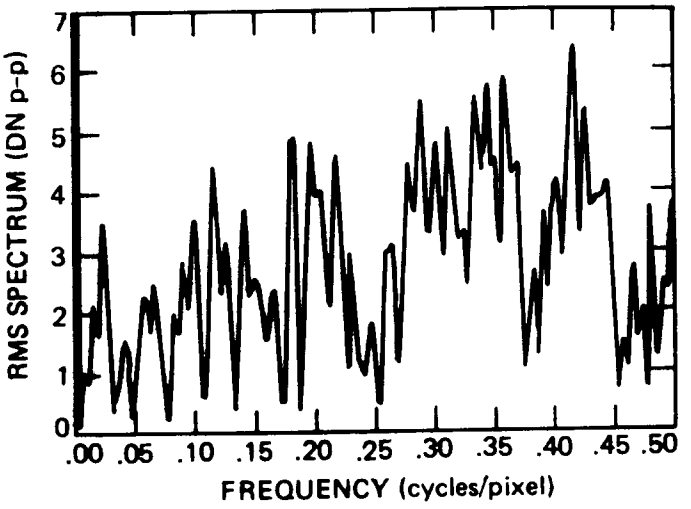

Figure 4-178. One-dimensional power spectrum plot for the horizontal coherent noise component of the image in Figure 4-177.

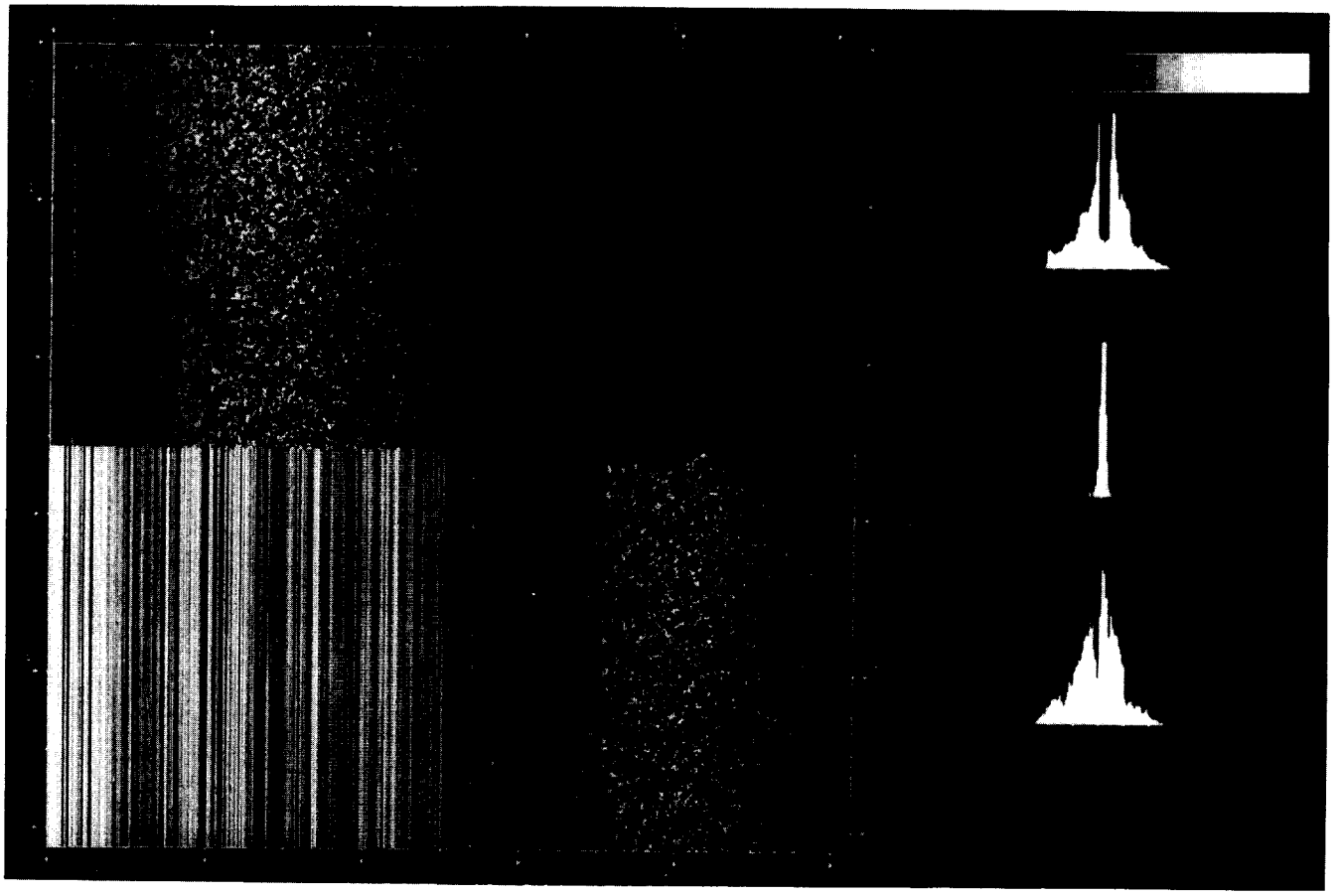

Figure 4-179. Noise analysis data for an uncalibrated dark frame image at 10° C in gain state 3, summation mode.

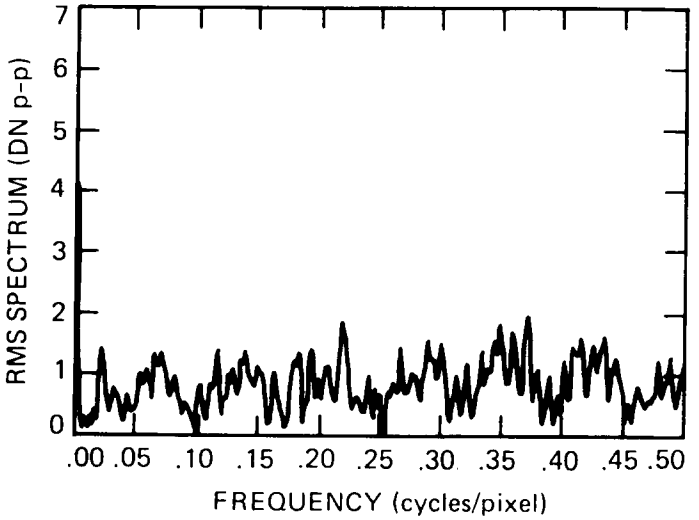

Figure 4-180. One-dimensional power spectrum plot for the horizontal coherent noise component of the image in Figure 4-179.

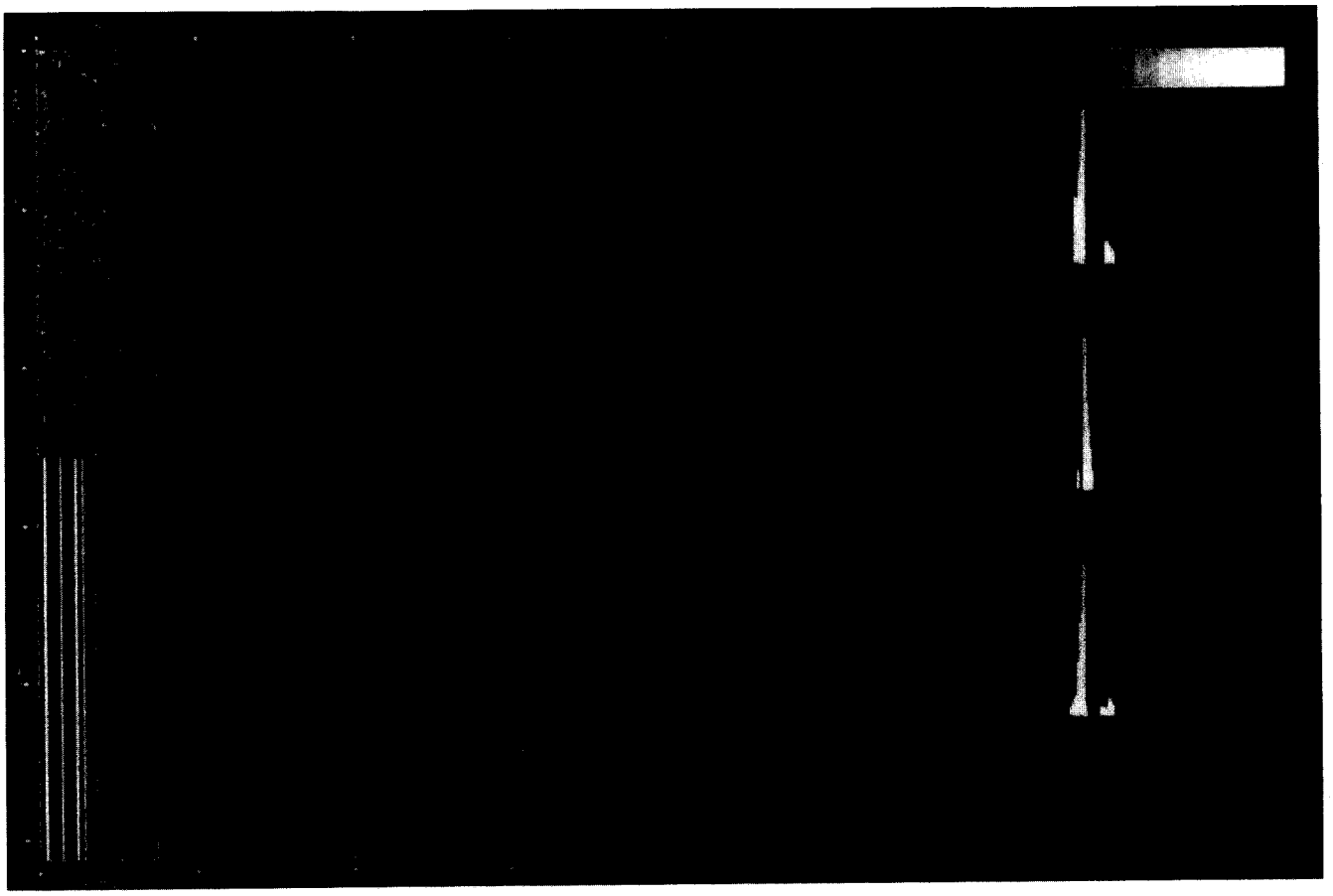

Figure 4-181. Noise analysis data for an uncalibrated dark frame image at 10^0 C in gain state 2, summation mode.

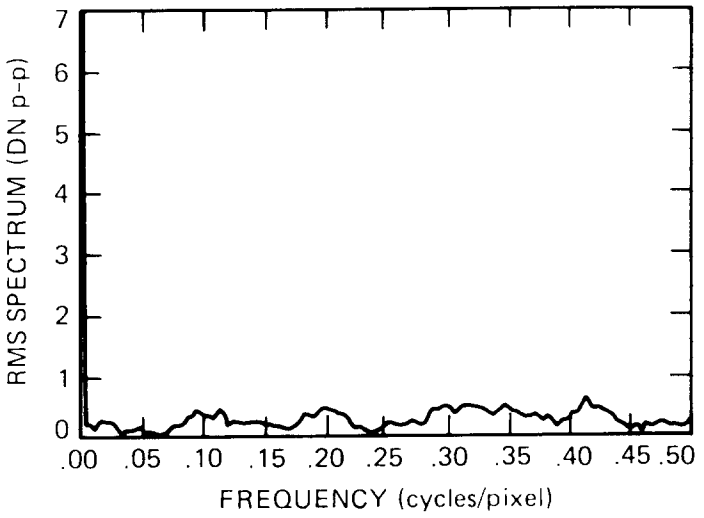

Figure 4-182. One-dimensional power spectrum plot for the horizontal coherent noise component of the image in Figure 4-181.

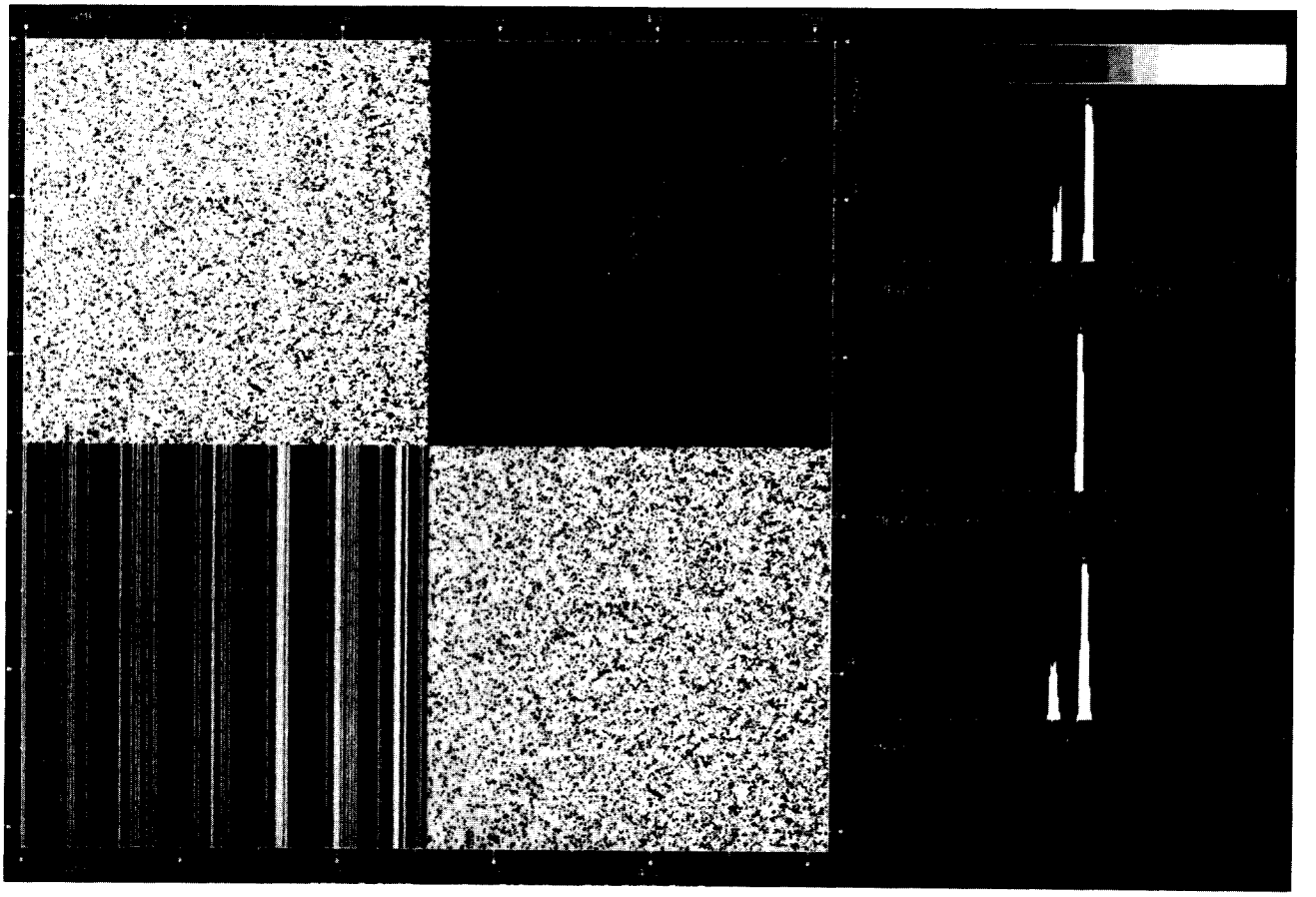

Figure 4-183. Noise analysis data for an uncalibrated dark frame image at 10° C in gain state 1, summation mode.

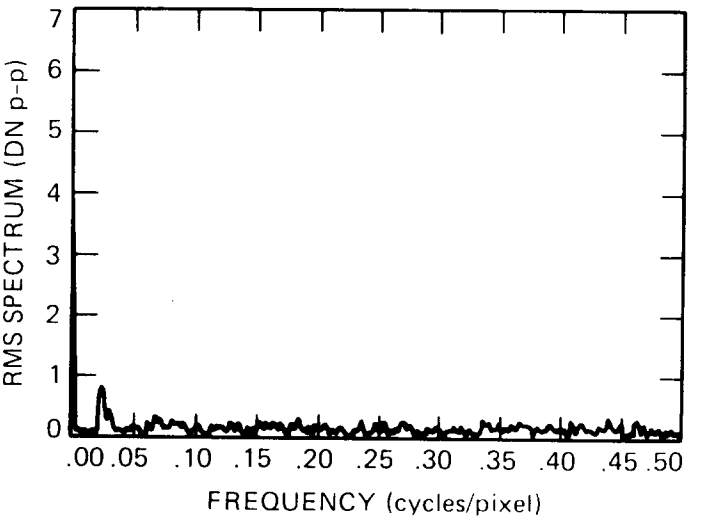

Figure 4-184. One-dimensional power spectrum plot for the horizontal coherent noise component of the image in Figure 4-183.

the analog-to-digital conversion and data reformatting appear as incoherent noise and thus increase the standard deviation of both the original image and the random noise image.

To evaluate the SSI noise characteristics without the effects of blemishes and CCD spatial sensitivity variations and to study how noise varies with signal level, selected images from the light transfer data sets were radiometrically calibrated and then analyzed for random and coherent noise levels as described above. Table 4-21 lists the noise statistics for the frames analyzed. The results for the dark frames are consistent with those described above for the spatially-filtered uncalibrated data. In all cases, the amplitude of the coherent noise is less than half of that of the random noise for dark frames and < 15% for all exposed frames analyzed. Figures 4-185 through 4-194 show the noise analysis images for selected frames and corresponding power spectra for the coherent noise components. In the dark frame in gain state 4 (Figure 4-185), the calibration has largely removed the 2400-Hz noise pattern. This is also true for the gain state 3 dark frame; however, in gain state 2 (Figure 4-187), the 2400-Hz coherent noise can still be isolated and several low-level horizontal features are apparent at frequencies matching 18, 28 and 42 Hz on the left side of the frame. For exposed frames, the 2400-Hz is only barely detectable in gain state 2 calibrated frames (e.g., Figure 4-190). In the summation mode, calibrated exposed frames in the lower gain states exhibit a faint pattern of horizontal bars in the coherent noise frame with a frequency matching 60 Hz (Figure 4-192).

When the noise statistics for exposed frames are analyzed, it appears that the random noise level remaining in flat-field images after calibration is nearly equivalent to the theoretical minimum level expected from a CCD read noise of 31 e- in the full-resolution mode or 44 e- in the summation mode, a quantization error of about 0.37 DN, and the signal shot noise due to photon statistics. There does exist an additional residual uncalibrated noise component that increases linearly with signal level in the proportions shown in Table 4-22.

The level of digitization noise is increased somewhat by unequal bit weighting, i.e., inaccuracies in the operation of the analog-to-digital converter (ADC) that result in DN bins of unequal width. This would result, for instance, if the ratios of the signal levels to which an observed signal is compared during the digitization process differed slightly from the intended powers of 2 (when expressed in DN units). This effect is most easily seen and studied in calibration images which contain a smooth, slowly varying distribution of signal levels over some range of signal. In the absence of bit weighting noise, a DN histogram of the pixels in such an image would be smooth except for the expected random variations. If DN bins are of

Table 4-21. Noise statistics of selected calibrated frames (units are DN).

exp.	gain	mode	raw mean	raw std. dev.	filtered mean	filtered std. dev.	random mean	random std. dev.	coherent mean	coherent std. dev.
0	4	NORM	33.40	0.85	127.50	0.84	127.50	0.82	128.01	0.17
5	4	NORM	52.22	1.43	127.50	1.43	127.48	1.42	127.02	0.09
7	4	NORM	105.89	1.90	127.48	1.90	127.50	1.90	127.98	0.06
8	4	NORM	159.50	2.32	127.49	2.30	127.50	2.30	127.99	0.05
9	4	NORM	212.62	2.80	127.43	2.74	127.44	2.74	127.99	0.07
0	3	NORM	2.02	0.42	127.47	0.42	127.47	0.40	128.00	0.09
9	3	NORM	187.72	1.24	127.50	1.24	127.51	1.24	127.99	0.03
0	2	NORM	2.01	0.22	127.35	0.22	127.33	0.21	128.02	0.04
9	2	NORM	201.80	1.09	127.49	1.09	127.49	1.09	128.00	0.01
0	4	SUM	8.72	1.70	127.48	1.69	127.48	1.63	128.00	0.43
9	4	SUM	176.94	3.66	126.97	3.38	126.97	3.33	128.00	0.46
0	3	SUM	3.49	0.92	127.50	0.86	127.51	0.77	127.99	0.35
9	3	SUM	199.82	1.86	127.50	1.84	127.51	1.83	127.99	0.16
0	2	SUM	2.67	0.53	127.51	0.48	127.52	0.44	127.99	0.18
9	2	SUM	192.80	1.24	127.51	1.24	127.51	1.23	128.00	0.09
0	1	SUM	1.78	0.57	127.49	0.56	127.49	0.56	128.00	0.03
9	1	SUM	225.67	0.84	127.50	0.83	127.50	0.83	128.00	0.04

Table 4-22. Noise component due to imperfect calibration as a percentage of mean signal.

gain	summation	residual (%)
10K	none	0.78
40K	none	0.38
100K	none	0.29
10K	2 x 2	1.36
40K	2 x 2	0.69
100K	2 x 2	0.45
400K	2 x 2	0.29

unequal width, the histogram would show variations in the number of pixels with a given DN in excess of what would be expected statistically based on other known noise sources, and it would be expected to show periodicity at DN intervals equal to some power of 2, depending on which bit of the output DN is being generated inaccurately by the ADC.

There are three groups of calibration images that were employed to detect and analyze this problem. The first consists of light leak analysis

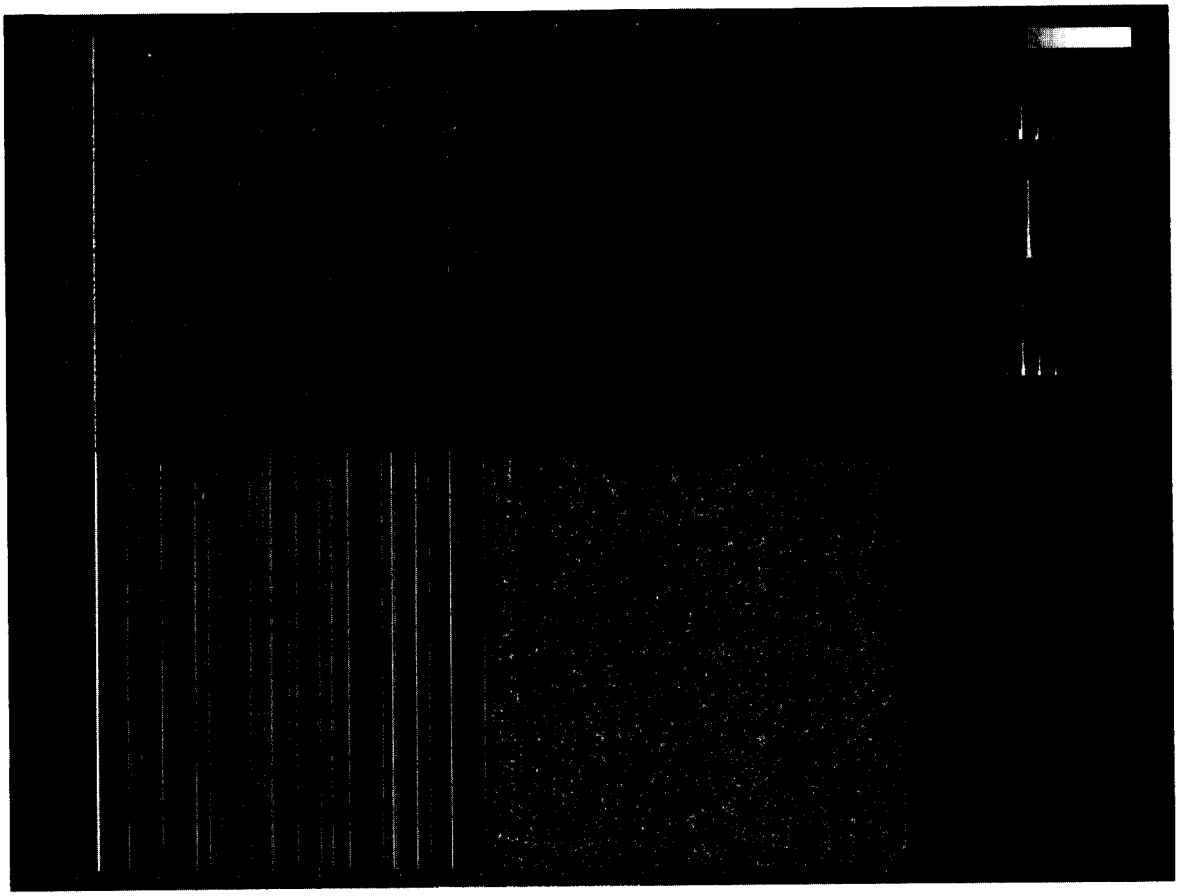

Figure 4-185. Noise analysis data for a radiometrically calibrated dark frame image at 10° C in gain state 4, normal mode.

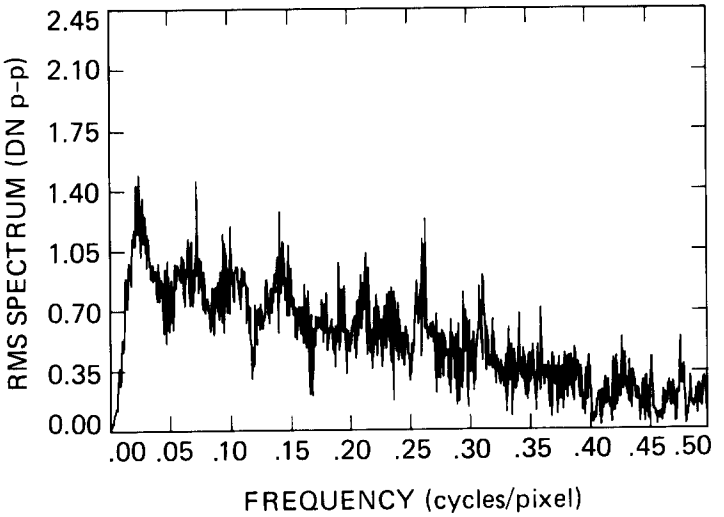

Figure 4-186. One-dimensional power spectrum of the horizontal coherent noise component of the image in Figure 4-185.

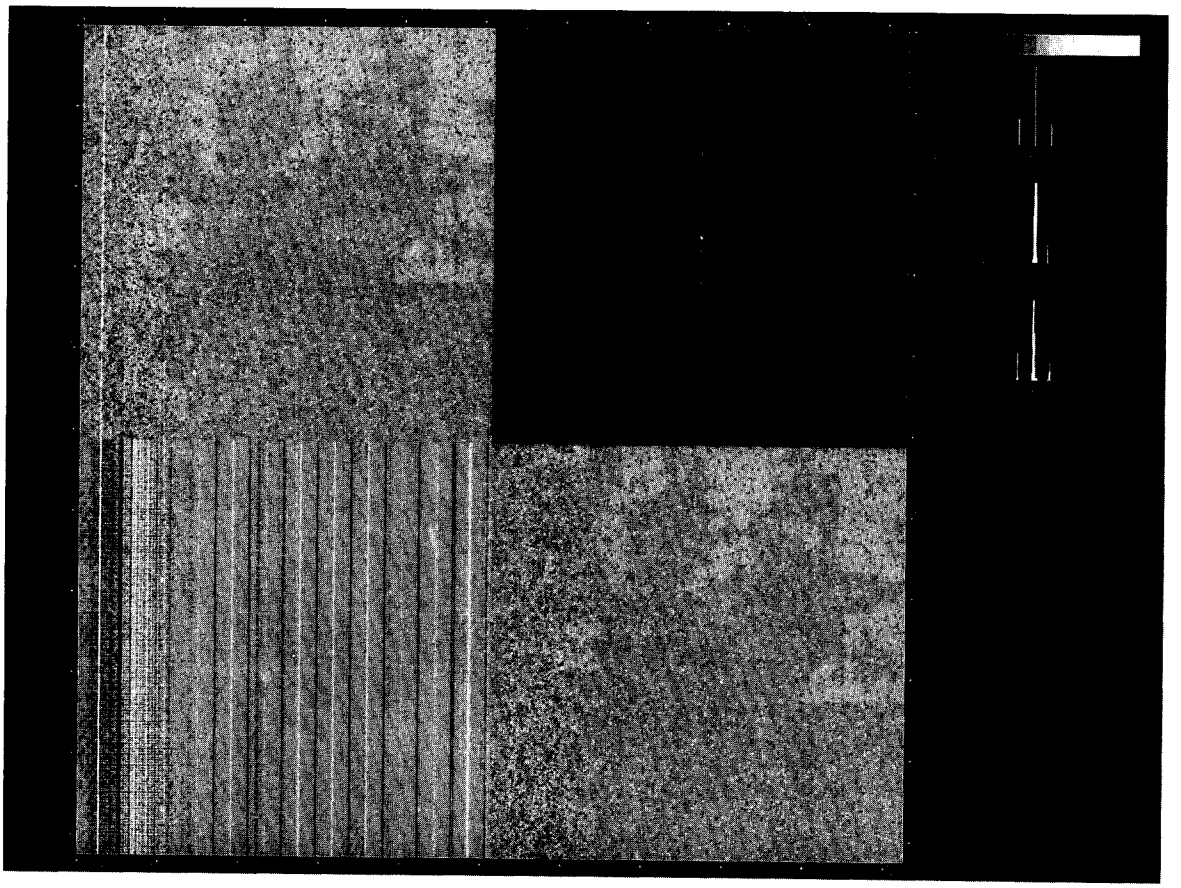

Figure 4-187. Noise analysis data for a radiometrically calibrated dark frame image at 10° C in gain state 2, normal mode.

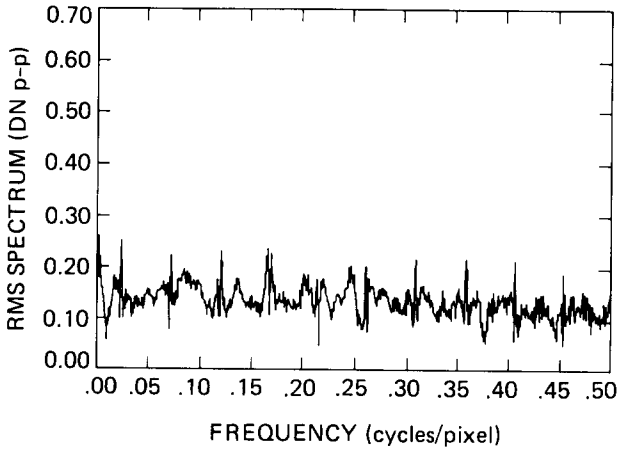

Figure 4-188. One-dimensional power spectrum of the horizontal coherent noise component of the image in Figure 4-187.

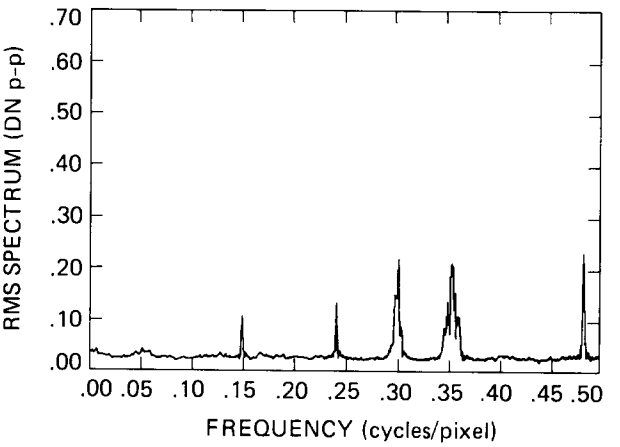

Figure 4-189. One-dimensional power spectrum of the vertical coherent noise component of the image in Figure 4-187.

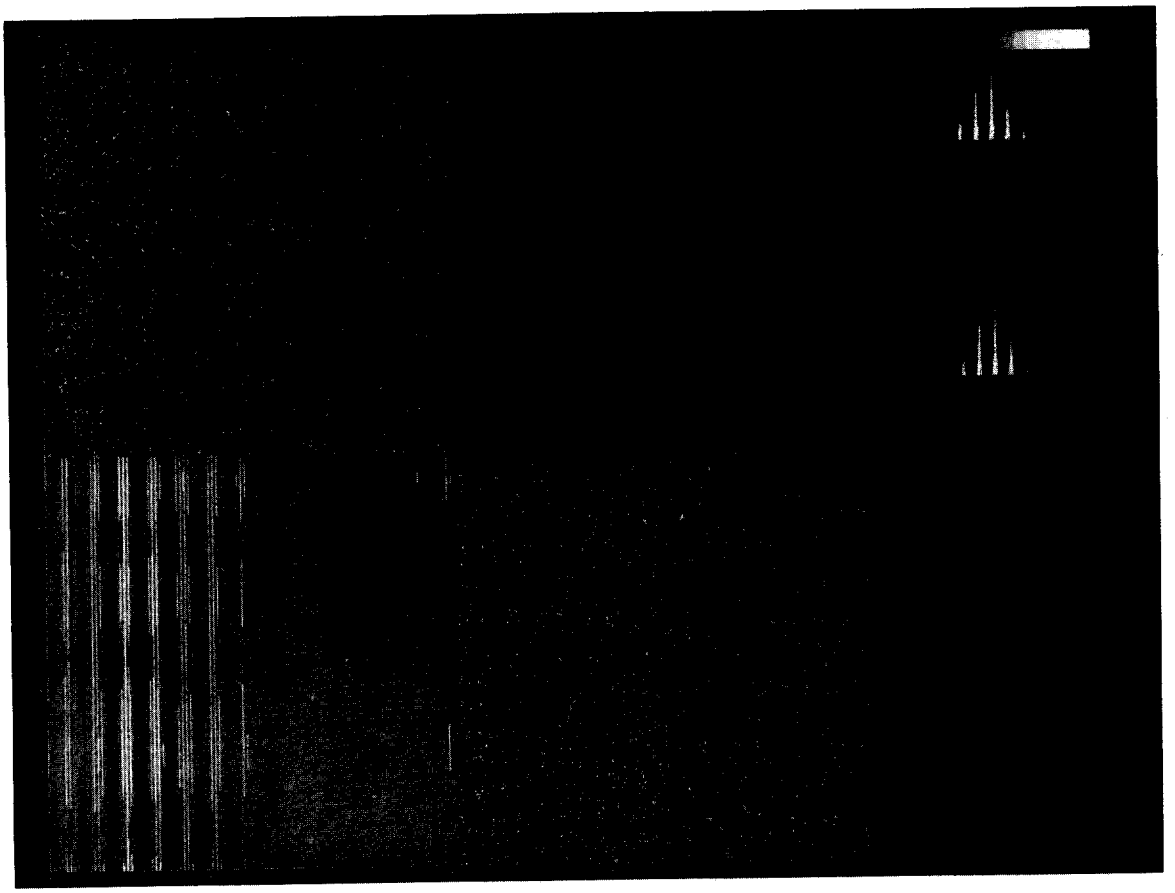

Figure 4-190. Noise analysis data for a radiometrically calibrated exposed frame image at 10° C in gain state 2, normal mode.

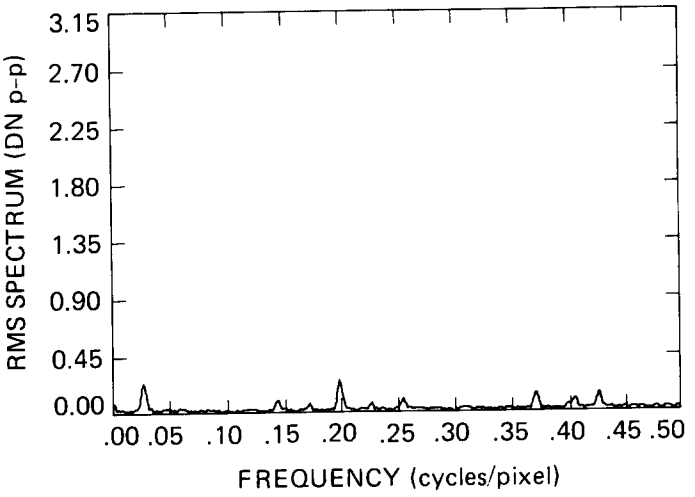

Figure 4-191. One-dimensional power spectrum of the horizontal coherent noise component of the image in Figure 4-190.

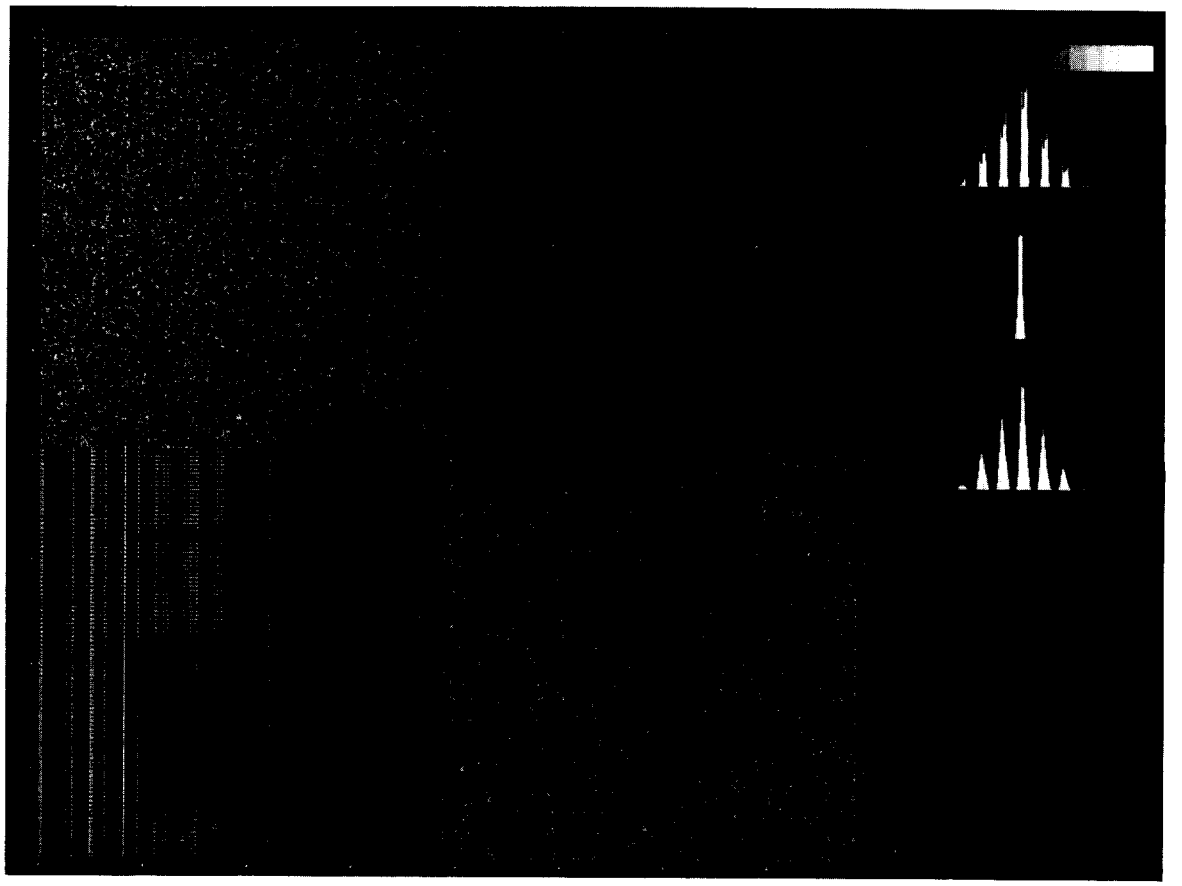

Figure 4-192. Noise analysis data for a radiometrically calibrated exposed frame image at 10° C in gain state 2, summation mode.

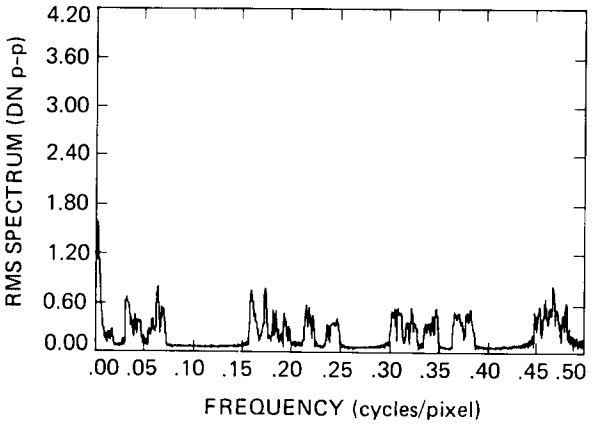

Figure 4-193. One-dimensional power spectrum of the horizontal coherent noise component of the image in Figure 4-192.

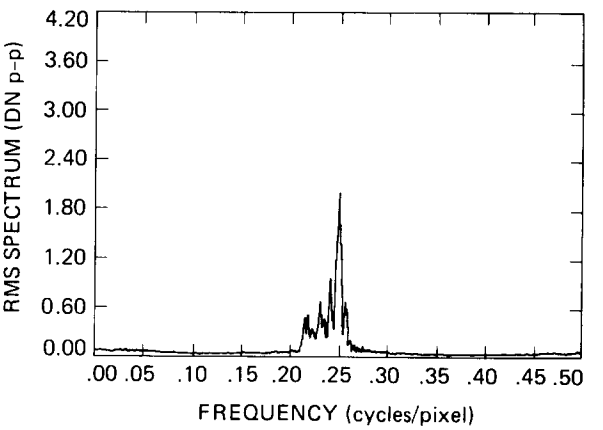

Figure 4-194. One-dimensional power spectrum of the vertical coherent noise component of the image in Figure 4-192.

frames obtained in 1984 in gain state 4 with the light source on, particularly those images taken at low frame rates (30 1/3 or 60 2/3 sec). A flat distribution of signal levels is produced by continued response to leakage light by the detector during the relatively long frame readout, resulting in low DN values for the first pixels read out and high DN values for the last pixels read out. Figure 4-195 shows a DN histogram of the pixels in a 50-column-wide sample from one such image. A strong 8-DN periodicity can be seen, with a deficiency of pixels (of up to 70% of the average number per DN) with DNs evenly divisible by 8 and a corresponding excess of up to 70% for the DNs one less than the multiples of 8. However, this pattern reverses for every fourth DN pair (i.e., every 32 DN), with the lower DN deficient and the higher DN overabundant, indicating that a 32-DN periodicity is also present. There are suggestions of weaker periodicities in lower-order bits as well. Similar effects are seen in zero-exposure frames taken for dark current analysis. Figure 4-196 shows a histogram of the pixels in a 50-column-wide sample from a zero-exposure frame obtained in 1984 at the 60 2/3-sec frame rate in gain state 4 in the inverted mode with blemish protection on. In this case, the overall distribution of signal levels (due primarily to spurious charge) is not flat, but it is smooth and slowly varying, so the DN deficiencies and excesses at multiples of 8 are again clearly seen. Histograms made of images produced from the pixel-by-pixel summation of three similar dark-current or light-leak images showing these effects did not show the effect, indicating that the anomalous DN distributions had to do with the DN encoding process itself and not with particular pixels in the CCD array.

After this effect was observed in the 1984 data, several frames were taken in 1985 using a gradient neutral-density filter target to study the problem. Since the filter's density varies linearly across its area, its transmission varies exponentially, so an exposure taken with this target ideally produces an image with an exponential DN distribution. Images were taken using the clear filter, gain state 2 and six different exposures to cover different parts of the DN scale. The longer exposures, which cover the largest DN range, show the same effects described above (Figure 4-197). The consistent appearance of these effects in very different data sets indicates no dependence on exposure or gain state.

Attempts to mathematically model this observed behavior in terms of the mode of operation of the ADC were not successful, although this was not attempted in great detail. Instead, the calibration data were used to derive fractional-DN corrections to be applied to the raw SSI data to correct for the unequal DN bin widths. The excess or deficiency in the number of pixels per DN in the calibration images relative to the expected number can be taken as a measure of the actual width of the DN bin. The expected number

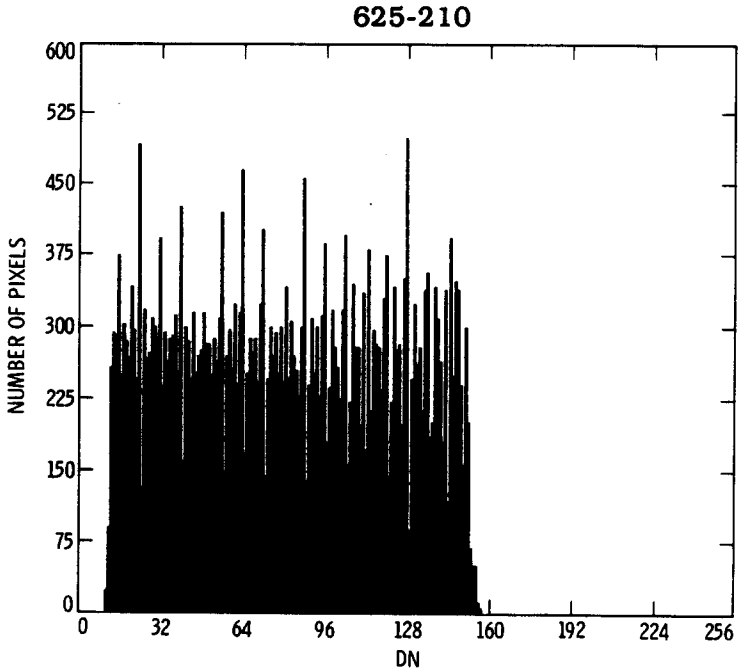

Figure 4-195. DN histogram of the pixels in a 50-column-wide sample from a light leak analysis frame obtained in 1984 at the 60 2/3-sec frame rate in gain state 4 with the light source on.

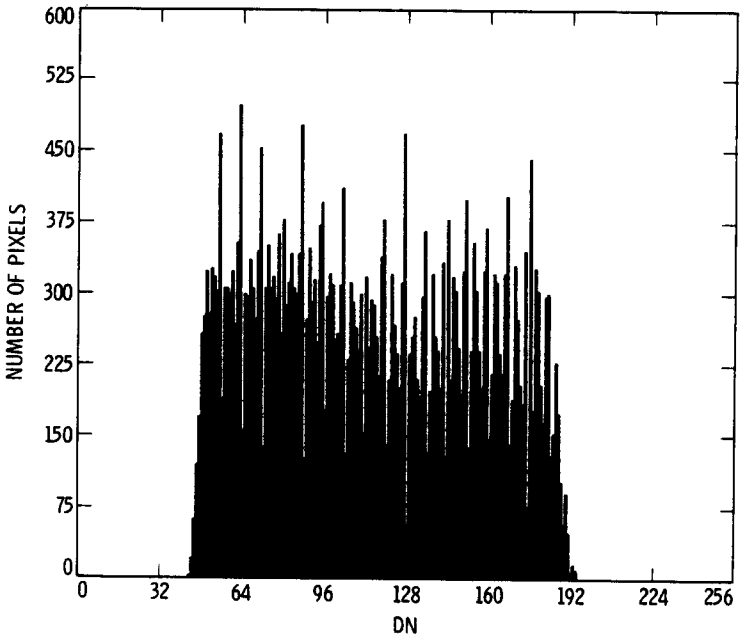

Figure 4-196. DN histogram of the pixels in a 50-column-wide sample from a zero-exposure frame obtained in 1984 at the 60 2/3-sec frame rate in gain state 4 in the inverted mode with blemish protection on.

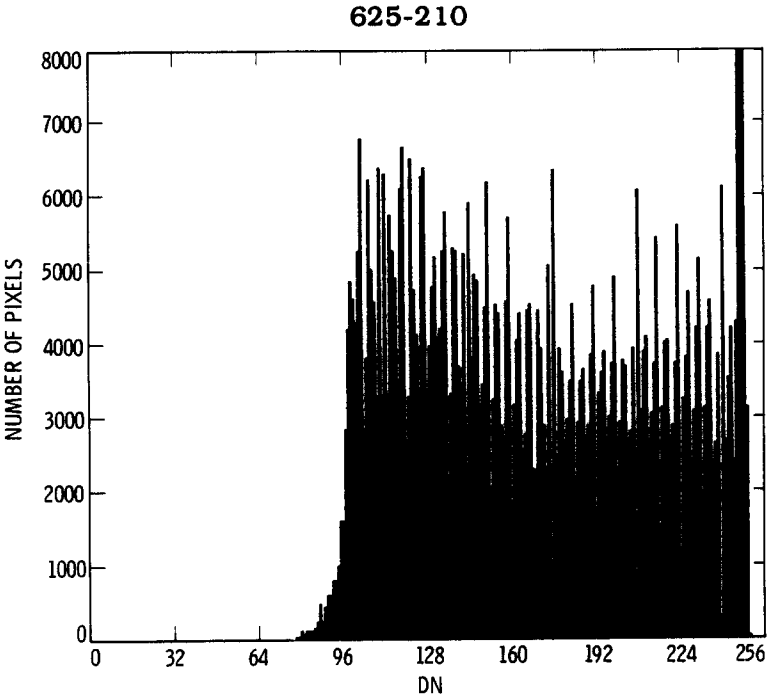

Figure 4-197. DN histogram of a gradient neutral-density filter image, taken in 1985 using the clear filter, gain state 2 and 400-msec exposure time.

for each DN was not obtained by fitting the data to an assumed functional form (e.g., exponential for the neutral-density filter data, or flat for the light leak data) because it was found that the data did not fit the functional form to sufficient accuracy. Instead, an 8-DN moving average was used. The eight DNs ended with an even DN value, were shifted two DNs at a time, and the numbers of pixels in the eight DN levels were averaged to get the expected number for the two central DNs of the eight; this ensured that the eight DNs used always contained both members of the highly anomalous pairs described above. DNs in the tails of the pixel distribution, at the top and bottom of the DN range covered by a given data set, were disregarded.

Once the true bin widths were obtained, fractional adjustments to the DN values to place them in the center of their bin could be made for all DNs covered by a given data set. An additional constant fractional DN offset correction was applied to these values to minimize the average deviation of all DNs from their nominal integral values. This approach results in corrected DNs that have the same meaning as the DN unit in the radiometric calibration files, which were produced from data uncorrected for any bit weighting effects. This procedure was carried out for a 50-column sample from each of three light-leak frames taken under identical conditions in the 60 2/3-sec mode, and for the sum of the histograms of these three samples; for a 50-column sample from each of three dark-

current inverted/blemish protection mode frames taken under identical conditions, and the sum of their histograms; and for five neutral density filter images.

The different data sets cover different parts of the DN scale. In order to obtain corrections for as much of the DN scale as possible, and to obtain the highest accuracy correction in regions of the scale where data sets overlap, the corrected DNs for the light leak 3-frame sum, the dark current 3-frame sum, and the two longest-exposure neutral density filter images were averaged. This provided corrections for DNs from 12 to 245, with the number of measured values contributing to the average ranging from one near the extremes of this range to four near the center. Where the data sets overlapped, there was no evidence of any one of the measurements differing significantly and systematically from the others, and the standard deviation of the contributing measurements averaged about 0.1 DN, which can be taken as an estimate of the residual noise due to the unequal bit weighting effect after correction using the resulting model. Therefore, after correction the total SSI mean digitization noise is about 0.31 DN (vs. 0.29 DN for a perfect ADC) while without correction the mean digitization noise is about 0.35 DN. These figures were confirmed with analytic calculations of the digitization noise for the stairstep function mapping signal to DN which was derived above. Below 12 DN or above 245 DN, no data are available, and the nominal integer DN values must be assumed.

Table 4-23 gives the adopted DN values corrected for unequal bit weighting. Figure 4-198 shows the adopted DN bin widths, and Figure 4-199 the deviation of each DN from its nominal integer value. The 8- and 32-DN periodicities noted in the calibration image histograms are evident in these plots as well.

7. Color Reconstruction

The purpose of the color reconstruction calibration is to characterize the color response of the SSI sufficiently to allow production of approximate visual representations of natural color using multispectral imagery. No accuracy requirement is levied beyond the ability to yield visually acceptable results.

Two types of color representations of scenes are of concern: (1) a volatile display on a CRT and (2) a photographic print. In the case of the volatile display, which is a self-luminous display, the spectral radiance of the display should ideally match that of the original scene. In the case of the photographic print, its spectral reflectivity should ideally match that of the original scene so that when viewed in sunlight (ignoring the effects of the Earth's atmosphere) its radiance will match that of the original scene. In actuality, it is only necessary to have the colors match, not the entire

Table 4-23. DN values adjusted to correct for digitization error caused by unequal bit weighting in the ADC.

nom.	corr.	nom.	corr.	nom.	corr.	nom.	corr.	nom.	corr.
12	11.833	59	58.844	106	105.868	153	152.935	200	200.258
13	12.800	60	59.856	107	107.009	154	153.974	201	200.951
14	13.819	61	60.840	108	108.104	155	155.151	202	201.975
15	14.926	62	61.824	109	109.044	156	156.136	203	203.115
16	15.990	63	63.099	110	110.046	157	156.911	204	204.067
17	16.951	64	64.147	111	110.965	158	157.905	205	204.881
18	17.939	65	64.920	112	111.942	159	159.279	206	205.894
19	18.837	66	65.882	113	113.025	160	160.268	207	206.574
20	19.792	67	66.874	114	114.005	161	160.942	208	207.561
21	20.830	68	67.863	115	115.052	162	161.932	209	208.916
22	21.796	69	68.830	116	116.006	163	163.106	210	209.949
23	23.060	70	69.840	117	116.904	164	164.103	211	211.130
24	24.108	71	71.132	118	117.931	165	164.893	212	212.115
25	24.877	72	72.129	119	119.243	166	165.934	213	212.937
26	25.890	73	72.842	120	120.224	167	167.262	214	213.919
27	26.825	74	73.852	121	120.894	168	168.247	215	215.244
28	27.827	75	74.924	122	121.911	169	168.891	216	216.251
29	28.866	76	76.024	123	123.030	170	169.885	217	216.924
30	29.849	77	77.047	124	124.012	171	171.144	218	217.961
31	30.985	78	78.042	125	124.862	172	172.207	219	219.136
32	32.054	79	78.994	126	125.839	173	172.991	220	220.131
33	32.977	80	79.992	127	127.215	174	174.015	221	220.964
34	33.944	81	81.044	128	128.228	175	174.861	222	221.946
35	34.874	82	82.036	129	128.901	176	175.878	223	223.324
36	35.820	83	83.026	130	129.895	177	177.115	224	224.283
37	36.845	84	83.945	131	131.016	178	178.102	225	224.896
38	37.848	85	84.853	132	132.047	179	179.270	226	225.921
39	39.067	86	85.856	133	132.916	180	180.195	227	227.138
40	40.089	87	87.181	134	133.937	181	180.990	228	228.144
41	40.865	88	88.206	135	135.238	182	182.003	229	228.914
42	41.890	89	88.895	136	136.212	183	183.341	230	229.931
43	42.897	90	89.881	137	136.876	184	184.384	231	231.225
44	43.941	91	90.913	138	137.888	185	185.086	232	232.209
45	44.975	92	91.933	139	139.117	186	186.032	233	232.920
46	45.961	93	92.917	140	140.232	187	187.054	234	233.964
47	46.967	94	93.918	141	141.108	188	188.052	235	235.226
48	48.061	95	95.110	142	142.104	189	188.917	236	236.229
49	48.986	96	96.110	143	142.962	190	189.941	237	236.968
50	49.930	97	96.932	144	143.912	191	191.241	238	237.951
51	50.857	98	97.929	145	145.058	192	192.211	239	238.585
52	51.831	99	98.994	146	146.098	193	192.959	240	239.575
53	52.857	100	99.977	147	147.272	194	194.001	241	240.942
54	53.867	101	100.899	148	148.236	195	195.127	242	241.909
55	55.103	102	101.890	149	149.016	196	196.112	243	243.113
56	56.117	103	103.148	150	149.962	197	196.963	244	244.144
57	56.863	104	104.144	151	151.166	198	197.976	245	245.187
58	57.848	105	104.853	152	152.255	199	199.276		

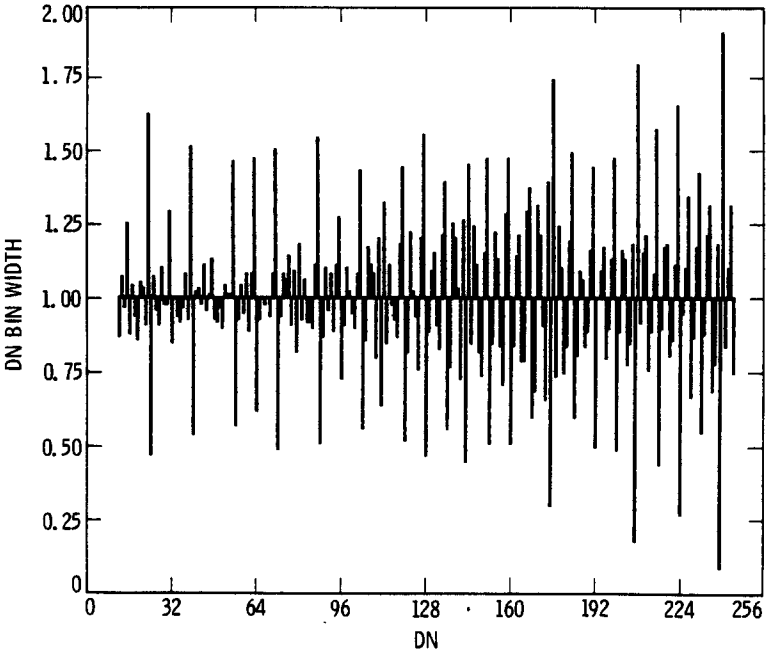

Figure 4-198. Effective DN bin widths resulting from unequal bit weighting.

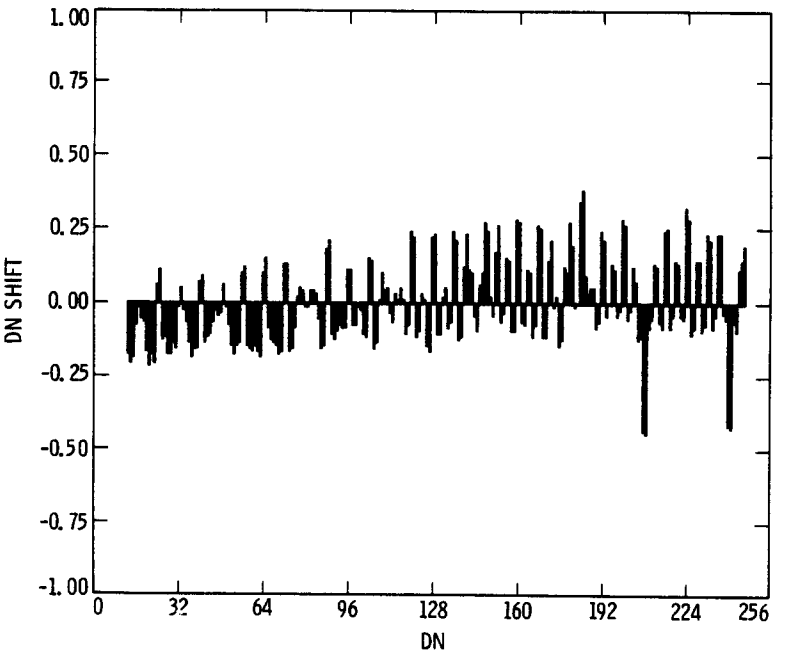

Figure 4-199. Deviation of each DN from its nominal integer value required to correct for unequal bit weighting.

spectrum.

To accomplish the desired color matching, we employ the tri-dimensional characteristics of color vision. In theory, it is possible to match any color by using the proper additive mixture of three components of light having suitably chosen chromaticities. By chromaticity we mean those characteristics of light specified by its dominant wavelength and its purity. Color-matching studies have shown that a suitably large gamut of colors can be produced if the three components are selected to have generally red, green and blue chromaticities. Using such selected components, the amount of each component required to match the color of a given sample has been determined for a series of "standard" observers. Graphs of the quantity (luminance) of each component required to match a sample of light at a given wavelength versus this wavelength have been generated. These curves are called color-mixture curves, and a given set of curves applies only for the original three components used to generate the data. However, comparable color-mixture curves can be generated for any other set of three components by fractional (also called linear homogeneous) combinations of the original color-mixture curves. The CIE has adopted standard color-mixture curves based on such a linear homogeneous combination, their green curve being identical to the standard luminosity curve for the human eye, and the other two curves having no negative values. There exists no set of three real components which can produce the CIE color-mixture curves directly; they are only a mathematical construct. However, the CIE curves do express all of the color information represented by any directly-determined set of color-mixture curves and are easy to use in computations.

For each of the chosen three standard stimuli, the magnitudes of light that are necessary to match a given sample are called tristimulus values. These values can be computed by integrating the product of each of the corresponding color-mixture curves multiplied by the spectrum (reflectivity or radiance) of the sample. The chromaticity of the sample can then be expressed using these tristimulus values. In particular, the normal way of specifying chromaticity is by stating the ratios of each of two of the tristimulus values to the sum of all three. These ratios can then be plotted in a standard two-dimensional Cartesian coordinate system. Such a plot is called a chromaticity diagram. The chromaticity coordinates for pure spectrum colors define the envelope of all colors whose chromaticities can be matched by the three components being used.

The first step in color matching using SSI data is to determine the tristimulus values of the colors (reflectivity or radiance) in the scene at each pixel location. Using the SSI calibration established in Section IV-A-3, the mean reflectivity or radiance can be determined across the filter bandpasses of a registered multispectral data set at each pixel location. However, to

accurately calculate the corresponding tristimulus values, the entire spectral reflectivity or radiance curve must be known. Since the spectrum outside of the filter bandpasses is unknown, the tristimulus values can only be estimated. This estimate could be done by constructing a continuous spectrum for each pixel somehow (linear interpolation or extrapolation between bandpasses, a linear combination of curve fitting functions, etc.) that is consistent with the SSI data and integrating this times each of the color-mixture curves. However, given the uncertainty in this approach, it has been decided instead to use a simpler approach that results in a fixed transformation from the multiple SSI reflectivity or radiance values to the (approximate) corresponding tristimulus values.

Each of the tristimulus values of a given pixel is written as a linear combination of the reflectivity or radiance values obtained using each SSI filter:

$$[T] = [M][R]$$

where

[T] is a 3 x 1 matrix of tristimulus values for the scene
[M] is a 3 x n transformation matrix corresponding to the n separately filtered SSI input images
[R] is a n x 1 matrix of reflectivity or radiance values for the n SSI filtered images

Since [T] and [R] can be computed for n known standard spectral scenes using the color mixture curves and the SSI spectral response curves, we can solve for [M]. More than n standard spectral curves can be used and [M] determined by a least-squares fit. Using this matrix [M] will yield the correct [T] for any linear combination of the n standard spectral curves, and for other spectral curves will yield reasonably acceptable values of [T] provided the $\geq$ n standard spectral curves are selected with discretion. In addition, the computational load is reduced since the same [M] matrix applies to every pixel.

The limits of the colors that are detectable by the SSI can be defined by their tristimulus values. In determining scene reflectivity or radiance from our calibration of the SSI, we have assumed that the quantity of interest is constant over the filter bandpass. This limits the degree of spectral purity in a scene that can be accurately detected and reconstructed. The tristimulus values of spectra having constant reflectivity or radiance across each SSI filter bandpass and zero reflectivity or radiance outside of that bandpass have been computed, where the bandpass is defined by the half-maximum points in the SSI system spectral response curve (using a

solar illuminant for the case of reflectivity). The corresponding chromaticity coordinates are shown in Figure 4-200 plotted on the standard CIE 1931 chromaticity diagram. The triangle formed by the violet, green and red points defines the limit of colors detectable by the SSI.

To properly display a reconstructed natural color image having known relative tristimulus values at each pixel, the correct transfer function from tristimulus values to the DN levels to apply to each output display channel (of which there are three) must be known. The tristimulus values of the color produced by applying a set of DN values to the three CRT channels are given by

$$[\,t\,] = [\,x\,][\,K'\,][\,I\,] = [\,x\,][\,K\,][\,DN^{2.6}\,]$$

where

- [t] is a 3 x 1 matrix of CIE tristimulus values for the resulting display color
- [x] is a 3 x 3 matrix of CIE tristimulus values for the color output by each of the three individual display channels
- [K'] and [K] are 3 x 3 diagonal matrices of constant factors that determine the color balance between the three channels of the CRT
- [I] is a 3 x 1 matrix of the intensities from each display channel

and $I \propto DN^{2.6}$ for most modern CRTs. For the case where a CRT display is used, the device is adjusted so that equal DNs applied to each channel result in a display radiance with some desired set of tristimulus values (e.g., equal to those of CIE standard illuminant D55, which closely approximates the solar spectrum). The example CRT adjustment mentioned here implies that

$$[\,t_{D55}\,] = [\,x\,][\,K\,][\,d\,]$$

where

[d] is a 3 x 1 matrix of equal DN values applied to all three channels.

Therefore,

$$[\,K\,][\,d\,] = [\,x\,]^{-1}\,[\,t_{D55}\,]$$

Taking the three elements of [d] to be 1 (since scaling the inputs to all three channels in the same way does not change the resulting color), we can solve for the diagonal elements of [K]. Since we want [t] = [T] for each pixel of a reconstructed image, the proper relative DNs to apply to each channel are then given by

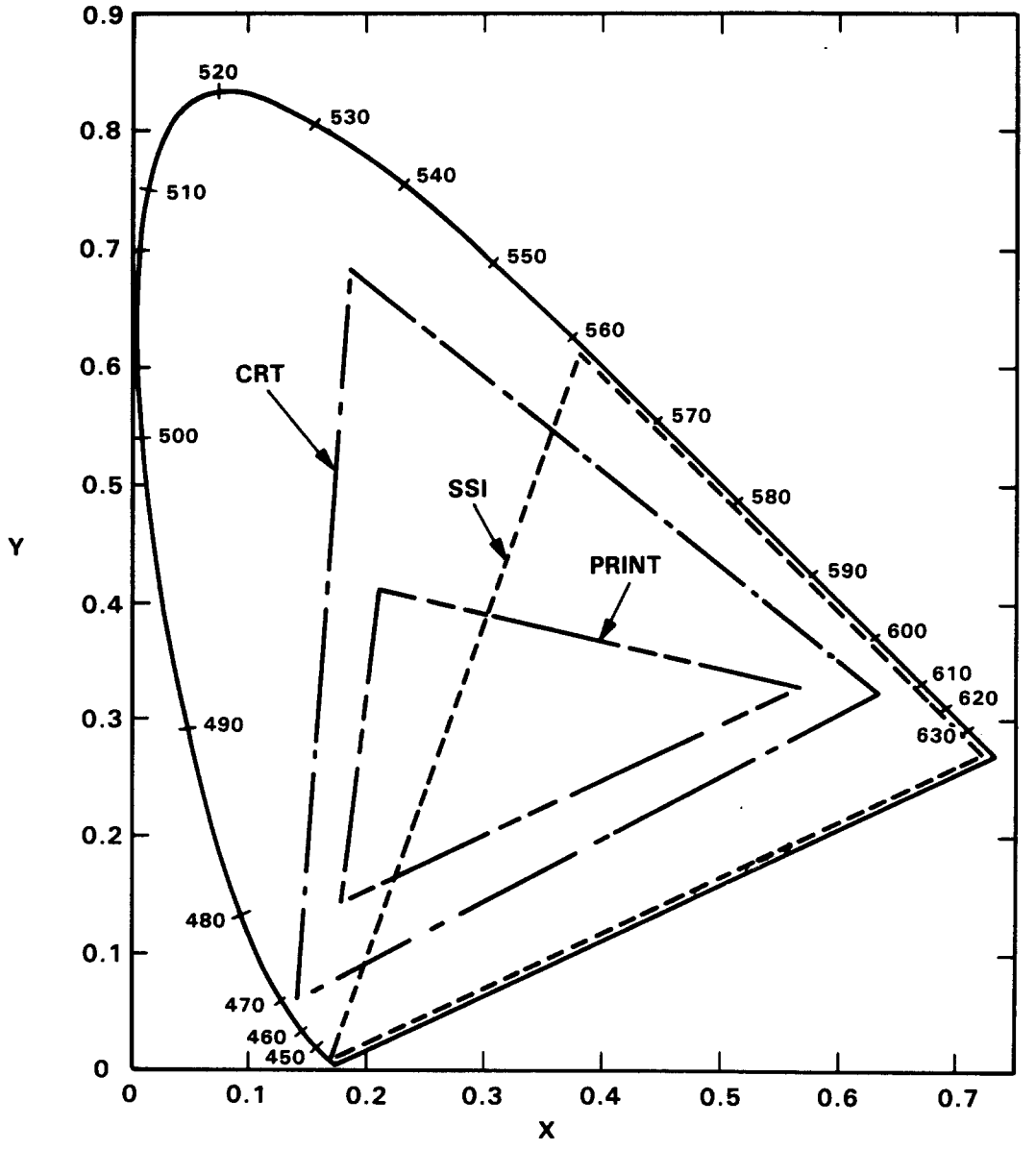

Figure 4-200. The standard CIE 1931 chromaticity diagram showing the chromaticity coordinates for the range of colors detectable by the SSI, the range of colors that can be displayed on a MIPL CRT display, and the range of colors that can be reproduced on a MIPL/JPL Photolab color print.

$$[\,DN^{2.6}\,] = [\,K\,]^{-1}\,[\,x\,]^{-1}\,[\,M\,]\,[\,R\,]$$

These relative DNs can all be scaled so that the maximum DN applied to any channel over the entire image equals 255 (saturation) in order to obtain a bright display of the properly balanced color image. Since the CRT display is calibrated in units of radiance, the matrix [R] should consist of radiance values from the SSI images when the output is to be displayed on a CRT. The transformation matrix [M] should have been determined for standard spectral radiance (not reflectivity) colors. In addition, one of the standard spectral radiance curves used to determine [M] should be the radiance curve of the standard neutral reference used to adjust the CRT (e.g., D55) when a CRT display is to be used.

For the MIPL CRT displays, the chromaticity coordinates of the three channels are plotted on the standard CIE 1931 chromaticity diagram in Figure 4-200. The triangle formed by the three points defines the limit of colors that can be displayed on the CRT. The standard radiance spectra used to determine [M] should all have chromaticity coordinates that are contained within both this triangle and the one defining those spectral radiance colors detectable by the SSI.

To properly display a reconstructed natural color image using a photographic print, a different transfer function from the desired tristimulus values to the DN level to apply to each of the three film recorder channels must be used. Since color photography involves a subtractive process (versus the additive process applicable to a CRT display), there is no analytical solution to the problem of color matching. Instead, empirical solutions are typically used to give satisfactory results. What is actually required to do accurate color reconstruction (assuming the transform from channel DN inputs to the desired tristimulus values is invariant) is a complete mapping of all combinations of three-channel DN values into the resulting photographic print reflectivity tristimulus values. Creating such a map (which could involve up to $255^3 = 1.66 \times 10^7$ different colors) is impractical. Simpler mappings of, say, 4^3 to 10^3 colors might be achievable, and interpolation could be used for intermediate colors not mapped directly. Simpler yet is to create a mapping by assuming that color reproduction on photographic prints is an additive process rather than subtractive. Although this assumption will result in color reconstruction errors due to color channel crosstalk and any nonlinearities in print reflectivity per DN, the goal of approximate color reconstruction that yields visually acceptable results can be met for many colors.

Using the additive approximation and assuming linear print reflectivity per DN, the tristimulus values of the spectral reflectance of a print produced

by applying a set of DN values to the three film recorder channels are given by

$$[\,t\,] = [\,Z\,][\,C\,][\,DN\,]$$

where

- [Z] is a 3 x 3 matrix of CIE tristimulus values for the spectral reflectivity produced from each of the three individual film recorder/print channels. These must be determined from spectral reflectivity measurements of a print having areas exposed by only one channel at a time.
- [C] is a 3 x 3 diagonal matrix of constant factors that determine the balance between the three channels of the film recorder/print.

The film recording, photoprocessing and printing procedures must be adjusted and controlled so that print reflectivity is linear with DN and equal DNs applied to each channel result in a print reflectivity having some desired set of tristimulus values (e.g., equal to those of a neutral gray surface). The example process adjustment mentioned here implies that

$$[\,t_{gray}\,] = [\,Z\,][\,C\,][\,d\,]$$

Therefore,

$$[\,C\,][\,d\,] = [\,Z\,]^{-1}\,[\,t_{gray}\,]$$

Taking the three elements of [d] to be 1, we can solve for the diagonal elements of [C]. Achieving [t] = [T] for each pixel of a reconstructed image then requires that the relative DNs applied to the film recorder be given by

$$[\,DN\,] = [\,C\,]^{-1}\,[\,Z\,]^{-1}\,[\,M\,][\,R\,]$$

These relative DNs can all be scaled so that the maximum DN applied to any channel over the entire image equals 255 (saturation) in order to produce a bright print of the color image. As long as the film recording, photoprocessing and printing procedures remain unchanged, the transformation matrix derived in this way will result in the correct colors being reproduced for neutral grays and for the colors that result from driving only a single channel at a time. Other colors will only be approximately correct. Since the photoprocessing procedures are adjusted to produce a desired print reflectivity, the matrix [R] should consist of reflectivity values from the SSI images when the output is to be a color photographic print. The transformation matrix [M] should have been determined for standard spectral reflectivity (not radiance) colors. And one

of the standard spectral reflectivity curves used to determine [M] should be the reflectivity curve of the standard neutral reference used to calibrate the photoprocessing (e.g., gray) when color prints are being made.

For the MIPL/JPL Photolab color prints, the chromaticity coordinates of the three component print colors are plotted on the standard CIE 1931 chromaticity diagram in Figure 4-200. The triangle formed by the three points defines the limit of colors that can be reproduced on a color print. The standard reflectivity spectra that are used to determine [M] should all have chromaticity coordinates that are contained within both this triangle and the one defining those spectral reflectivity colors detectable by the SSI.

The SSI was used to obtain images of the color target (see Section II-D) through each of its color filters whose bandpass overlaps the visual response curve (violet, green, red, 7270 Å and 7560 Å). Processing of these data is ongoing and the results will be presented in a future supplement to this report. Reconstructed color images will be created using the methods described above to verify that they result in visually acceptable color displays. Six different reconstructions will be done using data from the violet and green images plus one, two or all three of the "red" images. The resulting color prints will be included in the supplemental report to be published.

Verification that the color reconstructions are acceptably accurate cannot be done visually since what the SSI saw was a spectral combination of the collimator lamp, its optics, the target transmission and the thermal vacuum chamber window transmission. Since it is impractical for an observer to see what the SSI saw, the verification of correct color reconstruction will have to be done mathematically. The chromaticity coordinates for the actual spectral reflectivity curves of several color squares on each photographic print will be computed. The corresponding chromaticity coordinates will be computed for these squares for the spectral intensity seen by the SSI divided by the solar spectrum (to get an equivalent reflectance spectrum assuming solar illumination, since the SSI calibration conversion factors are derived for this case). The two sets of values will be compared in the supplemental report. Only squares whose chromaticity coordinates lie within the reproducible color range shown in Figure 4-200 will be compared.

8. Light Leaks

The light-leak test performed during subsystem-level calibration analyzed the effectiveness of the closed camera shutter in blocking out light. Zero-exposure frames were recorded through each filter in gain state 4 at

the 60 2/3-sec imaging rate; in addition, the 8 2/3-sec and 30 1/3-sec frame rates were tested using the clear filter. The test was conducted at instrument temperatures of -10° C, +8° C and +18° C. No differences were observed in the results for different temperatures. Only the data acquired at the nominal instrument temperature of +8° C were analyzed in detail. Images were made both in total darkness and with the SSI viewing a source of high- level illumination. Figure 4-201 shows an example of a zero-exposure image acquired at the 60 2/3-sec frame rate using the clear filter and with illumination on. The difference in DN values for the illuminated and non-illuminated frames is a measure of the magnitude of the light leak. The DN difference was averaged over the central 790 x 790 pixel square of each image.

Table 4-25 summarizes the results of these tests. The DN values were converted to electrons using a conversion factor of 42.3 e-/DN in gain state 4, and to an equivalent luminance level had the shutter been open using a conversion factor of 1049 DN/ftL-sec for the clear filter and an average integration time of 27.9 sec in the 60 2/3-sec imaging mode, 14.7 sec in the 30 1/3-sec mode and 4.6 sec in the 8 2/3-sec mode (maximum integration times are approximately twice these values). The leakage

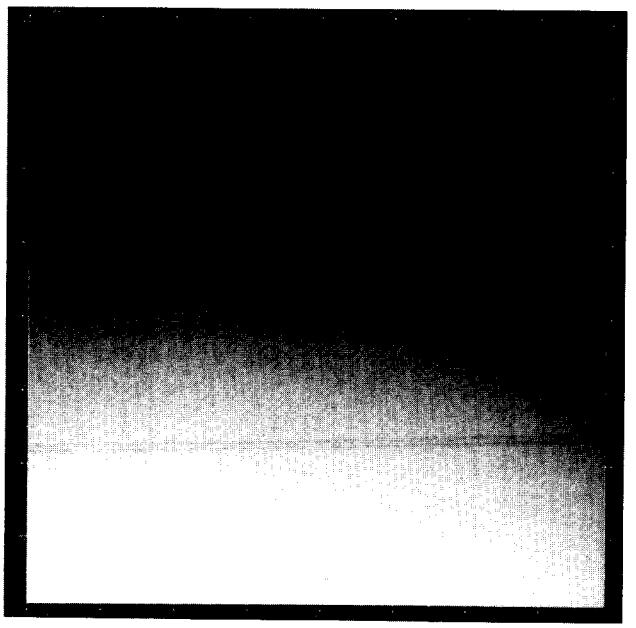

Figure 4-201. Zero-exposure frame acquired at the 60 2/3-sec frame rate using the clear filter and with the SSI viewing a source of high-level illumination.

equivalent luminance divided by the actual luminance of the calibration light source (6200 ftL) yields the fraction of the incident light reaching the detector with the shutter closed. The brightness of Jupiter at zero phase is 330 ftL, a factor of ~18 lower than the calibration light source, and hence the amount of light reaching the detector would be lower by this factor, as shown in Table 4-26. It can be seen that the light leakage impinging on the CCD from the disk of Jupiter ranges from about 3.5 DN for the clear filter in gain state 4 in the 60 2/3-sec mode down to ~0.5 DN or less in the

Table 4-25. Light leak measurements obtained by comparing zero-exposure images made in darkness and with a 6200-ftL calibration light source.

filter	frame rate (sec)	avg. gain state4 DN	avg e-	equivalent luminance (ftL)	leakage fraction
clear	8 2/3	10.0	392	2.51×10^{-3}	4.04×10^{-7}
clear	30 1/3	34.4	1349	2.55×10^{-3}	4.11×10^{-7}
clear	60 2/3	65.6	2573	2.51×10^{-3}	4.04×10^{-7}
5600 Å	60 2/3	1.0	39	3.8×10^{-5}	6.2×10^{-9}
6600 Å	60 2/3	2.6	102	9.9×10^{-5}	1.60×10^{-8}
< 4450 Å	60 2/3	0.0	0	0	0
7560 Å	60 2/3	2.3	90	8.8×10^{-5}	1.42×10^{-8}
> 9680 Å	60 2/3	6.6	259	2.52×10^{-4}	4.07×10^{-8}
7270 Å	60 2/3	1.1	43	4.2×10^{-5}	6.8×10^{-9}
8890 Å	60 2/3	8.1	318	3.10×10^{-4}	4.99×10^{-8}

Table 4-26. Expected light reaching the detector from the disk of Jupiter at zero phase in various imaging modes with the shutter closed.

filter	frame rate (sec)	avg. gain state4 DN	avg e-	equivalent luminance (ftL)
clear	8 2/3	0.53	21	1.33×10^{-4}
clear	30 1/3	1.83	72	1.36×10^{-4}
clear	60 2/3	3.49	137	1.33×10^{-4}
5600 Å	60 2/3	0.05	2	2.0×10^{-6}
6600 Å	60 2/3	0.14	5	5.3×10^{-6}
< 4450 Å	60 2/3	0.00	0	0
7560 Å	60 2/3	0.12	5	4.7×10^{-6}
> 9680 Å	60 2/3	0.35	14	1.34×10^{-5}
7270 Å	60 2/3	0.06	2	2.2×10^{-6}
8890 Å	60 2/3	0.43	17	1.65×10^{-5}

8 2/3-sec mode or with other filters in the 60 2/3-sec mode. The variation with filter selection suggests that the leakage is occurring along the optical axis of the instrument, since otherwise no dependence on filter choice would be expected. The signal due to light leakage is small and in most cases negligible. However, viewing Jupiter or its satellites at low phase angles when they fill the SSI FOV should be avoided when using the clear filter in the 30 1/3 or 60 2/3-sec modes in gain state 4 if high photometric accuracy is desired without having to correct for light leakage. Zero-exposure calibration frames in this SSI configuration will have to be acquired keeping the effects of light leak in mind.

9. Variable Vignetting

The purpose of this test was to determine the effects on the radiometric response of the SSI due to having variable amounts of the FOV vignetted by a simulated sunshade. This was accomplished by taking flat-field images through the clear filter in the highest gain state with the simulated sunshade positioned between the light cannon and the SSI aperture. Several exposures were taken with the sunshade vignetting from zero to 75% of the SSI aperture in five steps. The SSI was at a temperature of 0^{o} C for this test, with the CCD at its nominal operating temperature. The data were delivered to the Imaging Team for analysis, but they have not been analyzed as of this date.

B. SPATIAL RESOLUTION

1. Modulation Transfer Function

The resolution limits of the SSI are determined by computing the modulation transfer function (MTF). The procedure for computing the MTF is outlined below.

The image obtained of a light source by an optical system is described mathematically by a convolution of the spatial distribution of the source radiance with a point spread function (PSF), which is the optical system's image of a point light source. The line spread function (LSF) is the one-dimensional equivalent of the PSF and is defined by

$$LSF(x) = \int PSF(x,y)\, dy$$

in the x-direction. If a target containing a vertical step function is imaged, the horizontal profile S(x) in the image is a convolution of the step function with the LSF. The LSF is obtained by differentiation of the imaged step function.

$$LSF(x) = \frac{d}{dx} S(x)$$

The optical transfer function (OTF) is defined in each of the x and y directions as the normalized Fourier transform of the LSF in that direction, e.g.,

$$OTF(f_x) = \frac{\int LSF(x)\, e^{-2\pi i f_x} dx}{\int LSF(x)\, dx}$$

The MTF is defined as the magnitude or absolute value of the OTF

$$MTF(f_x) = | OTF(f_x) | = | a + ib |$$

and the phase is given by

$$phase(f_x) = \tan^{-1} (b/a)$$

In practice, the LSF is computed many times from several traces across the step function image. Each digital LSF is resampled using the Sampling Theorem so that the centroid C of each LSF is centered on a pixel, yielding the integral line spread function (ILSF):

$$C = \sum_{n=1}^{N} (n-1)\, LSF_n \Big/ \sum_{n=1}^{N} LSF_n$$

$$ILSF_m = \sum LSF_n \frac{\sin (m-n)\, \pi}{(m-n)\, \pi}$$

where m is some integer distance from C.

Each ILSF is used to generate an OTF, and all of the complex OTFs are averaged. The Sampling Theorem is used to interpolate to eliminate phase bias introduced by the shifted LSFs; this affects only the resulting phase, not the MTF. The complex OTF average is used instead of an average of the MTFs because the resulting MTF is independent of the random noise level in the image.

The MTF target consists of parallel alternating black and white stripes and may by oriented either horizontally or vertically so that the MTF can be measured along both the x and y axes. Note that the target is oriented with the bars horizontal to measure the MTF in the vertical direction and vice versa.

In 1985, data were collected with the camera in thermal vacuum at the nominal temperature of +8° C. Images were processed and curves obtained for full-resolution-mode images of the horizontal target with all eight filters and of the vertical target with the clear filter, and for summation-mode images of the target in both orientations with the clear filter. These images were all 1/2- or 2/3-full well exposures. Data products included photographic prints of images, line traces, and plots of MTF and phase curves as a function of spatial frequency. An example of a typical SSI image of the MTF target appears in Figure 4-202. Plots of MTF amplitude and phase and image line traces for selected frames are shown in Figures 4-203 through 4-213. The MTF values at the Nyquist frequency for all of the cases tested are tabulated in Table 4-26. These data allow comparisons of horizontal-bar and vertical-bar MTFs in both normal and summation mode, comparisons of horizontal-bar MTFs between different filters, and studies of how both horizontal-bar and vertical-bar MTFs depend on exposure time. The following observations were noted:

(a) At low signal levels (<10000 e-) in both normal and summation mode, the vertical-bar MTF improves with longer exposure time, but the horizontal-bar MTF is unaffected by exposure time in the normal mode. At higher signal levels (1/3 of full well and above) exposure time had no significant effect on any of the MTF curves.

(b) At 2/3-full well in both modes, there is no significant difference between the horizontal-bar and vertical-bar MTFs.

(c) The horizontal-bar MTF degrades slightly as the filter wheel is stepped from short-wavelength to long-wavelength filters. At the Nyquist frequency this degradation amounts to a factor of 2 between the <4450 Å and >9680 Å filters. This effect was expected. Only the 7560 Å filter does not fit this pattern.

(d) The vertical-bar phase shift amplitude decreases with exposure time in the full-resolution mode and increases with exposure time in the summation mode, while the horizontal-bar phase shift amplitude does not change significantly with exposure time in the full-resolution mode.

(e) The phase shift in both the vertical-bar and horizontal-bar directions for both full-resolution and summation modes at 2/3 full well is not seriously different.

(f) The horizontal-bar phase shift is not greatly affected by choice of filter.

Comparison of the 1985 data with similar data collected in 1983 and 1984 showed a degradation in MTF between 1984 and 1985.

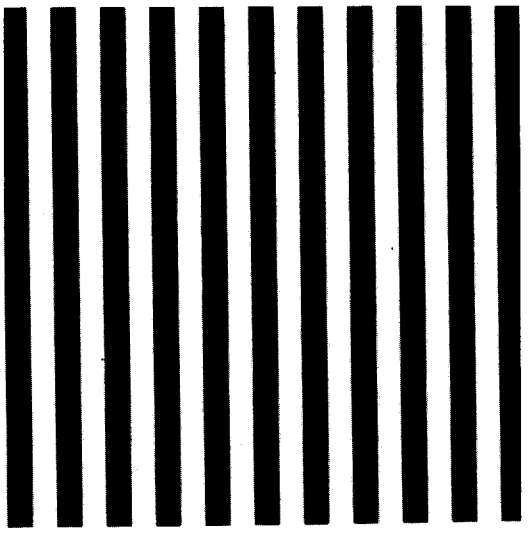

Figure 4-202. Image of the horizontal-bar MTF target through the clear filter with 50-msec exposure time, gain state 4, normal mode.

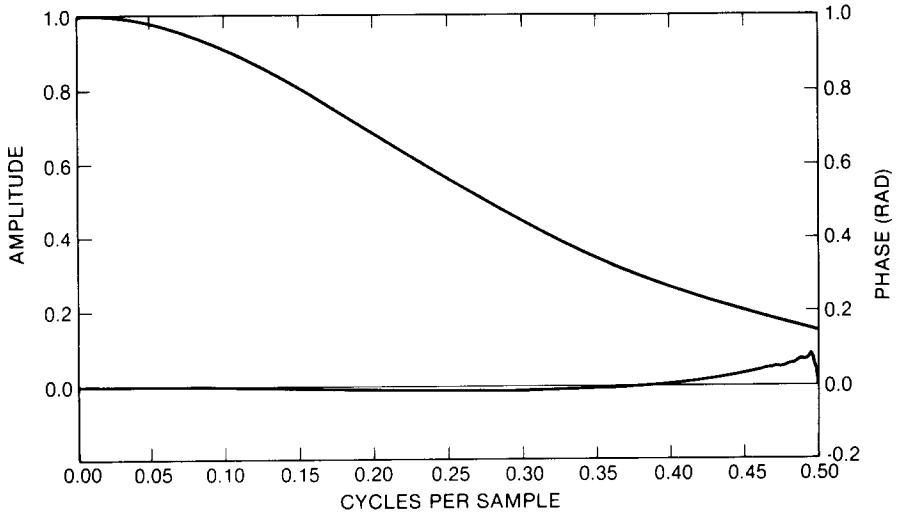

Figure 4-203. Horizontal-bar MTF amplitude and phase from an image through the clear filter with 4 1/6-msec exposure time, gain state 4, normal mode.

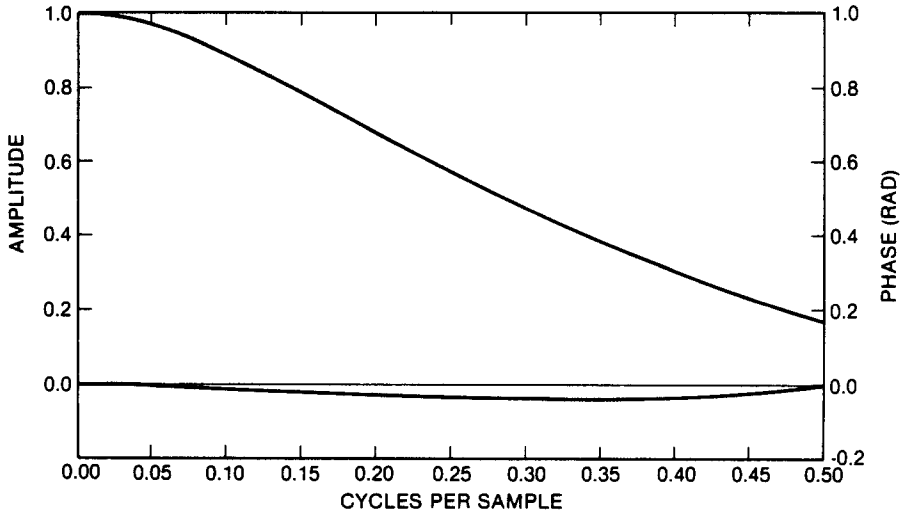

Figure 4-204. Horizontal-bar MTF amplitude and phase from an image through the clear filter with 50-msec exposure time, gain state 4, normal mode.

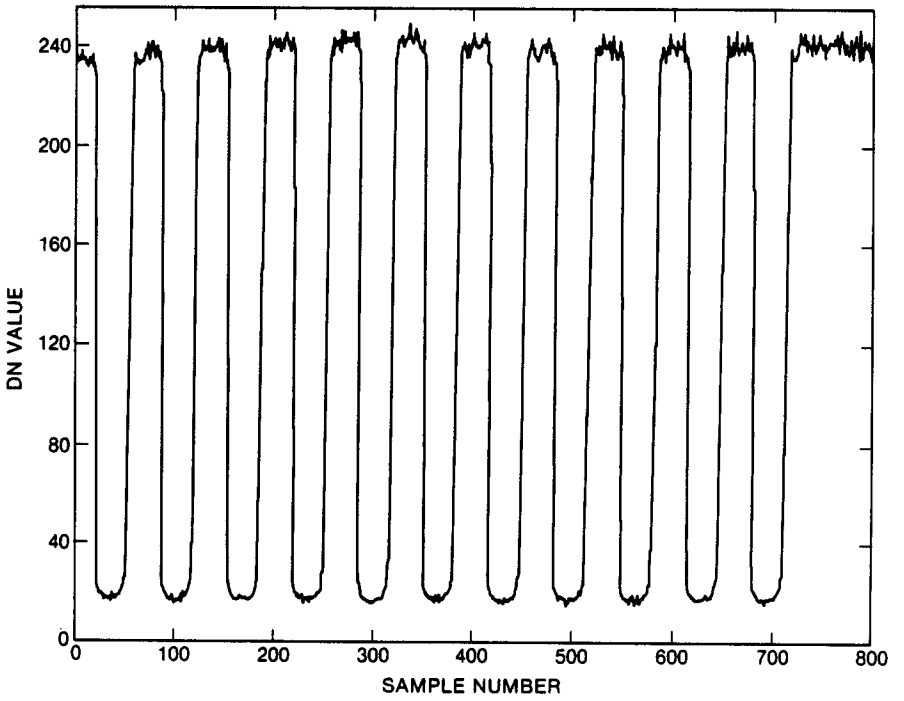

Figure 4-205. Horizontal-bar MTF image line trace from an image through the clear filter with 50-msec exposure time, gain state 4, normal mode.

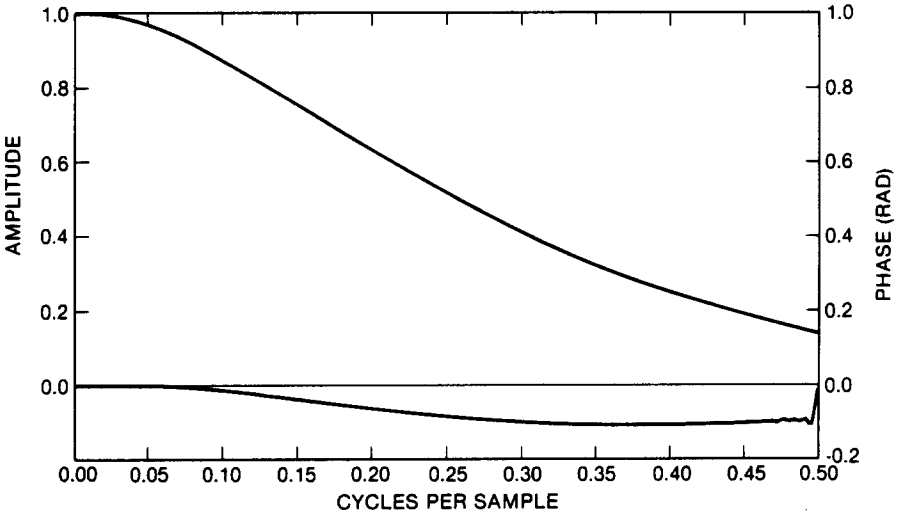

Figure 4-206. Horizontal-bar MTF amplitude and phase from an image through the violet filter with 266 2/3-msec exposure time, gain state 2, normal mode.

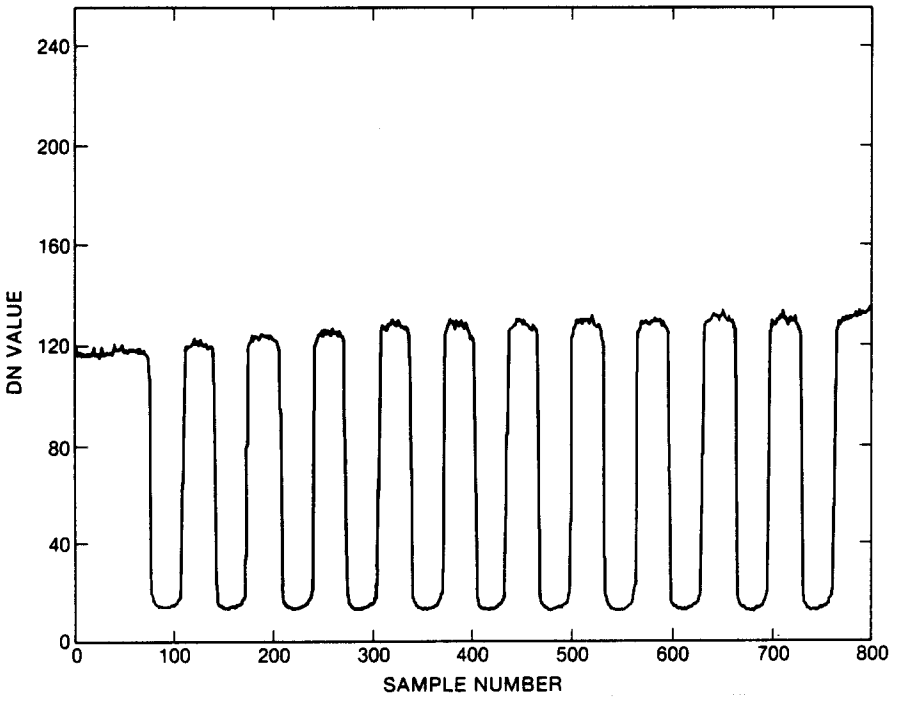

Figure 4-207. Horizontal-bar MTF image line trace from an image through the violet filter with 266 2/3-msec exposure time, gain state 2, normal mode.

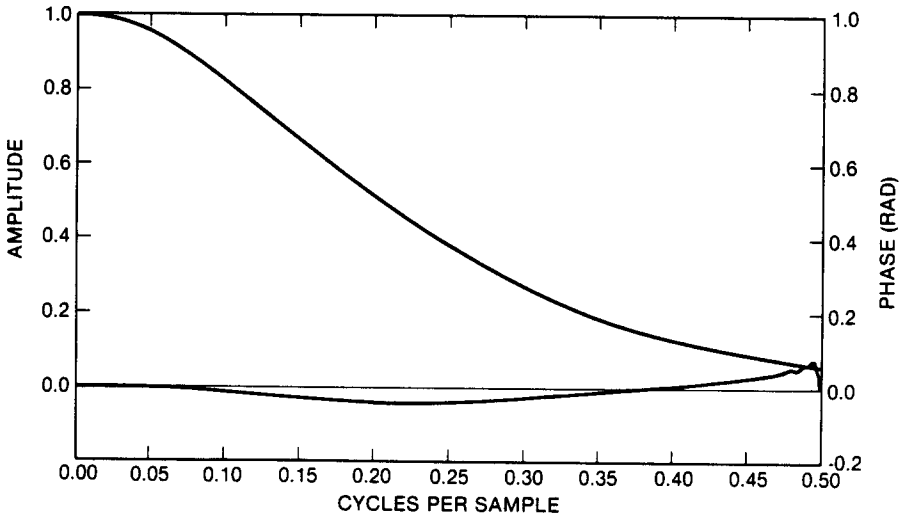

Figure 4-208. Horizontal-bar MTF amplitude and phase from an image through the >9680 Å filter with 133 1/3-msec exposure time, gain state 2, normal mode.

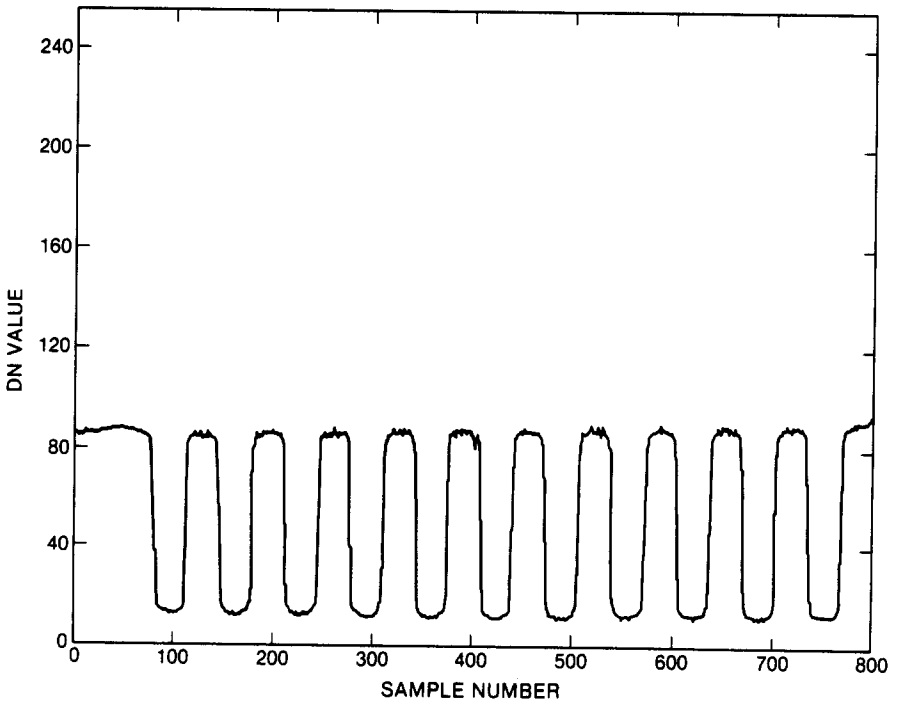

Figure 4-209. Horizontal-bar MTF image line trace from an image through the >9680 Å filter with 133 1/3-msec exposure time, gain state 2, normal mode.

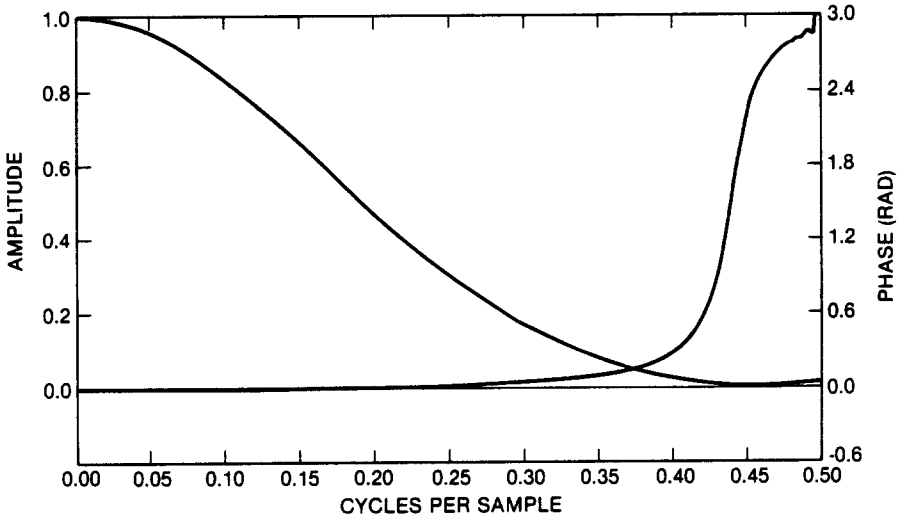

Figure 4-210. Vertical-bar MTF amplitude and phase from an image through the clear filter with 4 1/6-msec exposure time, gain state 4, normal mode.

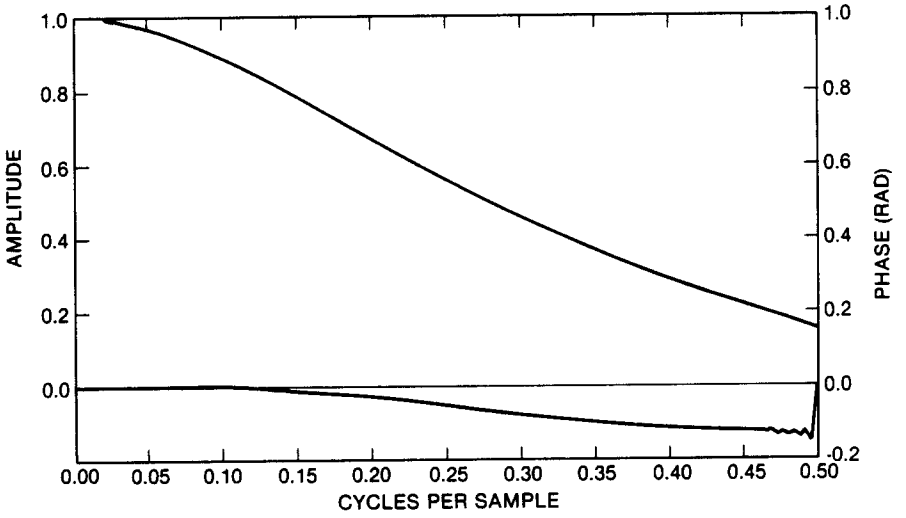

Figure 4-211. Vertical-bar MTF amplitude and phase from an image through the clear filter with 50-msec exposure time, gain state 4, normal mode.

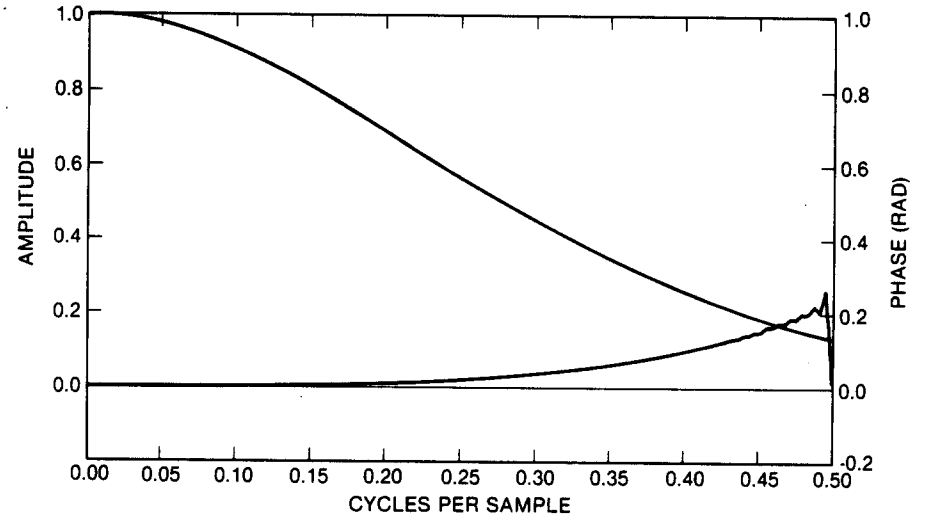

Figure 4-212. Vertical-bar MTF amplitude and phase from an image through the clear filter with 4 1/6-msec exposure time, gain state 4, summation mode.

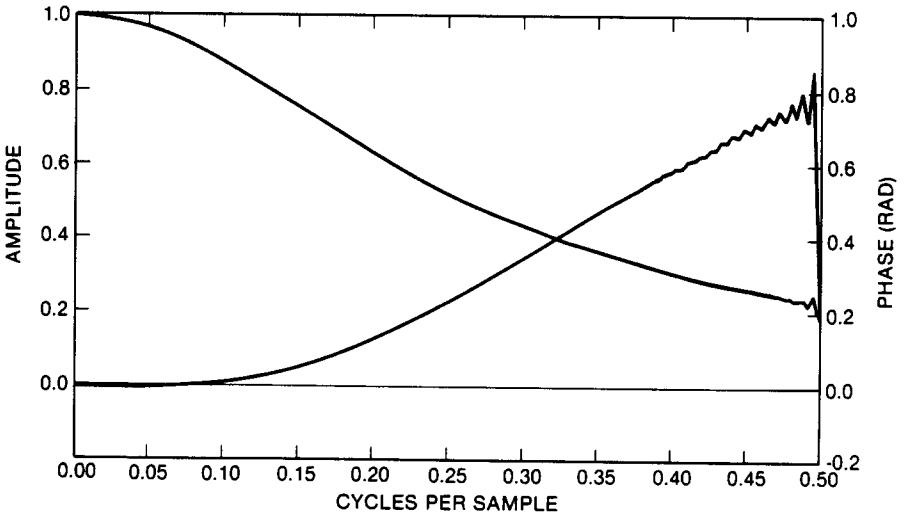

Figure 4-213. Vertical-bar MTF amplitude and phase from an image through the clear filter with 12 1/2-msec exposure time, gain state 4, summation mode.

Table 4-26. Modulation transfer function at the Nyquist frequency.

target orient. (V/H)	filter	mode	gain	exposure (msec)	approx. signal level (1000 e-)	MTF
H	clear	NORM	2	6.25	82	0.072
H	clear	NORM	4	50.00	11	0.176
H	clear	NORM	4	12.50	3	0.170
H	clear	NORM	4	4.17	1	0.148
H	>9680 Å	NORM	2	133.33	38	0.058
H	8890 Å	NORM	2	133.33	34	0.096
H	7560 Å	NORM	2	6.25	31	0.134
H	7270 Å	NORM	2	12.50	41	0.094
H	red	NORM	2	4.17	69	0.090
H	green	NORM	2	8.33	72	0.112
H	violet	NORM	2	266.67	55	0.138
V	clear	NORM	2	6.25	79	0.104
V	clear	NORM	4	50.00	11	0.154
V	clear	NORM	4	12.50	3	0.112
V	clear	NORM	4	4.17	1	0.010
H	clear	SUM	1	6.25	263	0.234
V	clear	SUM	1	6.25	276	0.260
V	clear	SUM	4	12.50	7	0.220
V	clear	SUM	4	4.17	3	0.134

Table 4-27. Modulation transfer function variability with temperature.

	MTF at Nyquist freq.			percent change $-10^{o} \rightarrow +10^{o}$		percent change $+10^{o} \rightarrow +18^{o}$	
filter	-10°C	+10°C	+18°C	Nyq.	avg.	Nyq.	avg.
clear	0.172	0.180	0.184	+4.85	+0.77	-2.09	+0.78
green	0.205	0.211	0.198	+3.20	+0.59	-6.07	-1.69
red	0.185	0.180	0.186	-2.82	-1.18	+3.48	+1.12
violet	0.233	0.258	0.228	+10.96	+3.40	-11.62	-2.60
7450 Å*	0.108	0.106	0.137	-1.90	-3.28	+29.25	+8.91
>9680 Å	0.113	0.096	0.109	-15.04	-6.26	+13.61	+5.19
7270 Å	0.156	0.152	0.157	-2.89	-2.28	+3.21	+1.00
8890 Å	0.145	0.126	0.149	-12.65	-4.81	+17.71	+5.11

* This filter later replaced by 7560 Å filter.

The cause of this is unknown but may be due to a degraded test environment (e.g., degraded collimator focus or increased vibrations) or poor focusing of the SSI. Little change (~5% or less) was seen between the 1983 and 1984 measurements except where attributable to the replacement of the original 7450 Å filter with the current 7560 Å filter.

The 1983 data set also included images obtained for each spectral filter in gain state 2 at temperatures of -10° C, +10° C and +18° C. This permitted the study of temperature effects on MTF. It was found that as the temperature departs from the nominal value, the horizontal-bar MTF decreases at short wavelengths (<6000 Å) and increases at longer wavelengths. Other than the later-discarded 7450 Å filter, only the 8890 Å and >9680 Å filters showed a possibly significant effect, averaging about a 4 to 6 percent increase in MTF going from +10° C to -10° C, and a 5 percent increase going from +10° to +18° C. As a function of spatial frequency, the percentage changes are larger as one approaches the Nyquist frequency. The temperature-dependent effects are summarized in Table 4-27. Included are the MTF at the Nyquist frequency for each filter and temperature, and the percentage change in MTF between the temperatures, both at the Nyquist frequency and averaged over all spatial frequencies.

In 1983, images were acquired through the clear filter in gain states 1 and 2 (1/3- and 2/3-full well exposures) with the MTF target in both orientations, and through all spectral filters in gain state 2 (1/2-full well exposure) with the MTF target in the horizontal orientation. Additional observations noted in this data include the following. Gain state had no significant effect on the MTF curves. The difference between the horizontal and vertical MTFs is minimal in the full-resolution mode, but the vertical-bar MTF is about 30% lower than the horizontal at the Nyquist frequency in the summation mode. MTF is in general worse in the summation-mode than in the normal mode at the same spatial frequency on the detector (i.e., comparing to the full-resolution mode at half the summation mode spatial frequency); however, at equivalent cycles/sample, the summation mode has significantly better MTF than the full-resolution mode. Ascending (black to white) and descending (white to black) edges yield nearly identical MTF curves. Nearly identical MTF curves obtained from the right, left and center parts of an image show that the spatial dependence of MTF is insignificant. The only unexpected change in MTF with filter choice was a greater-than-expected degradation in the middle frequencies for the later-rejected 7450 Å filter. The phase function is generally negative on ascending edges and positive on descending edges, indicating that the upper edge of a high-contrast feature is rounded off more than the lower edge. The amplitude of the phase function increases with temperature and is higher on the right edge of an image than it is on the left. The amplitude increases with exposure time in gain state 2 but is exposure-independent in gain state 1.

The phase function is relatively unaffected by filter selection, except that the amplitude was larger for the 7450 Å and 5600 Å filters than for the clear filter, and the 8890 Å filter had very little phase shift at all.

The accuracy of the MTF measurements can potentially be affected by adverse conditions in the calibration environment. Specifically, the vibrations caused by the vacuum chamber pumps and other machinery in the test facility, footsteps of test personnel, passing vehicles, and so on, can degrade the apparent resolution of the instrument. Although the vacuum pumps for the SSI chamber were shut off during the collection of MTF data to minimize this source of vibration, there were other potential vibration sources present that were beyond the control of the test personnel. Thus the MTF data represent a lower limit on the resolution performance of the SSI, and the true MTF, measured under ideal testing conditions, would be at least as high.

Another possible influence on the measured MTF is the MVM collimator used in the calibration, which has its own MTF. However, depending on the relative orientation of the two optical systems, the collimator would be as likely to improve as to degrade the measured MTF of the SSI, so no attempt has been made to factor out its effect on the MTF data.

To study the quality of resolution of the instrument at low light levels, the 1985 data also included images of the slant-bar target in gain state 4 through the clear filter, at eight different exposures in the full-resolution mode and two exposures in the summation mode. Examples of the full-resolution images (contrast-enhanced) are shown in Figures 4-214 and 4-215 for two different exposure values. The number adjacent to each striped block is the reciprocal of the number of pixels per stripe in that block, i.e., the spatial frequency of the block as a multiple of the Nyquist frequency. These data show that the instrument continues to resolve spatial frequencies of at least 0.4 cycles/sample at the lowest exposure, in which the highest raw DN value in the image is less than 30 (~1200 e- signal). In the summation mode (Figure 4-216) the resolution is poorer, with a maximum spatial resolution on the target of 0.3 cycles/sample at both exposure levels.

2. Point Response Function

The point response function (PRF) describes the response of the instrument to a point light source. It is related to the modulation transfer function as described in the preceding section. It was measured by imaging the point response function target through the clear filter at an instrument

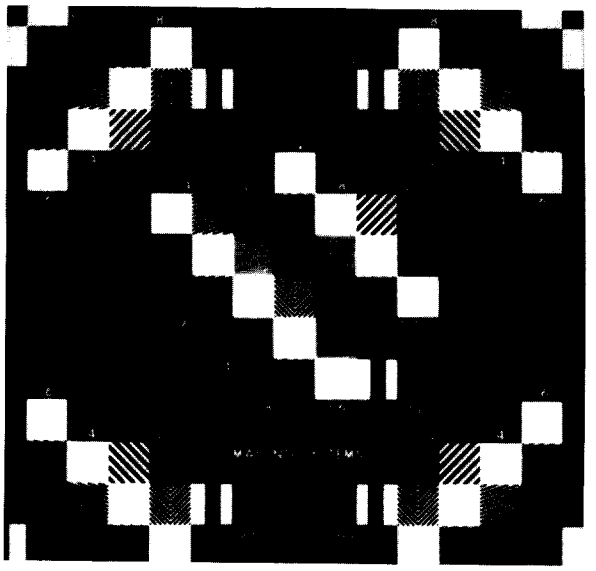

Figure 4-214. Contrast-enhanced full-resolution mode image of the slant-bar target in gain state 4 through the clear filter with an exposure time of 50 msec.

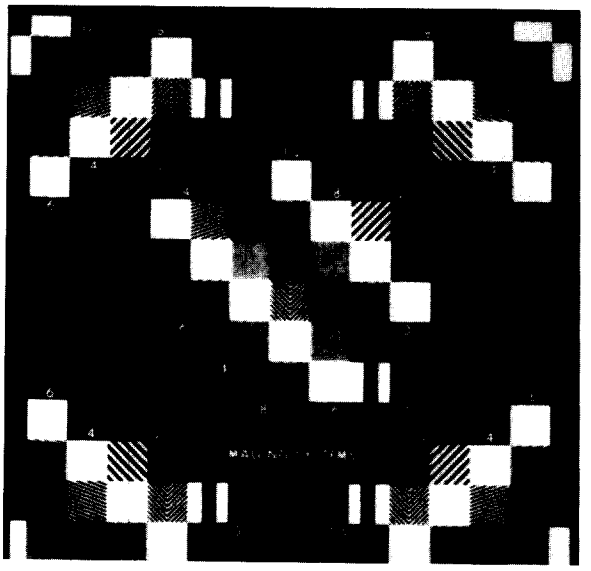

Figure 4-215. Contrast-enhanced full-resolution mode image of the slant-bar target in gain state 4 through the clear filter with an exposure time of 4 1/6 msec.

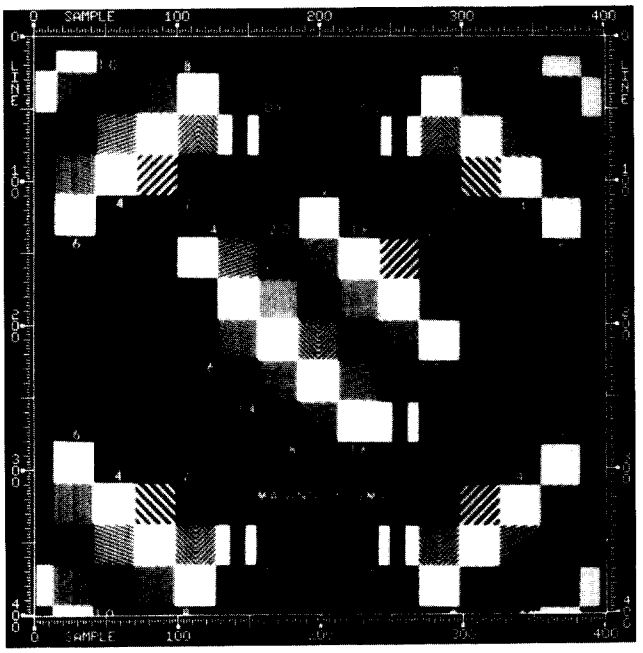

Figure 4-216. Contrast-enhanced summation-mode image of the slant-bar target in gain state 4 through the clear filter with an exposure time of 12 1/2 msec.

temperature of $+8^{o}$ C at five signal levels ranging from 1/5 full well to full well in both the full-resolution mode (8 2/3-sec frame rate) and in the summation mode. The PRF target contains 14 pinholes of approximately 10-μm diameter. Pixel DN listings were generated for the images of the pinholes in each frame. Figures 4-217 through 4-220 show examples of these pixel listings after radiometric calibration. Although the pinholes in the target are about the smallest that could be reliably manufactured, producing the best possible approximation to a point light source, the area covered by the geometric image of a pinhole (without diffraction) on the detector focal plane is comparable to 1 pixel in size. Thus the pinhole images should be regarded as an approximation to the point response function of the instrument.

The mean and sigma in the line and sample directions of the DN distribution for each pinhole image were calculated. It was found that the position of the means tended to vary from frame to frame by about ±0.2 pixel in the sample direction and ±1.0 pixel in the line direction in the normal mode, and by about ±0.1 pixel in the sample direction and ±0.5 pixel in the line direction in the summation mode. However, since this variation was well-correlated between different pinholes and showed no simple dependence on exposure, it is thought to be due to small shifts in the geometry of the calibration setup between exposures that shift the position

of the target image on the detector rather than to any anomaly in the camera performance. The sigmas of the point-spread distributions ranged between 0.75 and 1.1 pixel in the normal mode, and showed a clear correlation between the pinholes, with the sigma in both the line and sample directions consistently being highest in the 2/5-full-well image. The reason for this is not known. In the summation mode, the sigmas averaged about 0.4 pixel in both the line and sample directions and showed no consistent pattern with exposure. In the normal mode, no dependence of line or sample sigma on

sample number

line	583	584	585	586	587	588	589
333	3	4	2	1	2	2	4
334	-2	2	2	2	2	2	3
335	2	9	52	30	6	4	1
336	1	52	460	138	10	11	1
337	7	15	104	74	9	11	8
338	3	4	4	6	6	4	3
339	2	3	7	3	2	1	2

Figure 4-217.
Radiometrically calibrated DN listing of a point response function target pinhole image from a frame taken with the clear filter, normal mode, gain state 3 and 6.25-msec exposure

sample number

line	583	584	585	586	587	588	589
335	12	13	12	10	10	10	1
336	11	40	87	39	8	12	11
337	20	353	1305	313	21	11	11
338	26	320	1484	351	30	10	12
339	13	20	75	76	17	11	10
340	13	11	7	10	10	10	17
341	3	4	2	11	14	12	2

Figure 4-218.
Radiometrically calibrated DN listing of a point response function target pinhole image from a frame taken with the clear filter, normal mode, gain state 2 and 25.0-msec exposure.

sample number

line	290	291	292	293	294	295	296
333	-5	-3	-5	-7	3	2	-5
334	-5	3	3	5	1	0	-6
335	2	1	4	1	4	2	-7
336	-7	4	10	307	20	20	4
337	3	4	2	18	10	10	3
338	2	-6	1	2	1	1	3
339	-4	-4	3	2	-6	-6	-9

Figure 4-219
Radiometrically calibrated DN listing of a point response function target pinhole image from a frame taken with the clear filter, summation mode, gain state 1 and 8.33-msec exposure.

sample number

line	290	291	292	293	294	295	296
165	-5	3	-4	5	1	0	1
166	-5	-6	4	1	4	2	1
167	0	4	10	104	20	5	4
168	0	4	27	932	78	1	3
169	2	1	1	19	18	10	3
170	4	-4	3	2	2	3	0
171	-6	0	3	5	4	4	-5

Figure 4-220.
Radiometrically calibrated DN listing of a point response function target pinhole image from a frame taken with the clear filter, summation mode, gain state 1 and 25.0-msec exposure.

position of the peak relative to the pixel grid is apparent, perhaps because in this mode the signal is spread out over a large number of pixels. In the summation mode, it was observed that the calculated line and sample sigmas ranged from about 0.3 pixel when the mean of the distribution was nearly centered on a pixel up to about 0.6 pixel when the mean fell near the edges of pixels. However, there is a great deal of scatter in these data. These results indicate that in the summation mode, the charge distribution for a point image may have variable width due to insufficient spatial sampling of the point spread function. Insufficient spatial sampling may also account for the fact that the MTF values calculated by Fourier transform of the pinhole-image PRFs tend to be somewhat higher than the MTFs derived from the bar target images (Section IV-B-1), especially in the summation mode and at high spatial frequencies.

C. GEOMETRIC CALIBRATIONS

1. Distortion

No calibration requirements were initially levied for SSI geometric distortion since, at the time, the CCD manufacturer quoted a geometric accuracy of <1 μm (0.066 pixel) for the position of any pixel relative to another across the array and the optics distortion was thought to be negligible. Nevertheless, images of a geometric grid target were acquired and analyzed to confirm the expected SSI geometric fidelity.

The procedure utilized is defined in Reference 4-1, and is given below. The procedure follows the basic strategy of comparing the geometric characteristics of a picture of the grid target recorded by the SSI camera with the known characteristics of the target. The known target, or "object space", characteristics were determined by measuring the location of each grid intersection using a traveling microscope. Measurements were recorded in inches and scaled to line and sample coordinates. These are the locations that would result if the grid target were imaged through a geometrically perfect imaging system. The grid intersection locations in the picture of the grid target, or "raw image" coordinates, were determined using digital image processing techniques supplemented by a series of manual calculations.

The raw image coordinates are compared with the traveling microscope measurements by applying a linear transformation which minimizes the r.m.s. residual error between the two sets of data. Two r.m.s. values are computed, the first by allowing the transformation to adjust for differences in scale, translation and rotation between the two sets of data

(four degrees of freedom); and the second, by allowing the transformation to correct also for differences in skew and aspect ratio (unconstrained case).

Let (x_i, y_i), $i = 1,2,...,N$ be the raw image coordinates, and (u_i, v_i) be the corresponding traveling microscope measurements. In the unconstrained case, the r.m.s. residual is defined as follows:

$$R = \sum_{i=1}^{N} \left[(ax_i + by_i + e - u_i)^2 + (cx_i + dy_i + f - v_i)^2 \right]^{1/2}$$

where the values of a, b, c, d, e and f are chosen to minimize R. If only four degrees of freedom are permitted, the transformation is confined to a magnification, rotation and offset by requiring that $a = d$ and $b = -c$.

Adjusting for rotation and offset errors reduces variables introduced by the arbitrary orientation of the grid target relative to the camera focal plane. Adjusting for scale eliminates errors in camera and collimator focal length measurements. The r.m.s. value computed by allowing these four degrees of freedom is a measure of the total geometric distortion of the camera/collimator system, excluding measurement errors.

In the unconstrained case, the remaining two degrees of freedom, skew and aspect ratio, are also involved. The resulting r.m.s. is a measure of the nonlinear component of the total geometric distortion.

Table 4-28 presents r.m.s. residual error values representing the total and nonlinear ("unconstrained") distortion for the SSI image. It also lists the maximum pixel distortion and the approximate area in the grid pictures where that distortion occurs.

Figure 4-221 is a picture of the original grid target (the "raw image") with grid intersections marked by boxes. It illustrates the degree of success achieved using various image processing techniques to compute the grid intersection locations in the "raw image". The accuracy of computing the locations of the grid intersections is better than 0.1 pixel. The accuracy of centering the boxes at the computed intersections is limited to 0.5 pixel. The object space coordinate measurements are estimated to be accurate to about 0.1 pixel.

Figure 4-222 is a synthesized picture showing the residual errors in image space at each grid intersection for the unconstrained case. The brighter "+" marks represent the "object space" coordinates, while the

Table 4-28. SSI Geometric Distortion Measurements

total distortion			nonlinear distortion		
r.m.s. (pixels)	maximum distance (pixels)	maximum location in image (l,s)	r.m.s (pixels)	maximum distance (pixels)	maximum location in image (l,s)
0.215	0.81	(365,50)	0.157	0.81	(420,795)

duller "+" marks represent the "raw image" coordinates. Displacements have been exaggerated by a factor of 10.0 to aid in the visual interpretation of the data. A close examination of the SSI residuals plotted in Figure 4-222 shows that the distortion in SSI images is very small in the horizontal direction (i.e., along lines) and consists primarily of an apparent vertical shift of all lines in the first ~300 columns. Residual distortion was also computed for a second grid image as a measure of repeatability in the experiment. In the second image, the orientation of the grid target was unchanged and the target was shifted 30 samples to the left and up 34 lines relative to the optical axis. The distortion pattern was similar in both images.

The magnitude of the residual distortions shown in Table 4-28 is surprisingly large. As a result, more detailed study of the possible sources of the distortion was undertaken. An analysis of the image distortion in the SSI optics was performed using the CODE V ray tracing software package. The SSI optical system in combination with the MVM collimator and the thermal vacuum chamber window was also analyzed. This study showed that the SSI optics alone contains pincushion distortion which increases with field angle and reaches a maximum of 18.3 μm at the corner of the CCD (~1.2 pixels). Figure 4-223 shows the percent distortion versus field angle. However, for the calibration test setup, the analysis showed that, assuming zero manufacturing tolerances, the optical distortion should have been negligibly small (maximum of 0.0164 μm or 0.001 pixel) because the distortion of the SSI optics is canceled by the distortion of the MVM collimator optics, which is of nearly identical optical design.

The possible distortion in the MVM collimator was checked by measuring the grid locations of the target in the collimator target holder using a theodolite looking into the collimator optics. The results did not show a distortion pattern that correlated in any way with that seen in the SSI images. It did, however, show evidence of the theoretical pincushion distortion of the collimator optics.

The possibility that the MIPL grid intersection location software was mislocating the intersections by a fraction of a pixel due to some type of

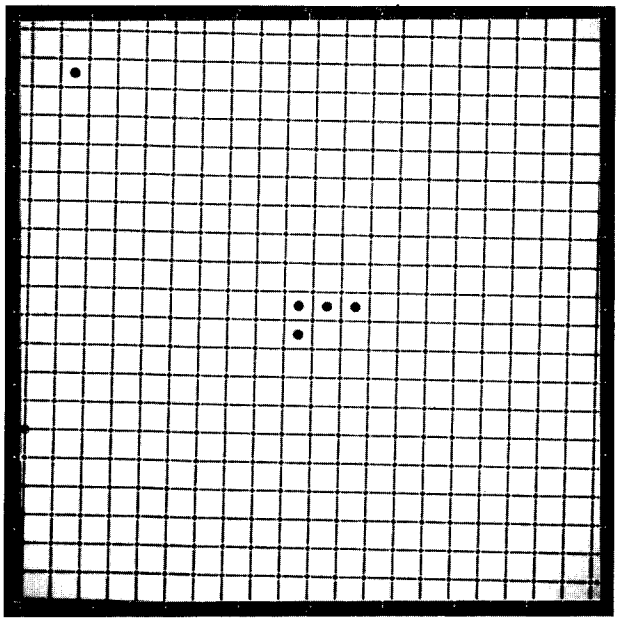

Figure 4-221. Image of the geometric grid target with grid intersections marked by boxes.

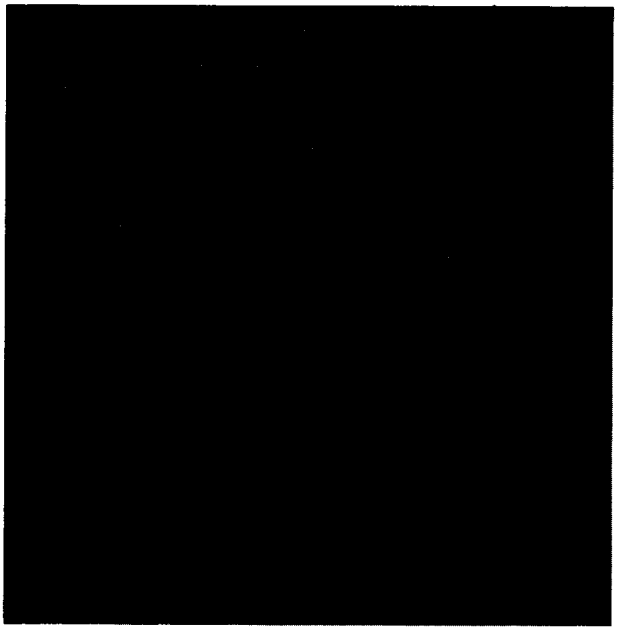

Figure 4-222. Synthesized picture showing the residual errors at each grid intersection for the unconstrained fit of the image coordinates of the intersections to the actual coordinates.

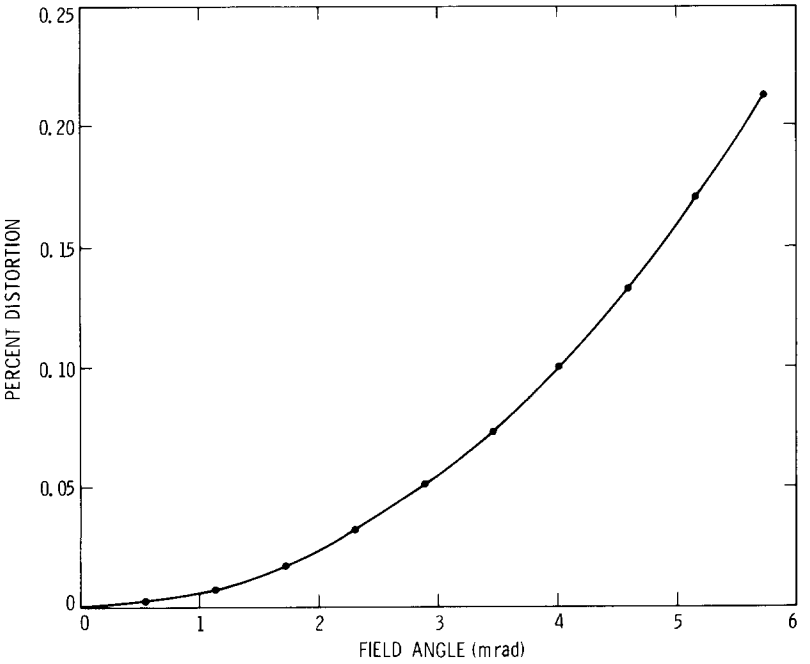

Figure 4-223. Percent distortion versus field angle of the pincushion distortion in the SSI optics.

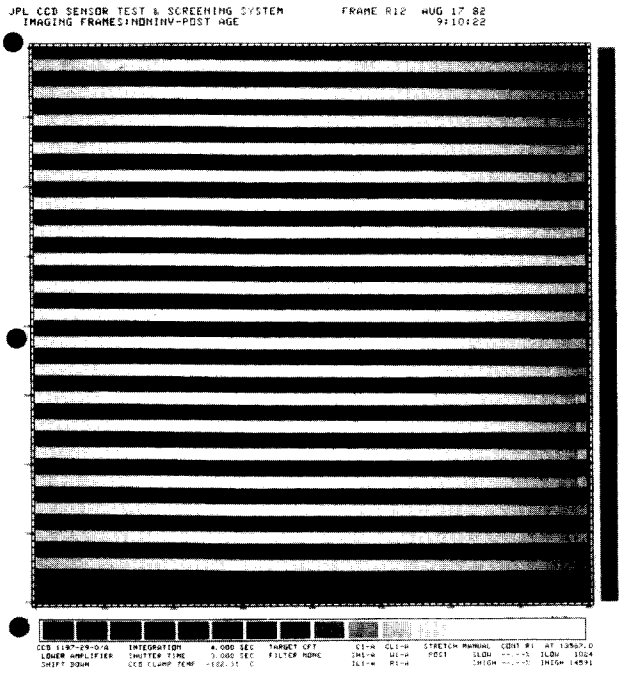

Figure 4-224. Image of a horizontal wide-bar target acquired at the component level using the Sensor Test Set (STS) camera.

aliasing effect was considered. Tests were done with different filter weights and with the grid target image flipped 180° to see if the resulting grid intersection locations changed; however, no differences were observed.

The structure of the virtual phase CCD does not allow pixel locations to be measured visually since the channel stops and virtual potential wells are formed by ion implantation into the silicon wafer and are therefore invisible. As a result, the SSI CCD itself was never geometrically calibrated directly. The gate structure that defines the CCD lines is visible, however, and since the observed distortion is apparent along the line direction, the straightness of the lines in another CCD from the same manufacturing lot as the SSI flight device was measured. No variation from perfect straightness was observed to less than 0.1 pixel.

Some images that contain some geometric information had been acquired at the component level with the SSI flight CCD using the Sensor Test Set (STS) camera. These images are of a horizontal wide-bar target and were intended for MTF and charge-transfer efficiency measurements. An example is shown in Figure 4-224. Since the STS bar target edges were measured and found to be straight to less than 0.2 pixel, the component-level CCD data allow us to determine whether similar distortions existed in STS images as were observed in the SSI subsystem grid target images. If so, the source of the distortion would appear to be within the CCD itself. Figure 4-225 plots the residuals to a straight line fit of three bar edges from Figure 4-224 (~lines 97, 395 and 635). These plots can be compared with plots of the residuals to linear fits of the grid target intersection coordinates in the SSI images in the horizontal direction, shown in Figure 4-226. The two residual plots are reasonably similar. Similar residuals were observed in STS images acquired several months apart at different signal levels with both inverted and non-inverted CCD parallel clock voltage settings. No differences in the shape of the edge profile were observed for different columns across the array, indicating that the charge transfer efficiency does not vary for different columns.

Further research into the cause of the observed distortion was conducted using additional SSI images of the grid target acquired through the Fairchild collimator at room temperature in the fall of 1987. Difference pictures of the grid target image minus a dark frame showed a vertical band around sample 200 where the CCD dark spikes (which become prominent with the CCD at room temperature) failed to subtract out. In addition, it was observed that line 1 was extraordinarily bright and line 800 was black to the left of this band. These effects demonstrated conclusively that a one-line shift in the image was occurring on the left side of the CCD and that the location of the line-shift boundary was somewhat signal-level

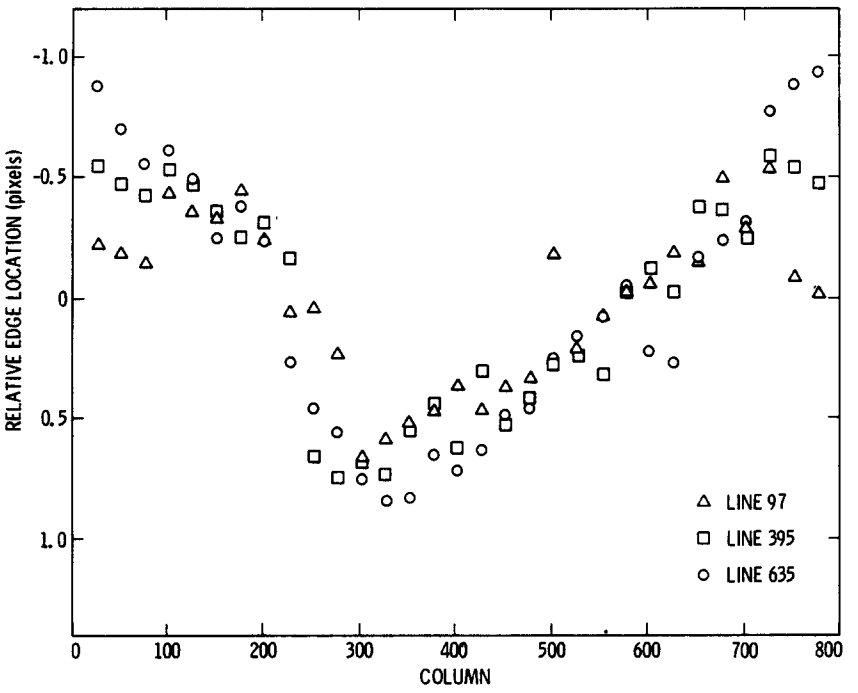

Figure 4-225. Plot of the residuals to a straight line fit of three bar edges from Figure 4-224.

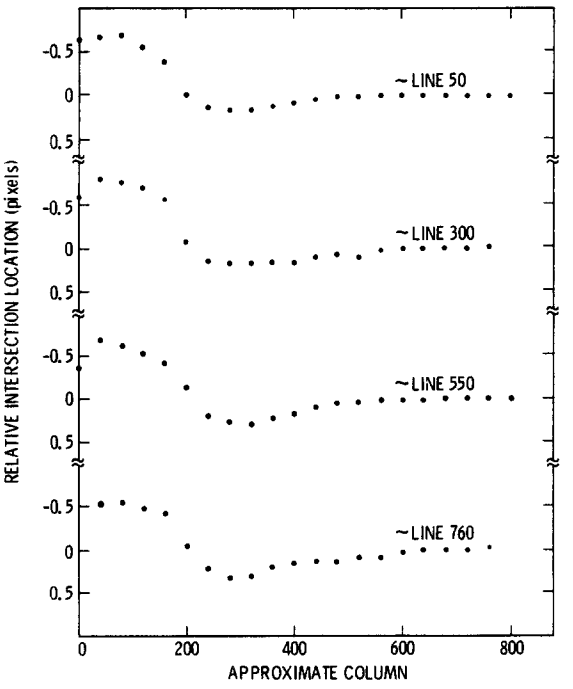

Figure 4-226. Plots of the residuals to linear fits of the grid target intersection coordinates in the horizontal direction.

dependent. The source of the problem was suspected to lie in the CCD transfer gate (located between the parallel and serial registers) since every line experienced the shift. Close examination of the CCD clock timing revealed that the shift was due to improper clocking of the transfer gate relative to the parallel gates. The line shift occurred only in part of the array due to clock pulse propagation delays in the gate itself. A hardware fix for this problem has been identified and will be implemented in the SSI.

It appears then that the SSI images acquired through 1987 do contain geometric distortion consisting of a combination of optical pincushion distortion plus a vertical shift of one pixel upward in the first ~300 columns. Assuming that the SSI hardware fix for the line shift problem is successful, the remaining distortion should be only the optical pincushion distortion. This expectation will be tested during the next calibration of the SSI.

2. Optical/Mechanical Alignment

In an ideal optical/mechanical alignment of the SSI, the boresight axis would be parallel to the instrument's scan platform mounting surface, and the columns of the CCD detector array would be perpendicular to the mounting surface. The goals of the Galileo boresight alignment procedure were to use autocollimation techniques to measure the angles (resolved into vertical and horizontal projections) between the telescope optical axis, a flat alignment mirror mounted on the front telescope mounting structure, and the instrument mounting surface, and to measure the rotation of the CCD detector with respect to the mounting surface. Figure 4-227 is a drawing showing the alignment geometry of the instrument. Figures 4-228 and 4-229 are photographs of the laboratory setup for the measurements, showing the SSI with the autocollimator and the alignment mirror. As given in Reference 4-2, the required accuracy of alignment between the SSI optical axis and the mounting surface is 0.3 mrad (1.0 arcmin), and the value should be known to within 0.15 mrad (0.5 arcmin). The CCD array columns should be perpendicular to the mounting surface to within 4.4 mrad (15 arcmin), and this value should be known to within 1.0 mrad (3.4 arcmin). Table 4-29 gives the measured values. It can be seen that the boresight/mounting platform alignment only marginally satisfies the specification, while the CCD rotation with respect to the mounting surface is well outside the specification. A waiver request (#33714) was submitted on account of this noncompliance of the hardware with the specification.

D. OPTICAL NAVIGATION CALIBRATIONS

In order to calibrate SSI images for optical navigation purposes, calibration frames were acquired using the optical navigation target. These data were delivered to the optical navigation group but have not yet been analyzed. These results may be reported in a future addendum to this report.

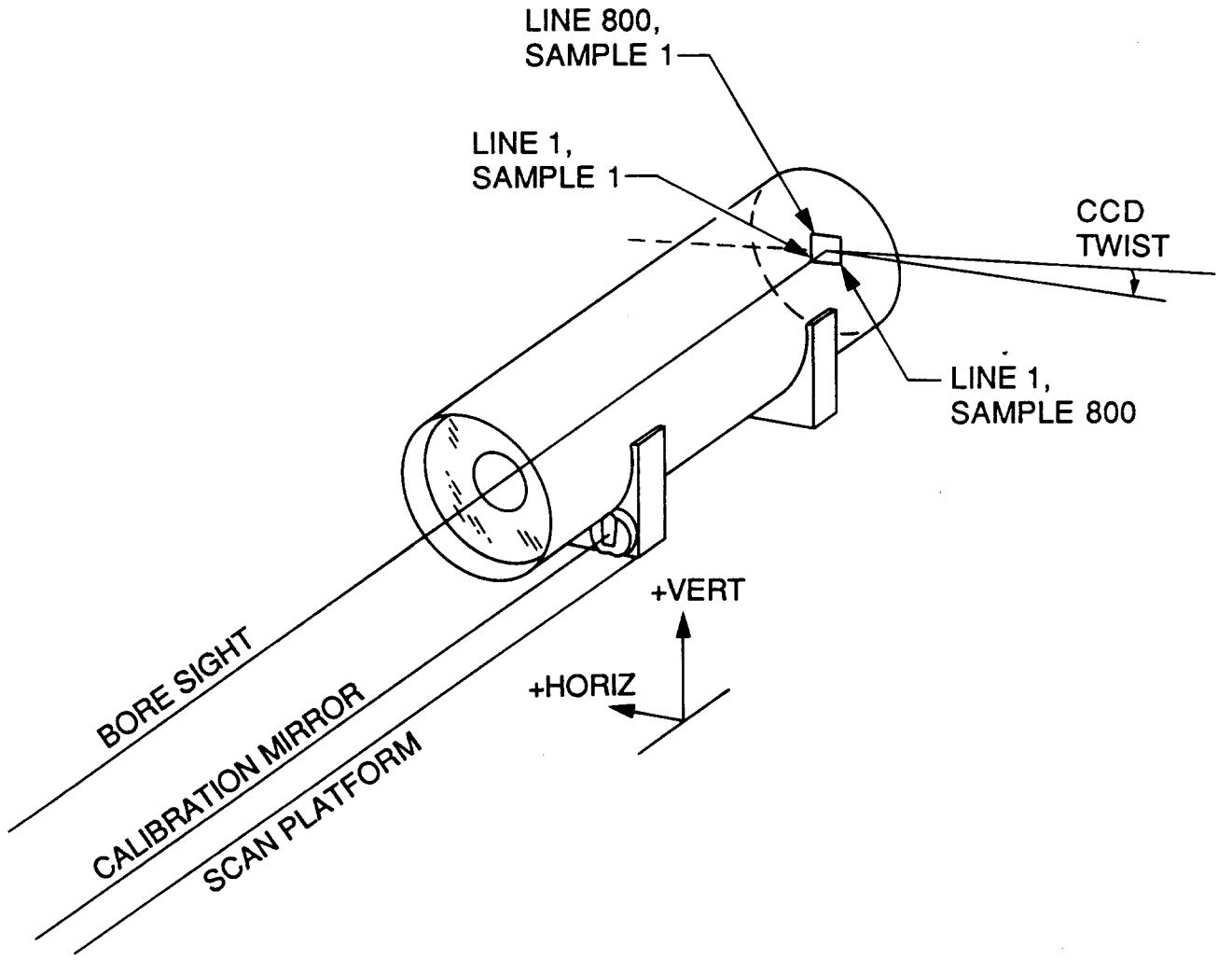

Figure 4-227. Drawing showing the alignment geometry of the SSI.

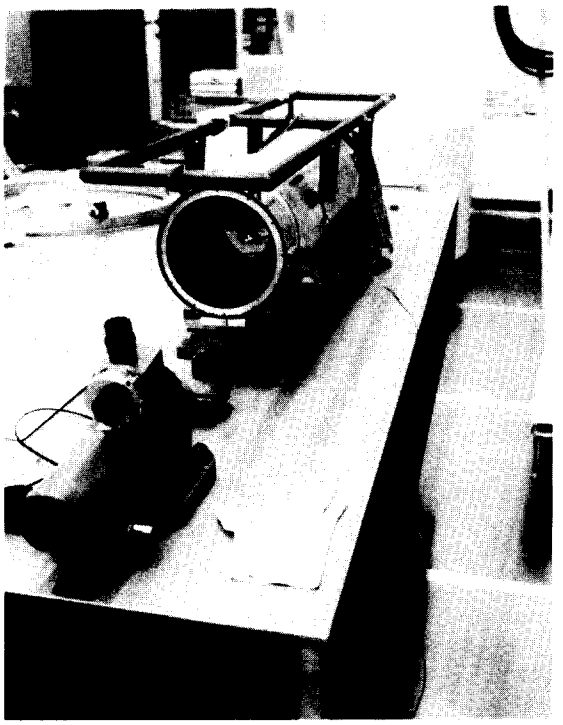

Figure 4-228. Photograph of the laboratory setup for the optical/mechanical alignment measurements.

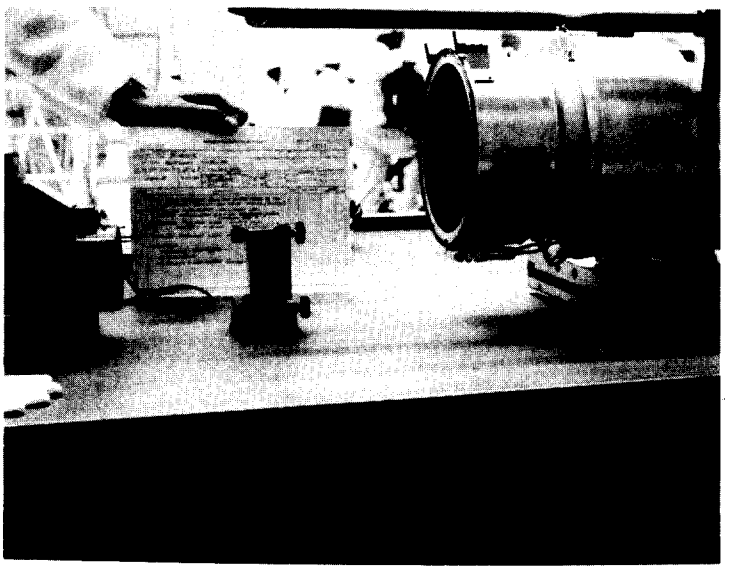

Figure 4-229. Photograph of the laboratory setup for the optical/mechanical alignment measurements.

Table 4-29. SSI Optical/Mechanical Alignment Data

		measured		knowledge (3σ)	
angle	comp.	mrad	pixels	mrad	pixels
boresight from scan platform	horiz.	-0.305	-30	±0.018	±1.7
	vert	+0.09	+ 9		
cal. mirror from scan platform	horiz	-0.27	-	±0.009	-
	vert.	+0.39	-		
cal. mirror from boresight	horiz.	+0.035	-	±0.020	-
	vert.	+0.30	-		
CCD rotation (clockwise)		11.8	10	±1.5	±1.2

REFERENCES

4-1. "Geometric Distortion Measurements for VGR Vidicon S/N 1-8", G. Yagi to P. Jepsen, IOM 324-IPL/SIPG-77-199, 23 September 1977.

4-2. "Functional Requirement, Galileo Orbiter -- Functional Accuracies and System Capabilities", GLL-3-170 Rev. B, 15 August 1983.

4-3. "Revised MTF Analysis Versus Temperature: June 1983 SSI Data", M. Morrill to K. Klaasen, IOM 15 January 1986.